Serpentinite phase relations – An experimental study on redox conditions and fluid migration in subduction zones

DISSERTATION

zur Erlangung des akademischen Grades einer Doktorin
der Naturwissenschaften (Dr. rer. nat.)
in der Bayreuther Graduiertenschule für Mathematik und Naturwissenschaften
(BayNAT) der Universität Bayreuth

vorgelegt von

Lisa Eberhard
aus *Biel/Bienne*
Bayreuth, 2020

Die vorliegende Arbeit wurde in der Zeit von Juli 2017 bis November 2020 in Bayreuth am Bayerischen Geoinstitut unter Betreuung von Herrn Professor Dr. Daniel Frost angefertigt.

Vollständiger Abdruck der von der Bayreuther Graduiertenschule für Mathematik und Naturwissenschaften (BayNAT) der Universität Bayreuth genehmigten Dissertation zur Erlangung des akademischen Grades einer Doktorin der Naturwissenschaften (Dr. rer. nat.).

Dissertation eingereicht am: 24.11.2020

Zulassung durch das Leitungsgremium: 26.11.2020

Wissenschaftliches Kolloquium: 18.12.2020

Amtierender Direktor: Prof. Dr. Markus Lippitz

Prüfungsausschuss:

Prof. Dr. Daniel Frost	(Gutachter)
PD Dr. Catherine McCammon	(Gutachterin)
PD Dr. Gerd Steinle-Neumann	(Vorsitz)
Prof. Dr. David Rubie	

七転び八起き

(Nana korobi ya oki)

Summary

The oceanic lithosphere sinks into the Earth's mantle at subduction zones, a process that provides an engine for material exchange between the surface and the Earth's deep interior. Serpentinisation fixes H_2O in the oceanic lithosphere. This process also oxidises ferrous to ferric Fe, so that the subduction of serpentinites is an important process through which oxidised material is transported into the mantle. This transport has consequences not only for the redox state of the mantle but for the oxidation state of carbon- and sulfur-bearing volatile phases and their transport into the overlying mantle wedge. The main aim of this study is to provide the first experimental data to determine the relationship between the oxidation state of Fe in serpentinites and the oxygen fugacity $f(O_2)$. Using this relationship, the effect of ferric Fe on the phase relations within subducting slabs and the speciation of volatile components can be constrained.

In the first part of this study multi-anvil experiments were performed between 2.5 and 5 GPa to examine the phase relations of antigorite- and lizardite-serpentinites. The $f(O_2)$ was buffered by various metal-oxide pairs. Mössbauer spectroscopy shows that Fe^{3+} is charge balanced by a coupled substitution with Al in both serpentine minerals. Thermodynamic properties are derived to describe the substitution of both elements in both minerals. Lizardite displays a higher $Fe^{3+}/\Sigma Fe$ ratio than antigorite under similar conditions, whereas the phase relations of antigorite and lizardite are found to be identical. Global Gibbs free energy minimisation calculations show that Al increases the stability of serpentine, whereas ferric and ferrous Fe decrease the stability. The effects are very small, however, and cannot explain differences among previous studies. Serpentine is found to dehydrate at lower temperatures with decreasing $f(O_2)$, due to a process termed redox dehydration.

Most serpentinites have compositions that result in $f(O_2)$ in the range ΔFMQ-0.5 to ΔFMQ$+2$ at 500 °C. As antigorite dehydrates at temperatures above 600 °C, the $f(O_2)$, regardless of the initial bulk $Fe^{3+}/\Sigma Fe$ ratio, will become buffered by the coexistence of magnetite and hematite. This oxidation state cannot be communicated to the mantle wedge through transfer of sulfate-rich fluids, since the $f(O_2)$ remains below the sulfide-sulfate equilibrium. The $f(O_2)$ during serpentinite subduction will also remain in the carbonate stability field. Previous observations of carbonate reduction to graphite associated with serpentinites and the disappearance of magnetite must result from the action of external reducing agents, such as H_2.

Calculations for the overlying mantle wedge, where antigorite forms from H_2O released by the slab, show this to be one of the most reduced regions of the upper mantle. CO_2 in fluids entering the wedge would consequently be reduced to CH_4 and the mantle would be oxidised. This might explain the apparent raised oxidation state of island arc magmas.

In the second part of the thesis phase relations in carbonated ($CaCO_3$-bearing) antigorite-serpentinites, similar to ophicarbonates, were examined. Ca-Mg exchange results in the formation clinopyroxene, which replaces orthopyroxene and leads to a strong decrease in antigorite dehydration temperature. This will prevent the antigorite stability field from reaching conditions where dense hydrous magnesium silicates form. The presence of ophicarbonates will, therefore, favour the subduction of carbonate-rich but water-poor assemblages into the deep mantle.

In the final part of this study a new technique was developed to measure permeabilities at high pressures and temperatures. The method was used to measure the permeability in serpentinites during dehydration. In multi-anvil experiments strongly foliated serpentine cylinders were embedded in MgO sleeves. Fluids, formed upon dehydration, migrate outward and react with MgO to produce brucite. The fluid flux is calculated from the amount of brucite formed. Using equations of state to determine the fluid overpressure, the permeability is subsequently calculated with Darcy's law. A slightly modified setup, using $Al(OH)_3$ as the fluid source, was used to analyse the permeability prior to dehydration of antigorite. The results indicate a large increase in permeability of about 2 log units upon serpentine dehydration to near $1 \cdot 10^{-18}\,\mathrm{m}^2$ at 3 GPa, whereas serpentinites are found to be impermeable below the dehydration temperature. Although previous studies performed at near room pressure and temperature indicate that foliated serpentinites exhibit strong permeability anisotropy, the results reported here indicate that all anisotropy is lost once dehydration commences. An anomalously low fluid flux measured at 5 GPa provides the first experimental evidence for pore fluid underpressure upon antigorite dehydration at pressures above 3 GPa, that may prevent fluids from leaving the slab. Below this pressure, however, the large increase in permeability and the lack of permeability anisotropy as antigorite starts to dehydrate will favour pervasive rather than channelised fluid flow, which will promote the decarbonatisation of the slab by dissolution of carbonates in H_2O.

Zusammenfassung

Die ozeanische Lithosphäre sinkt in den Erdmantel entlang von Subduktionszonen, ein Prozess der den Materialaustausch zwischen der Erdoberfläche und dem Erdinneren antreibt. Serpentinisierung am Ozeanboden bindet H_2O in der ozeanischen Lithosphäre, führt aber auch zur Oxidation von Fe^{2+} zu Fe^{3+}. Die Subduktion von Serpentiniten ist deshalb ein wichtiger Prozess, der oxidiertes Material in den Mantel transportiert. Dieser Transport beeinflusst den Redoxzustand des Erdmantels sowie auch den Oxidationszustand von kohlenstoff- und schwefelhaltigen Fluiden und deren Transport in den darüberliegenden Mantelkeil. Das Hauptziel dieser Arbeit ist, die ersten experimentellen Daten zur Beziehung zwischen dem Oxidationszustand von Eisen in Serpentiniten und der Sauerstofffugazität $f(O_2)$ zu liefern. Mit dieser Beziehung können Auswirkungen von Fe^{3+} auf die Phasenbeziehungen in subduzierten Platten sowie die Speziation von volatilen Komponenten berechnet werden.

Im ersten Teil dieser Arbeit wurden Experimente mit einer Viel-Stempel-Presse im Bereich von 2.5 bis 5 GPa durchgeführt, um die Phasenbeziehungen in Antigorit- und Lizarditserpentiniten zu untersuchen. Die $f(O_2)$ wurde durch verschiedene Metall-Oxid-Paare gepuffert. Mittels Mössbauerspektroskopie kann gezeigt werden, dass in beiden Serpentinmineralen die Ladung von Fe^{3+} ausgeglichen wird durch eine gekoppelte Substitution mit Al. Thermodynamische Eigenschaften wurden hergeleitet, um die Substitution von beiden Komponenten in beiden Phasen zu beschreiben. Lizardit hat ein höheres $Fe^{3+}/\Sigma Fe$ Verhältnis als Antigorit bei ähnlichen Bedingungen, wobei jedoch die Phasenbeziehungen gleich sind. Globale Minimierungen der freien Enthalpie zeigen, dass Al die Stabilität von Serpentin erhöht, Fe^{3+} sowie auch Fe^{2+} jedoch die Stabilität verringern. Die Auswirkungen sind allerdings klein und können die Unterschiede zwischen früheren Arbeiten nicht erklären. Mit abnehmender $f(O_2)$ dehydriert Serpentin bei tieferer Temperatur, ein Phänomen, das als Redoxdehydratation bezeichnet werden kann.

Die Zusammensetzung der meisten Serpentinite führt zu einer $f(O_2)$ im Bereich von ΔFMQ−0,5 und ΔFMQ+2 bei 500 °C. Wenn Antigorit bei Temperaturen über 600 °C dehydriert, wird die $f(O_2)$ unabhängig vom ursprünglichen Bulk-$Fe^{3+}/\Sigma Fe$ Verhältnis durch die Koexistenz mit Magnetit und Hämatit gepuffert. Dieser Oxidationszustand kann durch sulfatreiche Flüssigkeiten nicht an den Mantelkeil übertragen werden, da die $f(O_2)$ unterhalb des Sulfid-Sulfat-Gleichgewichtes bleibt. Die $f(O_2)$ von Serpentiniten in Subduktionszonen bleibt auch im Karbonatstabilitätsbereich. Frühere Beobachtungen wie die Reduktion von Karbonat zu Graphit in Gesteinen assoziiert mit Serpentiniten, sowie auch das Verschwinden von Magnetit können deshalb nur durch ein externes Reduktionsmittel wie H_2 erklärt werden.

Für den darüberliegenden Mantelkeil, in welchem sich Antigorit durch von der subduzierten Platte freigesetztes H_2O bildet, zeigte sich, dass dies eine der reduziertesten Regionen im oberen Erdmantel ist. In Flüssigkeiten gelöstes CO_2 wird reduziert zu CH_4, wobei der Erdmantel oxidiert wird. Dies könnte den hohen Oxidationszustand in Inselbogenmagmen erklären.

Im zweiten Teil dieser Arbeit wurden die Phasenbeziehungen von karbonatisierten ($CaCO_3$-haltigen) Antigoritserpentiniten, ähnlich zu Ophikarbonaten, untersucht. Der Ca-Mg-Austausch bildet Klinopyroxen, welcher Orthopyroxen ersetzt und die Dehydratationstemperatur von Antigorit stark erniedrigt. Dies wiederum verhindert, dass das Antigoritstabilitätsfeld Bedingungen erreicht unter welchen sich dichte wasserhaltige Magnesiumsilikate bilden. Das Vorhandensein von Ophikarbonaten begünstigt demnach die Subduktion von karbonatreichen aber wasserarmen Gesteinen in den tiefen Mantel.

Im letzten Teil dieser Arbeit wurde eine neue Methode zur Bestimmung von Permeabilitäten bei hohem Druck und Temperatur entwickelt. Die Methode wurde angewendet, um die Permeabilität in Serpentiniten während der Dehydratation zu bestimmen. In Experimenten in einer Viel-Stempel-Presse wurden Zylinder aus blättrigen Serpentiniten in eine Hülle aus MgO eingebettet. Während der Dehydratation gebildete Fluide migrieren nach außen und reagieren mit MgO zu Brucit. Der Fluidfluss wurde aus der Menge des gebildeten Brucits berechnet. Mittels Zustandsgleichungen wurde der Überdruck berechnet und daraus mit Hilfe des Gesetzes von Darcy die Permeabilität bestimmt. Eine leicht abgeänderte Konfiguration mit $Al(OH)_3$ als Wasserquelle wurde benutzt, um die Permeabilität vor der Antigoritdehydratation zu bestimmen. Diese Resultate zeigen, dass die Permeabilität während der Dehydratation um 2 Größenordnungen zunimmt auf nahezu $1 \cdot 10^{-18}\,\mathrm{m}^2$ bei 3 GPa. Unterhalb der Dehydratationstemperatur sind Serpentinite jedoch undurchlässig. Obwohl frühere Studien zeigten, dass bei nahezu Raumdruck und -temperatur Antigorit eine starke Permeabilitätsanisotropie aufweist, zeigen diese Resultate auch, dass sämtliche Anisotropie beim Einsetzen der Dehydratation verloren geht. Ein anomal tiefer Fluidfluss bei 5 GPa liefert den ersten experimentellen Nachweis eines Unterdrucks des Porenfluides bei der Dehydratation von Antigorit oberhalb 3 GPa, welcher das Fluid in der subduzierten Platte zurückhalten kann. Unterhalb dieses Druckes jedoch begünstigt die starke Zunahme der Permeabilität sowie der Verlust der Anisotropie einen pervasiven Fluidfluss gegenüber einem kanalisierten Fluidflusses, was wiederum die Dekarbonatisierung durch Auflösung von Karbonaten in H_2O begünstigt.

Contents

1 Introduction

1.1 Planet Earth and volatiles

Planet Earth is known as the blue planet in our Solar System as it has the unique feature that the majority of its surface is covered by liquid water. It is perhaps no coincidence that Earth is also a very dynamic planet: its climate and the distribution of land masses have changed over time, for example, from periods of almost complete ocean coverage to those of complete ice cover, and from the occurrence of single landmasses to periods where many different continents existed. There are significant reasons to believe that these changes, which are unique in the solar system, are coupled to some degree through processes that exchange materials between reservoirs at the surface and those within the deep interior of the Earth (Stanley, 2005; Stern, 2018).

Important information on the Earth's interior can be obtained from the action of volcanic activity and the occurrence of earthquakes. Volcanic activity transports rocks and magmas from deeper levels to the surface, from which direct evidence concerning the chemical composition of the Earth's interior can be obtained. Earthquakes release energy and generate seismic waves that travel through the planet. Based on the travel times and reflections of waves recorded at the surface it is possible to divide the Earth's interior into different layers. The Earth is divided into the crust, mantle and core by the Mohorovičić and the Wiechert-Gutenberg discontinuity. Further subdivision separates the mantle into the upper mantle, the transition zone and the lower mantle. The core is divided into a liquid outer and a solid inner core.

The outermost parts of the Earth can also be separated based on their rheological properties. The lithosphere is the outermost solid part of the Earth and comprised by the crust and the lithospheric mantle. The lithosphere forms the Earth's tectonic plates, which drift over the asthenospheric mantle, as first identified by Wegener (1912). Based on their composition, the individual tectonic plates are distinguished into the continental and oceanic lithosphere, making up the Earth's continents and ocean floors. The movements of the tectonic plates are caused by the creation and destruction of oceanic lithosphere. At spreading centres, called mid-ocean ridges (MOR), new oceanic lithosphere is created through partial melting caused by decompression of the upwelling mantle. Along subduction zones, the denser oceanic lithosphere is subducted below the lighter continental lithosphere and recycled into the mantle (fig. 1.1).

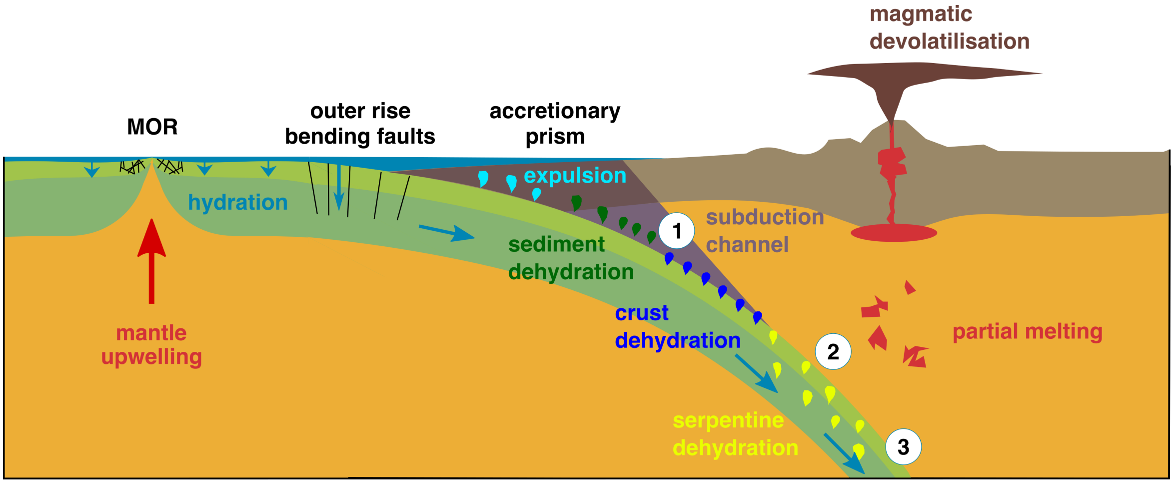

Figure 1.1: New oceanic lithosphere is formed at the MOR. Subsequent hydration by interaction with seawater affects the thin oceanic crust and upper part of the mantle lithosphere. Deeper parts of the lithosphere are accessed via bending faults. During subduction, successively deeper parts of the hydrated lithosphere are dehydrated. Numbers mark locations of fluid flux as discussed in section 1.2.1. Modified after Rüpke et al. (2004).

Compositionally, the oceanic lithosphere can be divided into 3 parts: an upper sediment layer which can vary significantly in composition and thickness depending on the location, the oceanic crust (0 - 10 km) consisting of basalts and gabbros formed through decompression melting of the mantle, and the lithospheric mantle (10 - 150 km) comprised of the residual mantle rocks after the extraction of melt.

An important process taking place is the geochemical exchange between the oceanic lithosphere and the ocean. A network of steep faults at the MOR allows hydrothermal fluids to circulate in the lithosphere. Low angle detachment faults expose the lithospheric mantle directly to the sea water along slow spreading ridges. Furthermore, steep and deep rooting bending faults in the outer rise region allow seawater to access deeper parts of the lithosphere. Fluid-rock interaction significantly alters the mineralogy and geochemistry of the lithosphere and in particular raises its volatile content (Ulmer and Trommsdorff, 1995; Kodolanyi et al., 2012; Schwarzenbach et al., 2016).

In order to maintain a constant Earth radius, in contrast to earlier theories that proposed Earth's expansion (Mantovani, 1889) or contraction (Sengor, 2014), oceanic lithosphere must be recycled back into the interior at destructive plate boundaries in a process known as subduction. This cycle of crustal material is of major interest since it allows geochemical reservoirs at the Earth's surface to interact with the interior. In this way volatile components, such as H_2O, O_2 and CO_2, that are added to the oceanic lithosphere at the surface, are transported to the interior (fig. 1.1). This has two potentially very important consequences. (1) The presence and cycling of volatiles into the mantle has likely affected transport properties and in particular the rheology of the mantle and consequently plate tectonics. (2) The compositions of both the atmosphere and the Earth's mantle have likely changed over time due to this exchange of material.

1.2 Volatile cycles

H_2O, O_2 and CO_2 are the most important volatile components for life. In the Earth's interior the same components influence physical and chemical properties such as viscosity, density, redox state and melting behaviour. It is thus important to understand how much of each of these components is stored in the Earth, how these interior reservoirs have interacted with the surface through deep volatile cycles, and how their proportions have consequently changed through time.

The initial stage of a deep volatile cycle is the fixation of the volatile compound into the oceanic lithosphere at the surface, followed by its transport into the Earth through subduction. The subsequent release of the volatile compound from the lithosphere depends on a number of factors and requires a more specific understanding of subduction processes. As the lithosphere heats up during subduction, devolatilisation reactions release volatiles that migrate into the overlying mantle. In the mantle they are eventually involved in hydration and partial melting. The resulting volatile-bearing magmas are responsible for arc volcanism, during which volcanic degassing transports volatiles back into the atmosphere (e.g Schmidt and Poli, 1998; Kerrick and Connolly, 2001). It is also possible that volatiles remain at least partially within the lithospshere and are subducted back into the deep mantle reservoir (Ohtani, 2020). The quantification of fluxes in the individual stages of this cycle, however, is very difficult and studies to date differ from each other in their estimates (van Keken et al., 2011; Cai et al., 2018).

1.2.1 Fluid fluxes

The subduction of oceanic lithosphere transports a large amount of H_2O into the Earth's interior. Estimated H_2O fluxes range from $0.1 \cdot 10^{12}$ - $3 \cdot 10^{12}$ kg yr^{-1} (Rüpke et al., 2004; van Keken et al., 2011; Korenaga, 2017; Cai et al., 2018). Discrepancies are attributed mostly to variations in the extent of hydration of the downgoing slabs. The extent of hydration varies between subduction zones due to the age, thermal structure and the occurrence of faults in the slab. Water is mainly stored as pore water and as OH-groups in hydrous minerals. In the sediment layer, hydrous minerals include sheet silicates such as clays and micas. Lawsonite, zoisite and amphiboles might also be present (Deer et al., 1992; van Keken et al., 2011). In the hydrated basaltic crust, the most important hydrous minerals are chlorite, epidote, zoisite and lawsonite (Deer et al., 1992; Schmidt and Poli, 1998; Kawamoto, 2006). In the hydrated peridotite, serpentine and chlorite are the major hydrous phases (Bailey, 1988; Deer et al., 1992).

Depending on how the fluid is bound in the subducting slab, it may be released in different stages of subduction. While pore water is expelled in the early stages of subduction due to overpressure, mineral bound water is carried to greater depths and is released via dehydration reactions. Hydrous minerals thereby dehydrate at different depths, depending on their individual stability limits, leading to fluids being released over a range of depths as shown in figure 1.1. While the fluids released early in the subduction process migrate upward along the subduction channel (① in fig. 1.1), fluids released deeper in the subduction zones interact with the mantle wedge (② in fig. 1.1). Large textural features such as mineral preferred orientation but also fault zones may have a major impact on the nature of fluid flow and might lead to focusing of the flow (Kawano et al., 2011; Okazaki et al., 2013; Plümper et al., 2016). Once the fluids reach the top of the slab, they may continue to migrate and thereby wet the mantle wedge (Smith, 2010; Pirard and Hermann, 2015; Guillot et al., 2000). However, some of the subducted fluid can also be transported towards the lower portions of the mantle, where it will rehydrate the Earth's deep interior (③ in fig. 1.1) (Kerrick and Connolly, 2001; van Keken et al., 2011). Fluids might thereby be retained in the slab as a result of the stability of dense hydrous magnesium silicates at pressures above 6 GPa (Kawamoto, 2006; Ohtani, 2020). Another possibility would be that released fluids are simply trapped along dihedral angles, a process that might strongly depend on the composition of the fluid (Huang et al., 2019).

Similar to the uncertainties in H_2O fluxes, the global carbon flux remains poorly constrained. Global carbon influx zones ranges from $4.0 \cdot 10^{10}$ - $8.8 \cdot 10^{10}$ kg C/yr (Dasgupta, 2013; Kelemen and Manning, 2015). Estimates on how much of this carbon is recycled back to the Earth's surface ranges from very little up to 80 % due to the unknown proportion of carbonation and decarbonation (Gorman et al., 2006; Dasgupta and Hirschmann, 2010; Cook-Kollars et al., 2014; Kelemen and Manning, 2015).

Carbon is mainly subducted in the form of carbonates in the sediment layer as well as in carbonated crust and peridotites. Additionally, carbon in the form of organic compounds and graphite might be present. Sediments contain marine and terrestrial carbonates as well as organic remains from organisms. However, the thickness and composition of the sediment layer varies between different slabs (Plank and Manning, 2019). Depending on the location of the slab with respect to land masses, as well as factors such as ocean currents, the continental carbon fraction varies between different slabs. The depth of a particular ocean might result in a loss of the accumulated carbon due to the carbon compensation depth (CCD). The CCD marks the depth in an ocean, below which no carbonate is preserved due to the increased solubility of carbonates at low temperature and high pressure conditions. Hydration and carbonation processes penetrate the lithosphere to different depths in different locations, altering the total quantity of carbon that the slab carries (Plank and Manning, 2019).

Carbonates are stable at pressures P and temperatures T in the range of upper mantle conditions. Thus, carbonated slabs might transport carbon deep into the Earth (Thomson et al., 2016). However, during devolatilisation within subduction zones a fraction of the total carbonate content is removed from the slab. An important mechanism for carbonate removal is the dissolution in H_2O-rich fluids. Although $X(CO_2)$, being molar $CO_2/(CO_2 + H_2O)$, in subduction zone fluids is relatively low (<0.01), it has been shown that in open systems H_2O-rich fluids can efficiently remove carbon through continuous fluid flux (Tian et al., 2019; Menzel et al., 2020). The very simple picture of having neutral molecules resulting in a H_2O-CO_2-CH_4 fluid does not match reality and many different species may occur, which might increase the total carbon load in the fluid (Ague, 2014; Tumiati et al., 2017).

The absolute amount of released carbon varies between different slabs based on various factors. For example the age of the subducting slab, one of the key parameters defining the dipping angle of the slab, results in varying PT-paths and thus affects how much carbon is released from the slab, because stability fields for various phases will be intersected in different depths for slabs descending at different angles. Also the nature of fluid migration has an influence on the extent of carbon release as focused fluid flow allows for less fluid-rock interaction in comparison to a pervasive fluid flow. A further complicating aspect is that the stability of carbon-bearing phases and components also depends on the oxygen fugacity. Reducing conditions must exist in the mantle because graphite and diamonds have been reported from subduction related localities (Frezzotti et al., 2011; Galvez et al., 2013). Although it is often assumed that carbonate is the main form in which carbon is subducted, organic carbon compounds are probably also present (Shilobreeva et al., 2011; Shirey et al., 2013), which has been based on low $\delta^{13}C$ isotopic signatures. A recent study by Li et al. (2019) nevertheless questioned the significant contribution of organic material to low $\delta^{13}C$ values in deep diamonds. However, when graphite or diamond forms either from organic materials or through the reduction of carbonates they are likely to fix carbon in the subducting slab where it remains into the deep mantle (Plank and Manning, 2019). Although a number of studies have examined the stability of carbonates and hydrous minerals in the past (e.g. Ulmer and Trommsdorff, 1995; Bromiley and Pawley, 2003; Padrón-Navarta et al., 2013; Menzel et al., 2019, 2020), less attention has been paid as to how these phases affect the phase relations by lowering the activities of either H_2O or CO_2 in fluids, as these phases break down. Furthermore it is also possible that the redox state of the lithosphere changes the stability field of volatile-bearing minerals by influencing the composition of COH-fluids produced by such devolatilisation reactions.

1.2.2 Hydration of the oceanic lithosphere

Fluid-rock interaction within the oceanic lithosphere at the surface produces distinct alteration mineralogy. Alteration of the plagioclase- and clinopyroxene-rich oceanic crust results in an assemblage of albite+chlorite+epidote, or so-called greenstones. The hydration of olivine-dominated peridotite forms the typical serpentinite mineral assemblage lizardite+magnetite±brucite (Liz+Mgt±Br). Serpentinites are the most important carriers of water into subduction zones (see also section 1.4 for a discussion of various serpentine minerals and their structure). The process forming serpentinites from hydration of olivine (Ol) and pyroxene (Px) is known as serpentinisation. At low temperature, typically below 200 - 300 °C, serpentinisation in a simple MSH (MgO-SiO_2-H_2O) system forms Liz according to:

$$\begin{array}{ccccccc} 2\ \mathrm{Mg_2SiO_4} & + & 3\ \mathrm{H_2O} & \rightarrow & \mathrm{Mg_3Si_2O_5(OH)_4} & + & \mathrm{Mg(OH)_2} \\ \mathrm{Ol} & & \mathrm{fluid} & & \mathrm{Liz} & & \mathrm{Br} \end{array} \tag{1.1}$$

$$\begin{array}{ccccccc} 2\ \mathrm{MgSiO_3} & + & \mathrm{Mg(OH)_2} & + & \mathrm{H_2O} & \rightarrow & \mathrm{Mg_3Si_2O_5(OH)_4} \\ \mathrm{Px} & & \mathrm{Br} & & \mathrm{fluid} & & \mathrm{Liz} \end{array} \tag{1.2}$$

Natural peridotites, however, contain ferrous Fe and consequently Fe^{2+}-bearing Liz is formed. Liz forming from Ol has a lower Fe#, being molar FeO/(MgO + FeO), with respect to Ol. Due to the slow kinetics of Fe^{2+}-Mg exchange in Ol, however, the Ol composition will not change upon the reaction. An additional Fe-bearing phase needs to be formed. The interaction between Fe^{2+} and H_2O also leads to Fe oxidation and the formation of Mgt along with hydrogen. This is an important redox process that raises the oxidation state of the oceanic lithosphere and forms of a fluid with a relatively high hydrogen fugacity ($f(H_2)$) (Evans, 2008). As proposed by Evans (2010), the formation of Mgt is likely a kinetic effect that occurs at low temperatures (50 - 300 °C) as a result of slow Fe^{2+} and Mg diffusion in Ol. If the hydration of Ol occurs at high PT conditions, on the other hand, the serpentine mineral antigorite (Atg) is formed along with only minimal or even no Mgt because Fe^{2+}-Mg exchange between the silicate phases can reach equilibrium. Evidence is found in Atg peridotite in the Green Knobs diatreme, where Atg is in equilibrium with Fe^{2+}-rich Ol in the absence of Mgt (Smith, 2010).

The ferric Fe content of natural serpentinites is highly variable. Figure 1.2 shows that the bulk $Fe^{3+}/\Sigma Fe$ ratio increases with bulk water content, ranging from zero to almost unity (Evans, 2008). Mgt can not account for all the ferric Fe and a part is also present in coexisting serpentine minerals. Evans (2008) proposed that a high Fe# in Liz indicates increased ferric Fe contents in Liz. This can be confirmed by decreased Si pfu, indicating a cronstedtite component in which the ferric Fe is charge balanced by a coupled substitution on a tetrahedral and octahedral sites as $Fe^{2+}{}_2Fe^{3+}|Fe^{3+}Si|O_5(OH)_4$ (compare section 1.4). Another substitution mechanism is proposed by Evans et al. (2009), who reported an occurrence of yellowish Liz-serpentinite containing essentially no Mgt, where the ferric Fe content was charge balanced by vacancies v on the octahedral site, i.e. $Fe^{3+}{}_2v|Si_2|O_5(OH)_4$. The constant effective Si pfu in this sample indicates an elevated silica activity, as might be found in the vicinity of Px. Consequently, both Mgt and serpentine minerals will transport ferric Fe into subduction zones where they might undergo

Fe redox reactions that could influence the oxidation state and the speciation of volatile elements in the descending slab.
The O_2-scavenging serpentinisation process not only affects the composition of circulating fluids but it might also have influenced the early Earth's atmosphere and the origin of life. High H_2 concentrations in the early oceans may have promoted the abiogenic synthesis of hydrocarbons through Fischer-Tropsch-type reactions, producing organic compounds, and possibly also served as an energy source for early life (Evans, 2010). Analogous processes might still be found today in places with active serpentinisation such as the Lost City hydrothermal field in the Atlantic Ocean, where both methane-producing and methane-consuming archaea have been detected in carbonate-brucite chimneys (Früh-Green et al., 2003; Kelley et al., 2005). It has also been proposed that serpentinisation of the predominantly mafic early Archean crust prevented the biologically driven rise of O_2 in the atmosphere due to the release of H_2 (Smit and Mezger, 2017). The O_2 level of the atmosphere could only rise once a significant proportion of mafic crust had been replaced by more silica-rich continental crust.

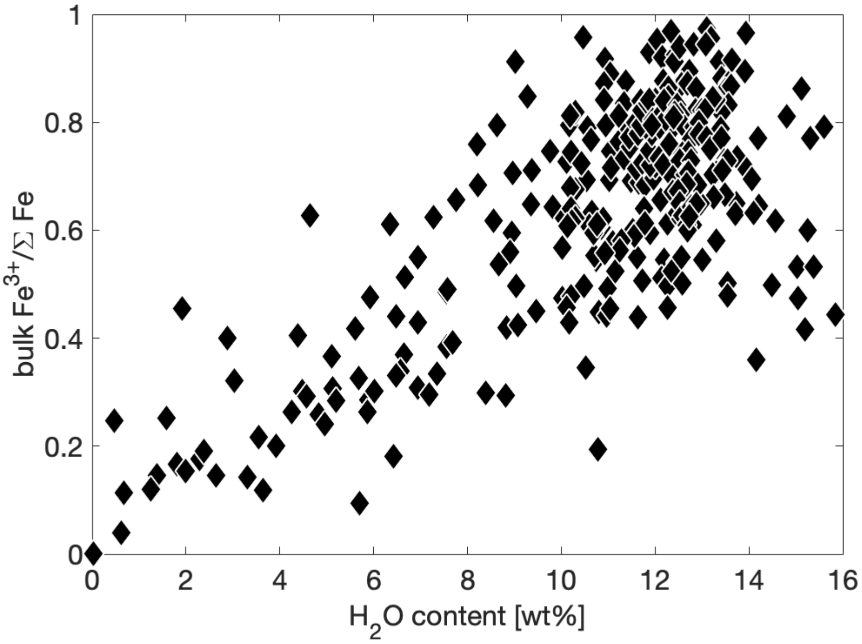

Figure 1.2: The range of bulk $Fe^{3+}/\Sigma Fe$ in natural serpentinites worldwide correlates with the bulk rock H_2O content, indicating that hydration and oxidation occur together. Modified after Evans (2008) and data therein.

1.2.3 Carbonation

Within a subducting slab carbonates mainly occur in the sediment layer and in the basaltic crust (Alt and Teagle, 1999). The underlying peridotites can contain carbonates formed either via mineral carbonation reactions with COH-fluids or via direct carbonate precipitation. The carbonation of a peridotite can be simplified by a stepwise alteration of Ol according to Kelemen et al. (2011):

$$\underset{\text{Ol}}{4\ \mathrm{Mg_2SiO_4}} + \underset{\text{fluid}}{6\ \mathrm{H_2O}} = \underset{\text{Liz}}{2\ \mathrm{Mg_3Si_2O_5(OH)_4}} + \underset{\text{Br}}{2\ \mathrm{Mg(OH)_2}}, \tag{1.3}$$

$$\underset{\text{Br}}{2\ \mathrm{Mg(OH)_2}} + \underset{\text{fluid}}{2\ \mathrm{CO_2}} = \underset{\text{Mgs}}{2\ \mathrm{MgCO_3}} + \underset{\text{fluid}}{2\ \mathrm{H_2O}}, \tag{1.4}$$

$$\underset{\text{Liz}}{2\ \mathrm{Mg_3Si_2O_5(OH)_4}} + \underset{\text{fluid}}{3\ \mathrm{CO_2}} = \underset{\text{Tlc}}{\mathrm{Mg_3Si_4O_{10}(OH)_2}} + \underset{\text{Mgs}}{3\ \mathrm{MgCO_3}} + \underset{\text{fluid}}{3\ \mathrm{H_2O}}, \tag{1.5}$$

$$\underset{\text{Tlc}}{\mathrm{Mg_3Si_4O_{10}(OH)_2}} + \underset{\text{fluid}}{3\ \mathrm{CO_2}} = \underset{\text{Qtz}}{4\ \mathrm{SiO_2}} + \underset{\text{Mgs}}{3\ \mathrm{MgCO_3}} + \underset{\text{fluid}}{\mathrm{H_2O}}, \tag{1.6}$$

where both CO_2 and H_2O are components of a COH-fluid. Reactions 1.3 to 1.6 show a stepwise change from silicates with a high Mg:Si ratio to silicates with a low Mg:Si ratio until pure quartz remains. The rock resulting from complete carbonation, which is comprised by the mineral assemblage quartz+magnesite (Qtz+Mgs), is also known as listvenite (Klein and Garrido, 2011; Hinsken et al., 2017). The carbonation thus ultimately increases the silica activity $a(\mathrm{Si})$ by scavenging divalent cations. The intrinsically very low $a(\mathrm{Si})$ in serpentinites thus makes them an ideal host rock for artificially sequestered CO_2 and these relations have therefore been well-studied (Frost, 1985). Recent contributions have shown that carbonation significantly affects the porosity and thus the permeability of serpentinites (Sieber et al., 2020). Such reaction-induced changes in porosity and permeability are important to allow fluid percolation, since serpentinites naturally have a low porosity (Kawano et al., 2011).

As discussed above, serpentinisation leads to increasing $f(\mathrm{H_2})$ in the circulating fluid due to the oxidation of Fe. At high $f(\mathrm{H_2})$ conditions carbonate formation will be suppressed by the stability of more reduced phases such as graphite (G) or methane based on the reactions:

$$\underset{\text{Mgs}}{\mathrm{MgCO_3}} + \underset{\text{fluid}}{2\,\mathrm{H_2}} = \underset{\text{Br}}{\mathrm{Mg(OH)_2}} + \underset{\text{fluid}}{\mathrm{H_2O}} + \underset{\text{G}}{\mathrm{C}} \tag{1.7}$$

$$\underset{\text{Mgs}}{\mathrm{MgCO_3}} + \underset{\text{fluid}}{4\,\mathrm{H_2}} = \underset{\text{Br}}{\mathrm{Mg(OH)_2}} + \underset{\text{fluid}}{\mathrm{H_2O}} + \underset{\text{fluid}}{\mathrm{CH_4}}. \tag{1.8}$$

The presence of Ca allows the formation of dolomite and calcite rather than magnesite. Fundamentally different from the process of replacing serpentine with a silicate+carbonate assemblage is the formation of ophicarbonates. Ophicarbonates, are rocks consisting of serpentinite clasts embedded in a carbonate matrix (fig. 1.3). Ophicarbonates typically form at mid ocean ridges where a volume increase during serpentinisation leads to fracturing and possibly also in faults formed at bending sites in the outer rise region shown in figure 1.1 (Driesner, 1993; Clerc et al., 2014). Carbonates precipitate in these fractures to form the matrix. Such rocks represent a unique assemblage of coexisting H_2O- and CO_2-bearing minerals. Depending on the composition of carbonates ophicalcites, ophidolomites and ophimagnesites are distinguished (Trommsdorff and Evans, 1977).
The redox reaction occurring during the serpentinisation process produces a fluid with a high $f(H_2)$. In such an environment it is possible to also precipitate sulfides (e.g. heazelwoodite, pentlandite, pyrite) and native metals such as awaruite, taennite or kamacite (Frost, 1985; Piccoli et al., 2019). Conversely, the precipitation of carbonates in such reducing environments would be suppressed and more reduced carbon phases are likely to form according to reactions 1.7 and 1.8. Frost (1985) proposed that natural assemblages where sulfides, native metals and carbonates do actually coexist can be interpreted as a time integrated serpentinisation process: first, while Ol and Px are serpentinised, Fe is oxidised to form Mgt and thus $f(H_2)$ in the fluid increases. At a sufficiently high $f(H_2)$, sulphides and native metals precipitate. With time the $f(H_2)$ decreases and $f(O_2)$ increases again due to the continuous circulation of water. Once a sufficiently high $f(O_2)$ is obtained carbonates precipitate. The presence of carbonate veins, as observed in ophicarbonates, within serpentinites is therefore likely to be an indication of very high fluid-rock ratios.

Figure 1.3: Ophicarbonate outcrop in the Valmalenco ophiolite. Freshly polished surfaces can be observed due to the retreat of the Ventina glacier. An ophicarbonate is a serpentinite breccia with serpentinite fragments of sizes varying from microscopic up to several meters. The clasts are embedded in a carbonate matrix, here consisting mainly of calcite.

1.2.4 Devolatilisation processes during subduction

Hydrated material starts to dehydrate due to increasing PT conditions during subduction. The stability field of Atg is extensively investigated both in the field and in experiments (Ulmer and Trommsdorff, 1995; Bromiley and Pawley, 2003; Padrón-Navarta et al., 2011, 2013). For example, a Br-bearing serpentinite in a simple MSH-system (fig. 1.4a), shows two dehydration reactions along a typical subduction PT path, being:

$$\text{Br-out:} \qquad \mathrm{Atg} + \mathrm{Br} = \mathrm{Ol} + \mathrm{H_2O} \tag{1.9}$$

$$\text{Atg-out:} \qquad \mathrm{Atg} = \mathrm{Ol} + \mathrm{Px} + \mathrm{H_2O}. \tag{1.10}$$

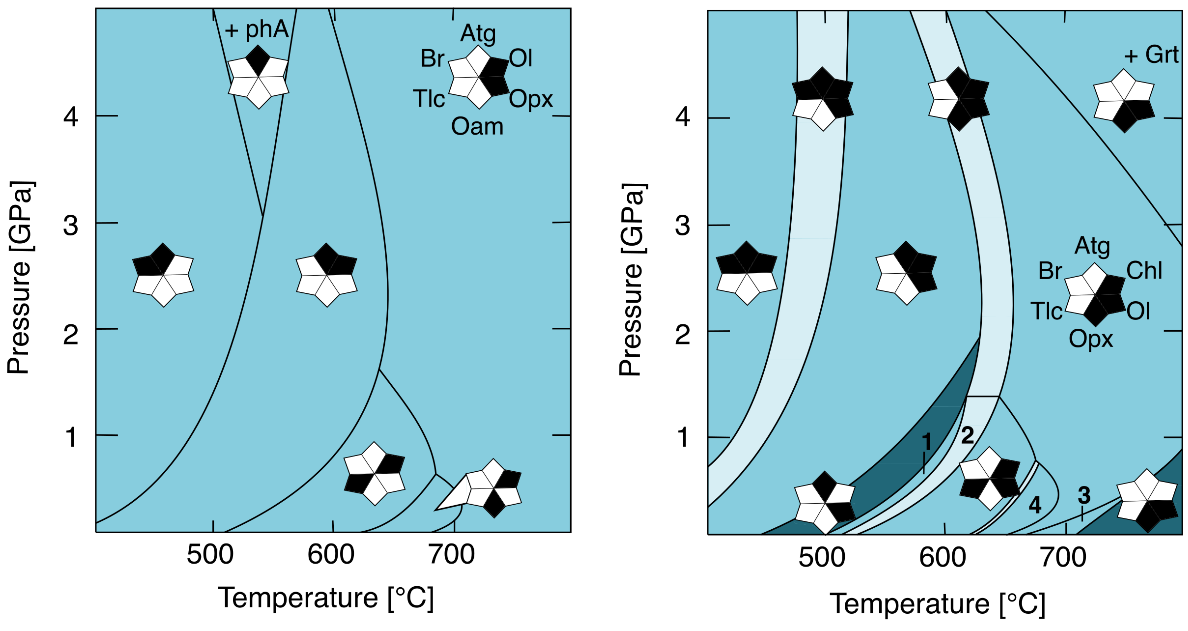

(a) **(b)**

Figure 1.4: Calculated phase relations for fluid saturated systems. Colour code indicates the variance of each field: lighter colours stand for lower variance. Phase diagrams are calculated with Perple_X version 6.8.1 with the HP'11 database (Connolly, 2005; Holland and Powell, 2011). a: Phase diagram for a simple MSH system. All reactions are univariant. b: Phase diagram for the system FMASH showing divariant reactions. The composition is taken from Padrón-Navarta et al. (2013), sample Al06-44. Small numbers mark field 1: Tlc+Ol+Atg, 2: Tlc+Chl+Ol+Atg, 3: Sp+Ol+Opx, 4: Chl+Oam+Ol. Abbrevations after Whitney and Evans (2010).

The first reaction typically releases about 2 wt% H_2O, whereas the second one releases up to 12-14 wt% H_2O. However, these simple phase relations are more complicated in natural samples. Firstly, the presence of ferrous Fe leads to Fe^{2+}-Mg exchange in all solid phases. The substitution of ferrous Fe decreases the stability of Atg (Merkulova et al., 2016). Furthermore, the univariant Atg dehydration reaction becomes a divariant reaction field, which has a width of approximately 5 - 10 °C at constant pressure (Padrón-Navarta et al., 2013). A major topological change arises from the incorporation of Al (Bromiley and Pawley, 2003; Padrón-Navarta et al., 2013). In Atg, Al causes the stability field to expand towards higher temperature (Bromiley and Pawley, 2003; Padrón-Navarta et al., 2013). Additionally, new Al-bearing phases such as chlorite (Chl), spinel (Sp) and garnet (Grt) become stable (fig. 1.4b). Hence, upon the Atg-out reaction a fraction of the total water content is retained in the newly formed Chl to higher temperatures. As a consequence, an additional dehydration reaction, i.e. the Chl-out, occurs at temperatures above the Atg-out reaction:

$$\text{Atg-out (MASH):} \qquad \text{Atg} = \text{Chl} + \text{Ol} + \text{Px} + \text{H}_2\text{O} \tag{1.11}$$

$$\text{Chl-out:} \qquad \text{Chl} = \text{Grt} + \text{Ol} + \text{Px} + \text{H}_2\text{O}. \tag{1.12}$$

The temperature at which Atg dehydrates was bracketed experimentally in various studies (Ulmer and Trommsdorff, 1995; Wunder and Schreyer, 1997; Bromiley and Pawley, 2003; Merkulova et al., 2016). The maximum stability of Atg as determined experimentally differs widely among different studies (fig. 1.5). The bulk composition of these studies differs mainly in total Fe and Al content. However, differences in these components alone cannot explain all discrepancies shown in figure 1.5. It is thus possible that a part of these discrepancies arise from various ferric Fe contents. In experiments and modelling to date it has been assumed that all iron in serpentine minerals is ferrous. However, measurements on natural samples show that ferric Fe is an important component in Atg (Evans et al., 2012). Although ferric Fe may have a similar effect on the stability of Atg as Al, there are no experimental data through which this effect can be examined. Most thermodynamic databases do not include ferric Fe at all or at best include it for only some individual phases such as andradite in the HP'11 database (Holland and Powell, 2011). However, the incorporation of ferric Fe is likely to affect the ambient oxygen fugacity. The relationship between the oxygen fugacity and ferric Fe content in serpentine minerals would certainly also influence the stability of other phases containing redox sensitive elements such as magnetite, carbonates and sulphides.

A further important issue concerning the breakdown of serpentine minerals is the mechanism through which the fluid is drained from the rocks. Fully serpentinised peridotites contain about 12 - 14 wt% H_2O, from which the majority is most likely liberated before or beneath the arc with only a small proportion transported towards the deeper mantle, depending on the depth of lithospheric hydration and the thermal path followed (van Keken et al., 2011). This liberated fluid migrates upwards due to its density contrast with the surrounding rock and the nature of this migration will have important consequences for the stability of other minerals such as carbonates, for the metasomatism and melting of the mantle wedge and possibly for the origin of deep focus earthquakes (Kerrick and Connolly, 2001; Schmidt and Poli, 2014; Menzel et al., 2020). In the uppermost parts of the subduction zone, released fluids may migrate up the dip of the subduction channel (Gerya et al., 2002; Rüpke et al., 2004). In deeper zones, released fluids likely migrate towards the mantle wedge but it is still a major point of discussion whether this migration occurs through pervasive flow along mineral grain boundaries or whether organisation into focused veins occurs (Okazaki et al., 2013). The former mechanism alone is too slow to allow for effective fluid release, whereas the latter mechanism limits the volume of the slab interacting with fluid and thereby affects the total amount of carbonate dissolution. Aside from determinations of the dihedral angles between minerals and fluid at high pressure, which may trap fluid pores in the lithosphere, if these angles are above 60 degrees (Huang et al., 2019), very little experimental work exists on flow mechanisms at high pressures.

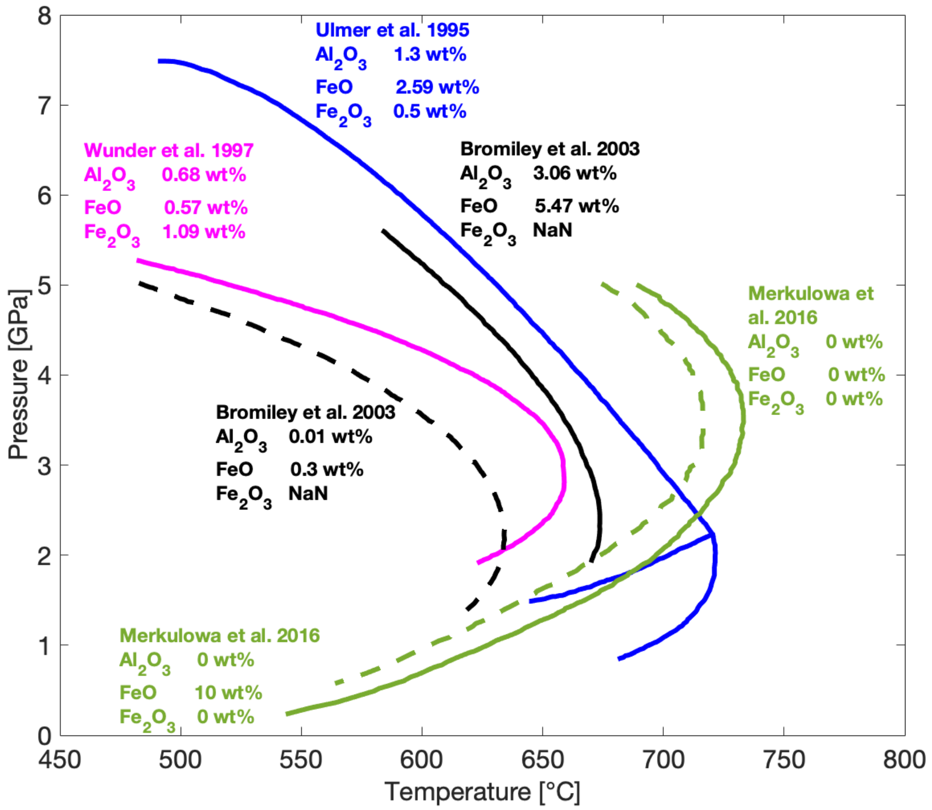

Figure 1.5: PT-diagram showing the stability of Atg from various studies. Also shown are respective bulk Al, Fe^{2+} and Fe^{3+} contents. Note that the ferric Fe content is not detremined in all studies.

1.3 Oxygen fugacity

Oxygen fugacity ($f(\mathrm{O}_2)$) is the effective partial pressure of oxygen that can be used as a measure of its chemical potential at conditions where it can no longer be approximated as an ideal gas. $f(\mathrm{O}_2)$ is used widely in order to compare redox conditions and reactions in the Earth. The partial pressure of O_2 itself is insignificant in the Earth. The $f(\mathrm{O}_2)$ of a particular rock assemblage, however, can still be calculated through an analysis of heterogeneous equilibria normally involving ferric and ferrous Fe-bearing minerals. The resulting $f(\mathrm{O}_2)$ can be compared with other redox equilibria for which there may be little evidence in the rock. An example is the speciation of volatile components in a transient fluid or melt phase that equilibrated with the rock but for which no more evidence exists. From the $f(\mathrm{O}_2)$ of an assemblage the stability of carbonate minerals relative to graphite or diamond can be constrained for example. $f(\mathrm{O}_2)$-dependent equilibria also shift with pressure and temperature. For example, while carbonates may be in equilibrium with a rock containing a certain amount of ferric and ferrous Fe at one set of conditions, reduction of these carbonates may occur as PT conditions change due to a shift in the redox equilibrium (Galvez et al., 2013). To understand such changes it is necessary to know how mineral phases change in composition and stability with varying $f(\mathrm{O}_2)$.

As the absolute values of $f(\mathrm{O}_2)$ change with pressure and temperature, it is useful to normalise the values relative to common oxygen buffering equilibria, which tend to have similar pressure and temperature dependencies. Some common reference buffers used in Earth Sciences are shown in figure 1.6.

In high-pressure experiments the redox state of certain elements can be used to calculate the intrinsic $f(\mathrm{O}_2)$ of the experiment by knowing the composition of coexisting phases (e.g. Stagno et al., 2013). An example of calculating the intrinsic $f(\mathrm{O}_2)$ is based on the often-used *Fayalite-Magnetite-Quartz*-equilibrium (FMQ):

$$3\ \mathrm{Fe_2SiO_4} + \mathrm{O_2} = 2\ \mathrm{Fe_3O_4} + 3\ \mathrm{SiO_2}. \tag{1.13}$$

The $f(\mathrm{O}_2)$ is calculated as

$$RT\ln(f(\mathrm{O}_2)) = \Delta G^0 + RT\ln\left(\frac{a(\mathrm{SiO}_2)^3}{a(\mathrm{Fa})^3}\right), \tag{1.14}$$

where T is the temperature, R the gas constant, ΔG^0 the Gibbs free energy change of the reaction, and $a(\mathrm{SiO_2})$ and $a(\mathrm{Fa})$ denote the activity of silica and fayalite, respectively. Alternatively one can make use of redox buffering assemblages to impose a fixed $f(\mathrm{O_2})$ on the experiment. In experiments performed in the past oxygen buffering assemblages have been used with a double capsule technique (compare Jakobsson, 2012). The oxygen buffer is placed in an outer H_2O saturated capsule and the diffusion of H_2 through the wall of the inner capsule allows the fugacity of H_2 and O_2 to be fixed in the H_2O saturated inner capsule. The disadvantage of this technique is that it requires an extended preparation time and the inner capsule has to be always H_2O saturated. Furthermore, an aspect that has been frequently overlooked is that the inner $f(\mathrm{O_2})$ is only the same as the buffering assemblage as long as the inner fluid has the same composition i.e. is dominantly H_2O. If an inner COH-fluid is present, the $f(\mathrm{O_2})$ can still be calculated but becomes a more complex and uncertain function of the fluid component equation of state. To overcome this complexity it is much simpler to place redox buffers directly into the inner assemblage. However, it is important that the buffer assemblage does not react significantly with the surrounding sample other than through the exchange of oxygen. Buffers that work quite well in this respect are Re-$\mathrm{ReO_2}$ and Ru-$\mathrm{RuO_2}$. The $f(\mathrm{O_2})$ is calculated from the equilibrium between the metal and oxide as for example:

$$\mathrm{Ru} + \mathrm{O_2} = \mathrm{RuO_2}. \tag{1.15}$$

Based on this the $f(\mathrm{O_2})$ is simply:

$$RT\ln(f(\mathrm{O_2})) = \Delta G^0. \tag{1.16}$$

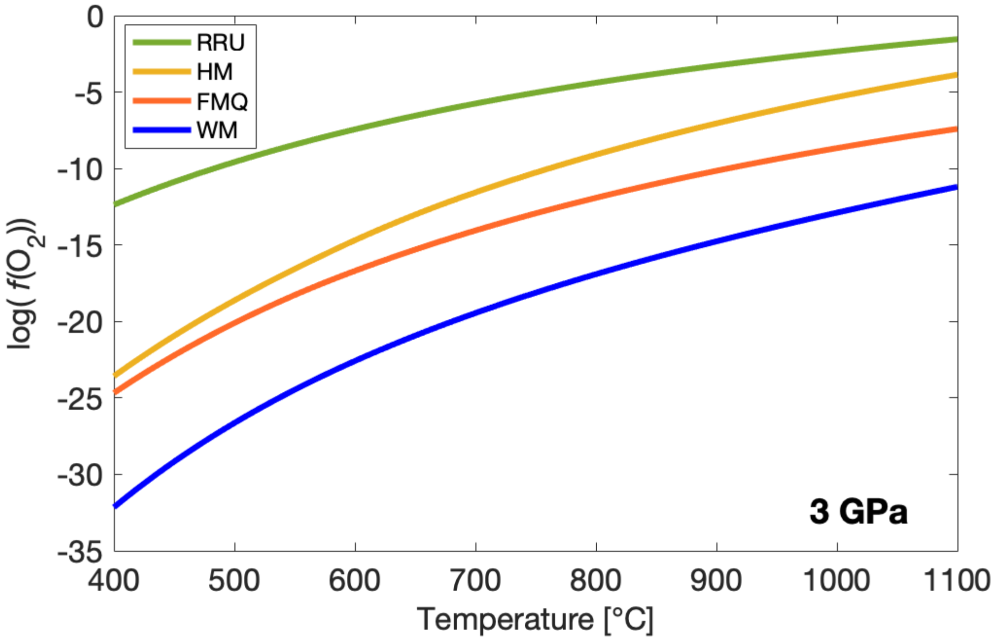

Figure 1.6: Calculated $f(O_2)$ of selected redox buffers: RRU = Ru-RuO_2, HM = hematite-magnetite, FMQ = fayalite-magnetite-quartz, WM = wustite-magnetite. Equilibria are calculated as explained in section 2.5.2.

1.4 Serpentine minerals

The serpentine group minerals are 1:1 trioctahedral hydrous sheet silicates containing about 12 - 14 wt% H_2O. The structure comprises of an octahedral and a tetrahedral layer (fig. 1.7). The octahedral sheet is fully occupied and followed by a pseudo-hexagonal tetrahedral network with the apices of the tetrahedra pointing towards the octahedral layer. Two independent OH-groups are present in serpentinites. The inner hydroxyl group is located in the six-fold rings so that the H atom is approximately at the same height as the tetrahedrally coordinated cation. The outer hydroxyl group links the octahedral sheet with the next tetrahedral layer. The relative sequence of layer stacking leads to a variety of crystal symmetries for each serpentine mineral, which can even coexist in a single sample (Bailey, 1969; Mellini et al., 1987).

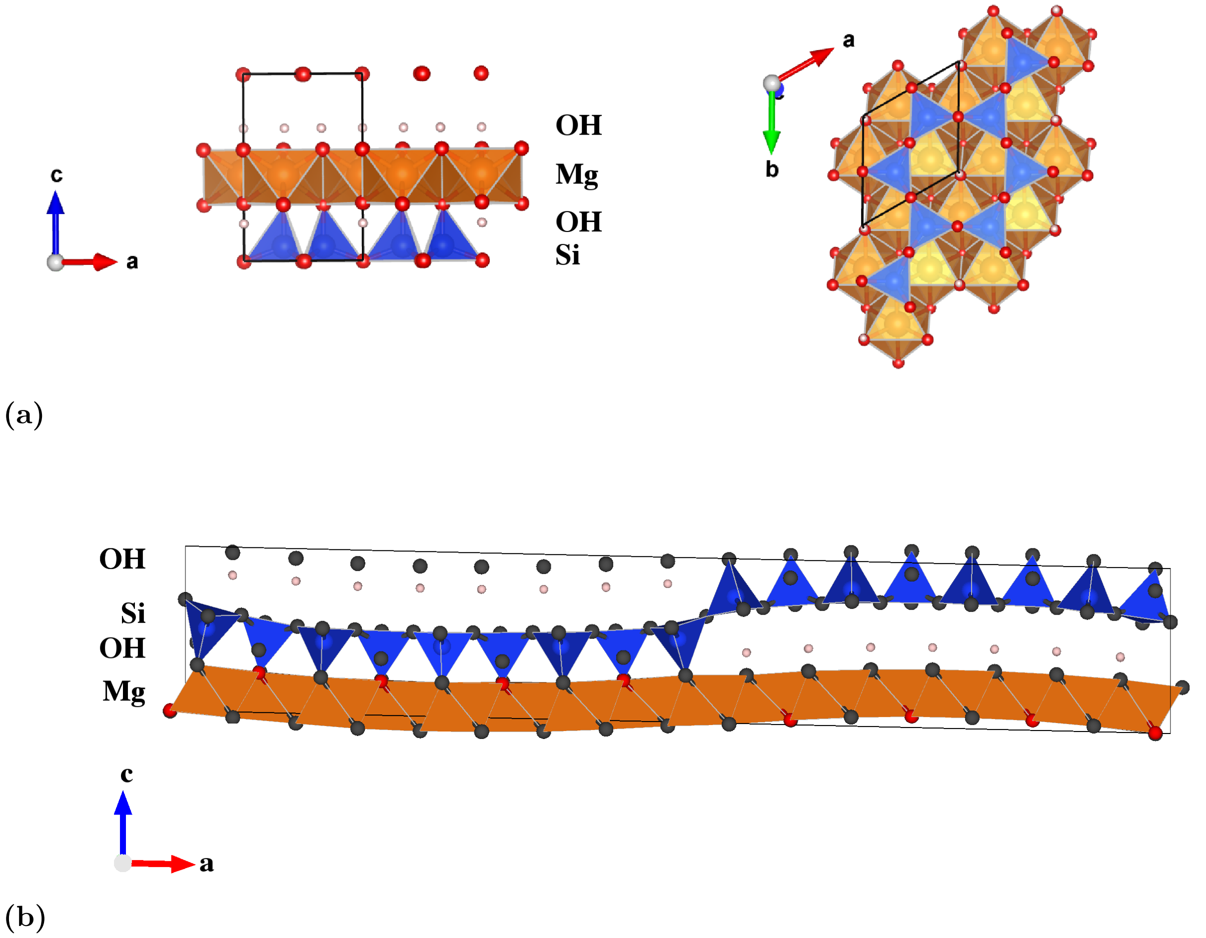

Figure 1.7: The serpentine minerals have a layered structure with an octahedral Mg- and a tetrahedral Si-layer. Hydrogens are located within the pseudo-hexagonal Si-layers as well as between adjacent Mg- and Si-layers. a: Crystal structure of Liz in two orientations. left: Liz shows a flat structure. right: the tetrahedral layer shows a pseudo-hexagonal structure. b: Crystal structure of Atg (m=17 polysome). Atg shows a modulated structure with a reversal of the tetrahedral Si-layer every half unit cell. References: Liz: Mellini (1982), Atg: Capitani and Mellini (2004).

Most serpentines belong to the Mg-Si serpentines with the stoichiometry $Mg_3Si_2O_5(OH)_4$. The three main minerals are lizardite (Liz), chrysotile (Chr) and antigorite (Atg), which are all rock forming and occur in similar environments. While Liz, Chr and Atg have a Mg-filled octahedral layer and a Si-filled tetrahedral layer, various substitution mechanisms produce other serpentine minerals that are much less abundant. Fe^{2+} substitution for Mg is observed in berthierine, coupled substitution of Al for Mg and Si results in the mineral amesite and the Fe^{2+}-Fe^{3+} endmember is known as cronstedtite. More exotic varieties include Ni-serpentines such as nepouite and pecoraite. Full solid solutions between these minerals are observed, giving rise to a large compositional space. Many components that are present only in small quantities can significantly influence phase relations.

The three principle forms are distinguished based on the geometry of the sheets. Different geometries arise from the mismatch in size between the octahedral and tetrahedral layers. Liz has a flat structure and the mismatch is essentially minimised by trivalent cation substitution (fig. 1.7a). Chr shows typical cylindrical structure, whereas Atg has a modulated structure (fig. 1.7b). The modulation of the sheets results in a reversal of the tetrahedral layer every half wavelength. Thus, the stoichiometry of Atg is slightly varied from the ideal serpentine and Atg is therefore not a polymorph *sensu stricto*, but rather represents a polysomatic series. The most comon polysome is the $m = 17$, having 17 tetrahedral sites per wavelength, resulting in the Atg stoichiometry $Mg_{48}Si_{34}O_{85}(OH)_{62}$. More generally, the stoichiometry can be written as a function of the polysome length as $Mg_{3m\text{-}3}Si_{2m}O_{85}(OH)_{4m\text{-}6}$. Atg is thus depleted in $3m$ $Mg(OH)_2$ relative to the ideal Liz stoichiometry. The wavelength is shown to change with the metamorphic grade (Mellini et al., 1987; Shen et al., 2020). Generally, it is very rare to find a unique m value in a single sample, which might point to sluggish reaction kinetics for Atg (Mellini et al., 1987).

Within a simple MSH system, Liz and Chr are stable phases up to 300 °C. Antigorite is the high PT serpentine formed by recrystallisation of lizardite in the range of 320 - 390 °C (Schwartz et al., 2013). Despite the fact that the transition is observed in nature, it was not found experimentally yet, probably due to a large energetic barrier involved in the formation of a modulated structure.

The substitution of Al increases the stability of Liz, so that Al-bearing Liz can be as stable as Atg at high temperature (Caruso and Chernosky, 1979). Liz is the serpentine with the highest observed Al content among the three principle forms. Newer studies also point out that the environments where serpentine minerals form play a major role for their structures. For example, Chr is considered to be metastable in oceanic serpentinites (Evans, 2004). However, these rocks always contain a certain amount of Al, which favours the formation of Liz.

1.5 Motivation

Despite many advances in the last decades, uncertainties remain regarding the nature and quantity of volatiles that are released from the subducting lithosphere and the conditions at which this occurs. Many experimental and computational efforts to date have helped understanding the phase relations within subduction zones. However, a number of potentially important details are either poorly constrained or have not been considered at all. These include the role of oxygen fugacity in the stability and speciation of volatile-bearing phases, the combined effects of H_2O and CO_2 on volatile phase stabilities and the mechanisms of fluid migration through mantle rocks.

Subduction zone fluids are often assumed to be oxidised, although field evidence for the reduction of carbonates to graphite by serpentinite-related fluids (Galvez et al., 2013) indicates that relatively reduced fluids might be produced in subducting altered mantle lithosphere under some conditions. In a recent study Piccoli et al. (2019) propose that fluids produced in the fore arc region are relatively reduced based on the thermodynamic behaviour of Mgt in serpentinite assemblages. However, studies to date do not consider the effect of ferric Fe as a component in serpentine minerals and assume that oxides such as Mgt are the only ferric Fe-bearing phases. The disappearance of Mgt from both natural and experimental serpentinite assemblages at high pressures and temperatures provides some indication that other phases can incorporating ferric Fe (Debret et al., 2015; Bretscher et al., 2018). Natural serpentinites are known to contain a significant proportion of ferric Fe (e.g. Evans et al., 2012). Changes in the $Fe^{3+}/\Sigma Fe$ ratio of serpentine with pressure and temperature during subduction may lead to important redox reactions with other phases such as Mgt and carbonates, but also possibly organic carbon phases as well as Fe-sulphides. A further open question is how the oxygen fugacity of a serpentinite assemblage changes during dehydration and what consequences this has for fluid speciation.

This thesis addresses three main aspects:

1) The influence of ferric Fe on the stability of Liz and Atg are examined using high-pressure experiments on natural samples. This allows to determine the relationship between the ferric Fe contents of these minerals and the $f(O_2)$. These results are the foundation for a thermodynamic model that allows the amount of ferric Fe in these serpentine minerals to be determined as a function of $f(O_2)$. With this model the extent to which the $Fe^{3+}/\Sigma Fe$ ratio of serpentine minerals affects the $f(O_2)$ of the lithospheric slab during

subduction is determined and compared with the speciation of other volatile components involving carbon and sulphur in the slab. This is an important step in understanding whether fluids released by the subducting slab are reduced or oxidised. The results are further used to analyse the hydration of the mantle wedge and the evolution of the $f(O_2)$ in these hydrated upper mantle peridotites.

2) The stability of an ophicarbonate assemblage is examined experimentally. In particular, the effect of carbonates on the stability of Atg is analysed. By placing pre-fractured single crystals inside these experiments, synthetic fluid inclusions are produced from which the composition of the fluid in equilibrium with the partially dehydrated assemblages can be determined. The experimentally determined phase relations are compared to thermodynamic models on carbonated serpentinites and carbonated peridotites in order evaluate the speciation of carbon in the subducting slab and the hydrated upper mantle peridotites.

3) A new method to measure rock permeabilities at high pressures and temperatures is developed and used to determine the permeability of serpentinites at subduction zone conditions. In particular it has been proposed that the strong fabric of serpentine minerals results in anisotropic fluid flow (Kawano et al., 2011). This would tend to focus fluid movement in the serpentinite foliation direction, which is likely to be parallel to the dip direction of the subducting slab. This would likely favour organisation of the flow into channels rather than encourage pervasive flow. However, there is currently no experimental method for determining the anisotropy of fluid flow or estimating the permeability at subduction zone conditions. The new experimental setup in combination with numerical modelling is a first step to close this gap.

2 Methods

2.1 Starting material

As previous attempts to synthesize serpentine minerals have produced generally very limited growth (Wunder et al., 1997; Caruso and Chernosky, 1979; Wunder et al., 2001), natural serpentinite samples were used in this study that were chosen based on their high serpentine content and differing $Fe^{3+}/\Sigma Fe$ ratio. All samples were analysed and characterised both macroscopically and microscopically prior to experiments.

2.1.1 Starting material characterisation

The samples **Zer_1701** and **Zer_1801** (Location: Zermatt, CH, kindly provided by Elias Kempf) are similar in texture and composition and described here together. Macroscopically the samples are dark greenish massive serpentinites consisting of antigorite (>95 %), magnetite (<5 %) and minor Fe-sulfides. The presence of some individual grains of Ti-clinohumite and diopside are confirmed by optical microscopy and electron microprobe analyses. HCl-tests did not indicate any carbonates.

On a microscopic scale antigorite is fine-grained (<1 mm) and shows a strong preferred orientation. Antigorite shows a weak pleochroism and undulous extinction. The interference colour is greyish to yellowish (thickness of section: 70 µm) and shows a slight pigeon-colour tint. The optical character of antigorite is determined as 2⊖. Fine-grained opaque phases (not further distinguished) are observed between the antigorite grains with a strong alignement along the antigorite preferred orientation. Individual larger, xenomorphic opaque phases (<1 mm) are identified as magnetites due to their rose to brownish tint in reflected light mode. Only few individual grains of Ti-clinohumites are observed. They are xenomorphic and have a brownish-reddish colour and a translucent character.

Mössbauer spectroscopy reveals the presence of one sheet silicate in addition to a magnetic phase (fig. 2.1a). The silicate is fitted with two doublets, belonging to ferrous and ferric Fe in antigorite, with a $Fe^{3+}/\Sigma Fe$ ratio of 0.28. The Mössbauer hyperfine parameters indicate that both ferrous and ferric Fe are octahedrally coordinated. The two magnetic sextets belong to magnetite. A magnetic fraction of 43.8 % is measured. The macroscopically observed Fe-bearing sulfides are below the limit of detection.

The X-ray powder diffraction (XRPD) pattern shows characteristics of both Liz and Atg, based on a moderate peak at 2θ(Co) = 22° (Liz) and a major peak at 2θ(Co) = 41°

(Liz/Atg) as well as the peak at $2\theta(\mathrm{Co}) = 70°$ (Atg) (Bailey, 1969; Peacock, 1987). The Raman shift for the symmetric SiO_4 vibration, however, indicates the presence of Atg rather than any other serpentine polymorph due to its relatively low wave number of $375\,\mathrm{cm}^{-1}$ (Rinaudo et al., 2003; Auzende et al., 2004; Schwartz et al., 2013).

The sample **Lig_1602** (Location: Val Graveglia, IT) is a massive serpentinite containing <5 % opaque phases and minor amounts of chlorite. The macroscopic colour is greenish with a yellowish translucent tint.

On a microscopic scale serpentine has a greyish interference colour and is identified as lizardite, in agreement with the rather low metamorphic overprint. Three different generations of lizardite can be observed in a mesh-like texture. A preferred orientation, however, is not observed. The first generation (lizardite I) shows a slight pleochroism. A second generation (lizardite II) has replaced a mineral with columnar habitus and a perfect cleavage, probably pyroxene. Lizardite II preserves the cleavage of the former mineral and is colourless. A few of the lizardite I and II grains are overgrown by greenish-brownish grains. The brownish anomalous interference colour identifies the phase as chlorite. A further and youngest generation of serpentine (lizardite III) is grown in cross-cutting veins. It shows an undulous extinction and often contains angular opaque phases, identified as magnetite based on their greyish to purple colour in reflected light mode. Beside the idiomorphic magnetites within the veins, magnetite is also observed as xenomorphic grains within the lizardite I and lizardite II grains with grain sizes from $\ll$1 mm to >1 mm. This is typical for ocean floor serpentinisation, leading to oxidation and therefore to the formation of Fe-oxide exsolutions. An additional minor opaque phase is identified as xenomorphic pyrite due to their slightly yellowish reflecting colour.

The Mössbauer spectrum shows the presence of a magnetic phase and a sheet silicate. The latter is fit with 3 doublets, which correspond to octahedral ferrous Fe and octahedral and tetrahedral ferric Fe in lizardite (fig. 2.1b). The $Fe^{3+}/\Sigma Fe$ ratio is 0.7. Two magnetic sextets confirm the presence of magnetite. A total magnetic fraction of 39.2 % is measured. The observed Fe-sulfides are below the limit of detection.

The XRPD pattern shows the presence of lizardite based on an asymmetric peak at $2\theta(\mathrm{Co}) = 22°$ and a moderate peak at $2\theta(\mathrm{Co}) = 41°$. The peaks are extremely broad, which makes analyses difficult. Raman spectroscopy shows the symmetric SiO_4 vibration at $390\,\mathrm{cm}^{-1}$ and thereby verifies the presence of lizardite (Rinaudo et al., 2003; Auzende et al., 2004; Schwartz et al., 2013).

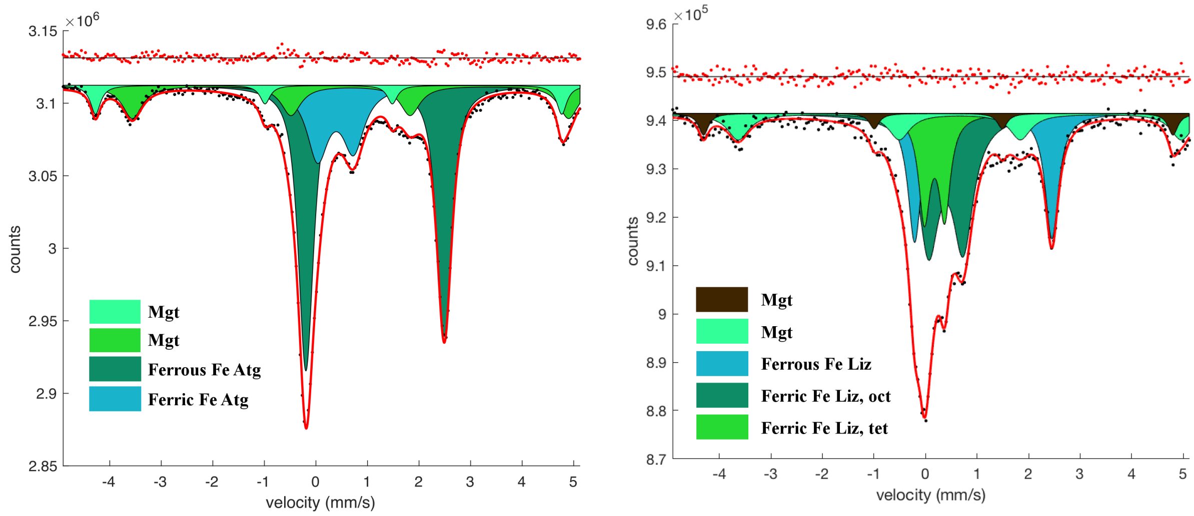

(a) **(b)**

Figure 2.1: Mössbauer spectra of starting materials. a: Zer_1701 is fitted with two doublets for Atg belonging to ferric and ferrous Fe and two sextets for Mgt. b: Lig_1602 shows a ferrous and two ferric doublets belonging to Liz beside two sextets of Mgt.

Chemical compositions of serpentines and magnetites in the starting materials were measured with electron microprobe. The mean composition of at least 10 measurements across the sample and the 1σ standard deviation is given in table 2.1. Ignoring contributions from minor phases, the bulk composition is calculated based on the composition of serpentine and magnetite. The calculated bulk composition is given in table 2.2.

Table 2.1: Composition of major phases in the starting material. Composition is given in wt%. Mg# refers to molar MgO/(MgO+FeO), with FeO being the ferrous Fe fraction as derived from Mössbauer spectroscopy. H_2O is calculated by difference for single measurements.

	Zer_1701				Zer_1801						Lig_1602			
	Serp		Mgt		Serp		Mgt		Cpx		Serp		Mgt	
oxide	mean	σ	mean	σ	mean	σ	mean	σ	mean	σ	mean	σ	mean	σ
SiO_2	40.76	0.32	0.02	0.03	41.95	0.23	0.01	0.01	56.07	0.30	38.14	2.20	0.64	0.15
Cr_2O_3	0.19	0.08	5.22	2.64	0.29	0.11	6.24	9.29	0.03	0.03	0.37	0.57	0.03	0.05
FeO	4.48	0.17	84.96	2.91	3.68	0.09	84.42	9.99	0.75	0.10	5.53	2.97	87.71	1.34
Al_2O_3	2.47	0.24	0.01	0.01	2.77	0.15	0.03	0.04	0.02	0.01	2.01	1.46	0.01	0.01
MgO	37.61	0.40	0.30	0.07	36.99	0.19	0.28	0.17	17.86	0.08	38.67	1.54	1.14	0.37
CaO	0.01	0.01	0.01	0.01	0.01	0.01	0.05	0.10	25.67	0.13	0.03	0.02	0.01	0.03
NiO	0.24	0.05	0.52	0.04	0.22	0.03	0.43	0.04	0.03	0.02	0.11	0.10	0.01	0.01
H_2O	14.18	0.24	-	-	14.01	0.22	-	-	-	-	14.98	0.78	-	-
$total_{solids}$	85.76	0.59	91.04	3.93	85.91	0.36	91.46	13.64	100.43	0.35	84.86	4.31	89.55	1.40
Mg#	0.95	0.01			0.96	0.01			0.98	0.01	0.98	0.04		
$Fe^{3+}/\Sigma Fe$	0.28	0.01			0.28	0.01					0.70	0.01		

Table 2.2: Bulk composition calculated for samples Zer_1701 and Lig_1602, based on mineral modes and composition. 3.0(5) wt% Mgt was used for Zer_1701 and 4.0(5) wt% for Lig_1602. Data are given in wt%.

	SiO_2	Cr_2O_3	FeO	Al_2O_3	MgO	CaO	NiO	H_2O
Zer_1701								
mean	39.54	0.34	6.89	2.40	36. 50	0.01	0.25	13.75
σ	0.37	0.11	0.46	0.23	0.43	0.01	0.05	0.24
Lig_1602								
mean	36.65	0.36	8.82	1.93	37.17	0.03	0.11	14.38
σ	2.12	0.55	2.89	1.40	1.50	0.01	0.10	0.75

2.2 Starting material preparation

High-pressure experiments performed in the first part of this study use powders as starting materials. Therefore, the bulk rock samples (Zer_1701 and Lig_1602) were crushed with a hammer. Pieces were carefully chosen in order to not insert weathering products or late vein filling material into the starting mix. The pieces were milled in ethanol for about 1 h with a pestle mill. The sample was further milled by hand with mortar and pestle after drying the slurry. Powder used for carbonate-bearing experiments was mixed with 20 wt% of reagent-grade $CaCO_3$.

In the high-pressure experiments the $f(O_2)$ was either calculated using the composition of coexisting phases or buffered by adding a buffering assemblage. In the first case 5 wt% of Ir powder was mixed to the starting material, that serves as a sliding redox sensor (Woodland and O'Neill, 1997; Stagno, 2011). Ir alloys with Fe from the sample during the experiment. The amount of Fe in the alloy is a direct function of the $f(O_2)$, which can be calculated as described in section 2.5.2. For buffered experiments 10 wt% of a powdered redox buffer assemblage was mixed with the starting material. Redox buffers used are the metal-oxides pairs Re-ReO_2 (RRE) and Ru-RuO_2 (RRU). To obtain a more reduced $f(O_2)$, 10 wt% graphite (C), carbonate+graphite (CbC) or Fe-metal (Fe) were added to the starting material. The ratio between reduced and oxidised buffer component was 0.2:0.8. All chemicals were reagent-grade powders.

The fluid flux experiments described in chapter 9 differ from the experiments performed in the first part of this study in that they use solid serpentinite drill cores rather than powders. The sample preparation for these experiments is treated separately in section 9.3.1.

2.3 High pressure experimental methods

All experiments were conducted in multi-anvil presses (MA). Two different presses were used in two different laboratories at the Bayerisches Geoinstitut (BGI) in Germany and at the Tohoku University (TU) in Japan. Standard BGI 18/11 and 25/11 assemblies were used. A detailed scheme of the setup is shown in figure 2.2.

The starting material was loaded in a gold capsule and welded on both ends with a Lampert PUK U3 welding device running in micro mode. In some experiments a prefractured single crystal was added to the powder prior to welding in order to form synthetic fluid inclusions. Single crystals used were San Carlos olivines, garnets from an eclogite sample from Alpe Arami and sapphires (kindly provided by Andreas Audétat). Impurity free crystal fragments of about 1 - 2 mm diameter were chosen under a microscope. The crystals were heated to 1000 °C in an oven for about 30 s and quenched in cold distilled water. After quenching the crystals were checked for the presence of fractures under a microscope.

The prepared capsules were placed inside an MgO sleeve, with MgO spacers on top and on bottom. Heating was performed with a stepped graphite cylindrical furnace consisting of 3 parts. The middle part of the heater is slightly thicker to reduce the temperature gradient over the capsule length. A Ca-doped ZrO_2 sleeve surrounds the heater to provide thermal insulation. The octahedral pressure medium is sintered MgO doped with Cr_2O_3.

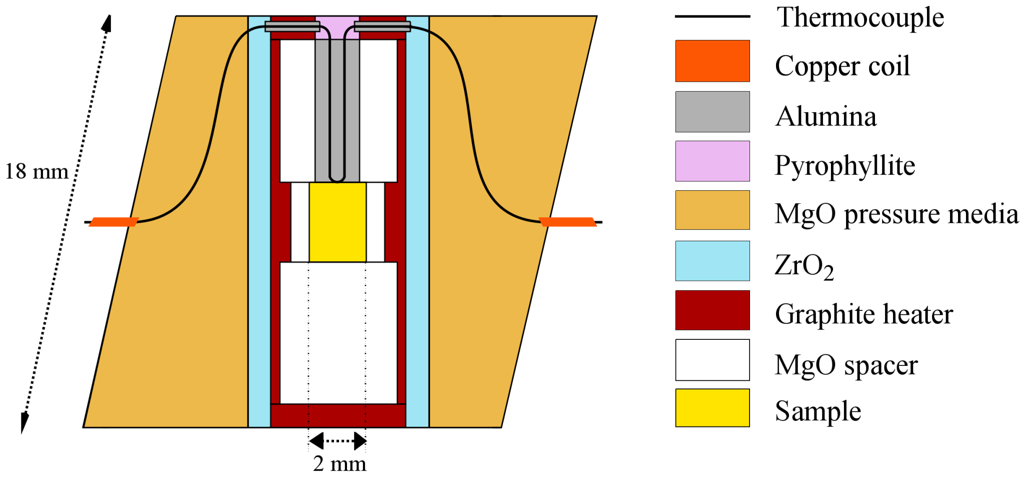

Figure 2.2: Scheme of a standard BGI 18/11 assembly. The sample capsule (2 mm outer diameter) is placed together with the heater and the thermocouple inside an octahedrally shaped MgO pressure medium. A Re-foil (not shown in the scheme) is placed between the capsule top and the thermocouple. The edge length of the octahedra is 18 mm.

A $W_{97\%}Re_{3\%}$-$W_{75\%}Re_{25\%}$ thermocouple (TC) was used to monitor the temperature during the experiment. The TC was separated from the capsule by a Re-foil to prevent the gold from intruding into the TC, which would shift the hot junction of the TC away from the top of the capsule. Temperature-current (TW)-correlations are used to obtain accurate temperatures in experiments where the TC did not work properly. The overall temperature measurements were improved by applying a geothermometer based on Mg-Fe partitioning between garnet and olivine (O'Neill and Wood, 1979). For all further calculations the temperatures obtained from these TW-correlations are used. Hernlund et al. (2006) calculated that in the 18/11 standard BGI assembly the temperature gradient is about 50 °C over the entire length of the capsule.

The pressure is generated by a hydraulic system. Two stages of anvils redirect and focus the uniaxial pressure to the sample. Both laboratories utilise a 6-8 MA design, referring to the first and second stage anvil geometry. The first stage is made up by 6 wedge-shaped anvils. In the Walker-type press at BGI they are cylindrically arranged and supported by an outer ring, which allows for cooling by internal water circulation. In the split-cylinder geometry used at TU the anvils are fixed in two guide blocks. The second stage consists of 8 corner-truncated WC-cubes. The truncations form an octahedral cavity in the middle, in which the octahedral assembly is placed. Variations in the truncation edge length (TEL) of the cubes and the size of the octahedra, described by the octahedral edge length (OEL), allows different maximum pressures to be obtained for each assembly. The first part of this study used standard BGI 18/11 assemblies, having 11 mm TEL and 18 mm OEL. For the experiments conducted in chapter 9 slightly larger standard BGI 25/17 assemblies were used.

The pressure for 18/11 experiments run at BGI was calibrated by the quartz-coesite (Qtz-Coe) transition and compared with garnet-perovskite (Grt-Pv) and coesite-stishovite (Coe-Sti) transition from earlier direct press calibrations on the same assemblies. The calibration was performed simultaneously with the actual experiments by placing a layer of Qtz powder with an approximate thickness of 200 µm below the capsule. A Re-foil was used to cover the Qtz. Phase identification was performed using Raman spectroscopy at BGI. The Qtz-Coe transition was calculated based on experiments from Bose and Ganguly (1995). In figure 2.3a the Qtz-Coe transition obtained in this study is compared to an earlier direct calibration curve as well as a calibration curve from Frost et al. (2004). The best fit with the experimentally determined phase transition is obtained by the calibration curve by Frost et al. (2004). For 25/17 assemblies the pressure calibration based on Qtz-Coe transition obtained from experiments over the last several years by various experimentalists was used. The 25/17 assembly used at TU was calibrated at the Qtz-Coe transition and the phases were analysed by XRPD at TU. An additional calibration at ambient temperature was performed at TU by resistivity measurements using Bi. Bi has two ambient temperature phase transitions at 2.55 and 2.7 GPa, which are both marked with a change in resistivity. Results from the calibration are shown in figure 2.3b.

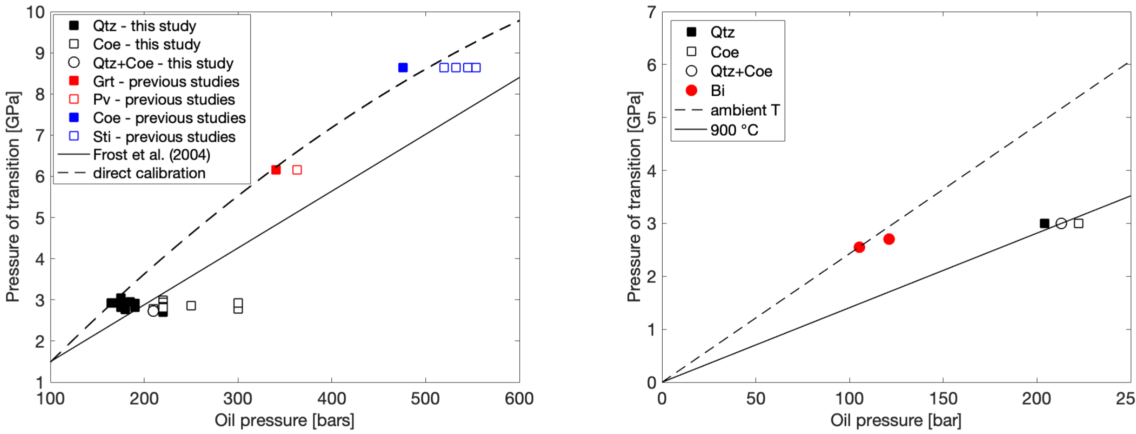

(a) **(b)**

Figure 2.3: a: Pressure calibration of the 18/11 assembly at BGI. Data points mark the Qtz-Coe transition obtained in this study and phase transitions from earlier calibration of the same assembly. Best fit with the new data is obtained from the calibration curve in Frost et al. (2004), which was calibrated on the Grt-Pv, Coe-Sti, olivine-wadsleyite and wadsleyite-ringwoodite transition. b: Pressure calibration performed on 25/17 assemblies at TU. The ambient temperature calibration based on Bi resistivity gives higher pressures for a given load.

2.4 Analytical methods

The recovered MA samples from the first part of this study were cut in half. One half was embedded in epoxy, polished and coated with a 12 nm thick carbon layer for further analyses with a scanning electron microscope (SEM) and an electron probe microanalyzer (EPMA). After chemical analyses electron backscattered diffraction (EBSD) measurements were performed on selected samples. For EBSD measurements the samples were polished for >8 h with a colloidal silica suspension on a multipole 2 polisher. A carbon coating of 4 nm was applied after polishing.

The other half of the sample capsule was prepared as a double polished thick section for Mössbauer spectroscopy. The ideal thickness for γ-ray absorption was calculated for the bulk composition to be 500 µm.

The San Carlos single crystals that were added to some samples were detached from the sections prepared for Mössbauer and polished to a thickness of 80 µm for performing Raman measurements on fluid inclusions.

2.4.1 Electron-sample interaction based methods

Several analytical methods take advantage of the interaction between high energy electrons and the sample. For this purpose high energy electrons are produced in an electron gun and focused towards the sample by one or more condenser lenses.

Electrons that collide with the sample interact in different ways (fig. 2.4). Elastic scattering of incident electrons might change their trajectory and leads to backscattering. Inelastic scattering leads to the release of secondary electrons from atoms in the sample. If an electron of an inner shell of the target is released via electron-sample interaction, outer electrons fall back to fill the gap and emit characteristic X-rays. Energy dispersive (EDX) and wavelength dispersive (WDX) analyses of these X-rays allow to determine the chemical composition of the sample material. The detection of the different particles or waves created during beam-sample interaction is done with specific detectors and leads to various information about the sample.

Scanning electron microscopy

The detection of backscattered electrons (BSE) allows a qualitative identification of mineral phases based on their density. BSE have a typical energy in the keV range. The intensity of the signal strongly depends on the sample material, as elastic scattering increases with the atomic number. Heavy materials thus appear brighter than light materials. Secondary electrons (SE) have generally lower energies in the order of few eV. Their interaction volume is thus strongly reduced and they are mostly used to image the topography of a sample.

A preliminary overview of texture, distribution and composition of the phases in the experimental products was obtained with a GEMINI LEO 1530 scanning electron microscope at BGI. Operating conditions were 20 kV acceleration voltage and a working distance of 15 mm. Semi-quantitative EDX measurements were performed on selected grains with INCA and AZtec softwares from Oxford Instruments. Relative intensities of major elements could be used to identify the phases.

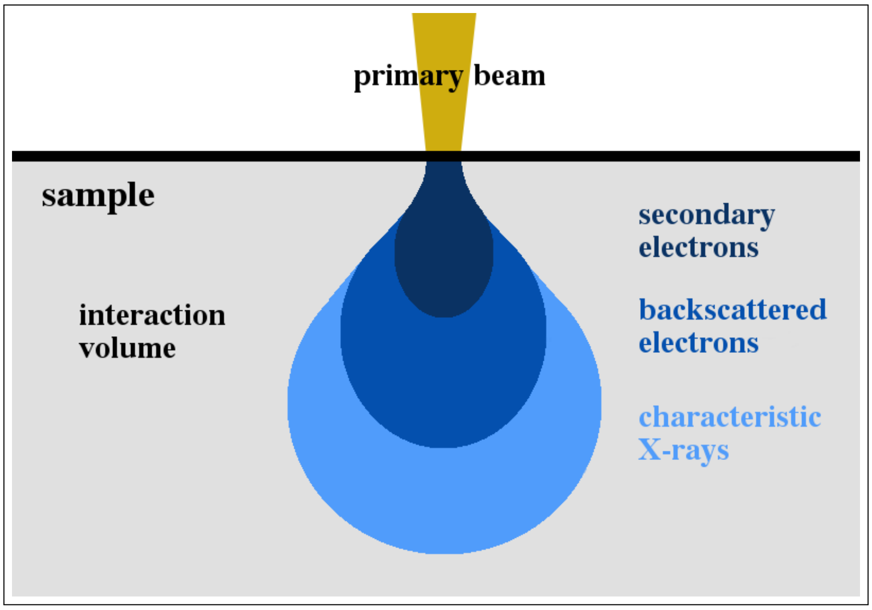

Figure 2.4: Schematic illustration of the interaction volume with the electron beam. High energy back scattered electrons thus give information of a larger sample volume than secondary electrons. Characteristic X-rays used for chemical analyses arise from an even larger volume.

Electron backscattered diffraction

The elastic interaction of the electrons from the primary beam with the sample scatters them in random directions throughout the sample and back from the sample. Some of the primary electrons that are back scattered satisfy the condition given by the Bragg equation

$$n\lambda = 2d\sin(\theta), \tag{2.1}$$

where n is an integer, λ the wave length, d the interplanar distance of the scattering plane and θ the angle between the sample surface and the electron path. These electrons produce a diffraction pattern also known as backscattered Kikuchi lines (Adams et al., 1993). Automated analyses of these patterns allow for fast determination of the phase and its orientation. By scanning over the sample it is possible to get a high resolution map of the crystallographic preferred orientation.

EBSD measurements were conducted with a GEMINI LEO 1530 scanning electron microscope equipped with a an EBSD detector. The sample was tilted to 70° in order to maximise the EBSD signal. An acceleration voltage of 30 keV and a working distance of

18 mm was used. Rastering was performed with a step size of 3.5 µm. Data acquisition and post-processing was performed with the AZtec software from Oxford Instruments. The indexing rate of antigorite was very low with a maximum of 15 %. The fact that antigorite is a sheet silicate and can have different stacking of adjacent layers results in differences in diffraction patterns within single rock samples (Bailey, 1988). A further uncertainty arises from the modulation in the antigorite crystallographic structure, so that the stoichiometry is not fixed. These factors make an automated phase identification difficult and contribute to the low EBSD indexing rates (Horn et al., 2020).

Electron probe microanalyzer

The major element compositions of phases in the run products as well as in the starting materials were measured with an JEOL JX8200 microprobe at BGI using WDX analysis. An acceleration voltage of 15 kV was used. In each session calibration was performed on native metals, oxides and silicates. Secondary standard San Carlos olivine samples were measured to check the consistency between the different measurement sessions. The beam current and diameter were optimised for each phase as followed: 20 nA and a focused beam was used for olivine, pyroxenes and oxides. 10 - 15 nA and a 2 - 5 µm beam spot was used for serpentine, chlorite and carbonates. Volatile contents of hydrous minerals and carbonates were estimated based on the deficit in the oxide sum. In some experiments the grain size of olivine and pyroxene was too small for individual measurements. Measurements on aggregates of olivine+pyroxene were thus used to create analysis trends that could be extrapolated to the compositions of each contributing phase. In carbonate-free experiments these are a (Mg,Fe):Si ratio of 1:1 for orthopyroxene and 2:1 for olivine. In carbonate-bearing experiments the stable pyroxene is a Ca-bearing clinopyroxene. The bulk olivine+clinopyroxene assemblage could thus be extrapolated to 0 wt% CaO for olivine and to 23 wt% CaO for clinopyroxene. The exact value chosen for the extrapolation does not significantly influence further calculations such as the mass balance and the oxygen fugacity. The value of 23 wt% CaO in diopside was chosen based on mean compositions of sample V1077 and lies on the diopside-hedenbergite join. Sulfides were excluded from measurements since they were only observed as minor phases and do not contain a significant amount of bulk Fe.

The chemical composition of the phases in each sample is averaged over the whole capsule to account for thermal gradients. Mean values and the corresponding 1σ standard deviation was used for further calculations.

2.4.2 Mössbauer spectroscopy

Mössbauer spectroscopy is used to probe the chemical environment of atomic nuclei in order to determine the coordination and oxidation state of the atoms. Mössbauer spectroscopy can be applied to a number of elements but is generally used in geosciences, as in this study, to examine the site environment and oxidation state of Fe in mineral phases. The method takes advantage of the nearly recoil free emission and absorption of γ-photons. In this process the energy of the absorbed and emitted photon is nearly identical. Hence, this effect can be exploited for very sensitive measurements of the chemical environment of target atoms due to the extremely narrow natural linewidth of the transition.

The source of radiation is ^{57}Co with a half life of 271.8 days. Via electron capture ^{57}Co decays to an exited state of ^{57}Fe with an excitation energy of 136.3 keV, which then decays to the ground state of ^{57}Fe through a series of γ-photon emissions. About 9% of the 136.3 keV excited ^{57}Fe decays directly into the ground state. The remaining 91% first relaxes to a 14.4 keV energy level before reaching the ground state by emitting characteristic radiation at 14.4 keV (Dyar et al., 2006).

Since the nuclear energy levels of an Fe atom in a crystal structure are modified from that of a free Fe atom, absorption of the γ-photon in the sample will happen at energies slightly different from the 14.4 keV energy level. An energy spectrum is generated by moving the source relative to the sample. Due to the Doppler effect the energy of emitted γ-photons shows a variation both to higher and lower energies relative to the 14.4 keV level. After a γ-photon is absorbed by the sample, it is reemitted in a random direction, which causes a dip in measured transmission spectrum.

The electronic environment of the Fe nucleus leads to several characteristics in the spectrum, which are described by the hyperfine parameters shown in figure 2.5a. The hyperfine parameters are used to identify the coordination and redox state of Fe. Typical values are shown in figure 2.5b. A non-zero centre shift (CS) is observed as a shift of the whole spectrum relative to the spectrum of a free Fe nucleus (fig. 2.5a). The CS, sometimes also referred to as isomer shift, arises from the overlap of the charge distribution of the s-electrons and the nucleus. The nuclear quadrupole moment of a nucleus without spherical charge distribution further interacts with the electronic field gradient and splits the nuclear energy level in two. As a result two possible transitions are observed. Additional splitting is observed as a response to a magnetic field, both external and internal. For magnetic phases the nuclear energy levels split into a sextet due to the Zeeman-effect.

The absolute values of the hyperfine parameters are specific for a certain redox state and coordination of an Fe atom as shown in figure 2.5b. In some instances minerals with similar hyperfine parameters coexist in the experimental products. The overlapping signals have to be deconvoluted by knowing the relative amount of each phase present. Furthermore, the relative peak areas of a doublet or a sextet must sometimes be adjusted as a result of preferred orientation in the sample. Doing so, it is possible to determine the $\mathrm{Fe}^{3+}/\Sigma\mathrm{Fe}$ ratio of serpentine in samples where other silicates are present such as chlorite, enstatite and olivine.

The starting material was analysed as a powder with a conventional Mössbauer source. Approximately 200 mg of powdered sample were loaded in a sample holder with a diameter of 12 mm. The mass was calculated based on the bulk composition and absorption coefficients. The maximum velocity of the source was $5\,\mathrm{mm\,s^{-1}}$.

The run products were measured with a Mössbauer point source. Thicksections of approximately 500 µm were prepared. A lead-foil with a hole was used to restrict the beam size on the sample to a diameter of 0.5 - 1 mm depending on the sample size. The samples are measured in transmission mode with a maximum velocity of $5\,\mathrm{mm\,s^{-1}}$ or $12\,\mathrm{mm\,s^{-1}}$. Cumulative spectra are acquired using a proportional counter. Multichannel scaling mode with 512 channels was used with a constant acceleration over a velocity range. The velocity range was calibrated with a 25 µm α-Fe foil. Fitting was performed with the free matlab code MossA (Prescher et al., 2012). A full transmission integral was used to account for the thickness effect of the point source. All spectra were fitted with the smallest amount of fit parameters needed to obtain a statistically good fit. To account for the effect of solid solution in all (Fe,Mg)-silicates, a pseudo-Voigt line shape was used, whereas a Lorentzian line shape was used for oxides, which are close to the ideal Fe-endmembers.

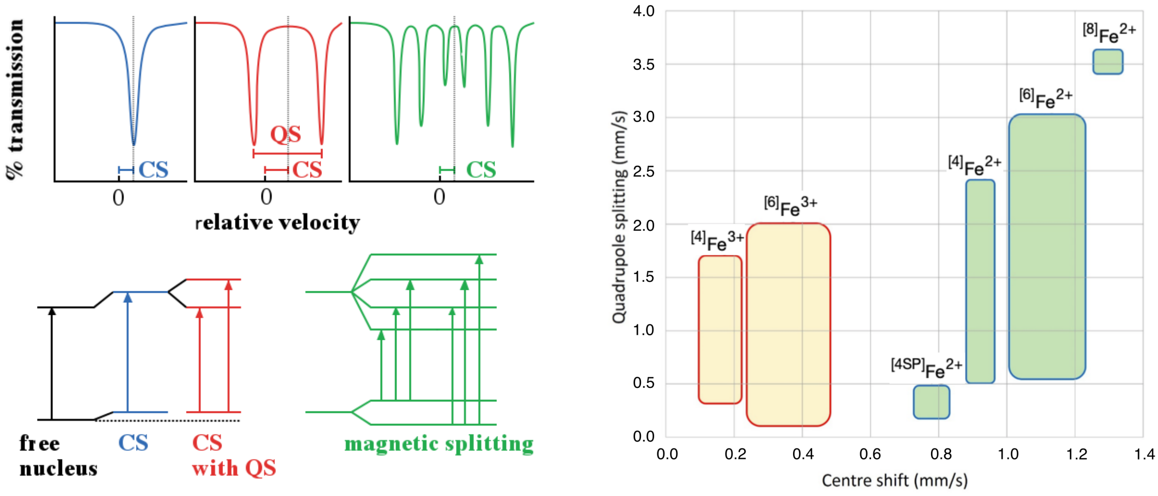

(a)

(b)

Figure 2.5: a: Schematic illustration of the interactions between the nucleus and the surrounding electrons. Modified after Dyar et al. (2006). b: CS and QS are characteristic to the redox state and the coordination of an Fe atom (after McCammon, unpublished, based on data from Burns and Solberg (1990)).

2.4.3 Raman spectroscopy

The Raman effect is based on the inelastic scattering of light. Upon interaction with a molecule the frequency of the electromagnetic wave is changed to both higher and lower values. Energy transfer from the photon to the molecule is known as Stokes scattering, whereas energy transfer from the molecule to the photon is known as Anti-Stokes scattering. According to the selection rule energy transfer is only allowed if the polarisability of the molecule is changed during a molecular vibration. This is the case for H_2O and many carbon-bearing molecules, e.g. the neutral molecules CO_2 and CH_4. The method is thus suited for identifying species in COH-fluids qualitatively.

In order to measure fluid inclusions in San Carlos olivines that were annealed in the experiments, the crystals were examined with optical microscopy and the positions of fluid inclusions marked on a sketch. The crystals are then polished by hand until the inclusion of interest was right below the surface. A Labram 800 HR UV confocal Raman spectrometer was used equipped with an argon ion laser operating at 514 nm with an output power of 200 mW. The spectra were obtained with a 50x objective lens, 1800 mm^{-1} grating and a Peltier-cooled CCD detector. The systems resolution is about 3 cm^{-1}.

Raman spectroscopy was also shown to be useful to distinguish various serpentine minerals (Auzende et al., 2004; Schwartz et al., 2013). Lizardite has four main peaks at low wave numbers near 230, 390, 690 and 1100 cm^{-1}. The Raman spectrum of antigorite is similar, while the peaks are shifted to lower wave numbers and are significantly broader with respect to lizardite. In order to distinguish lizardite and antigorite in starting material and experimental products (samples V1087, V1125, V1132a, V1132b), the peak near 370 cm^{-1}, belonging to the symmetric vibration of the SiO_4 tetrahedra (Rinaudo et al., 2003), was found to be most sensitive.

2.4.4 X-ray powder diffraction

X-ray powder diffraction (XRPD) is a powerful tool for identifying mineral phase assemblages by their respective crystallographic structure. An incident X-ray beam is focused on the sample and reflected at crystal planes. The relationship between the wavelength of the incident beam and the diffraction angle is given by Bragg's law shown in equation 2.1. In some instances when two incident beams reflect at parallel planes, a signal is detected if the path difference is an integer multiple (n in equation 2.1) of the wavelength, i.e. constructive interference occurs.

However, due to the complicated structure in sheet silicates and especially to the absence of a fixed stoichiometry in antigorite, it is difficult to distinguish serpentine minerals based on XRPD. Bailey (1969) showed that various stacking possibilities of the subsequent octahedral and tetrahedral layers in sheet silicates leads to alterations in the diffraction patterns. Peacock (1987) stated that a difference between antigorite and lizardite is the absence of a major peak in the range of 22.3 - 22.6° (2θ(Co)) in antigorite, while lizardite shows a moderate asymmetric peak. An asymmetric peak at this wavelength, however, was also found for antigorite by Schwartz et al. (2013). While antigorite has a major peak at $2\theta(\mathrm{Co}) = 41.5°$, lizardite shows this peak in the range of 41.9 - 42.1° (2θ(Co)) (Peacock, 1987). A moderate peak in the range of 69.8 - 69.9° (2θ(Co)) in antigorite is observed in lizardite at $2\theta(\mathrm{Co}) = 71.3°$. Bailey (1988) state that antigorite can be identified at its unique peak at $2\theta(\mathrm{Co}) = 70.1°$. Schwartz et al. (2013) indicate the appearance of peak at the low energy side of the 14° and 28° (2θ(Co)) peak in antigorite.

Both the starting materials and selected experimental products were analysed with microfocus X-ray diffraction. The starting materials were analysed as a thin section. The run products of samples V1087, V1125, V1132a,b, V1092 and V1114 were analysed in polished sample mounts, prepared for EPMA and SEM. A D8 DISCOVER diffractometer from

Bruker, equipped with a micro-focused Co-$K\alpha$ radiation source and a two-dimensional solid state detector was used. Operation conditions were 40 kV and 500 µA. The diffraction pattern was measured for 1200 s in the 2θ-range 25 - 85°. Peaks belonging to serpentine were found in all samples, however, the assignment to a specific serpentine polymorph was difficult based on broad peaks and the above mentioned similarities between the phases.

2.5 Computational methods

2.5.1 Mass balance calculations

Mass balance calculations were employed in order to asses the mode of each phase in the run products. Assuming constant mass in the experiment and no hydrogen loss is probably reasonable at the temperatures and relatively high oxygen fugacity of most experiments. A linear least square minimisation is applied of the form

$$A \cdot x = C, \tag{2.2}$$

where A is an $m \times n$ matrix containing phase compositions determined by EPMA measurements with m components and n phases. C is a vector of the length n, giving the starting material bulk composition (compare table 2.2) and x is a vector of the length m, containing the phase modes. Oxides used for the mass balance calculations are SiO_2, Cr_2O_3, FeO, Al_2O_3, MgO, IrO_2 and H_2O. In carbonate-bearing experiments additionally CaO and CO_2 were computed. Constraints on x are set so that

$$0 \leq x_i \leq 1 \tag{2.3}$$

$$\sum x_i = 1, \tag{2.4}$$

as no negative phase modes are possible (eq. 2.3) and the total amount of phases needs to sum up to unity (eq. 2.4).

In order to estimate the uncertainty of the phase modes due to uncertainties in the mineral composition, a Monte Carlo simulation is used. 1000 minimisation steps are calculated, each having values for A and C generated randomly with a Gaussian distribution around the mean and 1σ standard deviation obtained from measurements. The fluid composition is fixed to pure H_2O in carbonate-free experiments. As the presence of carbonate leads to a COH-fluid rather than pure H_2O, the fluid composition is rebalanced in carbonate-bearing experiments after each minimisation by the misfit in CO_2 component as

$$A_{CO_2}^{k+1} = (C_{CO_2} - A_{CO_2}^{k} x^k) + A_{CO_2}^{k} \tag{2.5}$$

where $1 \leq k \leq 1000$ denotes the k^{th} minimisation. Tests on various hypothetical compositions showed that the starting value of the fluid composition does not matter and the minimisation converges within hundred steps. An example is shown in figure 2.6. The hypothetical composition is calculated based on 10 wt% Mg_2SiO_4 (olivine), 10 wt% $MgCaSi_2O_6$ (diopside), 70 wt% $CaCO_3$ (calcite) and 10 wt% fluid with X(CO_2) of 0.9. The minimisation was started with X(CO_2) of 0 and already after 100 minimisation steps the fluid composition adjusted to its hypothetical value of 0.9.

The phase modes are generally close to a normal distribution. The mean values and standard deviations reported are based on all 1000 minimisations, although a slight anisotropy arising from the iterative fluid calculation is expected. However, since the fluid composition converges in the first 100 steps, this does not significantly change the resulting phase modes.

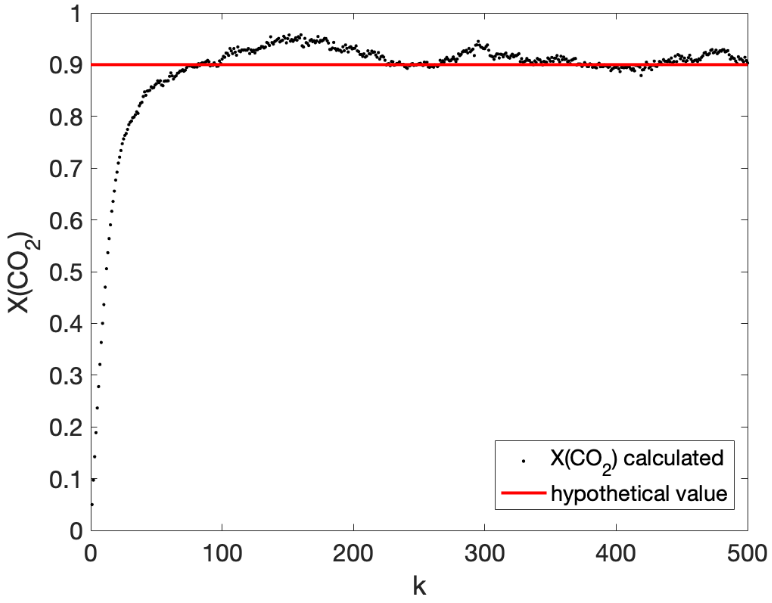

Figure 2.6: Evolution of the fluid X(CO_2) with increasing k. The red line denotes the hypothetical value. Only the first 500 minimisation steps are shown in the graph.

2.5.2 Oxygen fugacity determination

In experiments conducted at buffered $f(\mathrm{O}_2)$ conditions the oxygen fugacity is determined by the reaction

$$\mathrm{metal} + \mathrm{O}_2 = \mathrm{oxide}. \tag{2.6}$$

The $f(\mathrm{O}_2)$ for such metal-oxide pairs is calculated as

$$\log(f(O_2)) = \frac{\Delta G_r}{RT\ln(10)}, \tag{2.7}$$

where R is the gas constant, T the temperature in K, and $\Delta G_r = G_{PT}(\mathrm{product}) - G_{PT}(\mathrm{educt})$ is the standard state Gibbs free energy change of the reaction of the pure phases at the PT of interest.

When the stable mineral assemblage contains elements in different redox states then the $f(\mathrm{O}_2)$ can also be calculated from the mineral composition. Several redox equilibria involving phases observed in the run products are written and summarised in table 2.3. Equilibrium I, based on magnetite and IrFe-alloy, is relevant for all experiments where Ir was added. Equilibria II, III and IV contain the Fe^{2+}-bearing silicates ferrosilite and fayalite as the oxidised counterpart to the redox-sensor Ir. Since orthopyroxene is not stable together with carbonates, these equilibria are only valid for carbonate-free experiments. In carbonate-bearing experiments the ferrosilite component of clinopyroxene has to be taken instead. The run products do not contain quartz but the Si activity (a(Si)) can be calculated with equilibria XX that uses the enstatite component in orthopyroxene or clinopyroxene. Equilibria V and VI are written as a redox reaction between Mgt and coexisting silicates. At very high $f(\mathrm{O}_2)$ the stable oxide is hematite whereby equilibria V and VI can be reformulated to equilibria XV and XVI.

Table 2.3: Summary of equilibria employed for $f(O_2)$ calculations. En = enstatite, Fa = fayalite, Fo = forsterite, Fs = ferrosilite, Hem = hematite, (Ir)Fe = IrFe-alloy, Mgt = magnetite, Qtz = quartz.

equilibrium without silicates	
eq. I	3 (Ir)Fe + 2 O_2=Mgt
equilibria based on alloy and silicates	
eq. II	2 (Ir)Fe + O_2 + Qtz=Fa
eq. III	2 (Ir)Fe + O_2 + Fs=2 Fa
eq. IV	2 (Ir)Fe + O_2 + 2 Qtz=Fs
equilibria based on oxide and silicates	
eq. V	3 Fa + O_2=2 Mgt + 3 Qtz
eq. VI	3 Fs + O_2=2 Mgt + 6 Qtz
eq. XV	2 Fa + O_2=2 Hem + 2 Qtz
eq. XVI	2 Fs + O_2=2 Hem + 4 Qtz
Si-activity	
eq. XX	Fo + Qtz= En

The equilibria in table 2.3 have the general form

$$\mathrm{Fe}^0 + \tfrac{1}{2}\,\mathrm{O}_2 = \Omega\text{-FeO} \tag{2.8}$$

$$3\ \Omega\text{-FeO} + \tfrac{1}{2}\,\mathrm{O}_2 = \mathrm{Fe}_3\mathrm{O}_4 \tag{2.9}$$

$$2\ \Omega\text{-FeO} + \tfrac{1}{2}\,\mathrm{O}_2 = \mathrm{Fe}_2\mathrm{O}_3, \tag{2.10}$$

where Ω-FeO denotes a silicate (Ω) containing Fe^{2+}, e.g. olivine, orthopyroxene and clinopyroxene. In contrast to pure phases in eq. 2.6, activities have to be considered for silicates and alloys due to presence of solid solutions.

The $f(\mathrm{O}_2)$ is thus calculated as

$$\log(f(O_2)) = \frac{\Delta G_r}{RT\ \ln(10)} + \log(K), \tag{2.11}$$

where K is the equilibrium constant calculated as

$$\log(K) = \sum_{j=1}^{\text{products}} n_j\ \log(a_i^j) - \sum_{j=1}^{reactands} n_j\ \log(a_i^j), \tag{2.12}$$

with a_i^j being the activity of component i in phase j and n_j refers to the number of moles of phase j participating in the reaction. a_i^j is calculated as $(X_i^j \gamma_i^j)^m$ where X_i^j is the mole fraction of endmember component i in phase j, γ_i^j is the activity coefficient and m is the site multiplicity. For example, X_{Fe} refers to the fraction of Fe on the site of mixing and is calculated as

$$X_{Fe} = \frac{\mathrm{Fe}}{\mathrm{Fe} + \mathrm{Mg}}. \tag{2.13}$$

For all silicates a simple symmetric Margules model is used to calculate excess energies arising from mixing of two components on a site. Only for IrFe-alloy an asymmetric model with two Margules parameters W_1 and W_2 depending on P is used. Formulations of both X and γ are given in table 2.4. Although clinopyroxene might show cation ordering at low temperature, where Ca partitions to one of the octahedral sites, the EPMA data do not allow for site assignment of the elements. The clinopyroxenes diopside and hedenbergite are thus calculated as fully disordered, e.g. all octahedral cations distribute equally on both octahedral sites. This assumption has no effect on the calculated $f(\mathrm{O}_2)$.

Table 2.4: Formulations of X and γ of minerals in table 2.3. References: 1: von Seckendorff and O'Neill (1993), 2: Holland and Powell (1998), 3: Swartzendruber (1984), 4: Schwerdtfeger and Zwell (1968)

	formula	mole fraction as X^m
Fo	Mg_2SiO_4	$(1-X_{Fe})^2$
Fa	Fe_2SiO_4	X_{Fe}^2
En	$Mg_2Si_2O_6$	$(1-X_{Fe})^2$
Fs	$Fe_2Si_2O_6$	X_{Fe}^2
Di	$MgCaSi_2O_6$	$(1-X_{Fe})^2$
Hed	$FeCaSi_2O_6$	X_{Fe}^2
(Ir)Fe	(Ir,Fe)	X_{Fe}

	activity coefficient as γ^m	W_1 J/mol	W_2 J/mol	Reference
Fo	$\exp[(W_1 X_{Fe}^2)/(RT)]^2$	5625		1
Fa	$\exp[(W_1(1-X_{Fe})^2)/(RT)]^2$	5625		1
En	$\exp[(W_1 X_{Fe}^2)/(RT)]^2$	2145		1
Fs	$\exp[(W_1(1-X_{Fe})^2)/(RT)]^2$	2145		1
Di	$\exp[(W_1 X_{Fe}^2)/(RT)]^2$	2500		2
Hed	$\exp[(W_1(1-X_{Fe})^2)/(RT)]^2$	2500		2
(Ir)Fe	$\exp[(1-X_{Fe})^2(W_1+2X_{Fe}(W_2-W_1))/(RT)]$	-51814 +0.0736P	-62796 +0.0736P	3,4

The standard state Gibbs free energy G of each phase at PT conditions of interest was determined using the Tait equation of state described in Holland and Powell (2011). At ambient conditions of 1 bar and 25 °C, marked with the superscript ^{0}, G is given as

$$G^0 = H^0 - TS^0, \tag{2.14}$$

where H is the enthalpy and S the entropy. At temperature T of interest the expression is given as

$$G_{1\mathrm{bar},T} = G^0 + \int_{T^0}^{T} C_P \, dT - T \int_{T^0}^{T} \frac{C_P}{T} \, dT, \tag{2.15}$$

with C_P being the heat capacity function of the pure phases. At P of interest the equation is given with an additional volume term as

$$G_{PT} = G_{1\mathrm{bar},T} + \int_{P^0}^{P} V_{P,T}\,dP, \tag{2.16}$$

with V being the volume. The volume equation of state is divided into a cold compression term and a thermal contribution. The cold compression term is given at $T = T^0$ as

$$V_{P,T^0} = V^0[1 - a(1 - (1 + bP)^{-c})], \tag{2.17}$$

where a, b and c are parameters described in terms of the bulk modulus at ambient conditions κ_0 and its first and second pressure derivatives, i.e.

$$a = \frac{1 + \kappa_0'}{1 + \kappa_0' + \kappa_0\kappa_0''} \tag{2.18}$$

$$b = \frac{\kappa_0'}{\kappa_0} - \frac{\kappa_0''}{1 + \kappa_0'} \tag{2.19}$$

$$c = \frac{1\kappa_0' + \kappa_0\kappa_0''}{\kappa_0'^2 + \kappa_0' - \kappa_0\kappa_0''}. \tag{2.20}$$

The thermal contribution is described by the thermal pressure P_{TH}:

$$P_{TH} = \int_{T^0}^{T} \alpha\kappa\,dT\,|_V. \tag{2.21}$$

The term $\alpha\kappa$, where α is the expansion coefficient and κ the compressibility, must vanish at 0 K and remains constant at elevated temperatures. This is due to the Grüneisen relation $\alpha\kappa = (\gamma/V)\,C_V$ where γ is the heat capacity ratio and C_V is the heat capacity at constant volume. The term γ/V is nearly independent of T so that the term $\alpha\kappa$ has a similar form to the heat capacity function, which Holland and Powell (2011) described using an Einstein function of the form

$$\xi = \frac{u^2 e^u}{(e^u - 1)^2}, \tag{2.22}$$

where $u = \theta/T$. $\theta = 10636/(S^0/n+6.44)$ is the Einstein temperature and n is the number of atoms in the phase. The term $\alpha\kappa$ in eq. 2.21 thus becomes $\alpha\kappa = \alpha_0\kappa_0(\xi/\xi_0)$ with ξ_0 being ξ at $T = T^0$. The thermal contribution in eq. 2.21 can then be rewritten as

$$P_{TH} = \frac{\alpha_0\kappa_0\theta}{\xi}\left(\frac{1}{e^u - 1} - \frac{1}{e^{u_0} - 1}\right). \tag{2.23}$$

With $P = P^0 + P_{TH}$ the volume term in eq. 2.16 becomes

$$V_{P,T} = V^0[1 - a(1 - [1 + b(P - P_{TH})]^{-c})] \tag{2.24}$$

and thus

$$\begin{aligned}&\int_{P^0}^{P} V_{P,T}\, dP \\ =&P\ V^0\ (1 - a\left(1 - \frac{(1 - bP_{TH})^{(1-c)} - (1 + b(P - P_{TH}))^{(1-c)})}{Pb(c-1)}\right).\end{aligned} \tag{2.25}$$

For Qtz, RuO_2, Mgt and Hem an additional Landau potential is added due to second order phase transitions, i.e. changes in crystal structure or magnetic transitions. A tricritical phase transition model is used for all phases according to Holland and Powell (1998). The excess energy is first written as a polynomial expansion with the order parameter Q as

$$G_{Landau}(Q) = aQ + \frac{1}{2}AQ^2 + \frac{1}{3}bQ^3 + \frac{1}{4}BQ^4 + \frac{1}{5}cQ^5 + \frac{1}{6}CQ^6 + ... \tag{2.26}$$

In a tricritical phase transition the linear and all odd terms have to be absent and B is zero in order to fulfill the equilibrium criteria

$$\frac{\partial G_{Landau}}{\partial Q} = 0 \tag{2.27}$$

$$\frac{\partial^2 G_{Landau}}{\partial Q^2} > 0. \tag{2.28}$$

Further, A has to be positive above the critical temperature of the transition T_c to stabilise the ordered phase, but is required to change sign at temperatures below the transition. This is achieved by a T-dependent term given by $A = a(T - T_c)$, whereas all other terms are T-independent. The equilibrium requirement can then be written as

$$\frac{\partial G_{Landau}}{\partial Q} = 0 = a(T - T_c)Q + CQ^5. \tag{2.29}$$

In the high symmetry phase, which is stable above T_c, Q is 0. Below T_c the order parameter is given as

$$Q^2 = \sqrt{1 - \frac{T}{T_c}}. \tag{2.30}$$

With $a = 2S_{max}$ and equation 2.30 c can be obtained from equation 2.29. The potential can then be written as

$$G_{Landau} = S_{max}[(T - T_c)Q^2 + \frac{1}{3}T_c Q^6] \tag{2.31}$$

S_{max} is the tabulated maximum entropy of disorder. In order to account for P, a P-dependent critical temperature can be substituted, assuming that also only the first term is P-dependent. The P-dependency is taken from the relation

$$\frac{\partial T_c}{\partial P} = \frac{V_{max}}{S_{max}}, \tag{2.32}$$

where V_{max}, the maximum volume of disorder, is determined to match the P-T slope of the transition, resulting in

$$T_c^* = T_c + \frac{V_{max}}{S_{max}} P. \tag{2.33}$$

The potential thus becomes

$$G_{Landau} = S_{max}[(T - T_c^*)Q^2 + \frac{1}{3}T_c Q^6]. \tag{2.34}$$

The partial derivatives of the potential result in the excess enthalpy, entropy and volume being:

$$S_{Landau} = -\frac{\partial G}{\partial T} = -S_{max} Q^2 \tag{2.35}$$

$$V_{Landau} = \frac{\partial G}{\partial P} = V_{max} Q^2 \tag{2.36}$$

$$H_{Landau} = G_{Landau} + TS_{Landau} = S_{max} T_c \left(\frac{1}{3} Q^6 - Q^2 \right). \tag{2.37}$$

The excess energy arising from the Landau transition is given by the expression

$$\begin{aligned} G_{Landau} = S_{max} &\left[T_c \left(\frac{1}{3} Q^6 - \frac{1}{3} Q_0^6 + Q_0^2 \right) - T_c^* Q^2 \right] \\ &- TS_{max}(Q_0^2 - Q^2) + PV_{max} Q_0^2, \end{aligned} \tag{2.38}$$

where Q_0 is the order parameter at ambient conditions given as $Q_0^2 = \sqrt{1 - \frac{298}{T_c}}$. The final expression for the free energy of a phase is given as

$$G = G^0 + \int_{T^0}^{T} C_P \, dT - T \int_{T^0}^{T} \frac{C_P}{T} \, dT + \int_{P^0}^{P} V_{P,T} \, dP + G_{Landau}. \tag{2.39}$$

Thermodynamic data used for the calculation of Gibbs free energies in this work are summarised in table 2.5.

Table 2.5: Thermodynamic parameters used to calculate $f(O_2)$. Note that the volume change of reaction of Re-ReO$_2$ buffer is taken in a parameterised form. Heat capacity of Fe is divided in different T ranges as ^{a} T>1000 K, ^{b} 1000 K<T<1042 K, ^{c} T>1042 K. *enthalpy of Fe is given as $H_{T_{\mathrm{ref}}}$-H^{298}. References: 1: O'Neill (1987), 2: Holland and Powell (2011), 3: Pownceby and O'Neill (1994), 4: O'Neill and Nell (1997), 5: Armstrong (2018), 6: Campbell et al. (2006), 7: Komabayashi and Fei (2010), 8: Fabrichnaya et al. (2004)

	T_{ref}	$H_f{}^0$	$S_f{}^0$	a	b (10^3)	c(10^{-3})	d	Reference
	K	J/mol	J/(mol K)		$C_P = a + bT + cT^{-2} + dT^{-0.5}$			
Ru	298.15	0	28.5	13.054	10.052	-345.7	205.2	4
RuO_2	298.15	-314133.19	46.15	119.277	0.626	-105.8	-1074.6	4
Re	298.15	0	36.526	24.336	5.332	57.057	-21.762	3
ReO_2	298.15	-448943	47.827	79.067	9.633	-1033.24	-273.187	3
O_2	298.15	0	205.2	48.3	-0.691	499.2	-420.7	2
Fe^a	900	9564*	61.62	-263.454	255.810	0	0	1
Fe^b	1000	24400*	66.71	-641.905	696.339	0	0	1
Fe^c	1042	27300*	69.54	1946.255	-1787.497	0	0	1
Fo	298.15	-2172570	95.1	233.3	1.494	-603.8	-1869.7	2
Fa	298.15	-1477740	151	201.1	17.33	-1960.6	-900.9	2
En	298.15	-3090230	132.5	356.2	-2.99	-596.9	-3185.3	2
Fs	298.15	-2388720	189.9	398.7	-6.579	1290.1	-4058	2
Di	298.15	-3201690	142.9	314.5	0.041	-2745.9	-2020.1	2
Hed	298.15	-2841920	175	340.2	0.812	-1047.8	-2646.7	2
Mgt	298.15	-1114510	146.9	262.5	-7.205	-1926.2	-1655.7	2
Hem	298.15	-825650	87.4	163.9	0	-2257.2	-657.6	2

	V^0	α_0 (10^{-5})	α_1(10^{-9})	κ_0	κ_0'	κ_0"	$\partial\kappa_0/\partial T$	Reference
	J/bar	T^{-1}		GPa				
Ru	0.8176	2.16	-7.8	3012.4	4	-0.00162	-0.503	5
RuO_2	1.856245	1.57		2612197	4	-0.00153		5
Re	0.886		ΔV_r of Re + O_2 = ReO_2					6
ReO_2	1.8779		=-0.0699P + 0.0002(T-T_{ref})+9.9399					6
Fe	0.68468	6.40		1653000	5.5	-0.0033		7,8
Fo	4.366	2.85		128500	3.84	-0.003		2
Fa	4.631	2.82		1256000	4.68	-0.0037		2
En	6.262	2.27		1059000	8.65	-0.0082		2
Fs	6.592	3.26		1010000	4.08	-0.004		2
Di	6.619	2.73		1192000	5.19	-0.0044		2
Hed	6.795	2.38		1192000	3.97	-0.0033		2
Mgt	4.452	3.72		1857000	4.05	-0.0022		2
Hem	3.027	2.79		2230000	4.04	-0.0018		2

	T_{co}	S_{max}	V_{max}	Reference
	K	J/(mol K)	J/bar	
RuO_2	-1413.01	0.01	0.04	5
Qtz	847	0.00495	0.1188	2
Mgt	848	0.035	0	2
Hem	955	0.0156	0	2

3 Run product characterisation

In this chapter experimentally determined phase relations and compositions are reported. The multi-anvil experiments were performed on two powdered natural serpentinite samples, Zer_1701 (antigorite-serpentinite) and Lig_1602 (lizardite-serpentinite), at 2.5 - 5 GPa and 469 - 962 °C. A subset of experiments contained additional $CaCO_3$, whereas another subset of experiments was performed under controlled oxygen fugacity. These results are used to derive a thermodynamic model described in chapter 5 and to examine the implications of Fe^{3+}-bearing serpentine for the redox conditions in subduction zones (chapter 7). In chapter 8 the mutual influence of carbonate and serpentine minerals as a function of PT-$f(O_2)$ is investigated based on the mineral compositions. Results obtained from fluid flux experiments are treated separately in chapter 9.

3.1 Phase relations

The recovered samples were analysed with SEM and EPMA in order to determine the compositions of the stable phase assemblages. Table 3.1 and 3.2 summarise the experimental run conditions and the mineralogy of the run products.

Table 3.1: Experimental conditions and run products in unbuffered experiments. Phases in parentheses were observed but were too small to be measured with EPMA. The composition of phases marked with ^{e} are extrapolated (see section 2.4.1 for details in the extrapolation procedure). Mineral abbreviations used are: Serp = serpentine, Chl = chlorite, Grt = garnet, Ol = olivine, Opx = orthopyroxene, Cpx = clinopyroxene, Mgt = magnetite, Cal = Ca-carbonate, Dol = dolomite, Mgs = magnesite, Sp = spinel, MgO = Mg-hydroxide or carbonate (not further differentiated), m-p- = minor phases.

name	T	P	time	Serp	Chl	Grt	Ol	Opx	Cpx	Mgt	Cal	Dol	Mgs	m.p.
	°C	GPa	h											
Zer_1701														
V1087	469	3	72	x						x				
V1090	572	4	62	x			(x)			x				MgO
V1159b	572	5	98	x						x				
V1104	580	3	86	x			(x)			x				MgO
V1105	627	3	86	x	x		x	(x)		x				
V1111	644	3	62	x	x		x	(x)						(Sp)
V1092	696	3.5	96		x		x^e	x^e		x				
V1102	780	3	68			x	x	x^e						(Sp)
V1048	924	2.5	48				x	x						
V1056	962	2.5	72				x	x						Sp
Zer_1701 with 20wt% $CaCO_3$														
V1079	502	3	112	x						x	x			
V1124	550	3	99	x						x	x			
V1082	562	2.5	87	x	x		x		x^e	(x)		x		(Sp)
V1057	631	2.5	70	x	x		x		x	x		x		
V1076	633	2.5	86		x		x		x	(x)	x	x		Sp
V1071	656	2.5	72		x		x		x	x		x		
V1060	787	2.5	65		x		x		(x)	x		x		
V1062	776	2.5	92				x		x			x		Sp
V1064	797	2.5	76			x	x		x			x		Sp
V1077	756	2.5	67			x	x		x			x		
V1103	804	3	91			x	x		x			x	x	Sp
V1050	958	2.5	46			x	x		x		x	x		
V1065	821	2.5	73			x	x		x			x		Sp

Table 3.1: continued

name	T °C	P GPa	time h	Serp	Chl	Grt	Ol	Opx	Cpx	Mgt	Cal	Dol	Mgs	m.p.
V1089	782	4	86			x	x		x[e]			x	x	
V1099	880	3	68			x	x		x			x	x	
Lig_1602														
V1125	483	3	80	x			(x)			x				
V1114	526	3	98	x	x		(x)	(x)		(x)				
V1159a	572	5	98	x			x			(x)				
V1116	595	3	192	x	x		x	(x)		x				
V1117	609	3	48	x	x		x	(x)		x				
V1113	607	3	87		x		x	x		x				
V1115	648	3	110		x		x	x		x				

Table 3.2: Experimental conditions and run products in buffered experiments. Phases in parentheses were observed but were too small to be measured with EPMA. Phases marked with ^{e} are extrapolated (see section 2.4.1 for details in the extrapolation procedure). Mineral abbreviations used are: Serp = serpentine, Chl = chlorite, Ol = olivine, Opx = orthopyroxene, Cpx = clinopyroxene, Mgt = magnetite, Hem = hematite, Cal = Ca-carbonate, Mgs = magnesite, Sp = spinel, MgO = Mg-hydroxide or carbonate (not further differentiated), m.p. = minor phases. $f(O_2)$ buffers used are: RRu = Ru-RuO$_2$, CbC = carbonate-graphite, RRe = Re-ReO$_2$, C = graphite, Fe = Fe metal.

name	T °C	P GPa	time h	buffer	Serp	Chl	Ol	Opx	Cpx	Mgt	Hem	Cal	Mgs	m.p.
Zer_1701														
V1143a	494	3	90	RRu	x					x				
V1160b	526	3	99	RRu	x					x				
V1148a	487	3	97	CbC	x				x	x		x		
V1153b	526	5	98	CbC	x				x	x			x	
Lig_1602														
V1132a	481	3	96	RRu	x						x			
V1146a	528	5	96	RRu	x	x					x			
V1150a	580	5	92	RRu	x		x				x			
V1127	640	3	81	RRu	x	x	x	x			x			MgO
V1135a	685	3	93	RRu		x	x	x			x			MgO
V1138a	782	3	117	RRu			x	x			x			MgO
V1132b	481	3	96	RRe	x	x	(x)			x				
V1146b	528	5	96	RRe	x		(x)			x				Sp
V1150b	580	5	92	RRe	x		x^e			x				
V1128	631	3	84	RRe	x	x	x	x		x				MgO
V1135b	685	3	93	RRe		x	x	x		x				
V1138b	782	3	117	RRe			x	x						MgO/ Sp
V1148b	487	3	97	CbC	x				(x)	x			x	
V1153a	526	5	98	CbC	x				(x)	(x)			x	
V1143b	494	3	90	C	x		x			(x)				
V1139	498	3	63	Fe	x		x							FeO
V1140	592	3	94	Fe		x	x							

At lowermost temperatures the stable mineral assemblage in unbuffered experiments is serpentine+magnetite (Serp+Mgt) and additional Ca-carbonate in carbonate-bearing experiments, respectively (fig. 3.1a, 3.1b). Serpentine grains form a dense matrix with angular oxides and carbonates embedded. Raman and XRD measurements confirm, that in the Liz-bearing experiments the serpentine phase remains lizardite (Liz) even at *PT* conditions where antigorite (Atg) is expected to be stable, i.e. above 300 °C (Schwartz et al., 2013). A high MgO-bearing phase is observed as a minor phase in few experiments. Based on the low totals obtained in EPMA analyses the phase is identified as Mg-carbonate or -hydroxide. However, since only individual grains are observed the phase does not affect general phase relations and mineral compositions. It is thus not further considered in calculations.

With increasing temperature Fe-rich silicates form along the grain boundaries of serpentine and around oxides (fig. 3.1c). This marks the onset of serpentine dehydration. The grain size of these silicates when they first appear is generally <1 µm and too small to be characterised by EPMA but they were identified as olivine (Ol) through X-ray diffraction measurements. With increasing temperature the Fe-rich Ol grows and chlorite (Chl) and pyroxene (Px) appear additionally. Chl forms flakes with a diameter up to 10 µm (fig. 3.1d). Often, Px has a spinifex-like texture. The grain size of Px and Ol increases with temperature up to approximately 10 µm. Also observed is a gradual disappearance of Mgt with increasing temperature in experiments which are not $f(O_2)$ buffered. After Chl dehydration the main Al-bearing phases are orthopyroxene (Opx) and spinel (Sp) at low pressures, whereas garnet (Grt) is observed at $P \geq 2.5$ GPa (fig. 3.1e). Grt shows a poikilitic texture with various silicate and carbonate inclusions.

In the carbonate-bearing experiments clinopyroxene (Cpx) forms instead of Opx through Ca-Mg exchange with the carbonate fraction. The carbonate is pure Ca-carbonate (Cal) at low temperature and shifts to dolomite (Dol) and further to magnesite (Mgs) with increasing temperature. The carbonate composition is further a function of pressure, so that Mgs is only observed at $P \geq 3$ GPa.

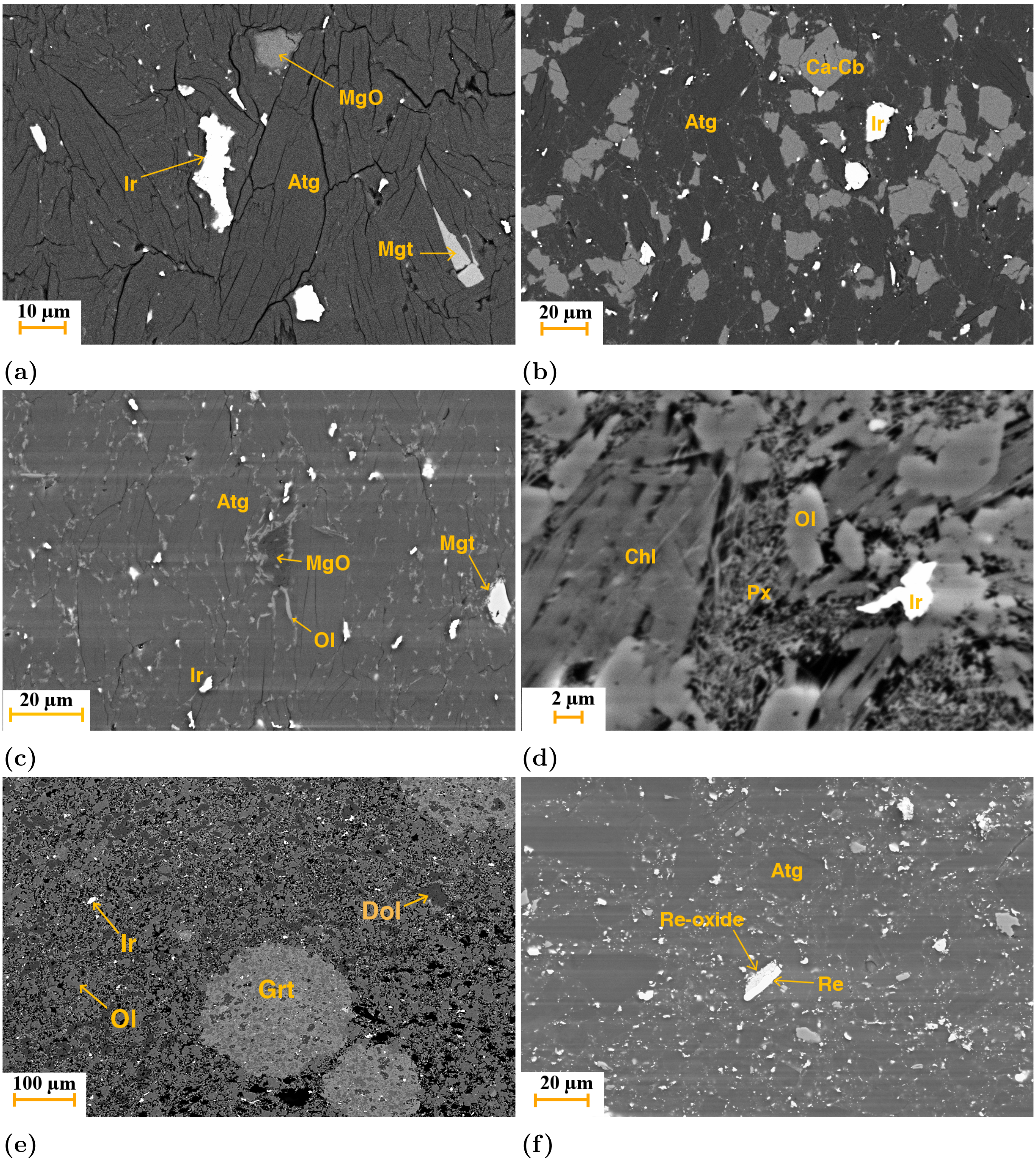

Figure 3.1: SEM figures showing typical mineral assemblages in run products. a: Atg with angular Mgt at low T (V1087: 469 °C, 3 GPa). b: At low T Ca-carbonate is the stable carbonate in equilibrium with Atg (V1079: 502 °C, 3 GPa). c: Ol forms along the grain boundaries at increased T (V1090: 572 °C, 4 GPa). d: Chl+Ol+Px is the stable mineral assemblage after the Atg dehydration. Px often shows a spinifex-like texture (V1092: 696 °C, 3.5 GPa). e: Grt is the stable Al-phase in a completely dehydrated mineral assemblages (V1065: 821 °C, 2.5 GPa). f: Buffer components are disseminated in the sample (V1135b: RRE, 685 °C, 3 GPa).

In the oxygen buffered experiments the buffer components are dispersed through the sample (fig. 3.1f). The presence of all buffer components was confirmed with SEM analyses. Only in Ru-RuO_2 buffered Atg-bearing experiments the buffer was found to not work as only the Ru-metal was confirmed (V1143a, V1160b). The overall silicate phase relations of buffered experiments are similar to the unbuffered experiments. However, when using the Ru-RuO_2 oxygen buffer the stable Fe-oxide is hematite (Hem). A T-dependent disappearance of Hem is not observed in contrast to Mgt. Some experiments were run with a buffer assemblage of carbonate ($CaCO_3$) and graphite (i.e. CbC buffer). In these experiments Mgs is formed in most experiments (compare also chapter 8 for detailed description). The presence of Mgs particularly at low T conditions is different from its occurrence solely at high PT conditions in Atg+Cb experiments. The lowest $f(O_2)$ was obtained by using an Fe-metal buffer in samples V1139 and V1140. Around the metal a layer of Ol with a very low Mg# of 0.57 formed. In between the Fe-metal and the Fe-rich Ol Mgt formed (fig. 3.2).

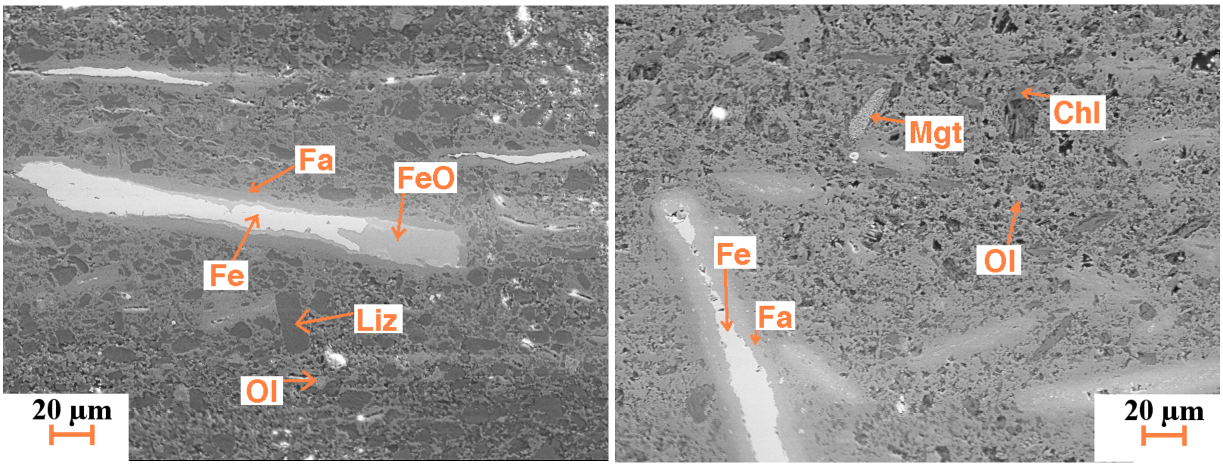

(a) (b)

Figure 3.2: The Fe-metal is surrounded with a layer of FeO and fayalitic Ol (Fa). a: V1139 (498 °C, 3 GPa). b: V1140 (592 °C, 3 GPa).

Figure 3.3 shows the experimentally determined stability of hydrous phases Atg, Liz and Chl, respectively. Two dehydration reactions, being the Atg/Liz-out and the Chl-out, are indicated. The presence of carbonates in a subset of Atg-bearing experiments decreases the dehydration temperature about 20 °C (fig. 3.3a, table 3.1). The dehydration temperature of unbuffered Liz is slightly lower with respect to Atg. In the buffered Liz-bearing experiments, however, there is a consistent extension of the Liz stability field with increasing $f(O_2)$ as shown in figure 3.3b and table 3.2. Similarly, at very low $f(O_2)$ the Liz dehydration is observed already between 500 °C and 600 °C in experiments buffered with Fe-metal. These are the first experiments to explore the high PT stability of Liz which appears, for the composition examined, to be similar or possibly slightly higher than that of Atg, particularly at high $f(O_2)$.

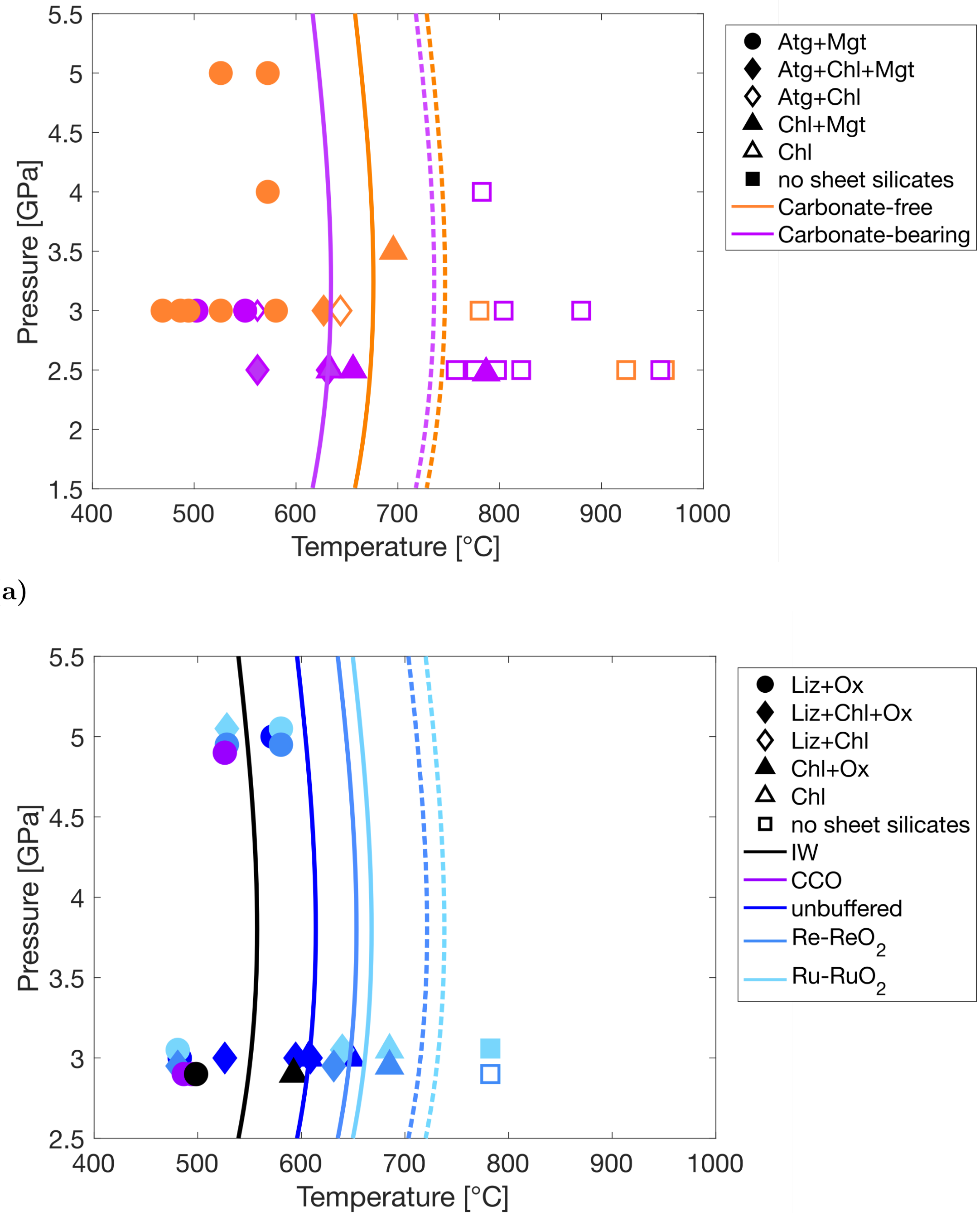

(a)

(b)

Figure 3.3: Serp and Chl stability as a function of P and T for various starting materials. Filled symbols indicate the presence of oxides. Vertical curves mark dehydration temperature for Serp (solid) and Chl (dotted). a: Atg starting material. Carbonate-bearing experiments are purple, carbonate-free experiments are orange. Mgt is observed only at temperatures below the Chl-out. b: Liz starting material, colour-coded for $f(O_2)$. Increasing $f(O_2)$ shifts the dehydration towards higher temperatures. Note that all Liz-bearing experiments were conducted at 3 and 5 GPa. The apparent P distribution serves for better visualisation.

3.2 Mineral compositions

The compositions of phases in each experiment varies as a function of PT-$f(O_2)$ and bulk composition. Mean compositions measured by EPMA are reported in appendix B.

Serpentine

The stoichiometric composition of Serp is calculated for a total of 5 cations pfu for Liz and 4.824 cations pfu for Atg. This results from the modulated structure of Atg that alters the ratio of octahedral sites, i.e. Atg is depleted in $3/m$ Br components pfu relative to Liz (section 1.4). Although the modulation itself might be a function of pressure and temperature (Shen et al., 2020) and varies therefore with the metamorphic grade (Mellini et al., 1987), the stoichiometry of Atg in this study was calculated relative to an $m = 17$ polysome for all experimental conditions.

The Mg#, defined as molar MgO/(MgO+FeO) with FeO being the ferrous fraction of total Fe derived from EPMA and Mössbauer analyses (see section 3.3), is between 0.937 and 0.961 for Atg and decreases with increasing temperature (fig. 3.4a). The values are comparable with the starting material Mg# of 0.95. The Mg# of unbuffered Liz ranges from 0.935 to 0.951, and also decreases with increasing temperature. The Mg# of Liz additionally changes with $f(O_2)$ and reaches near unity in Ru-RuO_2 buffered experiments. Furthermore, the data indicate that the Mg# is higher in Liz equilibrated at high pressure. MgO and total Fe as FeO in Liz decrease with increasing temperature (fig. 3.4b and 3.4c). For Atg the MgO content is independent of temperature whereas total FeO increases slightly.

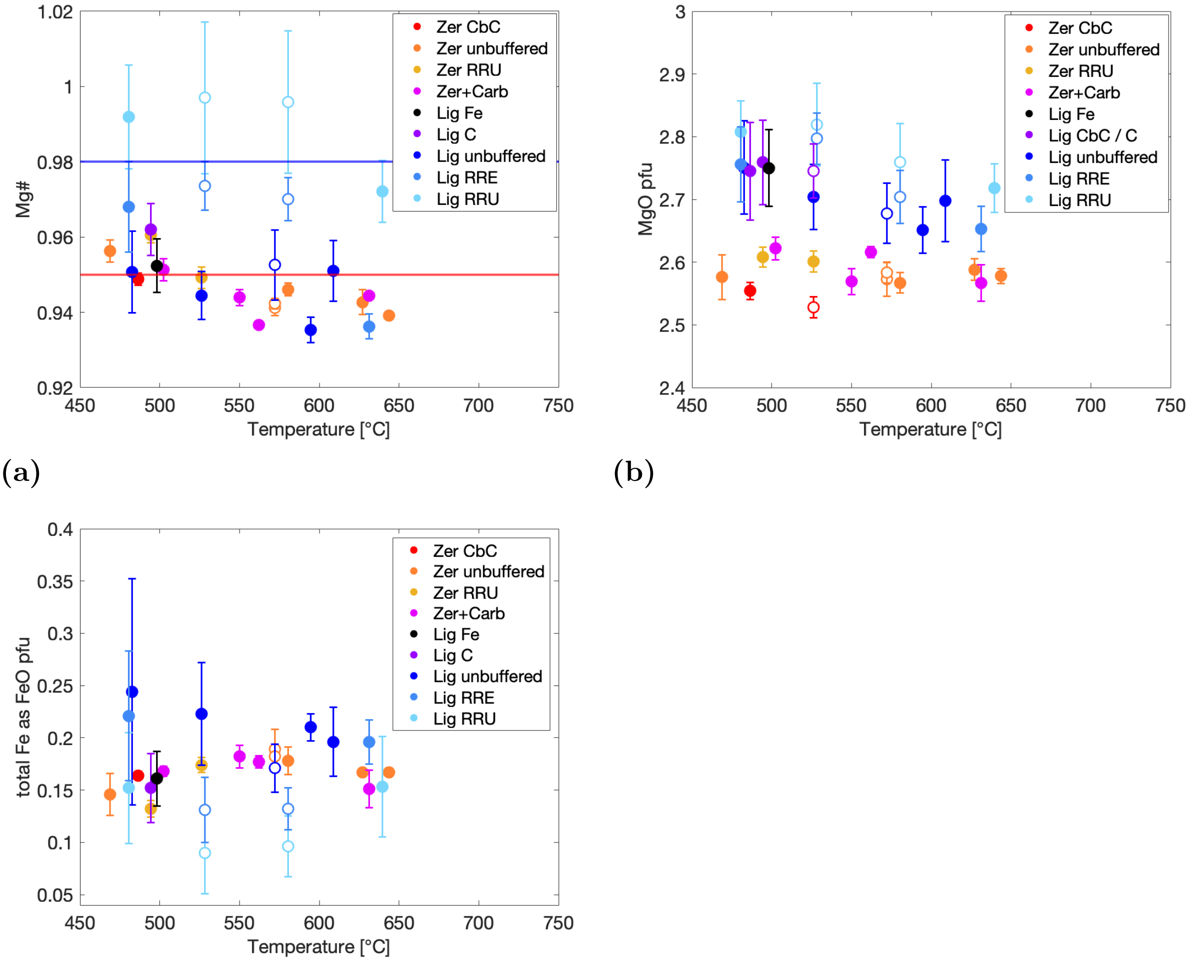

(a)

(b)

(c)

Figure 3.4: a: The Mg# of Atg and Liz in run products. Open symbols mark experiments conducted at $P \geq 4$ GPa. The Mg# of the starting material is indicated by horizontal lines (red = Atg, blue = Liz). b: A negative correlation with T is observed in MgO pfu in Liz. c: A decrease in total Fe as FeO with increasing T is observed in Liz, whereas total Fe as FeO increases in Atg.

Atg samples show very small variations in Al_2O_3 contents between 0.13 to 0.15 pfu over the entire experimental conditions and are essentially identical to the starting material as shown in figure 3.5. This finding confirms data from other studies, showing that the Al content in Atg does not change with respect to temperature within experimental time scales. There appears to be some T-dependence, however, in natural Atg samples reported in a study by Schwartz et al. (2013). Atg from the medium and high temperature domain of the Schistes lustrées complex and Monviso ophiolite complex were equilibrated at temperatures between 350 °C and 500 °C at 1.2 GPa and show increasing Al content with increasing temperature.

Liz samples show significant variations in Al_2O_3 contents, which increase with temperature from approximately 0.1 to 0.3 Al pfu between 483 °C and 640 °C. The Liz Al content appears to be only a function of temperature and shows no correlation with pressure or $f(O_2)$. Furthermore, the Liz Al content follows a very similar T-relation as observed in natural Atg reported by Schwartz et al. (2013).

The total trivalent cation content in serpentine measured in this study correlates with Si pfu as shown in figure 3.6a. This indicates a coupled substitution of trivalent cations on the octahedral (VI) and tetrahedral (IV) sites. Ferric Fe only partitions on to the octahedral site as shown by Mössbauer analyses (see section 3.3). Assuming ferric Fe and Al being the main trivalent cations, which is confirmed by EPMA data (table B.1), the tetrahedral Al content in each sample is calculated as

$$\mathrm{Al}^{\mathrm{IV}} = \frac{\mathrm{Fe}^{3+} + \mathrm{Al}^{\mathrm{tot}}}{2}. \tag{3.1}$$

The octahedral Al content is then simply given by

$$\mathrm{Al}^{\mathrm{VI}} = \mathrm{Al}^{\mathrm{tot}} - \mathrm{Al}^{\mathrm{IV}}. \tag{3.2}$$

While in Atg the partitioning of Al between the two sites is constant over the whole experimental T-range, the relative amount of octahedral and tetrahedral Al in Liz is strongly T-dependent (fig. 3.6b). At T<500 °C the Liz-bearing experiments have almost all Al partitioned on the tetrahedral site. With increasing temperature more Al partitions on to the octahedral site. The ratio between tetrahedral Al and octahedral Al approaches a value of 0.5 indicating uniform distribution of Al among all accessible sites in the Liz structure prior to dehydration. Although the relative amount of tetrahedral Al is decreasing with increasing temperature, the total amount of Al_2O_3 in Liz is increasing. Consequently, in order to balance an increasing total tetrahedral Al content, the Si pfu in Liz is decreasing with increasing temperature as shown in figure 3.6c.

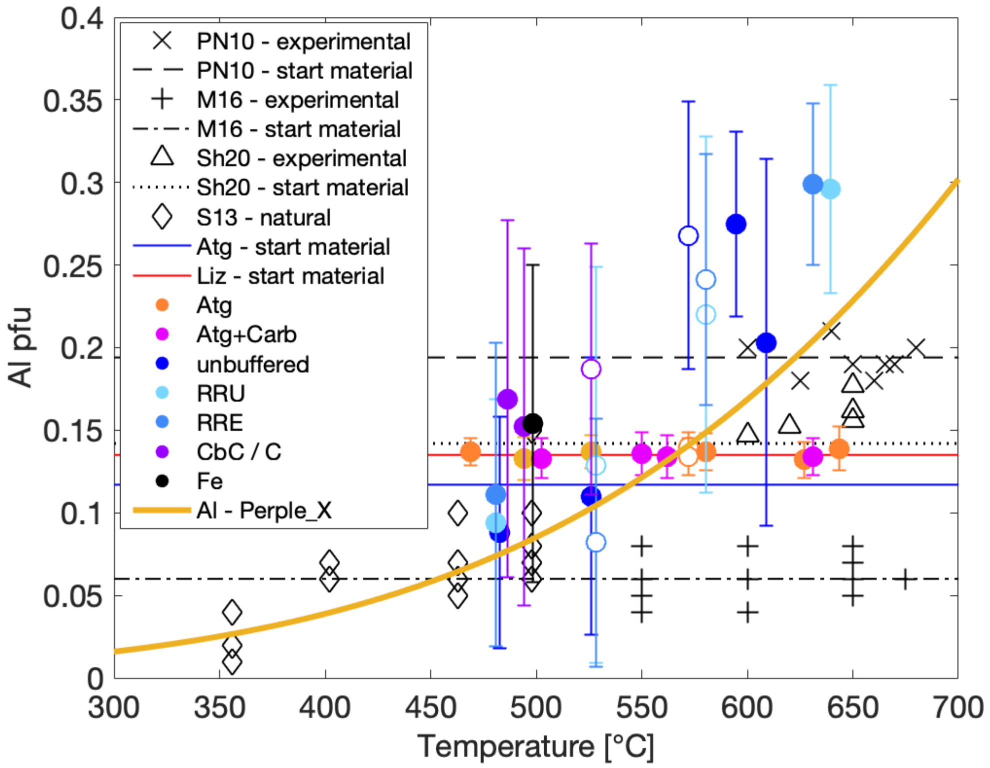

Figure 3.5: Al content of Atg and Liz in run products as a function of temperature for various starting material composition. Coloured open symbols mark experiments conducted at $P \geq 4$ GPa. Literature data are added for comparison. Atg in run products has a constant Al_2O_3 content similar to the starting material. The yellow line represents the T-dependent Al content as obtained from Perple_X (chapter 6): $\mathrm{Al}^{\mathrm{tot}} = (1 + \mathrm{erf}(\frac{T-999.726}{410.622}))$, where T is the temperature in celsius. References: PN10 = Padrón-Navarta et al. (2010), M16 = Merkulova et al. (2016), Sh20 = Shen et al. (2020), S13 = Schwartz et al. (2013).

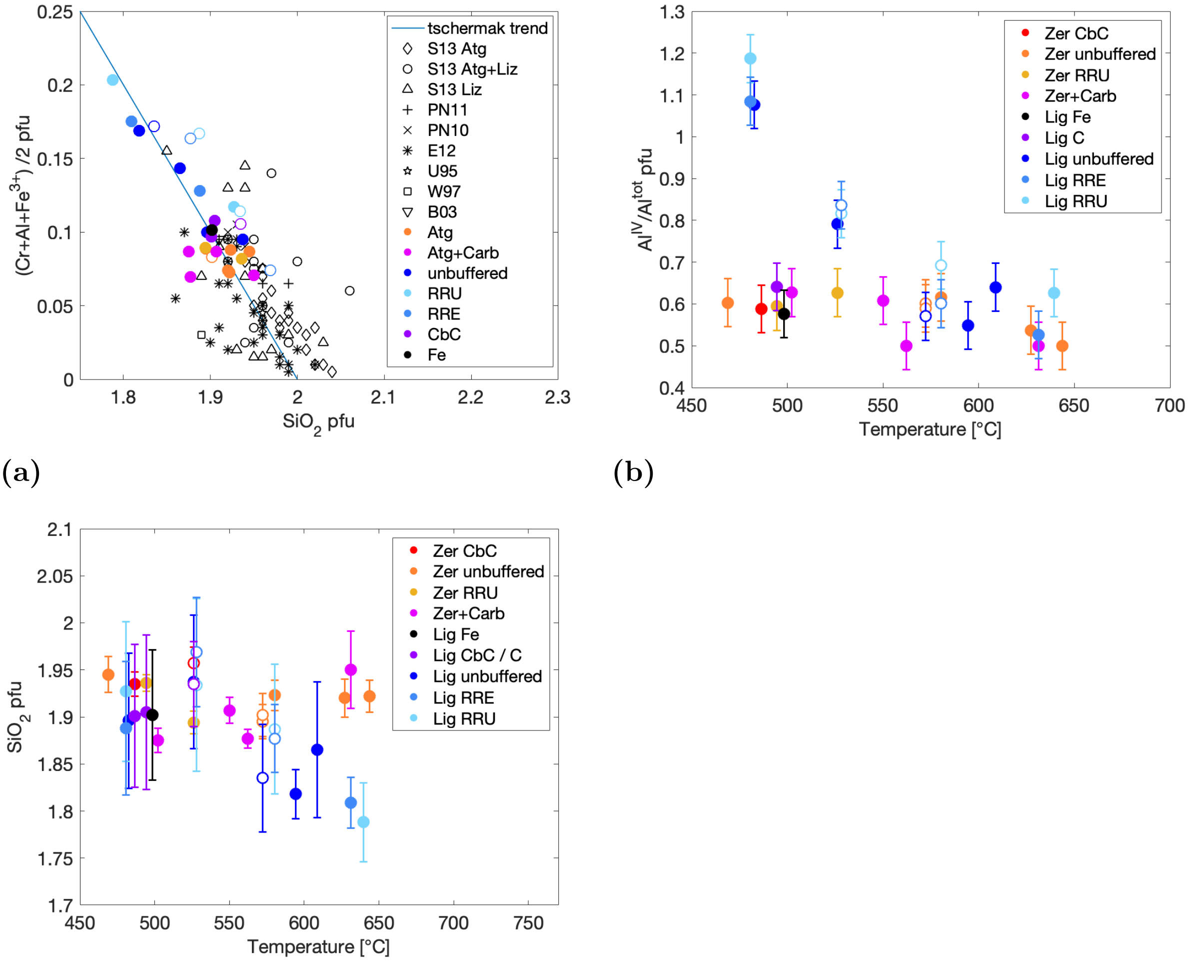

(a)

(b)

(c)

Figure 3.6: a: Total trivalent cation content vs. Si pfu for a total of 4.824 cations in Atg and 5 cations for Liz. The experiments follow the trend of Tschermak-substitution. Also shown are literature data for comparison. Note that Schwartz et al. (2013) and Bromiley at al. (2003) do not give ferric content. References: S13 = Schwartz et al. (2013) (natural), PN10 = Padrón-Navarta et al. (2010) (experimental), PN11 = Padrón-Navarta et al. (2011) (natural), E12 = Evans et al. (2012) (natural), U95 = Ulmer and Trommsdorff (1995) (natural), W97 = Wunder and Schreyer (1997) (experimental), B03 = Bromiley and Pawley (2003) (experimental). b: With increasing T the tetrahedral Al fraction strongly decreases. c: Si pfu in Liz and Atg samples. While the Atg samples do not show a T-dependency, Si pfu in Liz samples decreases with T.

Chlorite

Chl has a relatively constant Mg# of about 0.95. Only the samples buffered with Ru-RuO_2 show a slightly higher value of 0.97. The Chl Al content increases slightly with temperature from 1.4 to 1.8 pfu from 450 °C to 800 °C, for a total of 10 cations pfu. The Al content in Chl is thus not stoichiometric with respect to the ideal clinochlore composition of $Mg_5Al_2Si_3O_{10}(OH)_8$.

Garnet

In general garnet has a poikilitic texture and is full of inclusions. Garnet is stable above 2.5 GPa in carbonate free fully dehydrated assemblages. In carbonate-bearing experiments Grt has a large grossular component with a total CaO content between 10 - 20 wt%.

Pyroxene

The Px in carbonate-free experiments is a Mg-rich Opx. It shows similar trends as all other silicates in that Mg# is higher for high $f(O_2)$. The Al content in Opx is generally low (<0.15 pfu) but increases with temperature. The highest Al content (>0.2 pfu) is measured in experiments equilibrated at high temperatures and low pressures, i.e. where Grt is not stable (experiments V1048 and V0150).

In carbonate-bearing experiments the stable pyroxene is a Ca-bearing clinopyroxene (Cpx). The composition of Cpx shows only small variations over the whole PT-range covered in the experiments. The Ca content of Cpx ranges between 0.75 and 0.96 CaO pfu and is thus not stoichiometric. The Mg# varies between 0.91 and 0.94.

Olivine

Mg# of Ol in the run products is shown in figure 3.7 as a function of T. The first Ol forming upon serpentine breakdown in unbuffered experiments is Fe-rich with a value of $\leq$0.87. With increasing temperature the Mg# of Ol increases up to a value of 0.92 at 600 °C.

At very low $f(O_2)$, e.g. Fe-metal and CbC buffered experiments, Mg# as low as 0.7 are measured. Additionally, fayalitic Ol (Mg# 0.57) is observed surrounding the Fe-metal in one experiment, indicating significant oxidation of the Fe-metal. At high $f(O_2)$ in Ru-RuO_2 buffered experiments the Mg# is almost 1 due to Fe being oxidised to Fe^{3+}.

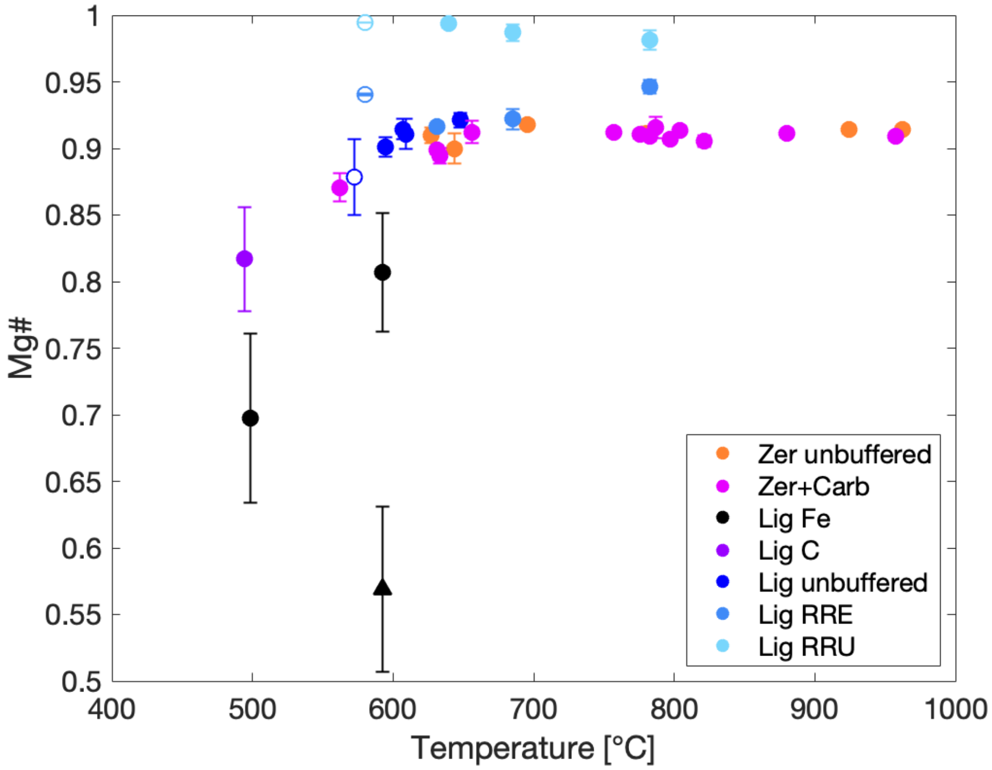

Figure 3.7: Mg# of Ol. The Mg# increases with temperature but becomes stable after the dehydration reaction. Very low Mg# are obtained at low $f(O_2)$ in Fe-metal and CbC buffered experiments. The black triangle marks additional Fa that formed around Fe-metal in experiment V1140. Open symbols mark experiments conducted at P=5 GPa.

Carbonate

Carbonate was added as pure $CaCO_3$. The composition of carbonates in the run products was found to depend on the coexisting phases, mainly Cpx and Grt. At 3 GPa pure Ca-carbonate is measured at low temperature. The prograde formation of Cpx at 550 °C results in a successive replacement of Ca-carbonate with Dol and Mgs (fig. 3.8). Ca-carbonate finally disappears around 650 °C. Only sample V1050 contains Ca-carbonate at high temperature. Ca-carbonate in this experiment might, however, be metastable as will be discussed later in chapter 8.

At intermediate temperatures of 550 - 950 °C Dol is the main carbonate. Its composition is constant around a Mg:Ca ratio of 1:1, although slightly higher Ca contents were observed for experiments V1062, V1076 and V1050 (marked with *** in figure 3.8, see also chapter 8). At >750 °C the carbonate becomes almost pure Mgs. Only in experiments buffered at low $f(O_2)$, i.e. CbC buffer, Mgs was also measured at low temperature (V1148b, V1153a and V1153b).

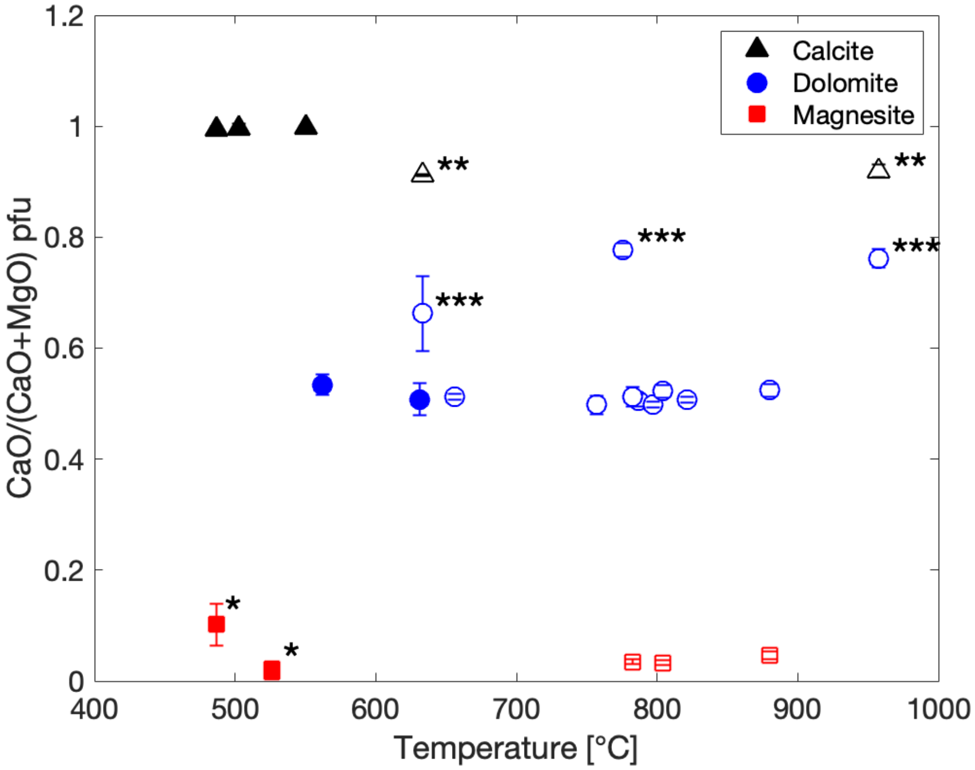

Figure 3.8: Composition of carbonates as a function of temperature. Open symbols mark absence of serpentine. Carbonate becomes more Mg-rich with increasing temperature. Exceptions are Mgs observed at low T and low $f(O_2)$ (marked with *). Dol generally has a Ca:Mg ratio of 1:1, with few exceptions marked as ***, which might result from intergrowth with metastable Ca-carbonate (**). See also chapter 8 for a detailed discussion on the carbonate composition.

Fe-oxides

Magnetite is present in the Atg and Liz starting materials. While Mgt forms angular grains embedded in the Serp matrix at low temperature (fig. 3.1a), it becomes porous with a more rounded shape upon the first dehydration reaction (fig. 3.9a). With further increasing temperature Mgt completely decomposes and only some metallic grains, generally very Cr-rich, are left behind (fig. 3.9b). In some experiments Mgt is replaced with a more Sp-like composition. The porous texture makes it, however, difficult to get accurate measurements.

Figure 3.10a and 3.10b compare the compositions of oxides. Mgt and Hem shift to more Cr_2O_3-rich compositions with increasing temperature. Sp replaces Mgt at temperatures above the serpentine dehydration, i.e. 650 - 700 °C.

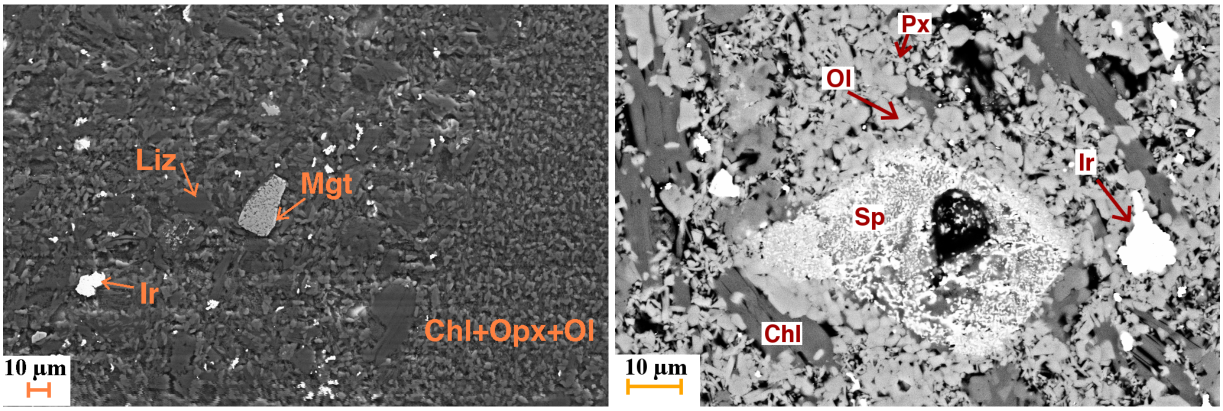

(a) **(b)**

Figure 3.9: a: Mgt showing a porous texture (V1116: 595 °C, 3 GPa). b: Sample V1076 (633 °C, 2.5 GPa) showing the formation of a spinel phase from Mgt.

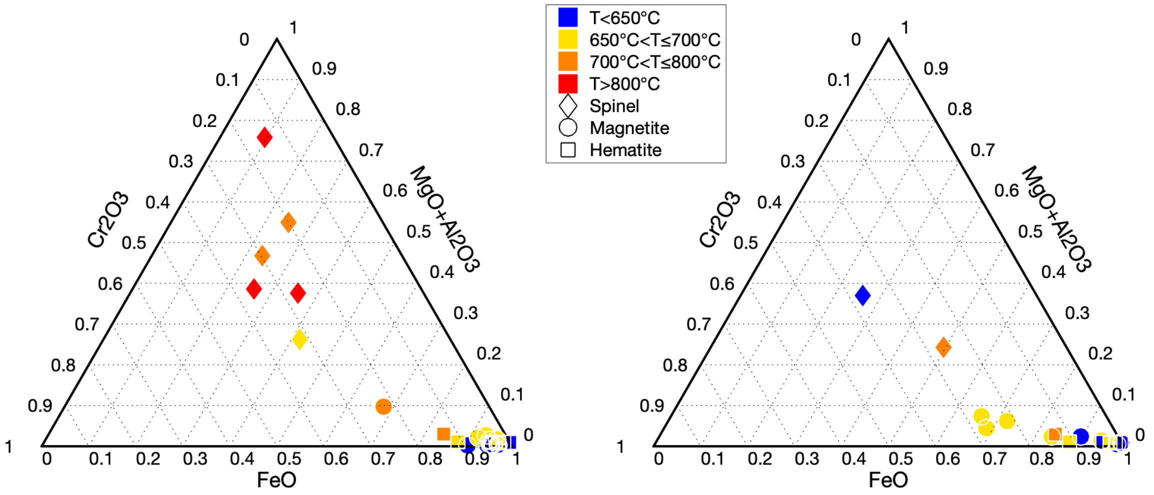

(a) Atg experiments **(b)** Liz experiments

Figure 3.10: T-dependent shift in composition of oxides. a: Atg-bearing samples have a constant composition of Mgt. Only at elevated temperature Sp appears. b: A slight increase in temperature leads to more Cr_2O_3-rich composition in Liz-bearing experiments.

3.3 Ferric Fe content

The $Fe^{3+}/\Sigma Fe$ ratios in run product phases was determined with Mössbauer spectroscopy. The hyperfine parameters of each phase are given in table C.1.

In the low temperature assemblages the spectra consist of several doublets belonging to Fe-bearing Atg or Liz and one or two magnetic sextets belonging to the oxide phase Mgt or Hem. Carbonates in the carbonate-bearing experiments have <0.2 wt% FeO and are below the limit of detection in the Mössbauer spectra.

Liz and Atg show 2 doublets, which can be assigned to ferrous (CS = 1.1 - 1.2 $\mathrm{mm\,s^{-1}}$, QS = 2.49 - 2.98 $\mathrm{mm\,s^{-1}}$) and ferric (CS = 0.26 - 0.47 $\mathrm{mm\,s^{-1}}$, QS = 0.56 - 0.89 $\mathrm{mm\,s^{-1}}$) Fe on the octahedral site. The hyperfine parameters obtained for octahedral Fe, both ferric and ferrous, are well within values reported in the literature (fig. 3.11). Strong preferred orientation of Serp results in different intensities for the low and high velocity peaks of the same doublet. Although the Lig_1602 starting material contains ferric Fe in tetrahedral coordination (fig. 2.1b) only octahedrally coordinated ferric Fe was found in the experimental run products indicating reequilibration of Liz.

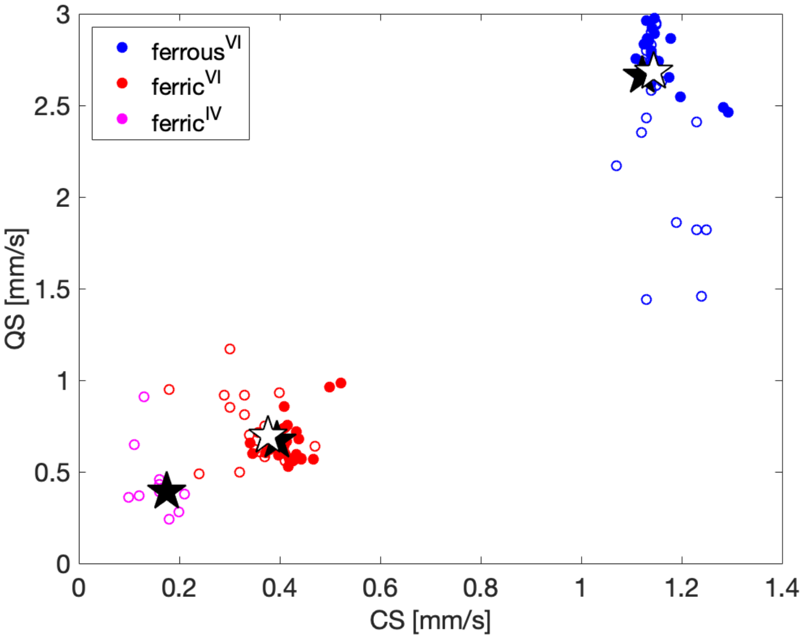

Figure 3.11: Hyperfine parameters of serpentine in run products: the CS and QS of doublets in all samples are close. Open symbols are literature data from Evans et al. (2012). Black and white stars indicate values of Lig_1602 and Zer_1701 starting material, respectively. Note that only the Lig_1602 starting material contained tetrahedral ferric Fe.

Magnetite was fit with two sextets, corresponding to the A and B site, where the one for the B site is generally broader due to electron hopping (fig. 3.12a). At high $f(O_2)$ only one magnetic sextet is measured, belonging to Hem (fig. 3.12b, table 3.2).

In spectra of experiments conducted at higher temperature two doublets having similar CS but slightly different QS are observed (fig. 3.12c). These doublets show a contribution of each coexisting Fe-bearing silicate, i.e. Serp, Chl, Ol and Px. The ferrous doublet of Ol can be distinguished by its unique QS of 2.0 - 2.5 $\mathrm{mm\,s^{-1}}$. All other phases contribute to the second ferrous doublet. The relative Fe content in each phase and thus its contribution to the doublet is calculated based on the phase mode and composition derived from mass balance and EPMA. In some instances a ferric doublet can be observed. It is assumed that Ol contains negligible amounts of ferric Fe. Annersten et al. (1978) could show that ferric Fe only substitutes into Opx in the presence of Al, which might be the case for some experiments. However, detailed analysis revealed that it does not significantly change the results whether the ferric Fe doublet in these experiments is fully assigned to the sheet silicates or whether Px is assumed to contribute to some extent. Therefore, in experiments where Serp, Chl and Px overlap a bulk $Fe^{3+}/\Sigma Fe$ ratio is obtained, whereas the true value of Serp is within the uncertainty.

The $Fe^{3+}/\Sigma Fe$ ratio of Liz changes drastically with $f(O_2)$ to values far above the starting material in some cases, where as it is also reduced at lower $f(O_2)$. With increasing temperature the $Fe^{3+}/\Sigma Fe$ ratio drops to almost zero (fig. 3.13). Atg in contrast does show a smaller T-dependency.

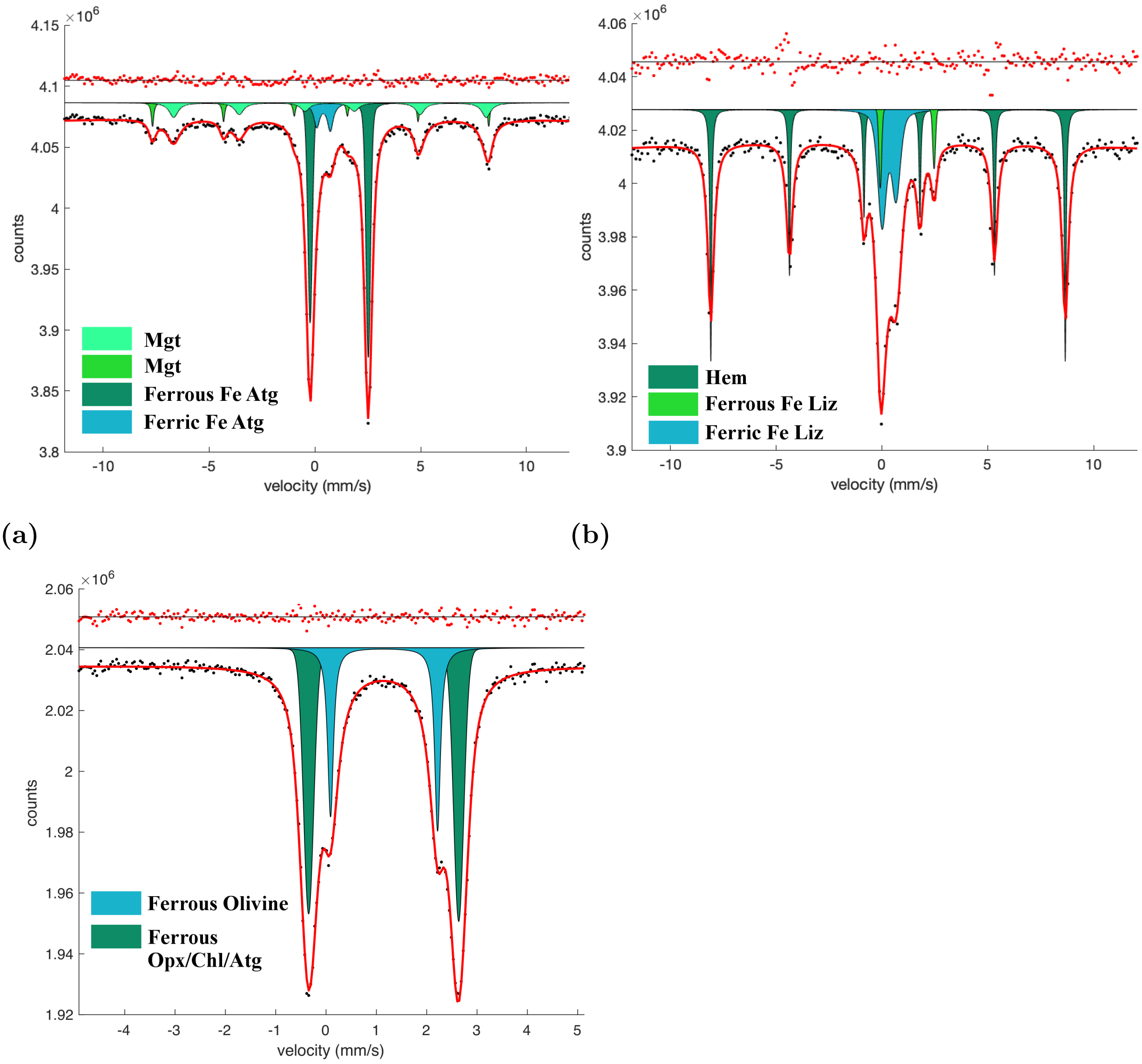

(a)

(b)

(c)

Figure 3.12: a: V1090 (572 °C, 4 GPa) showing 2 doublets of Atg and two sextets of Mgt. b: V1132a (481 °C, 3 GPa) is fit with 2 doublets for Liz belonging to ferrous and ferric Fe, and 1 sextet for Hem. Note the deviation of Hem from ideal Lorentzian peak shape. c: Sample V1111 (644 °C, 3 GPa) measured with a maximum velocity of 5 mm s^{-1}. Ol is observed as a single doublet. The second doublet belongs to En+Chl+Atg, all having similar hyperfine parameters. Ferric Fe was not detected.

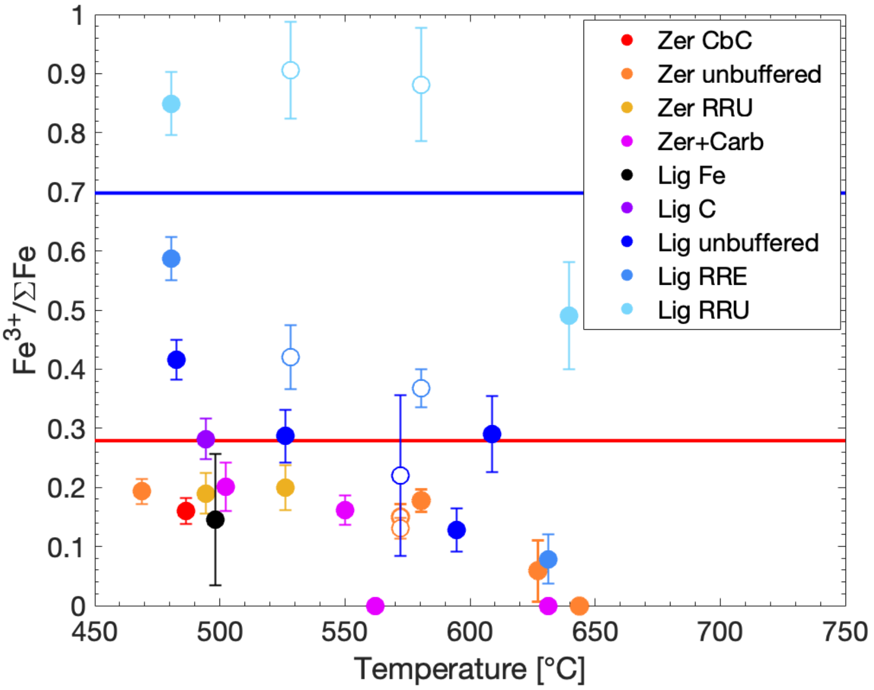

Figure 3.13: $Fe^{3+}/\Sigma Fe$ of serpentine-bearing experiments showing a negative correlation with temperature. The Liz $Fe^{3+}/\Sigma Fe$ ratio strongly depends on the $f(O_2)$. The red and blue line mark the starting material value for Atg (Zer_1701) and Liz (Lig_1701).

3.4 Oxygen fugacity $f(O_2)$

The oxygen fugacity of unbuffered experiments was calculated using the equations in section 2.5.2. Calculated values can be found in the appendix (table D). In order to check the reliability of the $f(O_2)$ obtained from the mineral assemblages, these calculations were also applied on buffered experiments and compared to the values obtained directly from the redox buffer. The $f(O_2)$ calculated from the buffer assemblage and the mineral assemblage is in agreement except for experiments buffered at Ru-RuO_2. However, the silicates at these conditions are almost pure Mg endmembers and the equilibria become less sensitive to $f(O_2)$ due to very low activity of the Fe endmembers. In Ru-Ru_2 buffered Atg experiments (V1143a, V1160b) only Ru metal could be confirmed. Together with the presence of Mgt it would appear that for some reason the buffer did not work in the Atg experiments.

Most experiments fall in the range between the FMQ and HM buffers, which is the region where Mgt is stable. Experiments buffered with Ru-RuO_2 oxygen buffer are above the

HM buffer, which is also confirmed by the presence of Hem. Most carbonate-bearing experiments at T >700 °C are below Mgt stability field.

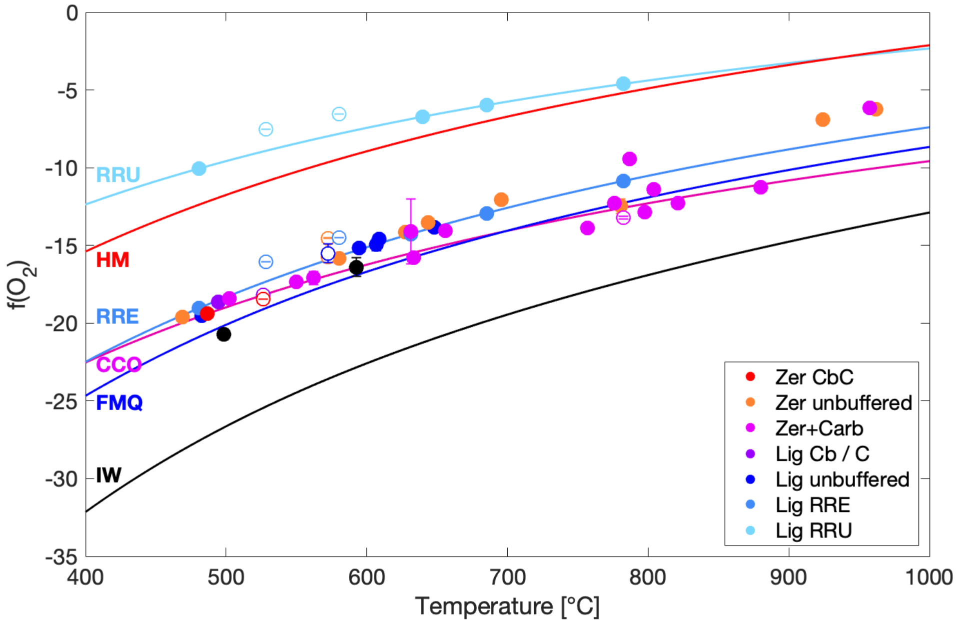

Figure 3.14: Mean values of calculated oxygen fugacities (table D.1) as a function of temperature. Note that standard deviation between all models is smaller than the symbol. Open symbols are experiments conducted at $P \geq 4$ GPa. Reference buffers are calculated for 3 GPa as mentioned in chapter 2.5.2, except for parameterised form of CCO: Frost and Wood (1997), FMQ: O'Neill (1987), HM: O'Neill (1987).

3.5 Mass balance

The calculated phase modes are consistent with SEM observations. The full data set can be found in the appendix (table E). The progress of the Serp dehydration reaction can be followed by a decrease of the Serp mode as shown in figure 3.15. The presence of Carb in Atg-bearing experiments decreases the onset of the reaction by approximately 50 °C (fig. 3.15a, 3.15b). The end of the reaction nevertheless, is shifted only slightly. Thus, the presence of carbonates mainly increases the width of the divariant field of reaction. The experiments indicate only a subtle effect on the final Atg-out, which might arise from reaction kinetics (section 8.1).

In unbuffered Liz-bearing experiments the dehydration reaction is generally shifted towards lower temperature with respect to Atg-bearing samples. However, at increased

$f(O_2)$ the Liz-out is shifted to higher temperatures. The divariant reaction field in buffered samples thus increases by about 50 °C and Liz becomes as stable as Atg with respect to temperature (3.15d).

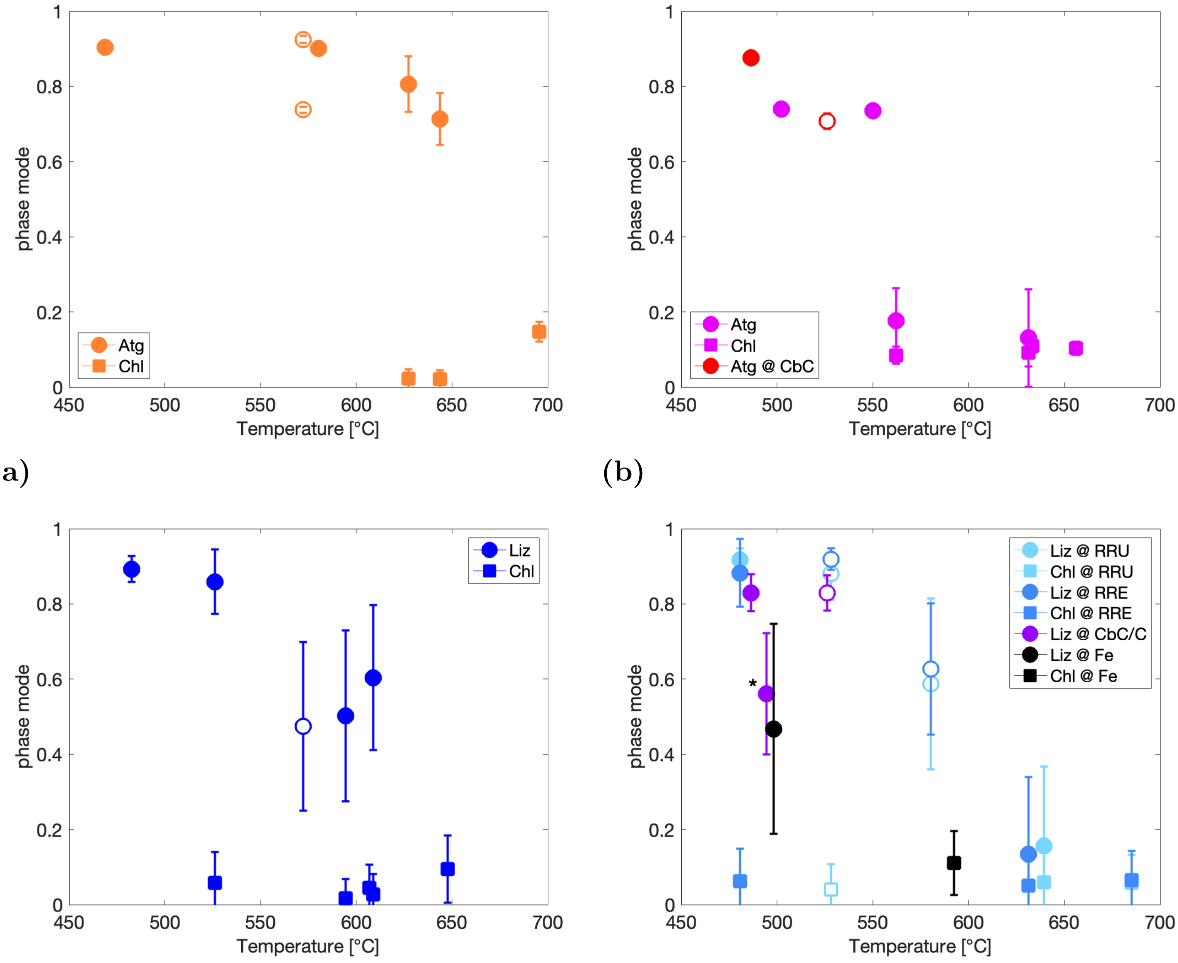

(a) (b)

(c) (d)

Figure 3.15: Calculated phase modes of serpentine in a: unbuffered Atg-bearing experiments, b: Atg+Cb experiments (marked in red are experiments with additional graphite) , c: unbuffered Liz-bearing experiments and d: buffered Liz-bearing experiments. Marked with * is experiment V1143b containing only graphite. Open symbols mark experiments conducted at $P \geq 4$ GPa.

Mass balance calculations for the carbonate-bearing experiments indicate that the total carbonate content decreases only slightly with increasing temperature (fig. 3.16a). 20 wt% Cal was added to the starting material. The total amount of carbonate decreases from a

20 wt% to 12 wt%.

The CO_2 content in the fluid is extremely low and does not show a correlation with temperature (fig: 3.16b). The values are between 0 to 12 wt%. Higher values of almost 30 wt% are obtained for experiments showing a negative deviation in the carbonate trend in figure 3.16a, being experiments V1076, V1062 and V1050 (marked with *). These are the same experiments, which show metastable Ca-carbonate at elevated temperature (fig. 3.8). Marked with ** is experiment V1079 (502 °C, 3 GPa), which also shows a high $X(CO_2)$, being molar $CO_2/(CO_2+H_2O)$. It remains questionable if the method is sensitive enough at such low CO_2 concentrations (compare also chapter 8).

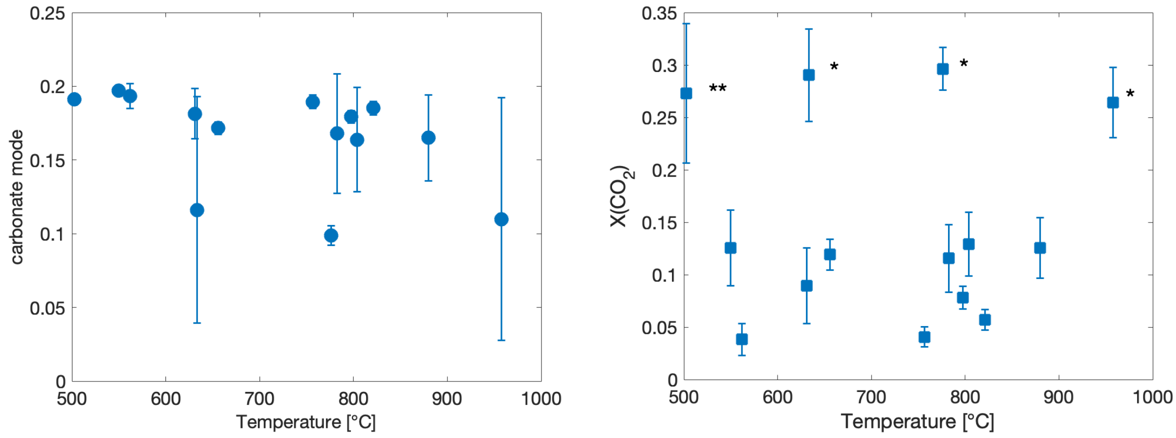

(a) **(b)**

Figure 3.16: Mass balance results obtained from carbonate-bearing experiments. a: The total carbonate content as a function of T is decreasing. b: The fluid $X(CO_2)$ does not indicate a T-dependency. * and ** mark experiments with a relatively high $X(CO_2)$.

3.6 Raman spectroscopy on fluid inclusions

In some of the carbonate-bearing experiments pre-fractured single-crystals were placed. Optical analyses of a 100 µm thick section revealed the formation of inclusions in San Carlos olivines (fig. 3.17a). All other single crystals used, i.e. garnet and sapphire, did not form fluid inclusions. The fluid inclusions formed in Ol are generally very heterogeneous. Most of the inclusions in Ol are located in trails along annealed fractures and have as size ≤20 µm. A few individual larger fluid inclusions are observed. The shape of most fluid inclusions is irregular and some even have branching forms. Most of the spherical inclusions contain one phase and only a few show coexisting liquid and gas. A dark blackish rim observed in some of the inclusions shows the precipitation of graphite. Raman spectra were taken on the spherical inclusions. The signal was very weak despite the manual polishing of each individual inclusion. However, the fluid inclusion could clearly be distinguished from the background Ol, which allows for a quantitative interpretation of the fluid composition (fig. 3.17b-3.17d). In all spectra the strongest peaks can be assigned to the host Ol by comparison. Some fluid inclusions contain only H_2O, which is observed as a broad band between 3000 and 3700 cm^{-1}. Other inclusions show the presence of carbon species. Carbon peaks can be assigned to both oxidised CO_2 and reduced graphite. In some inclusions even methane was observed. The coexistence of reduced and oxidised species is possible at the point where the graphite saturation curve has a minimum in the fluid carbon content, i.e. an aqueous fluid with an H/O ratio of 0.66 (Huizenga, 2011; Cesare, 1995).

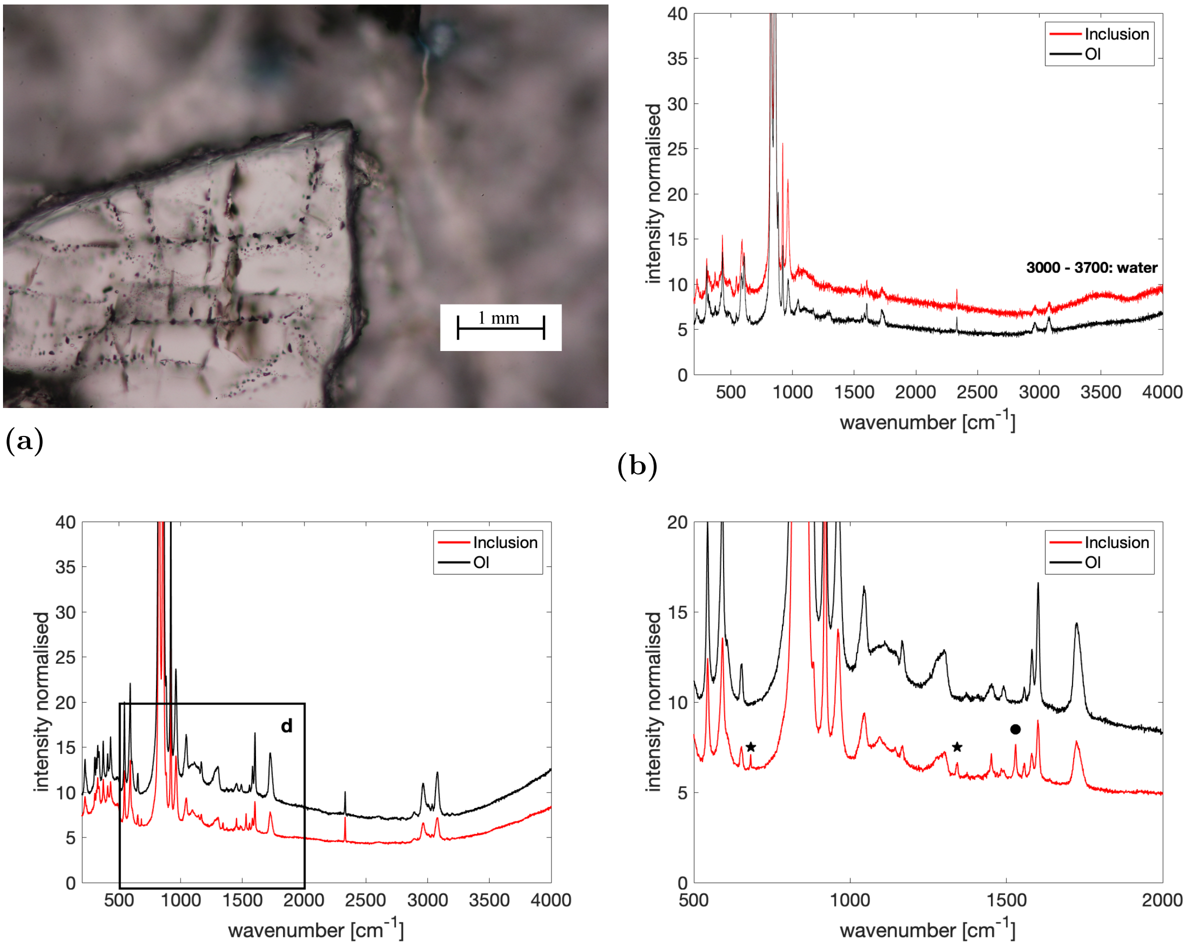

(a)

(b)

(c)

(d)

Figure 3.17: Raman spectroscopy on fluid inclusions. a: Microscopy image of San Carlos olivine showing fluid inclusions (V1077: 756 °C, 2.5 GPa). b: Raman spectra of an aqueous fluid inclusion in sample V1065 (821 °C, 2.5 GPa) showing the presence of water at high wavenumbers. c: Fluid inclusion and host Ol spectra of sample V1077. The marked rectangle indicates the area shown in d. d: Detail of a fluid inclusion in sample V1077, showing graphite (black circle) and CO_2 (black stars).

4 Compositional relations and partition coefficients

Compositional trends in serpentine minerals as a function of pressure, temperature and $f(O_2)$ include changes in Fe^{2+}-Mg exchange, $Fe^{3+}/\Sigma Fe$ ratio and Al content. Such changes result from interaction between coexisting phases. In order to fully describe the phase relations in a dehydrating serpentinite at subduction zone conditions it is thus essential to understand the mutual influence of phases on their composition as a function of P, T and $f(O_2)$.

The Fe content in serpentine is strongly influenced by Mgt and Hem, as their presence changes the bulk silicate Fe content. However, since all Mg-silicates in the run products are subject to Fe^{2+}-Mg exchange, the Fe content in serpentine is also influenced by Ol, Px and Chl. Distribution coefficients K_D describe the exchange of components x and y between phase A and B:

$$K_D = \frac{\mathrm{x}^{\mathrm{A}}/\mathrm{y}^{\mathrm{A}}}{\mathrm{x}^{\mathrm{B}}/\mathrm{y}^{\mathrm{B}}}. \tag{4.1}$$

For example the Fe^{2+}-Mg exchange between two silicates A and B can be tracked via K_D^{Fe-Mg} given as

$$K_D^{Fe-Mg} = \frac{\mathrm{Mg}^{\mathrm{A}}/\mathrm{Fe}^{\mathrm{A}}}{\mathrm{Mg}^{\mathrm{B}}/\mathrm{Fe}^{\mathrm{B}}}, \tag{4.2}$$

where Mg and Fe are the mole fractions of each element in phases A and B. K_D is the equilibrium coefficient for an exchange reaction written in a form that has the same proportion of exchanged component in each phase.

Over small ranges of composition K_D can generally be considered to be a constant with changing pressure and temperature. However, Evans et al. (2012) have shown that metamorphic Atg+Ol pairs have K_D values that depend on the bulk composition. Figure 4.1 shows the Fe# of coexisting Serp+Ol in experimental run products of this study, corrected to exclude the ferric Fe contents based on the Mössbauer analyses. Also shown are data from Evans et al. (2012), however, not ferric Fe corrected. Their cubic relation is given as

$$Fe\#^{Ol} = 104\ (Fe\#^{Serp})^3 + 3.6412\ (Fe\#^{Serp})^2 + 1.7966\ (Fe\#^{Serp}) - 0.0094. \tag{4.3}$$

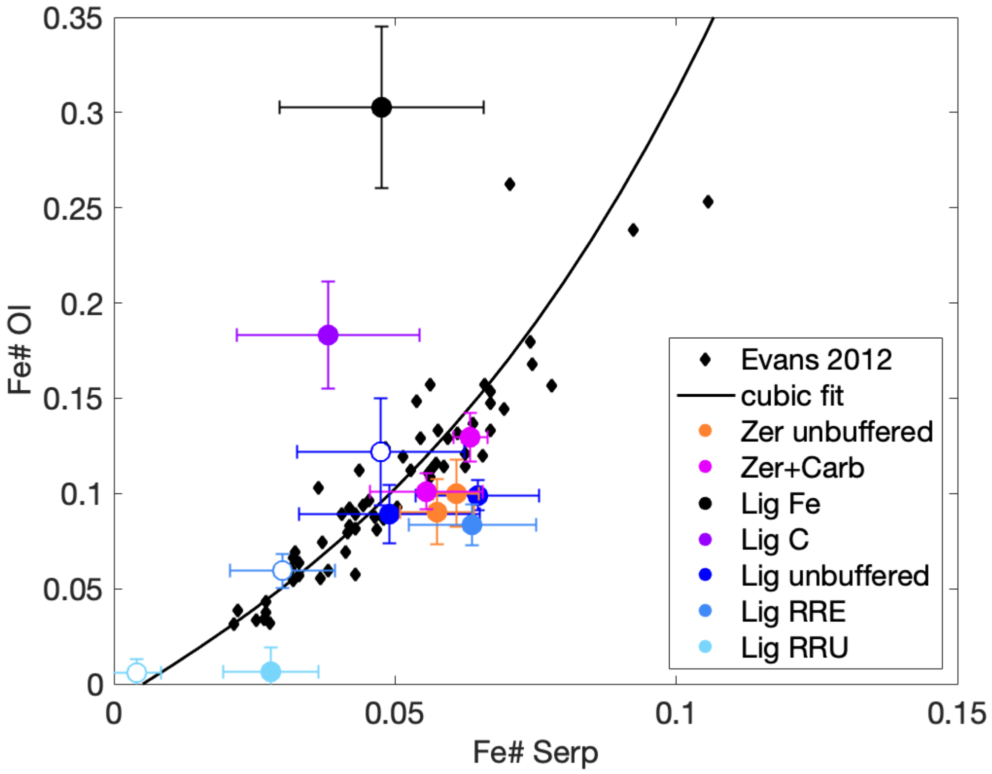

Figure 4.1: Composition of Serp and coexisting Ol. Data obtained for this study are corrected for ferric Fe content, which shifts the points towards lower Fe# with respect to the data from Evans et al. (2012), which are not corrected for ferric Fe. Not in line are samples at low $f(O_2)$ performed with graphite (C) and Fe-metal (Fe). Open symbols mark experiments conducted at P=5 GPa.

Since the experimental data from this study follow the natural data relatively well this is a good indication that Fe^{2+}-Mg equilibration took place in both Atg and Liz. Two exceptions observed are experiments buffered at low $f(O_2)$: The samples buffered with graphite (V1143b) and Fe-metal (V1139) clearly fall off the trend in that their Fe# in Ol is too high compared to coexisting Liz. In the presence of Fe-metal disequilibrium results from oxidation of Fe-metal to form FeO (fig. 3.2a). The Fe oxide then further interacts with Liz and forms Ol. Close to the Fe-metal flakes the Fe content in Ol is strongly increased with respect to Ol further away. This difference in composition results from very high chemical gradients around the metal flakes. A fast diffusion of Fe into Ol with respect to Liz results in Ol with a much higher Fe# compared to coexisting Liz. Due to shielding of the Fe-metal, however, it is assumed that the assemblage was not completely at IW-equilibrium and is thus not further taken for calculations. Nonetheless, Liz broke down to Chl already at very low temperature, showing that serpentine is not stable at such low $f(O_2)$, giving rise to a phenomena that can be described as redox dehydration and is discussed at length in section 6.4.

For the experiments containing graphite Ol is more Fe-rich due to the reduction of Mgt. Mgt is still observed in this experiment, but is extremely porous in texture and no accurate EPMA measurements could be conducted. The disequilibrium Fe^{2+}-Mg partitioning is again due to faster diffusion of Fe in Ol compared to Liz. This experiment is discussed in detail with respect to $f(O_2)$ and $f(CO_2)$ in section 8.3.

Figure 4.2 shows the same data as in figure 4.1 plotted in terms of K_D. Not shown are samples V1143b and V1139, which have Ol enriched in Fe with respect to equilibrium K_D as discussed above. K_D shows a dependence on the composition, represented by the Fe# of Ol. The experimentally observed dependency is similar to the dependency described by Evans et al. (2012). This implies that Fe^{2+}-Mg mixing in at least one of the phases is none ideal. The authors assumed that their serpentine is ideal in the range of 0 - 10 mol% Fe and obtained a symmetrical interaction parameter for Ol in the order of $W = 8500\,\mathrm{J\,mol^{-1}}$. This value is higher than interaction parameters obtained from Ol-Opx equilibrium by von Seckendorff and O'Neill (1993), being $5625(457)\,\mathrm{J\,mol^{-1}}$. A lower interaction parameter for Ol would be obtained by also assuming serpentine to be none ideal. However, for the model described in chapters 5 and 6 there is little to gain from non-zero interaction parameters in serpentine. The data also indicate that K_D depends on pressure as all experiments conducted at higher pressure are shifted towards higher K_D values.

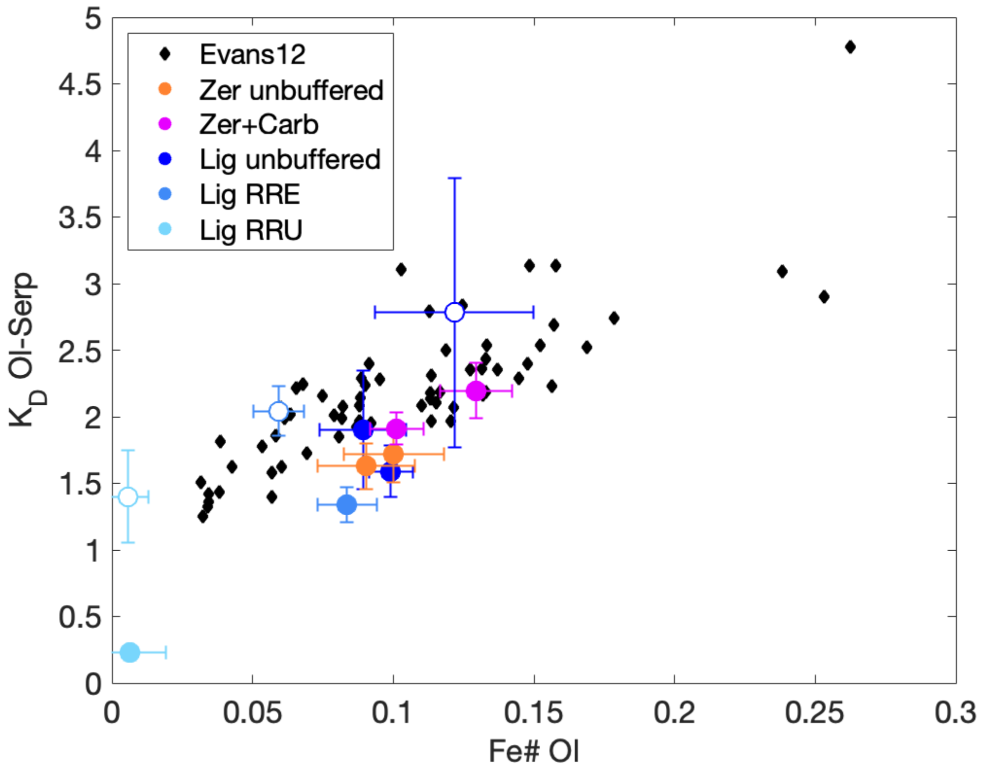

Figure 4.2: The corresponding K_D values show a dependency on the Fe# of Ol. The data also indicate that the K_D depends on pressure as shown by higher values for experiments conducted at 5 GPa, which are shown by open symbols.

The dehydration of serpentine forms also Px and Chl besides Ol. The Fe# of Px is strongly correlated to Ol as shown by Ol+Opx pairs in figure 4.3. The data obtained show that Opx is always less Fe-rich than coexisting Ol, following the relation given by von Seckendorff and O'Neill (1993). Fe^{2+}-Mg exchange between Ol and Opx is thereby independent on the temperature as the data from von Seckendorff and O'Neill (1993) include data from 1073 to 1423 K. The relation is almost linear and the agreement with literature data provides very good confirmation that the Fe^{2+}-Mg exchange is reaching equilibrium. The composition of Opx in equilibrium with Ol is given as

$$Fe\#^{Opx} = 0.8772(Fe\#^{Ol})^3 - 0.8804(Fe\#^{Ol})^2 + 0.9906(Fe\#^{Ol}) + 0.0017. \tag{4.4}$$

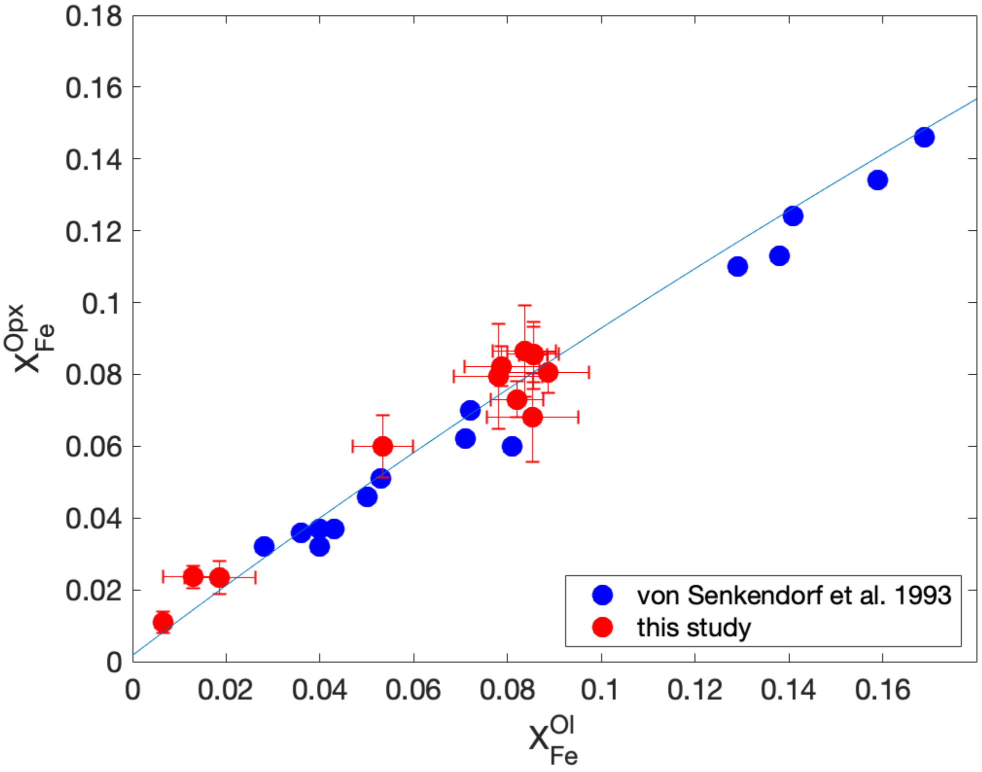

Figure 4.3: Fe# of Ol and coexisting Opx do agree with the equilibrium experiments of von Seckendorff and O'Neill (1993) conducted at 1.6 GPa and 1073 - 1423 K.

A linear relationship is observed in the Fe# of Chl+Liz pairs (fig. 4.4a) and given as

$$Fe\#^{Chl} = 0.64129\ Fe\#^{Serp} + 0.00014. \tag{4.5}$$

Both Chl and Serp Fe# are corrected for the ferric Fe contents, with the assumption that Chl has the same $Fe^{3+}/\Sigma Fe$ ratio as Serp. The Fe# of Atg in equilibrium with Chl is slightly lower to what would be expected from equation 4.5.

In the same way that the Serp composition correlates with Ol also Chl shows a relation with Ol. Figure 4.4b shows the composition of Chl as a function of the Fe# of coexisting Ol. The fit has been determined from a combination of the Serp-Ol and Chl-Ol dependencies i.e. substituting equation 4.5 into equation 4.3.

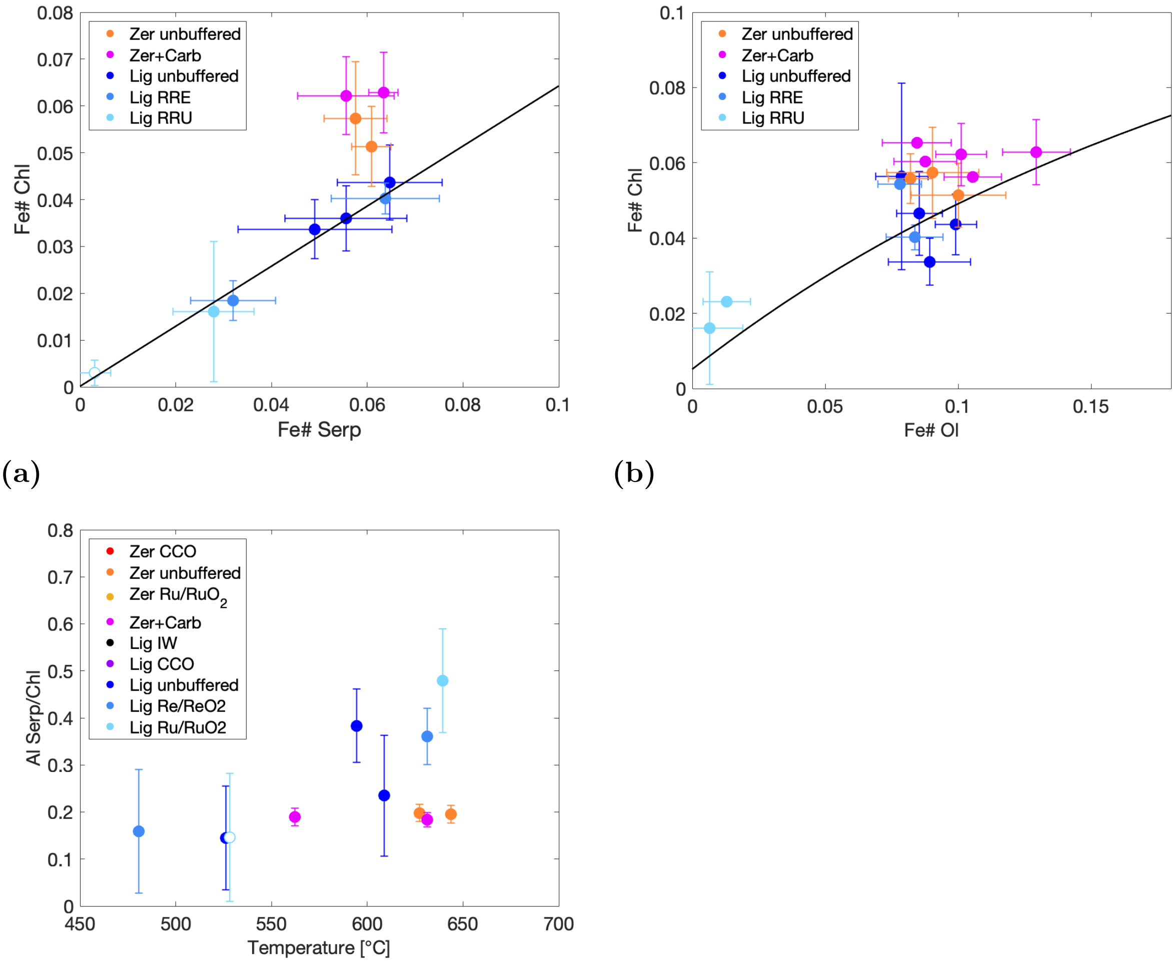

(a) **(b)** **(c)**

Figure 4.4: a: Figure showing the Fe# of coexisting Serp and Chl. Both phases are corrected for ferric Fe, assuming that they have the same $Fe^{3+}/\Sigma Fe$ ratio. Chl shows a linear relation to coexisting Liz, whereas Atg is slightly less Fe-rich with respect to Chl. b: Chl+Ol pairs showing the relation obtained by combining equation 4.3 and 4.5. c: The ratio of total Al pfu in Serp and Chl shown as a function of temperature. Al partitions preferentially into Liz with increasing temperature due to changing Liz composition. Atg+Chl pairs show an almost constant Al ratio over the experimental T-range. Open symbols mark experiments conducted at P=5 GPa

The Al content of Liz increases with temperature due to the Al partitioning with Chl formed upon the dehydration of Liz. For Atg, however, the Al content stays constant over the experimental temperature range (fig. 3.5). The T-dependency of the Al content in Chl, however, is very weak for both starting materials and increases from 1.4 to 1.8 Al pfu over a temperature range of 300 °C for a total of 10 cations pfu. Therefore, the

T-dependent Al partitioning between Liz and Chl is mostly a function of the Liz composition that changes with temperature as shown in figure 4.4c. Atg+Chl pairs indicate that the partitioning remains constant over the whole experimental temperature range as Atg does not change the Al content in experimental time scales. It is nonetheless expected that for natural Atg+Chl pairs a similar dependency to Liz+Chl pairs would be obtained.

In summary, there is clear evidence that the composition of coexisting minerals are interdependent and there is sufficient indication for the effects of equilibrium. The main factor controlling the Fe content of silicate minerals is the stability and proportion of Fe oxides and Fe-metal. At high $f(O_2)$ for example Fe is oxidised to ferric Fe. At such conditions Hem forms and increases the $Fe^{3+}/\Sigma Fe$ content in Liz and Chl but reduces the total Fe contents of silicates. If the $f(O_2)$ is such that Fe oxides are unstable, the bulk silicate Fe content is significantly increased. The similarity in Fe^{2+}-Mg partitioning with natural samples and previous experiments indicates that equilibrium is approached, except from a few outliers for which suitable explanations can be found.

The Al content of Liz changes due to interaction with coexisting Chl that is mainly temperature dependent. The resulting trend is in good agreement with previous natural samples (Schwartz et al., 2013) as shown in section 3.2. On the other hand the experimentally produced Atg samples show no change with temperature, in line with previous experimental studies (Padrón-Navarta et al., 2013; Merkulova et al., 2016; Shen et al., 2020), which would seem to indicate that it is not possible to reequilibrate the Al content on experimental time scales. One explanation might be that there are differences in diffusivities between different Atg sites. The Atg octahedral site is capable of re-equilibrating thus explaining the agreement in the Fe^{2+}-Mg partitioning, where as the kinetics are too slow for significant tetrahedral site changes to take place. Lizardite on the contrary does not have a modulated structure. The absence of a reversal of the tetrahedral layer every half unit cell length might allow for faster diffusion on the tetrahedral site, so that Liz can reequilibrate its Al content.

5 Thermodynamic parameters of Fe^{3+}-bearing serpentine

The experimental data obtained in this study show that the ferric Fe content of serpentine varies as a function of P, T and $f(O_2)$. In order to explore the consequences of ferric Fe on the phase stability, $f(O_2)$ and mineral compositions within a subduction zone, a thermodynamic model is required that relates the composition of serpentine to intensive variables. To do so an activity expression for ferric Fe in serpentine is needed. Based on the experimental data and equilibria with other phases with known thermodynamic properties, the Gibbs free energy of a Fe^{3+}-serpentine endmember can be obtained for different PT conditions. The resulting model is compared against the experimental data and the consequences of the Fe^{3+}-$f(O_2)$ relations can then be further explored.

While the ferric Fe content in lizardite (Liz) shows a clear dependence on $f(O_2)$, antigorite (Atg) samples do not adjust in their ferric Fe content to imposed oxygen buffers (fig. 3.13). This is probably due to sluggish reaction kinetics of the Atg tetrahedral site, as described in chapter 4, which inhibits the amount of Al on the tetrahedral site. As Fe^{3+} and Al are in a charge balanced substitution relation the Fe^{3+} content cannot change without reequilibrating the Al content. The $f(O_2)$ in these experiments, however, can still be measured using the IrFe-alloy redox sensor or any other redox equilibrium between coexisting phases in the run products.

The Fe^{2+}-Mg exchange on the octahedral site of Atg shows similar variations as a function of P and T as does Liz and indicates equilibration of Atg components (fig. 4.1-4.2). For the determination of a thermodynamic model, it is assumed that also the Al-Fe^{3+} relation in Atg is in equilibrium for the measured $f(O_2)$ of the samples. It is also assumed that Atg has the same activity model as Liz as the structures are similar and, as will be seen, this model is in good agreement with the experimental data. By further exploring the behaviour of Atg in a subduction zone it is assumed that the Al variation is the same as for Liz, as the comparison with natural samples seems to imply (see chapter 3).

5.1 Standard state formulation

To determine activity models for Liz and Atg suitable Fe^{3+} endmembers including charge balance are required for both phases. In the serpentine structure Fe^{3+} can be substituted

on both the tetrahedral and the octahedral site. Tetrahedral ferric Fe is reported in literature and a cronstedtite component does exist in natural samples (Evans et al., 2012). However, the data compilation in Evans et al. (2012) indicates that only 40 % of all Atg samples analysed do show tetrahedral ferric Fe and only two samples have more ferric Fe on the tetrahedral site than on the octahedral site. The Liz samples reported generally have more ferric Fe with respect to Atg but also show a tendency towards preferred occupancy of the octahedral site. The preferred partitioning on the octahedral site of course might be due to sampling bias since the amount of samples analysed in their compilation, adding up to 23 from which only 4 are Liz, is relatively low. Since the Mössbauer doublet of tetrahedral ferric Fe is small and overlaps with the low velocity peak of the ferrous doublet (compare figure 6 in Evans et al. (2012)), it might also be that tetrahedral ferric Fe is present in more samples but is simply below the limit of detection. The Liz starting material used in this study shows the presence of tetrahedral ferric Fe (fig. 2.1b). However, in the run products ferric Fe is completely redistributed to the octahedral site (fig. 3.11, table C.1). This result indicates a preferred occupancy of the octahedral site at high PT conditions. Therefore, the Fe^{3+}-serpentine endmember derived in this study is defined such that Fe^{3+} occupies the octahedral site only.
Na or K contents are too low to charge balance Fe^{3+} in the octahedral site ($\leq$0.01 wt%). Another possibility is to charge balance octahedral Fe^{3+} via octahedral vacancies as found in a sample by Evans et al. (2009). This mechanism was found to be favoured in environments with a high silica activity and Fe content and at low T. Initial tests with such a component, however, indicated that the resulting $f(O_2)$-Fe^{3+} relationship was not consistent with the experimental data. As described in section 3.2, the microprobe results show a correlation between Si pfu and the total trivalent cation content (fig. 3.6a). A coupled substitution is thus the most likeliest mechanism to obtain charge balance. Based on both, Mössbauer and EPMA data the ferri-alumina-Tschermak endmembers for Liz (f3Lizts) and Atg (f3Atgts) are proposed as

$$\text{f3Lizts: } \mathrm{Mg_2Fe^{3+}|AlSi|O_5|(OH)_4}$$

$$\text{f3Atgts: } \mathrm{Mg_{1.824}Fe^{3+}|AlSi|O_5|(OH)_{3.647}}$$

When normalised to the same amount of tetrahedral sites, Atg is depleted in $\frac{3}{m}$ brucite (Br) components per formula unit compared to the Liz stoichiometry. m denotes the number of tetrahedral sites along the a axis of the unit cell. An $m = 17$ polysome is chosen here in accordance with the thermodynamic database of Holland and Powell (2011). There is evidence, however, from both natural and experimental studies that the m value varies as a function of PT conditions (Mellini et al., 1987; Wunder et al., 2001; Shen et al., 2020). According to Wunder et al. (2001) $m = 17$ is the equilibrium value at 3 GPa and 500 °C, the value determined by Shen et al. (2020) is slightly higher with $m = 21$. It is possible that deviations from ideal stoichiometry obtained from the EPMA results indeed arise from an m value differing from 17 (table B.1). A transmission electron microscope (TEM) would be required in order to clearly identify the m value for each point measurement in the run product. However, for most applications this is unpractical and there is no significant improvement in data with respect to a single m value chosen here.

5.2 Gibbs free energy calculation

In the FMASH system several mineral equilibria based on the experimental phase assemblages that involve the ferri-alumina-Tschermak lizardite (f3Lizts) as well as forsterite (Fo), fayalite (Fa), enstatite (En), clinochlore (Clin) and magnetite (Mgt) can be written:

$$\text{A:} \qquad \text{Mgt} + \text{Clin} = \tfrac{1}{2}\ \text{Fo} + \tfrac{1}{2}\ \text{Fa} + 2\ \text{f3Lizts} \tag{5.1}$$

$$\text{B:} \qquad \tfrac{2}{3}\ \text{Mgt} + \tfrac{1}{6}\ \text{O}_2 + \text{Clin} = \tfrac{1}{2}\ \text{En} + 2\ \text{f3Lizts} \tag{5.2}$$

$$\text{C:} \qquad \text{Fa} + \text{Fo} + \text{Clin} + \tfrac{1}{2}\ \text{O}_2 = \tfrac{3}{2}\ \text{En} + 2\ \text{f3Lizts}. \tag{5.3}$$

With the relation Atg = Liz - $\frac{3}{17}$Br, the equilibria 5.1-5.3 can be rewritten for the ferri-alumina-Tschermak antigorite endmember (f3Atgts) as

$$\text{A:} \qquad \text{Mgt} + \text{Clin} = \tfrac{1}{2}\ \text{Fo} + \tfrac{1}{2}\ \text{Fa} + 2\ \text{f3Atgts} + \tfrac{6}{17}\ \text{Br} \tag{5.4}$$

$$\text{B:} \qquad \tfrac{2}{3}\ \text{Mgt} + \tfrac{1}{6}\ \text{O}_2 + \text{Clin} = \tfrac{1}{2}\ \text{En} + 2\ \text{f3Atgts} + \tfrac{6}{17}\ \text{Br} \tag{5.5}$$

$$\text{C:} \qquad \text{Fa} + \text{Fo} + \text{Clin} + \tfrac{1}{2}\ \text{O}_2 = \tfrac{3}{2}\ \text{En} + 2\ \text{f3Atgts} + \tfrac{6}{17}\ \text{Br}. \tag{5.6}$$

Although Br is not stable together with Atg at experimental PT conditions (fig. 1.4) it makes the equilibria computationally simpler than employing a free H_2O phase in that the equilibria are independent on the choice of the fluid equation of state. It makes, however, no difference to the result.

The experimental $f(O_2)$ range extends into the stability field of hematite (Hem). Therefore equilibria 5.1 and 5.2 as well as equilibria 5.4 and 5.5 have to be rewritten in terms of Hem for high $f(O_2)$ conditions:

$$\text{A}_{\;(f(\text{O}_2)>\text{HM}):} \qquad \tfrac{3}{2}\ \text{Hem} + \text{Clin} = \tfrac{1}{4}\ \text{O}_2 + \tfrac{1}{2}\ \text{Fo} + \tfrac{1}{2}\ \text{Fa} + 2\ \text{f3Lizts} \tag{5.7}$$

$$\text{B}_{\;(f(\text{O}_2)>\text{HM}):} \qquad \text{Hem} + \text{Clin} = \tfrac{1}{2}\ \text{En} + 2\ \text{f3Lizts} \tag{5.8}$$

and

$$\text{A}_{\;(f(\text{O}_2)>\text{HM}):} \qquad \tfrac{3}{2}\ \text{Hem} + \text{Clin} = \tfrac{1}{4}\ \text{O}_2 + \tfrac{1}{2}\ \text{Fo} + \tfrac{1}{2}\ \text{Fa} + 2\ \text{f3Atgts} + \tfrac{6}{17}\ \text{Br} \tag{5.9}$$

$$\text{B}_{\;(f(\text{O}_2)>\text{HM}):} \qquad \text{Hem} + \text{Clin} = \tfrac{1}{2}\ \text{En} + 2\ \text{f3Atgts} + \tfrac{6}{17}\ \text{Br}. \tag{5.10}$$

Mgt, Hem and Br are all assumed to be pure endmembers, i.e. $a_{Mgt} = a_{Hem} = a_{Br} = 1$. All other phases are solid solutions. Ol and Px are only subject to Fe^{2+}-Mg exchange. Since both phases might show a non-ideal contribution to their respective Gibbs free energy, activity models as outlined in section 2.5.2 (table 2.4) were used. The Mg# of both phases was either measured or, if not possible, calculated based on empirical relations outlined in chapter 4 (eq. 4.3 and 4.4).

Chl has Fe^{2+}-Mg mixing and shows a small deviation from the stoichiometric Al content of clinochlore. The ideal clinochlore composition is given as $Mg_5Al|AlSi_3|O_{10}(OH)_8$. Thus Al partitions equally on one octahedral and one tetrahedral site. Since the Al content in Chl is almost constant over the experimental PT-range, this can be approximated by having 0.8 Al pfu on both the octahedral and tetrahedral site. Ferric Fe in Chl is a relatively minor component in most experiments based on Mössbauer results (chapter 3.3 and table C.1) and is therefore ignored. The activity for the clinochlore endmember is then calculated as

$$a^{Clin} = \left(\frac{\text{Mg}}{5}\right)^5 \cdot 0.8^2, \tag{5.11}$$

where Mg is the number of Mg pfu in the 5 remaining octahedral sites, i.e. the Mg# assuming equal Fe^{2+}-Mg exchange on all octahedral sites. In experiments where the composition of Chl could not be determined, the Mg# is estimated based on the partitioning relation given in chapter 4 (eq. 4.5).

Even with a coupled substitution of Fe^{3+} and Al on the octahedral and tetrahedral site respectively, there are still a number of possibilities for the activity expression depending on the type of ordering assumed. Ferric Fe might mix on all octahedral sites or it might prefer to be on only a subset of these sites, e.g. mixing on a single site. The same can be assumed for Al, which might either mix on both tetrahedral sites or be assigned to one of them. A completely disordered endmember, i.e. mixing of ferric Fe on all octahedral M sites and Al on all tetrahedral T sites, results in the activity expression given as

$$a^{Serp} = \left[\left(\tfrac{m-1}{m}\right)^{m-1}\left(\tfrac{1}{m}\right)\left(\tfrac{1}{2}\right)^{2}\right]^{-1}\left[(X_{Mg,M})^{m-1}X_{Fe^{3+},M}X_{Al,T}X_{Si,T}\right], \tag{5.12}$$

where m is the total number of octahedral sites, being 3 for Liz but only 2.824 for Atg and $X_{i,j}$ is the fraction of component i on site j calculated as:

$$X_{Mg,M} = \frac{\text{Mg}}{m} \tag{5.13}$$

$$X_{Fe^{3+},M} = \frac{\text{Fe}^{3+}}{m} \tag{5.14}$$

$$X_{Al,T} = \frac{\text{Al}^{\text{IV}}}{2} \tag{5.15}$$

$$X_{Si,T} = \frac{\text{Si}}{2}. \tag{5.16}$$

Mg, Fe^{3+} and Si are atoms per formula unit. The tetrahedral Al (Al$^{\text{IV}}$) is calculated as half of the total trivalent cations (eq. 3.1). Consequently, the octahedral Al (Al$^{\text{VI}}$) is given by the difference to the total Al content (eq. 3.2).

Due to disordering $X_{i,j}$ of the endmember is <1. However, for an ideal endmember the activity has to be unity. This requirement gives rise to the prefactor in equation 5.12. Ordering results in splitting the octahedral sites into M1 and M2 sites, and the tetrahedral sites into T1 and T2 sites. Assigning Fe^{3+} to the M2 site and Al to the T1 site results in the activity expression given as

$$a^{Serp} = (X_{Mg,M1})^{m-1} X_{Fe^{3+},M2} X_{Al,T1}. \tag{5.17}$$

The site occupancy in the ordered model is given as

$$X_{Mg,M1} = \frac{\mathrm{Mg_{M1}}}{m-1} \tag{5.18}$$

$$X_{Fe^{3+},M2} = \mathrm{Fe}^{3+} \tag{5.19}$$

$$X_{Al,T1} = \mathrm{Al}^{\mathrm{IV}}. \tag{5.20}$$

It is assumed that the ratio of Mg and Fe^{2+} on the M1 and M2 site is identical, i.e. $\mathrm{Mg_{M1}}/(m-1)$ is simply the Mg#. Since the T2 site is filled only with Si $X_{Si,T2}$ becomes unity. Ordering on only the octahedral site results in the expression:

$$a^{Serp} = 4\left[X_{Mg,M1}^{m-1} X_{Fe^{3+},M2} X_{Al,T} X_{Si,T}\right] \tag{5.21}$$

and for tetrahedral ordering:

$$a^{Serp} = \left[\left(\tfrac{m-1}{m}\right)^{m-1}\left(\tfrac{1}{m}\right)\right]^{-1}\left[X_{Mg,M}^{m-1} X_{Fe^{3+},M} X_{Al,T1}\right]. \tag{5.22}$$

With these activity expressions the Gibbs free energy at PT conditions for the ferri-alumina-Tschermak lizardite endmember ($G_{PT}^{f3Lizts}$) can be calculated from equilibria 5.1-5.3 as

$$G_{PT}^{f3Lizts} = \tfrac{1}{2}[RT\ln\left(\frac{a^{Clin}}{(a^{Fo})^{1/2}\ (a^{Fa})^{1/2}\ (a^{Serp})^2}\right) - \tfrac{1}{2}G^{Fa} - \tfrac{1}{2}G^{Fo} + G^{Clin} + G^{Mgt}] \tag{5.23}$$

$$G_{PT}^{f3Lizts} = \tfrac{1}{2}[RT\ln\left(\frac{a^{Clin}}{(a^{Fo})^{1/2}\ f(O_2)^{1/6}\ (a^{Serp})^2}\right) - \tfrac{1}{2}G^{En} + \tfrac{1}{6}G^{O_2} + G^{Clin} + \tfrac{2}{3}G^{Mgt}] \tag{5.24}$$

$$G_{PT}^{f3Lizts} = \tfrac{1}{2}[RT\ln\left(\frac{a^{Fo}\ a^{Fa}\ a^{Chl}\ f(O_2)^{1/2}}{(a^{En})^{3/2}\ (a^{Serp})^2}\right) - \tfrac{3}{2}G^{En} + \tfrac{1}{2}G^{O_2} + G^{Clin} + G^{Fo} + G^{Fa}] \tag{5.25}$$

and for the ferri-alumina-Tschermak antigorite endmember from equilibria 5.4-5.6 as

$$G_{PT}^{f3Atgts} = \frac{1}{2}[RT\ln\left(\frac{a^{Clin}}{(a^{Fo})^{1/2}\ (a^{Fa})^{1/2}\ (a^{Serp})^2}\right) - \frac{1}{2}G^{Fa} - \frac{6}{17}G^{Br} - \frac{1}{2}G^{Fo} + G^{Clin} + G^{Mgt}] \tag{5.26}$$

$$G_{PT}^{f3Atgts} = \frac{1}{2}[RT\ln\left(\frac{a^{Clin}}{(a^{Fo})^{1/2}\ f(O_2)^{1/6}\ (a^{Serp})^2}\right) - \frac{1}{2}G^{En} - \frac{6}{17}G^{Br} + \frac{1}{6}G^{O_2} + G^{Clin} + \frac{2}{3}G^{Mgt}] \tag{5.27}$$

$$G_{PT}^{f3Atgts} = \frac{1}{2}[RT\ln\left(\frac{a^{Fo}\ a^{Fa}\ a^{Clin}\ f(O_2)^{1/2}}{(a^{En})^{3/2}\ (a^{Serp})^2}\right) - \frac{3}{2}G^{En} - \frac{6}{17}G^{Br} + \frac{1}{2}G^{O_2} + G^{Clin} + G^{Fo} + G^{Fa}]. \tag{5.28}$$

Here, the Gibbs free energy of the phases on the right hand side are taken from the HP'11 database (Holland and Powell, 2011). For experiments containing Hem, the equations 5.7-5.10 are used.

The calculated values for the ferri-alumina-Tschermak endmember depend on T and P (fig. 5.1 - 5.3). At 550 °C and 3 GPa, G^0 of the ferri-alumina-Tschermak Liz endmember is $-4.042 \cdot 10^3$ kJ mol^{-1} for complete order and $-4.051 \cdot 10^3$ kJ mol^{-1} for complete disorder. Models having ordering only on the octahedral or tetrahedral site result in values for G^0 that are between the complete ordered and complete disordered endmembers. The endmember values are about 380 kJ mol^{-1} higher than the G^0 for the pure Mg Liz endmember (see section 5.4).

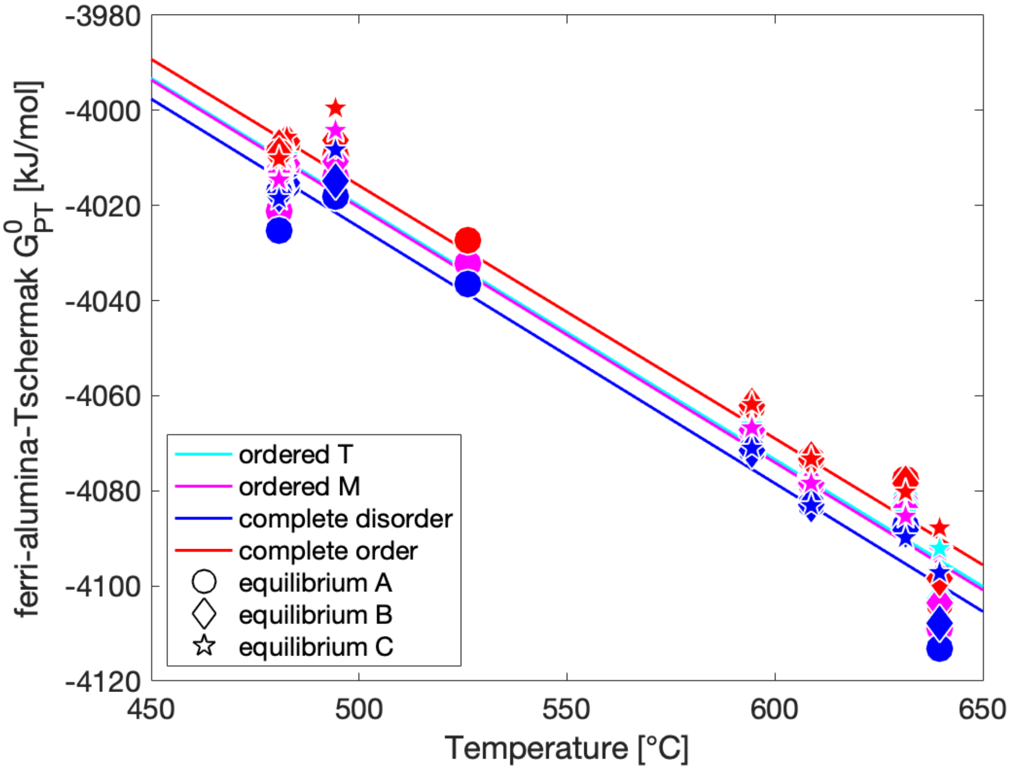

Figure 5.1: Calculated G^0 of the f3Lizts in experiments at 3 GPa. Different symbols mark different equilibria assuming the same state of ordering. Curves are least square fits through all experiments. The best correlation with experimental data is obtained for complete disordering with $G^0 = -0.539T - 3755.1$, where T is the temperature in °C. Note that for experiment V1114 (526 °C, 3 GPa) G^0_{PT} values could only be obtained for the O_2-independent equilibrium C, since the $f(O_2)$ could not be determined due to the limited EPMA data.

The ferri-alumina-Tschermak Atg endmember shows similar characteristics in that the free energy decreases with increasing temperature and that the complete ordered f3Atgts has a higher free energy with respect to the complete disordered f3Atgts (fig. 5.2). The absolute values are about 175 kJ mol^{-1} higher compared to the ferri-alumina-Tschermak Liz at 550 °C. This difference is comparable with the expected difference between Liz and Atg in the pure MSH system of 160 kJ mol^{-1} obtained from the HP'11 database Holland and Powell (2011). More important is the difference in T-dependency between the two endmembers. This becomes most visible by comparing the experimentally determined values for f3Atgts with values obtained by substracting $\frac{3}{17}$ Br component from the f3Lizts endmember, shown as dashed lines in figure 5.2. The difference is 12 kJ mol^{-1} at 550 °C and strongly T-dependent. As addressed previously, Al and consequently the charge balanced ferric Fe in Atg did not equilibrate with respect to temperature. However, it is reasonable to assume that the T-dependency should be similar to Liz as the Al content in natural Atg samples and the Liz-bearing experiments behaves similar. The Atg starting material used experienced peak metamorphic conditions at 550 °C and 2.5 GPa (Angiboust et al., 2009). The pressure has no effect on the absolute Al and ferric Fe content in the phase and can be ignored for now. Thus, assuming that the sample did not reequilibrate during retrograde metamorphism, the G^0_{PT} value at 550 °C can be assumed to be correct, whereas a more accurate T-dependency is obtained by simply using the value for f3Lizts. The resulting G^0_{PT} as used in the following is given as a thick black line in figure 5.2.

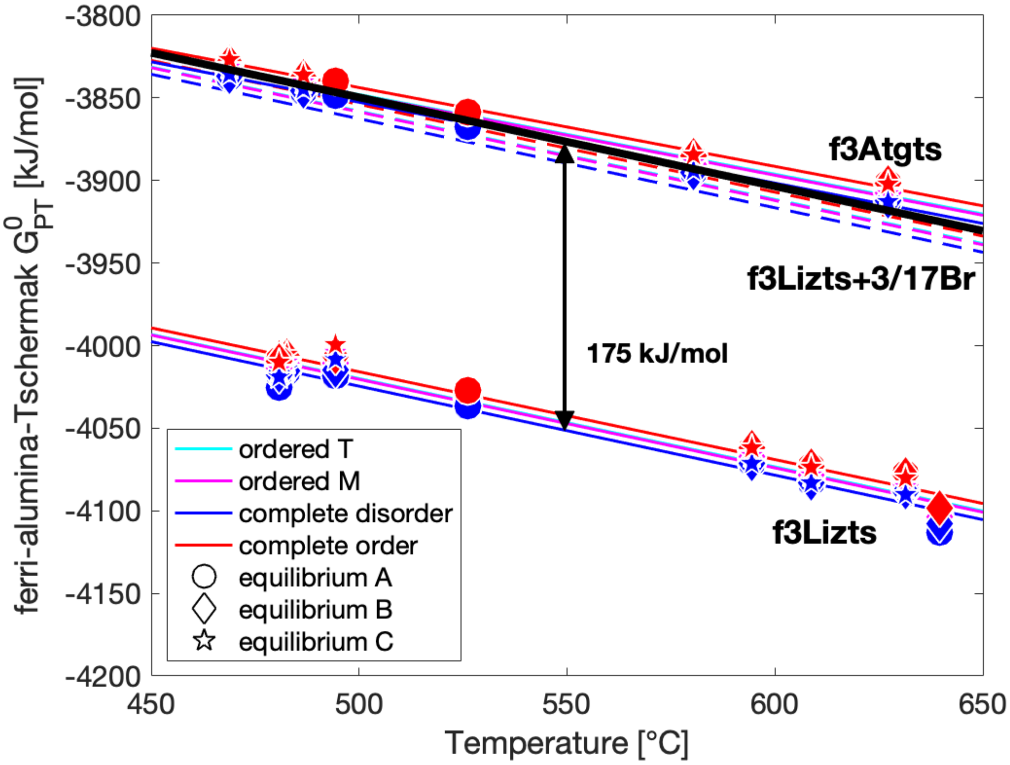

Figure 5.2: Calculated G^0 for ferri-alumina-Tschermak Atg in experiments conducted at 3 GPa. Different symbols mark different equilibria assuming the same state of ordering. Curves are least square fits through all equilibria. The values for f3Atgts are about 175 kJ mol^{-1} higher with respect to f3Lizts at 550 °C. Dashed lines show the free energy of f3Atgts as obtained by substracting Br from f3Lizts. The values differ from experimentally obtained values, which results from Atg not being equilibrated at experimental PT conditions. The black line marks the G^0 for f3Atgts obtained at 550 °C with the T-dependency of f3Lizts.

5.2.1 Pressure-dependency

The pressure dependent contribution to the Gibbs free energy of the ferri-alumina-Tschermak Liz endmember can be fitted from the experimental data. Two Liz-bearing samples at 5 GPa indicate a T-independent pressure term of 103 kJ mol^{-1} GPa^{-1} (fig. 5.3). The volume is obtained from the pressure derivative of G:

$$V = \frac{\partial G}{\partial P}. \tag{5.29}$$

Assuming a linear pressure contribution to the free energy, i.e. a constant volume, a volume of 103(3) cm^3 mol^{-1} is obtained for f3Lizts in the pressure range of interest. This value is very similar with respect to values obtained for natural Al- and Fe-bearing Liz by Hilairet et al. (2006) at ambient temperature, who report a mean molar volume of 104 cm^3 mol^{-1} in the pressure range 3.54 - 5.34 GPa. Two Atg-bearing experiments were conducted at higher pressure and close to the equilibrium temperature of 550 °C: V1090 was conducted at 4 GPa and 572 °C and V1159b at 5 GPa and 572 °C. A P-dependency for f3Atgts is obtained as 97(2) kJ mol^{-1} GPa^{-1} and 99(1) kJ mol^{-1} GPa^{-1}, respectively. The corresponding volumes are 97(2) cm^3 mol^{-1} and 99(1) cm^3 mol^{-1}, which are also very close to values obtained by Hilairet et al. (2006), indicating a mean molar volume of 97 cm^3 mol^{-1} for a natural Al- and Fe-bearing $m = 17$ polysome in the pressure range of 3.81 - 5.87 GPa. The data of Hilairet et al. (2006) confirm that Atg and Liz behave similarly with respect to pressure.

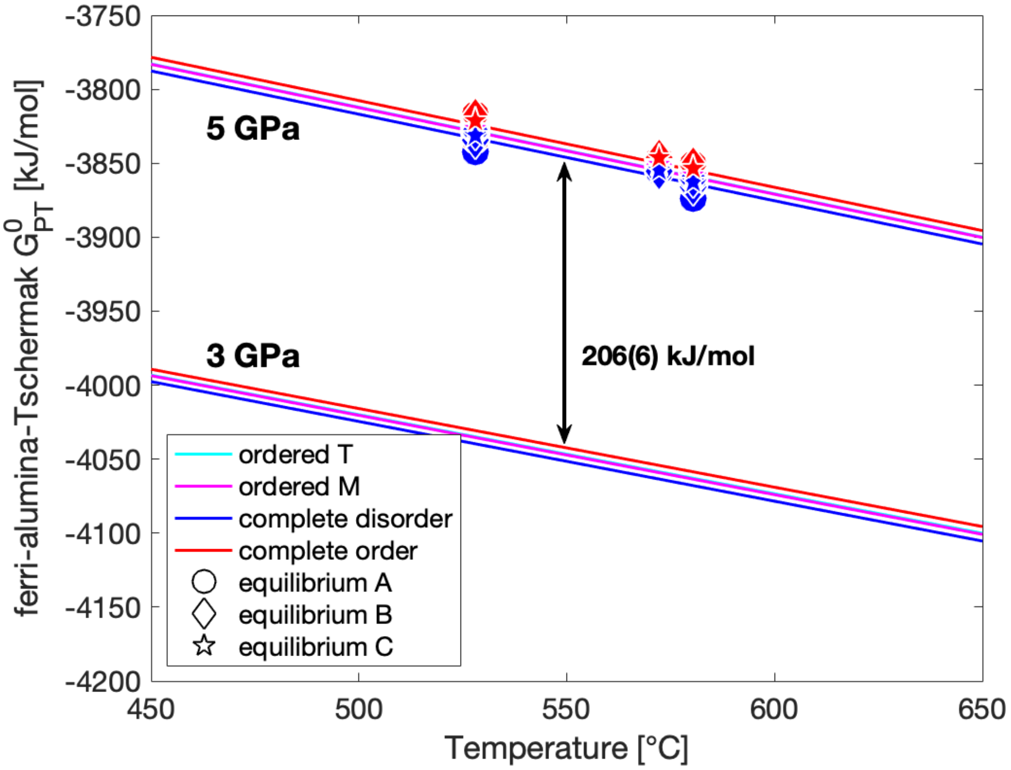

Figure 5.3: Fit obtained from Liz-bearing experiments at 3 GPa compared to 5 GPa experiments. 3 GPa data are from figure 5.1. An offset of 103(3) kJ mol^{-1} GPa^{-1} is observed.

5.3 Configurational entropy

The configurational entropy S_{conf} depends on the ordering model assumed and is calculated from

$$S_{conf} = -R\Sigma^{sites}(\nu_i X_i \ \ln(X_i)), \tag{5.30}$$

where R is the gas constant, X_i the fraction of the component mixing on site i and ν_i the stoichiometric proportion of site i. The configurational entropy for the different models is calculates as

$$S_{conf}^{\text{complete disorder}} = -\,\mathrm{R}\left(\mathrm{M}\left[\tfrac{\mathrm{Mg}}{\mathrm{M}}\ln(\tfrac{\mathrm{Mg}}{\mathrm{M}}) + \tfrac{\mathrm{Fe}^{3+}}{\mathrm{M}}\ln(\tfrac{\mathrm{Fe}^{3+}}{\mathrm{M}})\right] + \mathrm{T}\left[\tfrac{\mathrm{Al}^{\mathrm{IV}}}{\mathrm{T}}\ln(\tfrac{\mathrm{Al}^{\mathrm{IV}}}{\mathrm{T}}) + \tfrac{\mathrm{Si}}{\mathrm{T}}\ln(\tfrac{\mathrm{Si}}{\mathrm{T}})\right]\right) \tag{5.31}$$

$$S_{conf}^{\text{ordered T}} = -\,\mathrm{R}\left(\mathrm{M}\left[\tfrac{\mathrm{Mg}}{\mathrm{M}}\ln(\tfrac{\mathrm{Mg}}{\mathrm{M}}) + \tfrac{\mathrm{Fe}^{3+}}{\mathrm{M}}\ln(\tfrac{\mathrm{Fe}^{3+}}{\mathrm{M}})\right]\right) \tag{5.32}$$

$$S_{conf}^{\text{ordered M}} = -\,\mathrm{R}\left(\mathrm{T}\left[\tfrac{\mathrm{Al}^{\mathrm{IV}}}{\mathrm{T}}\ln(\tfrac{\mathrm{Al}^{\mathrm{IV}}}{\mathrm{T}}) + \tfrac{\mathrm{Si}}{\mathrm{T}}\ln(\tfrac{\mathrm{Si}}{\mathrm{T}})\right]\right) \tag{5.33}$$

where M is the total number of octahedral position (3 for Liz, 2.824 for Atg), T the total number of tetrahedral positions.

For f3Lizts the calculated S_{conf} is 27.41 $\mathrm{J\,mol^{-1}\,K^{-1}}$ (complete disorder), 15.88 $\mathrm{J\,mol^{-1}\,K^{-1}}$ (ordered tetrahedral) and 11.53 $\mathrm{J\,mol^{-1}\,K^{-1}}$ (ordered octahedral) for the three models showing disorder on at least one of the two sites of mixing.

If it is assumed that mixing in the ferri-alumina-Tschermak endmember is ideal the enthalpy of mixing δH_{mix} is 0. This is not necessarily the case but the changes in the ferric Fe and Al contents are relatively small so that the activity coefficients would not change significantly with composition and their contribution would be mainly constant, which in effect in the model is simple combined with G^0. From these assumptions it is possible to determine S_{conf} from the experimental results by the difference between G^0 of the completely ordered model and any model of interest. The experimentally determined S_{conf} obtained at 550 °C for f3Lizts is 11.04 $\mathrm{J\,mol^{-1}\,K^{-1}}$ (complete disorder), 5.85 $\mathrm{J\,mol^{-1}\,K^{-1}}$ (ordered tetrahedral) and 5.19 $\mathrm{J\,mol^{-1}\,K^{-1}}$ (ordered octahedral), respectively. The experimental values are smaller than the hypothetical values, which may be an indication for an excess enthalpy contribution, which is currently simply assumed to be part of the G^0 term.

5.4 Relative stability

To date, no ferric Fe solution model has been reported for any serpentine mineral. However, it is possible to compare the free energy of the ferri-alumina-Tschermak endmembers with other serpentine endmembers. The absolute values for G^0 determined for the different serpentine endmembers allow a simple assessment of the effects of element substitutions on serpentine stability. Figure 5.4 shows the calculated G^0 for various endmembers as a function of temperature at P=3 GPa. Also shown is the Atg+Br Gibbs free energy, which crosses below that of Liz at the Liz-Atg transition at 242.85 °C. The two curves remain close to each other over the whole computed T-range.

The Fe^{2+} endmembers are all based on linear combinations with talc (Tlc) and Fe^{2+}-bearing talc (fTlc), such that

$$\mathrm{Fe}^{2+}\text{-}\Omega = \mathrm{Mg}\text{-}\Omega - \tfrac{n}{3}\ \ \mathrm{Tlc} + \tfrac{n}{3}\ \ \mathrm{fTlc} \tag{5.34}$$

where Ω denotes the silicate of interest, e.g. Liz, Atg, Atgts, and n is the number of Mg cations that have to be exchanged.

Padrón-Navarta et al. (2013) proposed a model for Al mixing. The alumina-Tschermak Atg endmember (Atgts), written for the full $m = 17$ polysome with 34 tetrahedral sites, has the stoichiometry $\mathrm{Mg_{44}Al_4|(Al,Si)_8Si_{26}|O_{85}(OH)_{62}}$. G^0 is calculated from the reaction

$$\mathrm{Atgts} = 4\ \mathrm{clin} + \tfrac{9}{17}\ \mathrm{atg} - \tfrac{24}{17}\ \mathrm{Br}. \tag{5.35}$$

In their model Padrón-Navarta et al. (2013) assumed mixing of Al only on 4 octahedral and 8 tetrahedral sites. As a consequence the standard state entropy is raised by $R8\ln(2)\,\mathrm{J\,K^{-1}}$ to account for the configurational entropy. An additional enthalpy correction δH_{Atgts} of $-1.4\,\mathrm{kJ\,mol^{-1}}$ is obtained by fitting natural and experimental data. The correction for the pure Atgts endmember without Cr and ferric Fe is estimated to be $-2\,\mathrm{kJ\,mol^{-1}}$.

At 3 GPa and 500 °C, G^0 of the Atgts endmember thus results in $-7.11 \cdot 10^4\,\mathrm{kJ\,mol^{-1}}$ based on

$$G^0_{Atgts} = 4G^0_{clin} + \tfrac{9}{17}G^0_{atg} - \tfrac{24}{17}G^0_{Br} - 2\ \mathrm{kJ} + T \cdot 0.0461\ \mathrm{kJ\,K^{-1}}. \tag{5.36}$$

G^0 of the Fe^{2+} endmembers is higher with respect to the Mg endmembers, indicating the often observed destabilisation effect of Fe (Merkulova et al., 2016). The Atgts endmember, on the contrary, is indeed more stable than the pure Mg endmember. In previous studies this is attributed to the fact that Al relaxes the misfit between the length of the tetrahedral and octahedral layer in serpentine sheet silicates (Caruso and Chernosky, 1979).

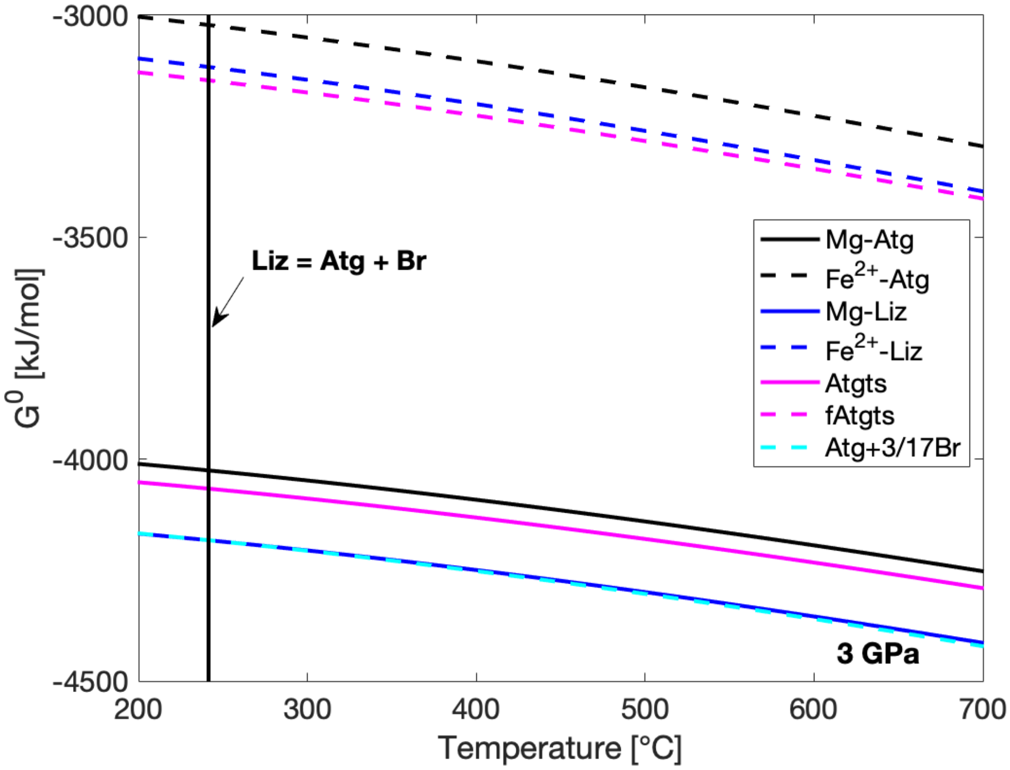

Figure 5.4: G^0 calculated for various phases at 3 GPa. The Mg endmembers are more stable than the corresponding Fe^{2+} endmembers. The Liz-Atg transition is located at 242.85 °C. The Atgts endmember is based on the relations in Padrón-Navarta et al. (2013).

In order to asses the relative position of the new ferri-alumina-Tschermak endmembers the models with complete disorder are used. Ordering of Al on the tetrahedral site can occur due to the principal of Al avoidance, which results from Al-O-Al bonds being unfavourable (Ganguly and Ghose, 1979; Loewenstein, 1953). However, it is not possible to determine the state of ordering from EPMA data. Since the disordered model does fit better with the experimental data, it is used for further calculations.

Figure 5.5 shows the relative position of the new endmember. G^0 for the Fe^{2+} and Mg endmembers as shown in figure 5.4 is indicated by shaded areas. The coupled ferri-alumina-Tschermak substitution is more stable than Fe^{2+} endmembers but less stable than the Mg endmembers. Also shown in figure 5.5 is G^0 for the ferri-alumina-Tschermak endmember calculated based on the linear combination of free energies, i.e. f3Atgts = Atgts - $\frac{1}{2}$ corundum + $\frac{1}{2}$ hematite. Although Hem has magnetic ordering the magnetic contribution to the Gibbs free energy at 500 °C and 3 GPa is only 1.3 kJ mol^{-1} based on the model of Holland and Powell (1998) and is thus negligible. This estimate shows that the free energy obtained from linear combinations of minerals which have significantly different structure, e.g. silicates and oxides, still results in reasonable values and can be used as a first order estimate on the free energy.

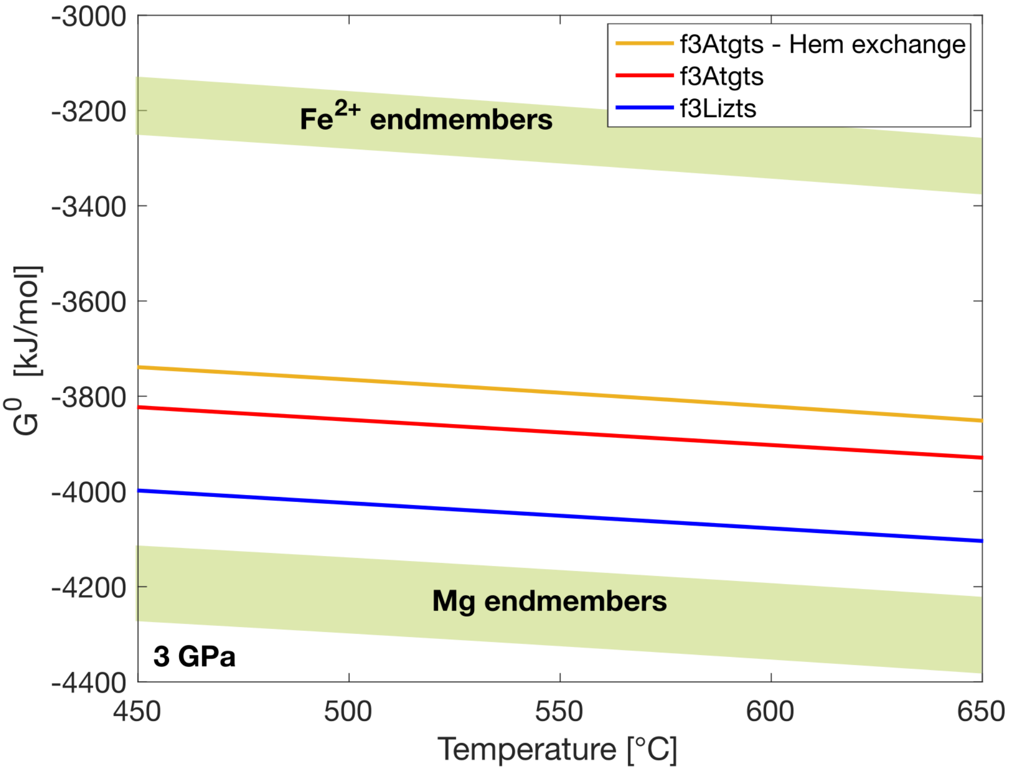

Figure 5.5: The new ferri-alumina-Tschermak endmembers are less stable than the pure Mg endmembers but more stable than Fe^{2+} endmembers. Shaded areas mark Mg and Fe^{2+} endmembers shown in figure 5.4. The orange line shows the f3Atgts endmember based on the relation f3Atgts = Atgts - $\frac{1}{2}$ corundum + $\frac{1}{2}$ hematite.

5.5 A thermodynamic model for Fe^{3+}-$f(O_2)$ relations in serpentine

In previous sections, experimental data were used to assess trends in mineral composition upon changing P, T and $f(O_2)$. Using the derived thermodynamic data, however, it is possible to invert this relationship and calculate how mineral compositions change with P, T and $f(O_2)$. This allows the oxidation state of Fe in serpentine minerals at subduction zone conditions as a function of $f(O_2)$ to be calculated.

Liz and Atg both have a total of 2 tetrahedral sites, filled with Al and Si. Liz has 3 octahedral sites, whereas in Atg there are only 2.824. The octahedral sites are filled with Mg, ferrous and ferric Fe and Al. In order to calculate the composition of serpentine, expressions for each of these components as a function of intensive variables are required. In addition the compositions of coexisting phases have to be determined from their partitioning relations with serpentine.

The Al content in Liz coexisting with Chl is buffered in experiments and changes only as a function of temperature. Evidence that Atg behaves similar if enough time is provided is given in Schwartz et al. (2013) as explained earlier. With the constraints from the end-member formulation, i.e. the total Al has to be in the range of $0 \leq \mathrm{Al}$ pfu ≤ 2, the results obtained by pseudosection calculations in section 6.3 can be fitted with an error function. The total Al content in serpentine as function of temperature thus becomes

$$\mathrm{Al}^{\mathrm{tot}} = 1 + \mathrm{erf}\left[\frac{T - 999.726}{410.622}\right], \tag{5.37}$$

where T is the temperature in celsius. Since the total trivalent cation content in Serp is charge balanced via Tschermak-style substitution, the partitioning of Al on the octahedral and tetrahedral site are directly related to the ferric Fe content. The latter is partitioned fully onto the octahedral site as shown by Mössbauer analyses. The partitioning of Al is thus a function of both, the total Al content and the ferric content and is given via equations 3.1 and 3.2. It is important to note here, that at a fixed Al content the maximum $\mathrm{Al}^{\mathrm{IV}}$ is reached if all Al is partitioned into the tetrahedral site, i.e. $\mathrm{Al}^{\mathrm{IV}} = \mathrm{Al}^{\mathrm{tot}}$. The Si pfu results from the total amount of 2 tetrahedral sites and can also be written in terms of ferric Fe as

$$\mathrm{Si} = 2 - \mathrm{Al}^{\mathrm{IV}} = 2 - 0.5\ (\mathrm{Al}^{\mathrm{tot}} + \mathrm{Fe}^{3+}). \tag{5.38}$$

With the total octahedral sites m fixed to 3 for Liz and 2.824 for Atg, the Mg and Fe^{2+} contents are calculated from

$$\mathrm{Mg} = m - \mathrm{Fe}^{\mathrm{tot}} - \mathrm{Al}^{\mathrm{oct}} = m - \mathrm{Fe}^{\mathrm{tot}} - \tfrac{1}{2}\left(\mathrm{Al}^{\mathrm{tot}} - \mathrm{Fe}^{3+}\right) \tag{5.39}$$

$$\mathrm{Fe}^{2+} = m - \mathrm{Mg} - \mathrm{Fe}^{3+} - \mathrm{Al}^{\mathrm{oct}} = m - \mathrm{Mg} - \tfrac{1}{2}\ \mathrm{Fe}^{3+} - \tfrac{1}{2}\ \mathrm{Al}^{\mathrm{tot}}. \tag{5.40}$$

The Mg# of Serp is then calculated as

$$\mathrm{Mg\#}^{Serp} = \frac{\mathrm{Mg}}{\mathrm{Mg{+}Fe^{2+}}}. \tag{5.41}$$

Due to correlations of Serp-Ol, Ol-Opx and Serp-Chl the Fe^{2+}-Mg exchange in all coexisting minerals can be expressed as a function of the Mg# in Serp, following equations 4.3, 4.4 and 4.5. The composition of each mineral in equilibria 5.1 to 5.10 can thus be expressed as a function of the Serp composition. At a given temperature the Al content in Serp is a constant and thus the Serp composition itself is only a function of ferric Fe for a fixed total Fe content. It is now possible to calculate the Fe^{3+}/ΣFe ratio of serpentine as a function of several parameters such as T, $f(O_2)$ and composition (fig. 5.6 - 5.7).

5.6 Comparison between the thermodynamic model and experimental data

In figure 5.6a and 5.6b the Fe^{3+}/ΣFe ratios of Liz and Atg are calculated at 3 GPa as a function of $f(O_2)$ in the T-range of 500 - 700 °C. The equilibria used to derive the Fe^{3+}/ΣFe ratios are equilibrium 5.3 and 5.6, respectively. These equilibria do not involve Fe oxides and no conversion from Mgt to Hem is needed. The Al content in Serp is a function of temperature only and is thus constant along each curve in figures 5.6a and 5.6b. The total Serp Fe content is fixed to 0.2 Fe pfu. Due to coupled substitution of trivalent cations and the necessity of charge balance, the upper limit for total ferric Fe is therefore given by either the total Al content or the total Fe content, depending on which is lower.

The Fe^{3+}/ΣFe ratio increases with $f(O_2)$ in both phases, with a sigmoidal trend observed for both Liz and Atg. When the maximum ferric Fe content is reached any further increase in $f(O_2)$ does not affect the ferric Fe content, which results in a constant ratio at high $f(O_2)$ due to the fixed total Fe content.

Increasing temperature decreases the Fe^{3+}/ΣFe ratio at a fixed $f(O_2)$ as it is observed in Liz-bearing experiments. An increase in temperature also shifts the maximum Fe^{3+}/ΣFe ratio to higher values due to the higher Al content. Although the range of measured Fe^{3+}/ΣFe ratio in Atg was smaller, as the experiments could not be buffered, a shift towards lower Fe^{3+}/ΣFe ratio between experiments conducted at T <600 °C and experiments conducted at T >600 °C is observed and follows the expectations from the model. However, it should be noted that in the Atg experiments the total Al content is fixed at the equilibrium value for 550 °C as Atg does not reequilibrate. Changes in the $Fe^{3+}/\Sigma Fe$ ratio with increasing temperature arise from small changes in partitioning during dehydration reaction (fig. 3.6b).

Figures 5.7a and 5.7b show the dependency of the $Fe^{3+}/\Sigma Fe$ ratio as a function of total Fe and Al. Changing the total Fe content has very little influence unless ferric Fe saturation is reached: At 600 °C the total Al content is 0.169 Al pfu. If all Al is partitioned on the tetrahedral site, a maximum of 0.169 Fe^{3+} pfu can occupy the octahedral site and a maximum $Fe^{3+}/\Sigma Fe$ ratio is eventually reached at high total Fe contents. An increase in the Al content has a larger effect and results in a decrease in the $Fe^{3+}/\Sigma Fe$ ratio at given conditions. Further, an increase in Al also affects the maximum ferric Fe content.

There are two factors that combine to cause a decrease in the serpentinite $Fe^{3+}/\Sigma Fe$ ratio with increasing temperature: the T-dependence of the standard state Gibbs free energy and the fact that the Al content of serpentine increases with temperature.

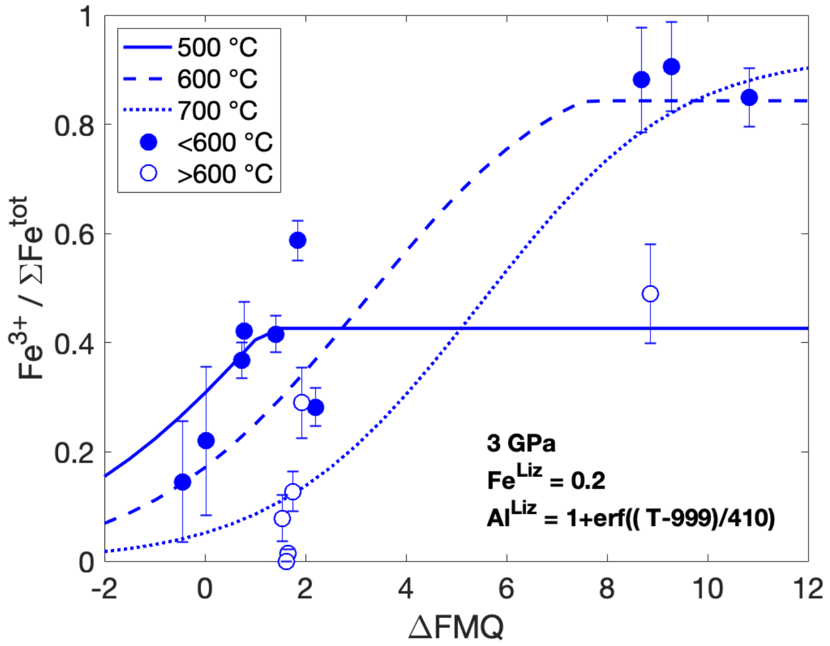

(a)

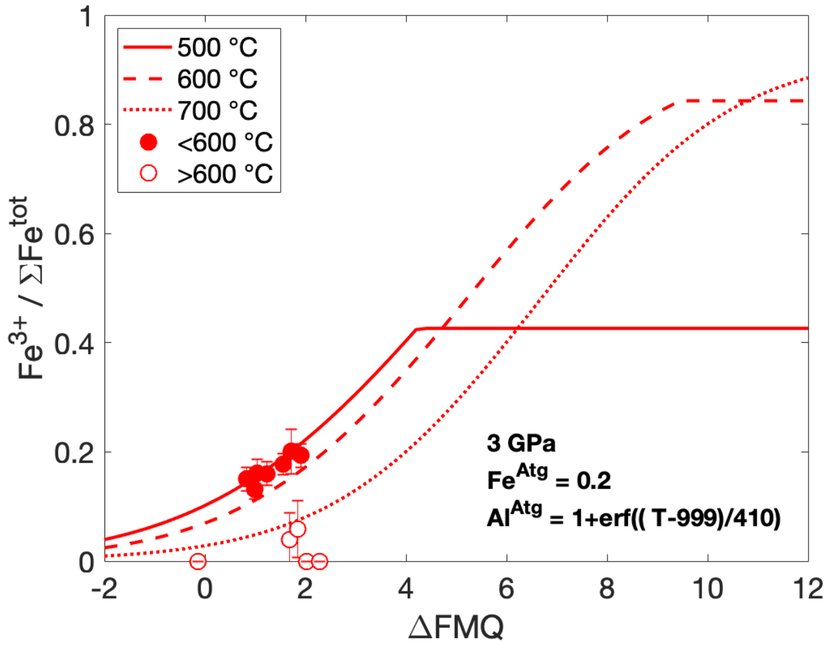

(b)

Figure 5.6: Calculated $Fe^{3+}/\Sigma Fe$ ratios at 3 GPa as well as experimental values for a: Liz and b: Atg. The horizontal line at $T \leq 600\,°C$ indicates ferric Fe saturation. This is the point where all Al is partitioned to the tetrahedral site and thereby limits the amount of octahedral ferric Fe due to charge balance.

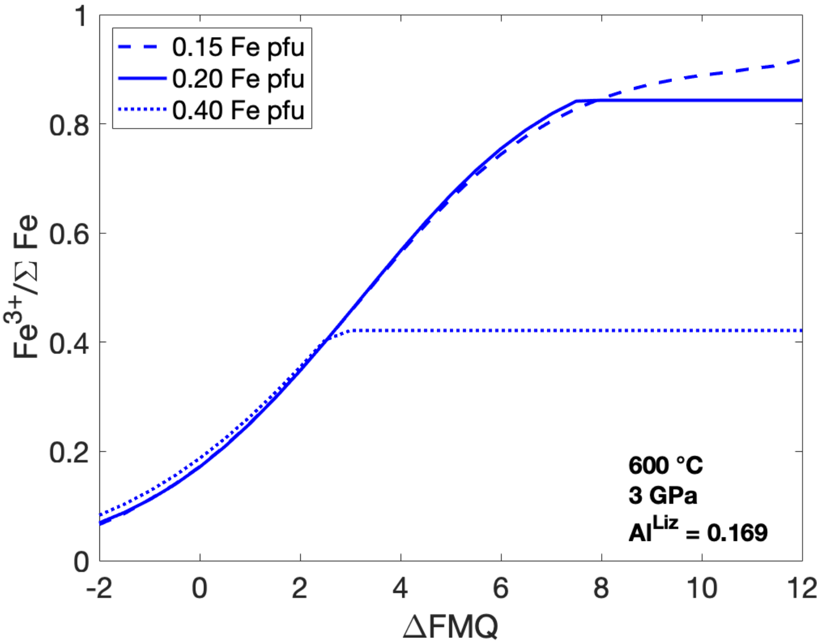

(a)

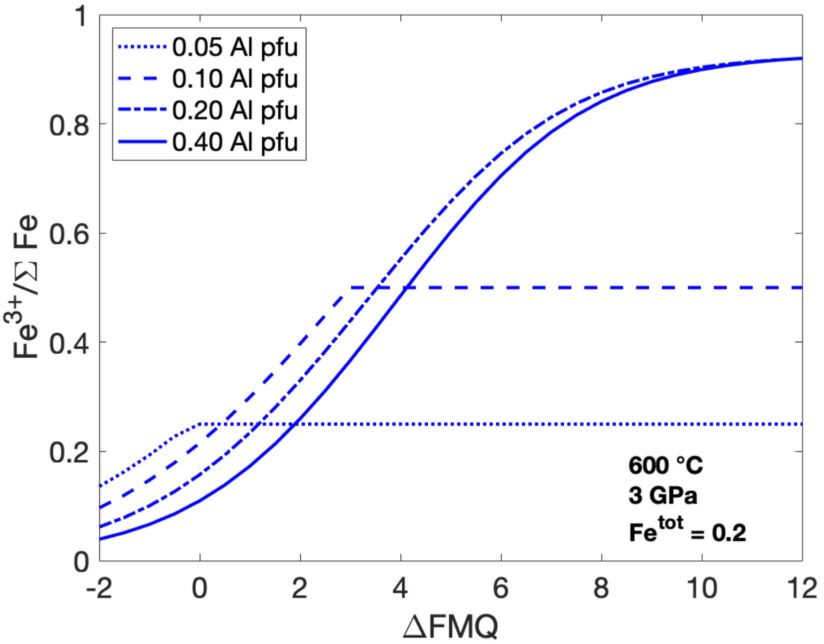

(b)

Figure 5.7: Models showing the influence of changing composition in Liz at fixed PT conditions. a: A change in total Fe only has minor effect on the calculated $Fe^{3+}/\Sigma Fe$ ratio. b: A change in Al content has a larger effect shown by decreasing $Fe^{3+}/\Sigma Fe$ ratio at a fixed $f(O_2)$. Horizontal lines mark ferric Fe saturation.

Four distinct ΔFMQ values were chosen, for which the T-dependency of various compositional variables is computed (fig. 5.8a - 5.8d). The compositional trends are calculated based on the same model as outlined above. The Al content is a function of temperature only, whereas the total Fe content is fixed at 0.2 Fe pfu. Since in the experiments the Al content of Atg did not equilibrate, it is not possible to compare the experimental data of Atg with the model directly. The trends are computed only for Liz and compared with data obtained from Liz-bearing experiments. At low temperature the T-dependent Al content is lower than the fixed Fe content. It thus occurs that the Fe^{3+} content is limited by the total Al pfu at low temperature. The ferric Fe saturation at low temperature is consequently a function of temperature.

The Fe^{3+}/ΣFe ratio is predicted to decrease at a fixed $f(O_2)$ value with increasing temperature, which is in good agreement with the experiments (fig. 5.8a). Deviations between the experiments buffered at high $f(O_2)$ and the model at low temperatures might result from tetrahedral ferric Fe, which is not included in the model. Tetrahedral ferric Fe was, however, not detected in the Mössbauer spectra for these experiments. If present, it is thus below the limit of detection. Due to the fixed total Fe content, the Fe# of Liz, calculated as molar FeO/(FeO+MgO), consequently has to increase with increasing temperature. Since the Al content increases with temperature, the fixed total Fe content also results in a decrease in MgO pfu as shown figure 5.8b. Similar trends are observed in the experiments. A T-dependent increase in Al content results in a decrease in Si. A calculated overall decrease of Si pfu of >0.15 pfu is consistent with experimental trends (fig. 5.8c). The calculations nevertheless indicate a decrease in Si pfu with increasing $f(O_2)$, which is hard to confirm due to the uncertainties of the measured Liz compositions. The measured and calculated Al^{IV}/Al^{tot} ratios in Liz are in reasonable agreement and would in fact imply a trend towards lower Si contents at higher $f(O_2)$ (fig. 5.8d).

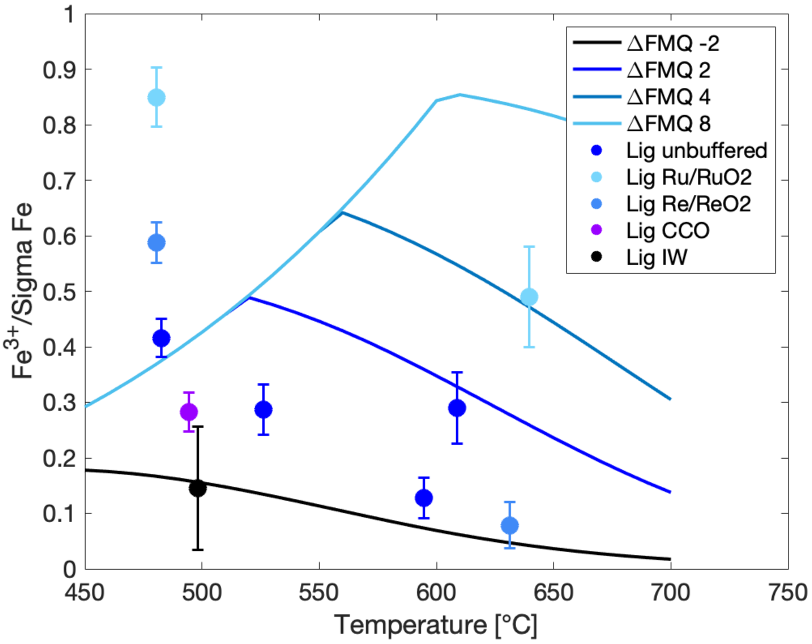
Fe^{3+}/Sigma Fe
Temperature [°C]
0
0.1
0.2
0.3
0.4
0.5
0.6
0.7
0.8
0.9
1
450
500
550
600
650
700
750
ΔFMQ -2
ΔFMQ 2
ΔFMQ 4
ΔFMQ 8
Lig unbuffered
Lig Ru/RuO2
Lig Re/ReO2
Lig CCO
Lig IW

(a)

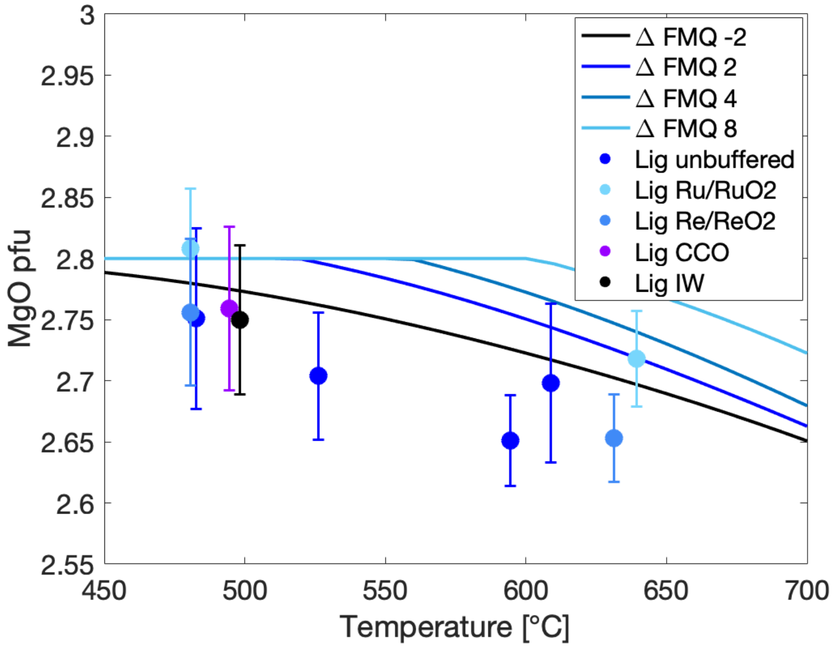
MgO pfu
Temperature [°C]
2.55
2.6
2.65
2.7
2.75
2.8
2.85
2.9
2.95
3
450
500
550
600
650
700
Δ FMQ -2
Δ FMQ 2
Δ FMQ 4
Δ FMQ 8
Lig unbuffered
Lig Ru/RuO2
Lig Re/ReO2
Lig CCO
Lig IW

(b)

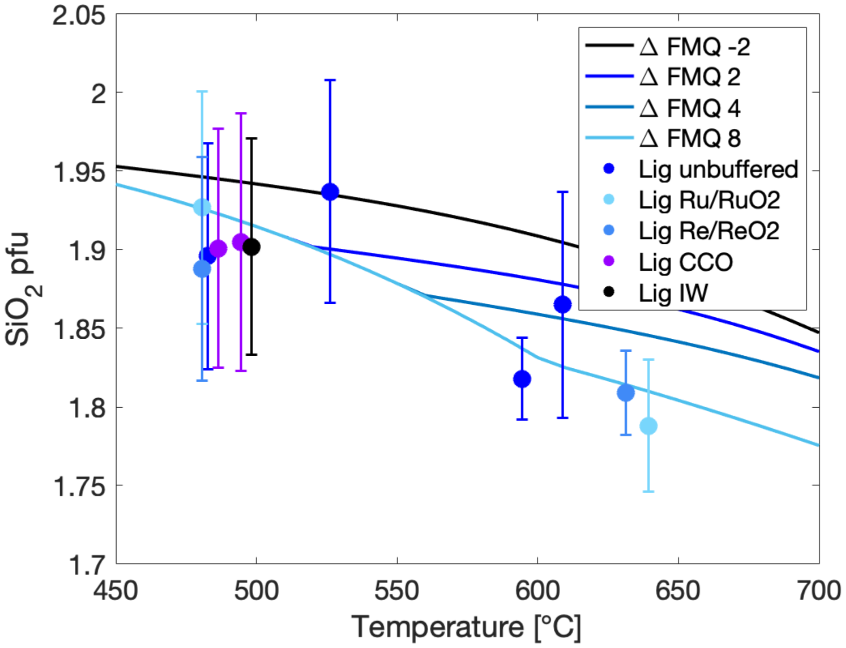

(c)

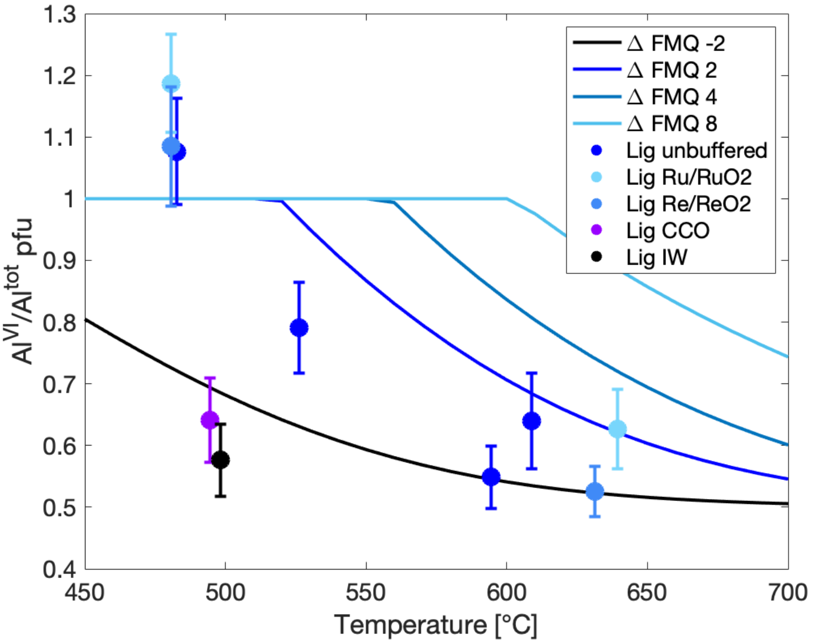

(d)

Figure 5.8: T-dependent composition of Liz calculated from the model. Ferric Fe saturation occurs at low T due to fixed total Fe in Liz. At these conditions, the Fe^{3+} content is fully determined by the T-dependent Al content. a: The Fe^{3+}/ΣFe ratio decreases with increasing T. Note the deviation of experiments buffered at high $f(O_2)$ with respect to the model at low T. b: As a consequence of a fixed total Fe content, a T-dependent increase in Al content ultimately results in a decrease in Mg content. c: The Si content decreases with increasing T. Due to large errors on the experimental data an $f(O_2)$-dependency could not be confirmed. d: The Al^{VI}/Al^{tot} ratio decreases with increasing T.

Some of the differences between the model and experimental data results from the fact that the total Fe content in Serp is assumed here to be constant. However, in experiments the bulk composition remains constant rather than the composition of a single phase. Changes in composition of each phase upon changing mineralogy are therefore expected (compare also fig. 3.4c for changing total Fe content in Serp). The model does reproduce the experimentally obtained $Fe^{3+}/\Sigma Fe$ ratios for both Atg and Liz relatively well particularly given the very low temperatures at which the experiments are performed. The model is also relatively simple in that it only has one adjustable parameter at each PT condition which has therefore to fit the data over the entire range of $f(O_2)$ at each condition. Furthermore, it also reproduces the chemical trends in Mg, Si and Al measured for Liz. As outlined earlier, it seems reasonable to assume that the equilibrium Al and Si contents in Atg change in a similar way to Liz. Therefore, the model can be used to calculate the relationship between Atg compositions and P, T and $f(O_2)$ in order to examine processes occurring during subduction.

6 Free energy minimisation with Perple_X

In the previous chapters, phase relations and mineral compositions were investigated using individual equilibria that examine single substitutions. This is suitable for fitting thermodynamic parameters from experimental data because the activities of other components can be simply taken from the analyses of the mineral phases. In order to model changes in mineral compositions for a particular rock composition as a function of pressure, temperature and $f(O_2)$, however, multiple substitutions between coexisting phases have to be considered simultaneously.

In this chapter Perple_X is used to calculate phase relations in a multicomponent system with more than one independent variable and numerous cation substitutions. Perple_X is a compilation of FORTRAN 77 programs for calculation and graphical presentation of stable phase assemblages and physical and chemical properties (Connolly, 2005). The calculation is based on the concept of gridded minimisation. A grid is created with two independent variables, e.g. P, T or a compositional variable. Constraints can be placed on additional independent variables. A global free energy minimisation is performed on each node of the predefined grid to find the stable mineral assemblage. As a result a map of stable phase assemblages is obtained. The phase boundaries are subsequently refined in several steps. By controlling the mesh size of the grid and the refinement parameters, the user can directly influence the resolution of the resulting phase diagram.

In the previous chapter thermodynamic properties were derived for the ferri-alumina-Tschermak serpentine endmembers that allow the ferric Fe content of antigorite and lizardite to be calculated as a function of P, T and $f(O_2)$. With a global minimisation routine it is possible to explore the influence of Al and ferric Fe on the phase relations in the PT-$f(O_2)$-space. During implementation of the new ferri-alumina-Tschermak antigorite, however, it was necessary to also reevaluate the alumina-Tschermak endmember in order to be consistent with data from this study and to overcome inconsistencies and an error in the implementation of this endmember in a previous treatment (Padrón-Navarta et al., 2013). The Perple_X version 6.9.0 (updated on July 7, 2020 in order to allow linear combinations of 7 phases) was used together with the HP'11 database (Holland and Powell, 2011). For H_2O the CORK equation of state (EoS) (Holland and Powell, 1991) was used. For the model shown in figure 6.6 a hybrid fluid equation of state (fEoS) was used, taking the CORK EoS for H_2O and the modified Redlich-Kwong EoS for H_2 (Santis et al., 1974). The components used are SiO_2 - MgO - FeO - Al_2O_3 - H_2O - O_2, whereas ferric Fe is computed as FeO + $\frac{1}{2}O_2$ and H_2 as $H_2O - \frac{1}{2}O_2$.

6.1 Endmember definition

In order to calculate the antigorite composition and phase relations in the full compositional range, antigorite endemembers for Mg, ferrous and ferric Fe as well as Al are required. The HP'11 database (Holland and Powell, 2011) provides thermodynamic parameters for the Mg antigorite endmember. The ferrous endmember is obtained by simple constraints on Fe^{2+}-Mg exchange. A ferric Fe endmember for antigorite is not available in the existing Perple_X databases but, is implemented in the following using the ferri-alumina-Tschermak endmember data derived in chapter 5. On the other hand, an alumina-Tschermak antigorite endmember and a corresponding solution model is available based on the analysis made by Padrón-Navarta et al. (2013). The alumina-Tschermak model of Padrón-Navarta et al. (2013), however, assumes a total of 8 Al pfu normalised to 34 tetrahedral positions (see also chapter 5). The ferri-alumina-Tschermak antigorite endmember used in this study, as derived in chapter 5, assumes that half of the tetrahedral sites are Al, i.e. 17 Al pfu. A consistent corresponding alumina-Tschermak endmember, therefore, requires a total of 34 Al pfu. In order to retain this consistency, a new alumina-Tschermak endmember has also been implemented into Perple_X. During implementation of the new alumina-Tschermak endmember it was also possible to correct inconsistencies in the configurational entropy and to refine the PT-dependence of the Al content in Atg such that a better fit is obtained to the available data compared to the model of Padrón-Navarta et al. (2013).

A simple and frequently used approach to implement a new thermodynamic endmember in Perple_X is to estimate its properties from a linear combination of properties of existing endmembers to obtain the required stoichiometry. In this way it is possible to calculate the standard state Gibbs free energy of a phase without knowing its heat capacity, expansivity or compressibility coefficients. The free energy can, however, additionally be determined directly from experimental data, as described for the ferri-alumina-Tschermak endmember in chapter 5. The experimental Gibbs free energies are generally determined at a few individual pressures and temperatures that can only be fitted by very simple, normally linear, expressions. These expressions take no account of the effects of variations in heat capacity for example and are unlikely to extrapolate back to realistic room temperature values, where most thermodynamic parameters are compared and assessed. However, they can be used to anchor values obtained from linear combinations at fixed PT conditions. To do this free energies, entropies and volumes obtained by a linear combination of endmember thermodynamic values are adjusted to the experimentally determined data (G^{exp}) by adding a correction term, here and after referred to as G^{diff}:

$$G^{exp}_{PT} = \sum n_i \; G^i_{PT} + G^{diff}, \tag{6.1}$$

where G^i_{PT} is the Gibbs free energy of phase i at PT of interest used in the linear combination. Perple_X allows the implementation of a G^{diff} term in the form

$$G^{diff} = a + b\;T + c\;P, \tag{6.2}$$

where a, b and c are parameters in $\mathrm{J\,mol^{-1}}$, $\mathrm{J\,mol^{-1}\,K^{-1}}$ and $\mathrm{J\,mol^{-1}\,bar^{-1}}$, referring to the difference to the free energy, entropy and volume at ambient conditions, i.e. ΔH^0, -ΔS^0 and ΔV^0.

6.1.1 Fe^{2+}-Mg endmember

The Mg endmember of antigorite (Atg) as used in the HP'11 database is defined as an $m = 17$ polysome with the stoichiometric formula $\mathrm{Mg_{48}Si_{34}O_{85}(OH)_{62}}$. The Fe^{2+}-Mg exchange on the octahedral site is implemented through a linear combination of talc endmembers. Tlc and fTlc, referring to Mg talc and Fe^{2+} talc, are real entities in the thermodynamic database and allow the extent of Fe^{2+}-Mg exchange between various silicates to be estimated. Assuming that the relative free energy change between Fe^{2+} and Mg endmembers of antigorite is similar to talc, the Fe^{2+} endmember of antigorite (fAtg) is calculated as

$$\begin{aligned} \underset{\text{fAtg}}{\mathrm{Fe_{48}Si_{34}O_{85}(OH)_{62}}} \;&= \\ &\underset{\text{Atg}}{\mathrm{Mg_{48}Si_{34}O_{85}(OH)_{62}}} \;-\; 16\;\underset{\text{Tlc}}{\mathrm{Mg_3Si_4O_{10}(OH)_2}} \;+\; 16\;\underset{\text{fTlc}}{\mathrm{Fe_3Si_4O_{10}(OH)_2}}. \end{aligned} \tag{6.3}$$

6.1.2 Alumina-Tschermak endmember

A new alumina-Tschermak endmember (Atgts) is implemented in Perple_X by first estimating the underlying thermodynamic properties for Atgts from the linear combination

$$\underset{\text{Atgts}}{\mathrm{Mg_{31}Al_{34}Si_{17}O_{85}(OH)_{62}}} = \underset{\text{Clin}}{17\ \mathrm{Mg_5Al_2Si_3O_{10}(OH)_8}} - \underset{\text{Br}}{37\ \mathrm{Mg(OH)_2}} - \underset{\text{En}}{\tfrac{51}{2}\ \mathrm{Mg_2Si_2O_6}} + \underset{\text{Fo}}{17\ \mathrm{Mg_2SiO_4}}. \tag{6.4}$$

The corresponding alumina-Tschermak lizardite endmember (Lizts) is given as

$$\underset{\text{Lizts}}{\mathrm{Mg_2Al_2SiO_5(OH)_4}} = \underset{\text{Clin}}{\mathrm{Mg_5Al_2Si_3O_{10}(OH)_8}} - \underset{\text{Br}}{2\ \mathrm{Mg(OH)_2}} - \underset{\text{En}}{\tfrac{3}{2}\ \mathrm{Mg_2Si_2O_6}} + \underset{\text{Fo}}{\mathrm{Mg_2SiO_4}}. \tag{6.5}$$

The Gibbs free energy for the alumina-Tschermak endmembers is then further refined in the same way as the Gibbs free energy of the ferri-alumina-Tschermak endmember in chapter 5 using experimental results at 3 and 5 GPa. To do so the activity for brucite (Br) is taken as ideal, whereas activities for olivine (Ol), orthopyroxene (Opx) and chlorite (Chl) are determined from the experimental compositions or, if these phases could not be measured, approximated based on the Mg# of serpentine via equations 4.3, 4.4 and 4.5. Following the endmember formulation in the previous chapter, normalised to 2 tetrahedral sites, the stoichiometry of Atgts is $\mathrm{Mg_{1.824}Al|AlSi|O_5(OH)_{3.647}}$ and for Lizts $\mathrm{Mg_2Al|AlSi|O_5(OH)_4}$. The activity of the alumina-Tschermak component is written similar to the ferri-alumina-Tschermak component (eq. 5.17) but with $\mathrm{Fe^{3+}}$ replaced by octahedral Al (eq. 3.2 and 5.37), i.e. for the completely disordered model normalised to 2 tetrahedral sites:

$$a^{Serp} = \left[\left(\tfrac{m-1}{m}\right)^{m-1}\left(\tfrac{1}{m}\right)\left(\tfrac{1}{2}\right)^{2}\right]^{-1}\left[(X_{Mg,M})^{m-1}X_{Al^{VI},M}X_{Al^{IV},T}X_{Si,T}\right]. \tag{6.6}$$

Since the experimental data are normalised to 2 tetrahedral sites, equilibrium 6.4 becomes

$$\underset{\text{Atgts}}{\mathrm{Mg_{1.824}Al_2SiO_5(OH)_{3.647}}} = \underset{\text{Clin}}{\mathrm{Mg_5Al_2Si_3O_{10}(OH)_8}} - \tfrac{37}{17}\,\underset{\text{Br}}{\mathrm{Mg(OH)_2}} - \tfrac{3}{2}\,\underset{\text{En}}{\mathrm{Mg_2Si_2O_6}} + \underset{\text{Fo}}{\mathrm{Mg_2SiO_4}}. \tag{6.7}$$

The free energy at PT conditions of interest is then directly calculated using the available experimental data with the equations 6.7 and 6.5 by

$$G^{Atgts}_{PT} = RT\ln\left(\frac{a^{Clin}\ a^{Fo}}{(a^{En})^{3/2}\ a^{Atgts}}\right) - \tfrac{3}{2}G^{En} - \tfrac{37}{17}G^{Br} + G^{Fo} + G^{Clin} \tag{6.8}$$

$$G^{Lizts}_{PT} = RT\ln\left(\frac{a^{Clin}\ a^{Fo}}{(a^{En})^{3/2}\ a^{Lizts}}\right) - \tfrac{3}{2}G^{En} - 2G^{Br} + G^{Fo} + G^{Clin}. \tag{6.9}$$

In figure 6.1a the experimentally determined G^{exp}_{PT} values for Atgts and Lizts are shown. It is important to note that, as discussed previously, Al in antigorite does not reequilibrate in experimental time scales, i.e. the Al content remains identical to the starting material. This is also reported in previous experimental studies (e.g. Padrón-Navarta et al., 2010; Merkulova et al., 2016). However, this is not the case for lizardite where the Al content increases with temperature in equilibrium with Chl as expected. For this reason the T-dependence of the ferri-alumina-Tschermak antigorite component was taken from the ferri-alumina-Tschermak lizardite dependence and anchored at 550 °C (chapter 5). The same methodology is also applied here for the alumina-Tschermak antigorite component, for which the T-dependence is assumed to be the same as for the alumina-Tschermak lizardite component. The resulting free energy is given in figure 6.1a as a thick black line. In figure 6.1b Liz-bearing experiments conducted at 3 and 5 GPa are shown. The difference in the free energy is 222(14) kJ mol^{-1}, i.e. 111(7) kJ mol^{-1} GPa^{-1}, resulting in a volume of 111(7) cm^3 mol^{-1}. For the Atgs endmember a volume of 106(2) cm^3 mol^{-1} is obtained by fitting experiments V1090 (572 °C, 4 GPa), V1159b (572 °C, 5 GPa) and

V1153b (526 °C, 5 GPa). These values are slightly larger than the values obtained for the ferri-alumina-Tschermak endmembers, which are 103(3) $\mathrm{cm^3\,mol^{-1}}$ and 98(2) $\mathrm{cm^3\,mol^{-1}}$, respectively (chapter 5, fig. 5.3). Given the small size of an Al cation, it would be expected that the volume of the alumina-Tschermak endmember is smaller with respect to the ferri-alumina-Tschermak endmember. However, the values are close within errors and differences might also be due to experimental uncertainties.

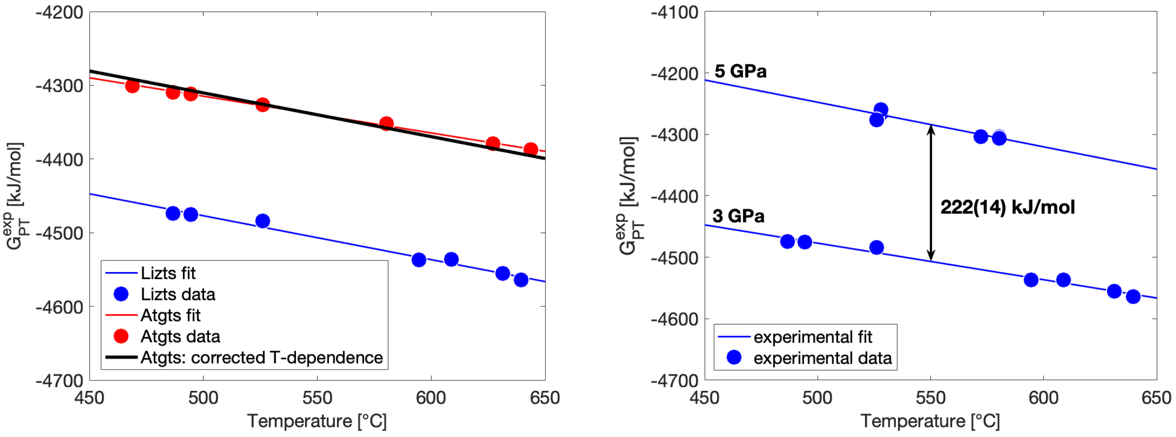

(a) **(b)**

Figure 6.1: a: Experimentally determined G^{exp}_{PT} of the completely disordered alumina-Tschermak endmember of antigorite (Atgts) and lizardite (Lizts) at 3 GPa. The black line marks the free energy of the Atgts endmember with the T-dependence of the Lizts endmember with $G^{Atgts} = -0.593T - 4013.746$, with T being the temperature in celsius. b: Liz-bearing experiments conducted at 3 GPa and 5 GPa. The linear P-dependence is 111(7) $\mathrm{kJ\,GPa^{-1}\,mol^{-1}}$.

6.1.3 Ferri-alumina-Tschermak endmember

Using the Gibbs free energy of the Atgts endmember, the free energy of the ferri-alumina-Tschermak antigorite endmember (f3Atgts) is estimated by using a linear combination that replaces the octahedral Al with ferric Fe. The only way to do this by using endmembers that are relatively well constrained is via corundum (Cor) and hematite (Hem):

$$\underset{\text{f3Atgts}}{\mathrm{Mg_{1.824}Fe^{3+}AlSiO_5(OH)_{3.647}}} = \underset{\text{Atgts}}{\mathrm{Mg_{1.824}Al_2SiO_5(OH)_{3.647}}} - \tfrac{1}{2}\underset{\text{Cor}}{\mathrm{Al_2O_3}} + \tfrac{1}{2}\underset{\text{Hem}}{\mathrm{Fe_2O_3}}. \qquad (6.10)$$

It is to note here that Hem is magnetic. The excess energy arising from magnetic ordering can be calculated from a Landau potential. Following Holland and Powell (1998) the Landau free energy at 3 GPa and 500 °C is only $-1.3\,\mathrm{kJ\,mol^{-1}}$ and thus does not significantly contribute to the absolute values.

6.1.4 Excess energy for Al and Fe^{3+} endmembers

G^{diff} must be determined to bring the free energies estimated for the Al and Fe^{3+} endmembers, using the linear combinations described in the previous sections, into agreement with the experimentally determined free energies. Figure 6.2 compares the experimentally determined free energies of both Atgts (red) and f3Atgts (blue) endmembers with the values calculated from linear combinations using equilibria 6.4 and 6.10. Also shown is the Mg endmember from the HP'11 database as well as the alumina-Tschermak endmember from Padrón-Navarta et al. (2013) for comparison. It is to note that all values in figure 6.2 are based on an $m = 17$ polysome, e.g. the stoichiometry normalised to 34 tetrahedral positions. In general, adding Al alone decreases the free energy of the endmember. The new Atgts endmember has a lower free energy than the endmember obtained from Padrón-Navarta et al. (2013) due to the substitution of 34 Al pfu instead of only 8 Al pfu. The substitution of ferric Fe, however, shifts the free energy to higher values (compare also section 5.4). The experimentally obtained data are generally higher than the values derived from linear combinations using endmember equilibria 6.4 and 6.10.

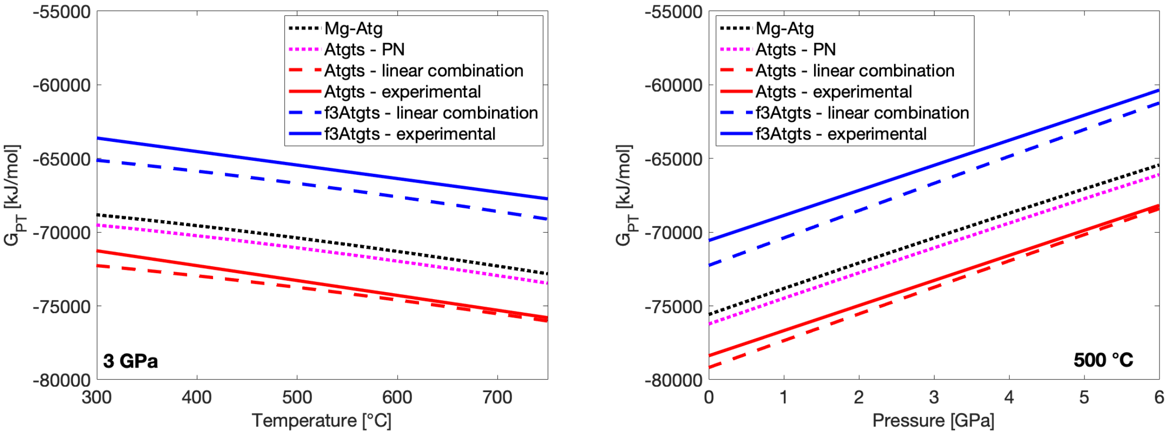

(a) **(b)**

Figure 6.2: a: Gibbs free energy G_{PT} of various Atg endmembers ($m = 17$ polysomes). Shown are both hypothetical values based on linear combinations (dashed lines) as well as experimentally determined values (solid lines). Atgts-PN is the alumina-Tschermak endmember from Padrón-Navarta et al. (2013). Adding Al decreases the free energy whereas Fe^{3+} substitution results in a higher free energy. b: The P-dependence of the same endmembers as in figure 6.2a.

The molar volume at ambient conditions obtained from the linear combination yields 182.8 J bar^{-1} mol^{-1} for the Atgts and 182.3 J bar^{-1} mol^{-1} for the f3Atgts endmember, which transforms to 1828 cm^3 mol^{-1} and 1823 cm^3 mol^{-1}, respectively. Experimental volumes were obtained for both endmembers in the range of 3 - 5 GPa and are assumed to be constant, as it is expected that the compressibility and expansivity only have a minor effect on the volume in this pressure range. Hilairet et al. (2006) showed that the volume of antigorite and lizardite are close within errors and the two minerals behave similar with respect to pressure. Given the experimental uncertainties a volume of about 100 cm^3 mol^{-1} for all serpentine endmembers is used. This accounts for an $m = 17$ Atg volume of 1700 cm^3 mol^{-1} or 170 J bar^{-1} mol^{-1}. For both f3Atgts and Atgts consequently a difference of about 12 J bar^{-1} mol^{-1} to the volume determined from the linear combination is obtained. The value for c in equation 6.1 is thus set to -12. Although this value is a rough estimation, it will be shown that this value is able to reproduce data obtained from experiments and natural samples.

To correct the entropies obtained from the linear combination the configurational entropy is used because this should be the main source of difference with the experimental determinations. Based on equation 5.31 the configurational entropy of an $m = 17$ polysome is 455.3 J K^{-1} mol^{-1} for both f3Atgts and Atgts. From this value it directly follows that

$b = -455.3$ in equation 6.1. The negative sign results from the fact that the free energy decreases with increasing configurational entropy according to $G = H - TS$. For the alumina-Tschermak endmember of Padrón-Navarta et al. (2013) the b term was also determined based on the configurational entropy but was incorrectly implemented with a positive sign. This results in an increase in the free energy, which causes a flatter T-dependence in the Al content of Atg, as shown later in figure 6.4.

The constant term a in equation 6.1 was finally refined to obtain the best fit between the Perple_X model and the experimental data with respect to mineral composition and phase relations. The final G^{diff} terms used to implement the new endmembers into Perple_X are given by

$$G^{diff}(\text{Atgts}) = 1.57 \times 10^6 - 455.3T - 12P \tag{6.11}$$

and

$$G^{diff}(\text{f3Atgts}) = 1.78 \times 10^6 - 455.3T - 12P, \tag{6.12}$$

where T is the temperature in kelvin and P is the pressure in bar.

For both Atgts and f3Atgts additional Fe^{2+}-Mg exchange takes place on the octahedral site. Similar to the Fe^{2+}-Mg endmembers (equilibrium 6.3), the Fe^{2+}-Mg exchange is calculated based on Tlc and fTlc without an additional G^{diff} term. A summary of all antigorite endmembers used with Perple_X is given in table 6.1.

Table 6.1: Antigorite endmembers used in the Perple_X model. The ideal stoichiometric formula is given as $M_{48}T_{34}O_{85}(OH)_{62}$, with M octahedral and T tetrahedral sites. Given are the abbreviations as used in Perple_X, the stoichiometry of the phase as well as the definition based on other endmembers.

phase	stoichiometry	combination	G^{diff} J/mol
Atg	$Mg_{48} \mid Si_{34} \mid O_{85}(OH)_{62}$	real entity	-
fAtg	$Fe^{2+}{}_{48} \mid Si_{34} \mid O_{85}(OH)_{62}$	Atg - 16 Tlc + 16 fTlc	-
Atgts	$Mg_{31}Al_{17} \mid Al_{17}Si_{17} \mid O_{85}(OH)_{62}$	17Clin - 37Br - $\frac{51}{2}$En + 17Ol	$1.57\times10^6-455.3T-12P$
fAtgts	$Fe^{2+}_{31}Al_{17} \mid Al_{17}Si_{17} \mid O_{85}(OH)_{62}$	Atgts- $\frac{496}{48}$ Tlc + $\frac{496}{48}$ fTlc	$1.57\times10^6-455.3T-12P$
f3Atg	$Mg_{31}Fe^{3+}_{17} \mid Al_{17}Si_{17} \mid O_{85}(OH)_{62}$	Atgts - $\frac{17}{2}$ Cor + $\frac{17}{2}$ Hem	$1.78\times10^6-455.3T-12P$
ff3Atg	$Fe^{2+}_{31}Fe^{3+}_{17} \mid Al_{17}Si_{17} \mid O_{85}(OH)_{62}$	fAtgts - $\frac{17}{2}$Cor + $\frac{17}{2}$ Hem	$1.78\times10^6-455.3T-12P$

6.2 Solid solution model

The solid solution model used with the new endmembers is written as a macroscopic 2 site reciprocal model. The 6 Atg endmembers shown in table 6.1 are used. The two reciprocal equations between these endmembers are given as

$$\begin{aligned} &Mg_{2.824}Si_2O_5(OH)_{3.647}+\tfrac{48}{31}\ Fe_{1.824}AlAlSiO_5(OH)_{3.647} = \\ &\qquad Fe_{2.824}Si_2O_5(OH)_{3.647} + \tfrac{48}{31}\ Mg_{1.824}AlAlSiO_5(OH)_{3.647} \end{aligned} \tag{6.13}$$

$$\begin{aligned} &Mg_{2.824}Si_2O_5(OH)_{3.647}+\tfrac{48}{31}\ Fe_{1.824}Fe^{3+}AlSiO_5(OH)_{3.647} = \\ &\qquad Fe_{2.824}Si_2O_5(OH)_{3.647} + \tfrac{48}{31}\ Mg_{1.824}Fe^{3+}AlSiO_5(OH)_{3.647}. \end{aligned} \tag{6.14}$$

The contribution of the resulting activity coefficient terms based on relations outlined in Gudmundsson and Wood (1995) is small with respect to the free energy of the reaction. Furthermore, non-ideal mixing terms on individual Atg sites result in very little improvement between the model and the experimental data, mainly because the concentrations of both Al and Fe^{3+} are relatively low over the range of interest. Therefore, mixing between all endmembers is taken as ideal.

Consistent with a completely disordered model, site assignments were performed on the 2 sites M and T. M is the octahedral site that is occupied by divalent cations Mg and Fe^{2+} as well as trivalent cations Fe^{3+} and Al^{VI}. Fe^{2+}-Mg exchange is independent of the trivalent cations. The later however defines the trivalent cation content on the T site in order to achieve charge balance. T is the tetrahedral site on which Al-Si mixing occurs. The complete solid solution model is given in appendix A.

6.3 Aluminium content of Atg compared with other studies

The Al content in antigorite and the effect of Al on Atg stability, can be determined through a free energy minimisation using the new Atgts model described in the previous sections. The results can be compared to the previous Atgts model of Padrón-Navarta et al. (2013). Fluid saturated PT-pseudosections in the Fe^{3+}-free system FMASH (i.e. by excluding ferric Fe endmembers) are calculated with the Atgts solid solution model from Padrón-Navarta et al. (2013) (fig. 6.3a) and the new solid solution model derived above (fig. 6.3b). The bulk composition is taken from sample Al06-44 (Padrón-Navarta et al., 2013). A list of all solid solution models used is given in table A.1. The dashed horizontal lines in figure 6.3 indicate the isobaric profiles along which the Al content in Atg is calculated in figure 6.4.

The general phase relations as well as the dehydration temperature of Atg are similar for both models (fig. 6.3). The Atg dehydration in the Al-bearing system is about 20 °C higher at a given pressure compared to the Al-free system (shown by the fine dashed lines). Differences between the two models are observed in the PT-dependence of the Atg Al content (fig. 6.4), which becomes less P-dependent but has a steeper T-dependence in the new model compared to the model of Padrón-Navarta et al. (2013).

A smaller P-dependence is in agreement with the experimental data obtained from Liz-bearing experiments at 3 and 5 GPa, which do not differ from natural samples equilibrated at only 1.2 GPa (Schwartz et al., 2013) as shown in figure 3.5. As a consequence the maximum Al content moves from 0.5 GPa to 2 GPa. This results also in changes in the Chl-free fields observed at pressures below 2.5 GPa, which are caused by the Al content of Atg increasing to the point where Chl is consumed. The extent of these fields depends strongly, however, on the amount of Al in the starting material.

The steeper T-dependence in Atg Al content is also in better agreement with the experimental data and natural samples. The experimental data used to derive the model of Padrón-Navarta et al. (2013) were all collected at temperatures above 600 °C (fig. 6.4). The Al contents in Atg in these experiments, however, are all similar to the natural starting materials used. This is not surprising, since it could be shown in the current study that Al in Atg does not reequilibrate at different temperatures within experimental time scales. The same is observed in the study of Merkulova et al. (2016) as their Al contents in Atg are similar to the starting material at all temperatures. Therefore it is not possible to determine the T-dependence of Al from Atg experiments. The evolution of Al in Atg as a function of temperature can, however, be studied in natural samples, e.g. in the Schistes lustrés (Schwartz et al., 2013). The new model reproduces these natural data from Schwartz et al. (2013) and shows a similar T-dependence to the experimental data for Liz in the current study (fig. 6.4). The overall Al content in Atg as calculated with Perple_X, however, is slightly lower with respect to the Liz-bearing experiments at the highest temperature. This results from the fact that these Liz experiments have a high ferric Fe content, which was not considered in this model.

It should be noted that the Al content of Atg must change during dehydration due to the formation of Chl, which should act to stabilise Atg at slightly higher temperatures. The fact that the Al content cannot change during the experiments means that the effect of Al on the stability field of Atg cannot be determined experimentally, whereas thermodynamic determinations are likely to be more accurate. The T-dependence of the Al content in Atg in equilibrium with Chl could be used as a very effective geothermometer as the new model shows that this relationship is not strongly P-dependent. High pressure experimental results for the Al content of Atg in figure 6.4 simply reflect the Al contents of the natural Atg starting materials employed. The Atg starting material used in this study for example, Zer_1701, does not contain Chl, which means it must have equilibrated at temperatures equal or greater than approximately 550 °C. This is well in agreement with peak metamorphic conditions obtained for the Zermatt ophiolite (Angiboust et al., 2009). The sample used in the study of Padrón-Navarta et al. (2010) appears to have the highest Atg Al content possible before dehydration and must therefore have equilibrated at temperatures above 600 °C. Also this is in agreement with experimentally determined peak conditions for Cerro del Almirez (Padrón-Navarta et al., 2010).

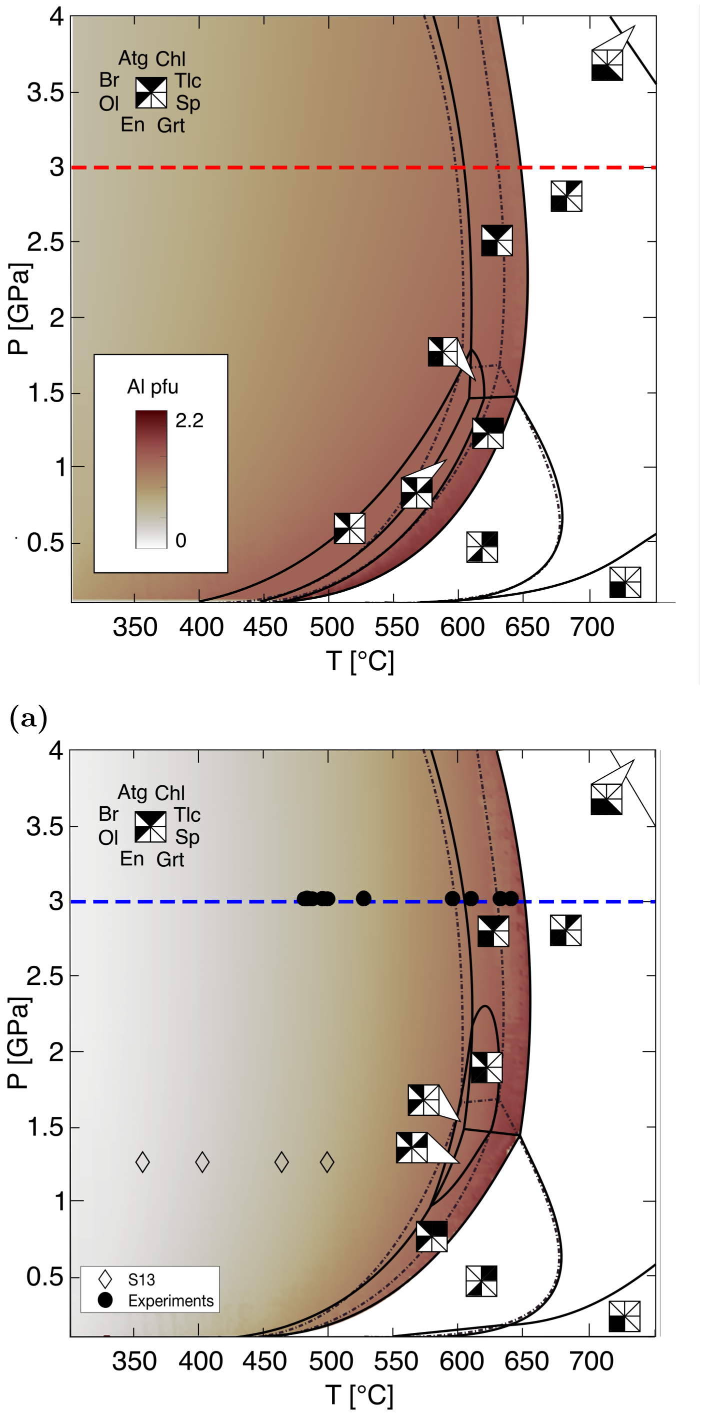

(a)

(b)

Figure 6.3: Phase relations in the FMASH system with bulk composition of Al06-44 in (Padrón-Navarta et al., 2013). a: Solid solution model from Padrón-Navarta et al. (2013), b: New solid solution model (this study). Black dotted lines indicate MSH phase relations. Experimental points are from Liz experiments at 3 GPa (this study). S13 are data from (Schwartz et al., 2013). Blue and red dashed lines are isobaric profiles used in figure 6.4. Shading marks Al content in Atg. Colour code is equal in both figures.

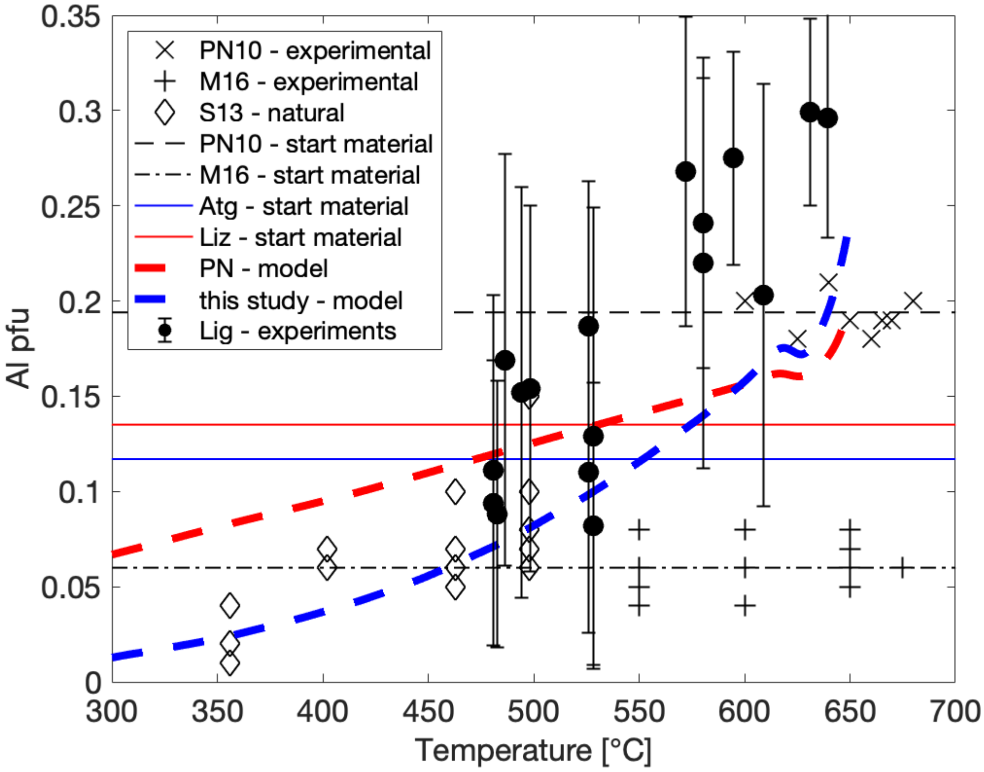

Figure 6.4: The Al content in Atg as a function of T at 3 GPa calculated along the path shown in figure 6.3. Wiggles in the range of 610 - 650 °C result from changes in mineralogy at the onset of Atg dehydration. The Al content from the new model can be approximated by an error function given as $\mathrm{Al}^{\mathrm{tot}} = 1 + \mathrm{erf}\left[\frac{T-999.726}{410.622}\right]$. Filled data points indicate measurements from Liz-bearing experiments. Other data points are Atg samples derived from: S13: natural samples from Schwartz et al. (2013), M16: experiments Merkulova et al. (2016), PN10: experiments Padrón-Navarta et al. (2010) used to derived the model in Padrón-Navarta et al. (2013). Experimental Atg samples do not differ in composition from the respective natural starting materials but are plotted at the conditions reported for the experiments.

6.4 The effect of Fe^{3+} and oxygen fugacity on serpentinite phase relations

This study is the first to present data on the ferric Fe content of Atg as a function of pressure, temperature and $f(O_2)$. The experimentally obtained results are compared here to the model results obtained using Perple_X, which also allows the effect of $f(O_2)$ on the stability of Atg and other minerals in serpentinites to be determined. Figure 6.5 shows a pseudosection calculated for the Zer_1701 bulk composition (table 2.2) assuming that H_2O-fluid is the only fluid component and taking its fugacity from the CORK EoS (Holland and Powell, 1991). The phase relations in figure 6.5 are divided into 4 different coloured regions, which mark the coexistence of Fe-metal (grey), at the lowest $f(O_2)$, Mgt (green) at intermediate $f(O_2)$ and Hem (orange) at the highest $f(O_2)$. In the white region no accessory Fe-rich phases are present. The thick black solid lines mark the limits of the stability fields of the hydrous minerals, Br, at the lowest temperature, Atg between 600 - 700 °C and Chl just below 800 °C. The coloured vertical lines mark specific temperatures at which the $Fe^{3+}/\Sigma Fe$ ratio of antigorite has been extracted and is compared as a function of $f(O_2)$ to the model obtained in chapter 5 in figure 6.7.

The variation in $f(O_2)$ affects the stability of Fe-rich accessory phases but this in turn also affects the stability of other phases. In the Fe-metal and Hem stability fields, the majority of the bulk Fe is partitioned in the respective Fe-phase. Thus, the silicate fraction is enriched in Si with respect to MgO+FeO. As a consequence Si-rich phases such as Tlc and Opx become stable together with Atg. The highest Fe content in the silicate fraction is observed in the phase fields with Mgt and where no oxide is stable. The silicates in this region are depleted in Si with respect to MgO+FeO, which allows Br to be stable at low temperatures. In the absence of accessory Fe-rich phases Opx is formed only at the onset of Atg dehydration.

The diagram also allows the effects of different substitutions on the stability of Atg to be understood. In the Fe-metal field at the lowest $f(O_2)$ all bulk Fe is reduced to metal and the silicate fraction is essentially ferrous and ferric Fe-free. Atg is thus left with only its Al content influencing its stability field, which is raised compared to the MSH system by approximately 20 °C. With increasing $f(O_2)$ Fe-metal becomes oxidised to FeO as the field without an Fe-rich accessory phase (white) is reached. All FeO is partitioned into the silicate phases, which decreases the Atg stability field by approximately 30 °C. The combined effects of Al and FeO on Atg stability, therefore, cancel out and Atg dehydrates at almost the same temperature as in the MSH system, which is comparable to most of the experimental values (table 3.1). At higher $f(O_2)$, as the Hem field is reached, Fe is partitioned increasingly into Hem and Atg contains less ferric and ferrous Fe. This leads eventually to the formation of Fe-free Al-bearing Atg, which has the same dehydration temperature as in the Fe-metal field. The main effects on the Atg stability field, therefore, arise from FeO and Al rather than Fe_2O_3.

The boundary between the Mgt-free (white) and Mgt-bearing (green) fields marks the point where Atg reaches the highest ferric Fe content for a given temperature and becomes saturated in this component. The Atg ferric Fe content at this boundary increases with temperature but as discussed in chapter 7 this increase is insufficient to remove significant amounts of Mgt from the assemblage with increasing temperature. For a fixed $Fe^{3+}/\Sigma Fe$ ratio of the bulk composition it is, therefore, not possible to pass from the Mgt-bearing to Mgt-free field with increasing temperature unless only very small amounts of Mgt are present. However, in natural samples (Debret et al., 2014, 2015) and in experiments (Merkulova et al., 2016, 2017) Mgt is reported to disappear with increasing temperature in serpentinite assemblages. While it is difficult to explain this observation as it would appear to require a decrease in the bulk $Fe^{3+}/\Sigma Fe$ ratio, figure 6.5 shows one possibility as to how this might occur. The FMQ buffer, shown in figure 6.5 by the red dashed line, indeed passes from the Mgt-bearing to Mgt-free fields with increasing temperature. As many buffering equilibria have oxygen fugacities that are parallel to FMQ, one possibility is that in serpentinite assemblages where Mgt disappears the $f(O_2)$ is in fact buffered by some other equilibrium and the bulk $Fe^{3+}/\Sigma Fe$ ratio is not constant. As will be examined in chapter 8 the presence of carbon in natural or experimental samples might provide one explanation for Mgt disappearance. In experiments performed with graphite furnaces hydrogen permeability through the metal capsules might be sufficient to achieve this. Regardless of how this occurs, however, the disappearance of Mgt with temperature appears to be only possible if the relative $f(O_2)$ is buffered rather than the bulk $Fe^{3+}/\Sigma Fe$ ratio being constant.

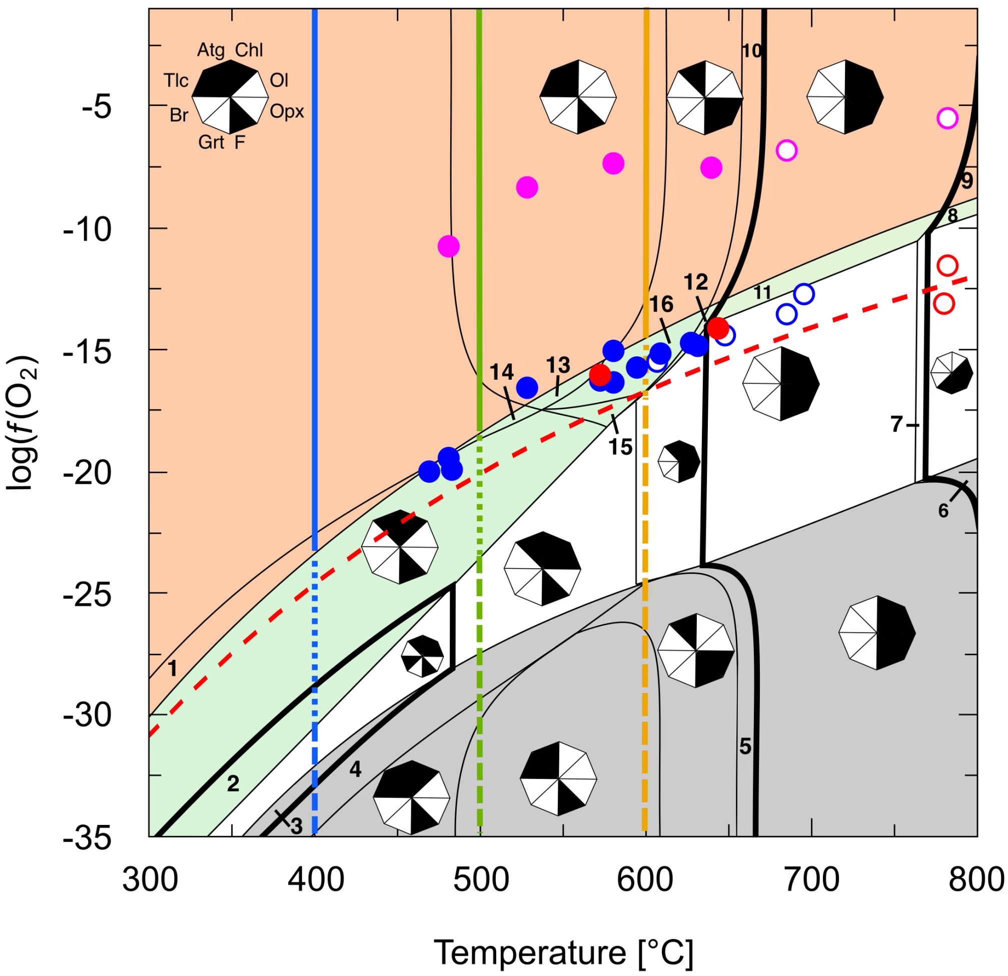

Figure 6.5: T-$f(O_2)$ pseudosection for the Zer_1701 bulk composition at 3 GPa. The CORK EoS was used to compute the H_2O-fluid. Colours show the stable Fe-phase as: orange = Hem, green = Mgt, grey = Fe-metal, colourless: no additional Fe-oxide. The coloured paths mark the isogrades shown in figure 6.7. The red dashed line marks the FMQ equilibrium. Points are buffered and unbuffered Liz- and Atg-experiments. Not shown are carbon-bearing experiments and experiments buffered with Fe-metal. Magenta: Hem-bearing, blue: Mgt-bearing, red: no oxide. Open symbols mark dehydration of Serp. Fields labelled with numbers consist of the assemblages 1: Chl+Atg+Hem+F, 2: Chl+Mgt+Atg+Br+F, 3: Chl+Atg+Br+Fe+F, 4: Chl+Atg+Fe+F, 5: Ol+Opx+Atg+Fe+F, 6: Opx+Ol+Grt+Fe+F, 7: Opx+Chl+Ol+Grt+F, 8: Opx+Ol+Mgt+Grt+F, 9: Opx+Ol+Grt+Hem+F, 10: Opx+Ol+Atg+Hem+F, 11: Opx+Chl+Ol+Mgt+F, 12: Opx+Ol+Atg+Mgt+F, 13: Tlc+Mgt+Atg+F, 14: Chl+Tlc+Mgt+Atg+F, 15: Mgt+Atg+F, 16: Atg+Ol+Opx+Mgt+F.

As described in chapter 3, two experiments V1139 and V1140 were performed on the Liz bulk composition in the presence of Fe-metal at approximately 500 °C and 600 °C respectively. In the higher temperature experiment Liz was absent indicating a significant decrease in the stability field of Liz at $f(O_2)$ compatible with the stability of Fe-metal. The most likely explanation for this is that the fluid phase at these conditions is no longer pure H_2O, as assumed in figure 6.5, but contains a significant component of H_2, which destabilises Atg in a process which could be termed redox dehydration. To compute this redox dehydration, the fluid in the calculation shown in figure 6.6 was allowed to be a mixture of H_2O and H_2 depending on the $f(O_2)$, with the H_2 fugacity calculated with a modified Redlich-Kwong EoS (Santis et al., 1974). As a consequence a strong decrease in the Atg stability field at low $f(O_2)$ resulting from the reduction of the H_2O in Atg to an H_2-rich fluid is observed. The experiments buffered with Fe-metal are shown as yellow points in figure 6.6 at their respective temperature. The $f(O_2)$, however, was estimated from the mineral assemblage and is probably only applicable locally around the metal flakes. As shown in figure 3.2a and 3.2b the Fe-metal is surrounded by FeO and it has to be assumed that equilibrium was not achieved throughout the capsule. Nonetheless, in the higher temperature experiment conducted at 592 °C Liz was absent throughout the assemblage, well below the typical dehydration temperature, which seems to imply that it is an overall effect of the low $f(O_2)$. The truncated field where Fe-metal and Atg are stable is in reasonable agreement with the experimental data on the Liz-bearing samples, implying that the H_2 model provides a good explanation for these observations. Such redox dehydration is a poorly explored phenomena but could be important for understanding volatile cycles in the lower mantle, where Fe-metal might be stable (Frost and McCammon, 2008) or in the mantles of the Moon and Mars where the $f(O_2)$ might be much lower than that in the Earth's mantle (Herd et al., 2002; Herd, 2003; Papike et al., 2004).

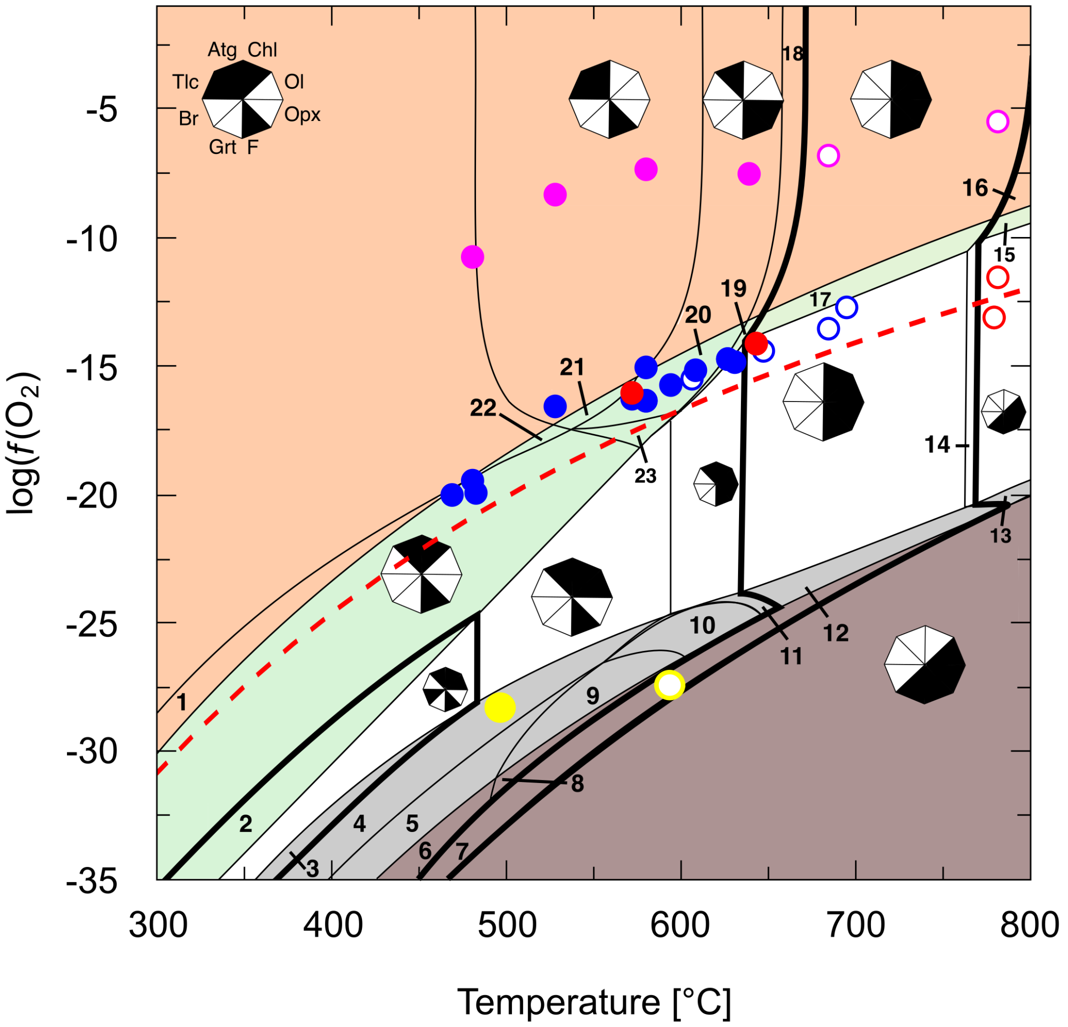

Figure 6.6: The same pseudosection as in figure 6.5 with H_2. The fluid is computed with a hybrid EoS, using the CORK EoS for H_2O (Holland and Powell, 1991) and the MRK EoS for H_2 (Santis et al., 1974). Points are buffered and unbuffered Liz- and Atg-experiments without carbon. Magenta: Hem-bearing, blue: Mgt-bearing, red: no oxide, yellow: Fe-metal. Open symbols mark dehydration of Serp. Fields labelled with numbers consist of the assemblages 1: Chl+Atg+Hem+F, 2: Chl+Mgt+Atg+Br+F, 3: Chl+Atg+Br+Fe+F, 4: Chl+Atg+Fe+F, 5: Chl+Tlc+Atg+Fe+F, 6: Chl+Tlc+Atg+Fe+H_2, 7: Opx+Chl+Ol+Fe+H_2, 8: Tlc+Atg+Fe+H_2, 9: Tlc+Atg+Fe+F, 10: Opx+Atg+Fe+F, 11: Opx+Ol+Atg+Fe+F, 12: Opx+Chl+Ol+Fe+F, 13: Opx+Ol+Grt+Fe+H_2, 14: Opx+Chl+Ol+Grt+F, 15: Opx+Ol+Mgt+Grt+F, 16: Opx+Ol+Grt+Hem+F, 17: Opx+Chl+Ol+Mgt+F, 18: Opx+Ol+Atg+Hem+F, 19: Opx+Ol+Atg+Mgt+F, 20: Atg+Ol+Opx+Mgt+F, 21: Tlc+Atg+Mgt+F, 22: Chl+Tlc+Atg+Mgt+F, 23: Atg+Mgt+F.

Figure 6.7 shows the Atg $Fe^{3+}/\Sigma Fe$ ratio along the isotherms in figure 6.5. The paths are solid in the Hem-stability field and dotted in the Mgt-stability field. At an $f(O_2)$ below Mgt-stability they are shown as dashed lines. At a fixed temperature an increase in $f(O_2)$ results in an increase in the relative ferric Fe content of Atg. The Perple_X model reproduces the sigmoidal relations obtained in chapter 5 from individual equilibria applied to the experimental data. In contrast to the results described in chapter 5, however, in the Perple_X calculation the effects resulting from the coexistence of different Fe oxides can be assessed. While the sigmoidal trend is observed in the absence of Mgt, the presence of Mgt significantly decreases the $f(O_2)$-dependence by buffering the $Fe^{3+}/\Sigma Fe$ ratio, particularly below 600 °C. At 600 °C, the presence of Opx eliminates this effect. The red dashed line corresponds to the data at 600 °C obtained from the model outlined in chapter 5 showing overall excellent agreement with the Perple_X model and therefore also very good agreement with the experimental data. Differences at high $f(O_2)$ are due to the use of a fixed total Fe content in the model from chapter 5.

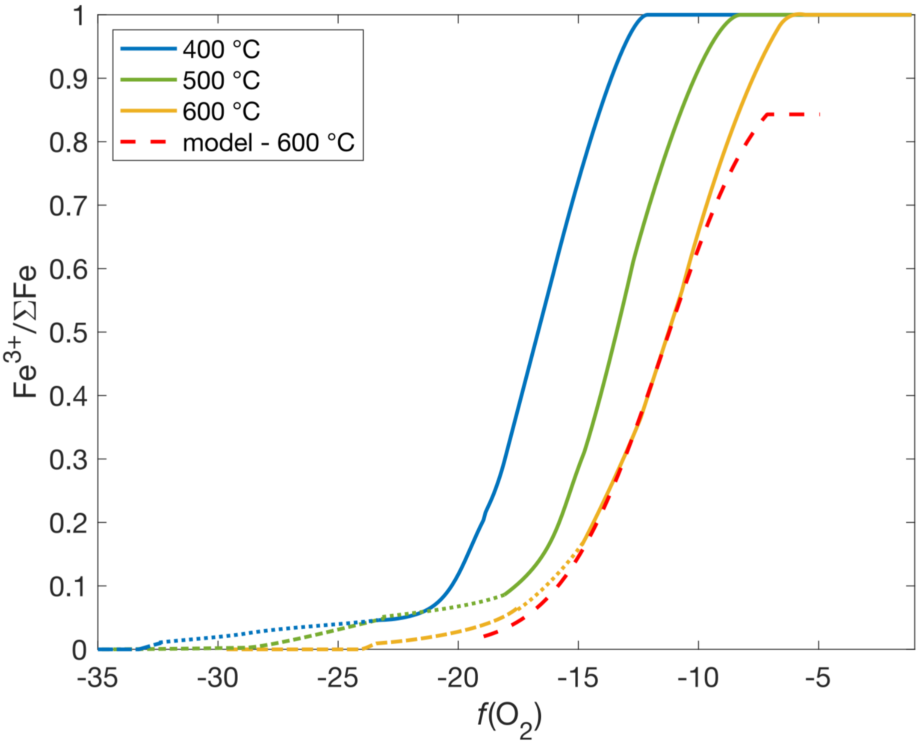

Figure 6.7: The $Fe^{3+}/\Sigma Fe$ ratio of Atg for different temperatures derived from the Perple_X model along isotherms shown in figure 6.5. Dashed = Mgt, dotted = no additional Fe-phase, solid = Hem. The red dashed line shows values obtained from a single equilibrium in chapter 5, which is in very good agreement with the experimental data.

In conclusion the Al content in Atg is buffered by the presence of Chl and increases with increasing temperature. The new Al model shows a slightly stronger T-dependence of the Atg Al content compared to the previous model from Padrón-Navarta et al. (2013) but is in much better agreement with the compositions of Atg in natural Chl-bearing assemblages. It also follows more closely the trend determined from Liz-bearing experiments where reequilibration of the Al content can occur in experimental time scales. As the Al content in serpentine is not found to be P-dependent the T-dependence could be used as an effective thermometer for natural samples.

Thermodynamic calculations show that Al and ferrous Fe have small positive and negative effects, respectively, on the thermal stability field of Atg. The ferrous Fe effect is in agreement with the experimental data of Merkulova et al. (2016) but it is doubtful that experiments can yield useful information on the phase relations of Al-bearing Atg due to the slow reaction kinetics. In chapter 3 phase equilibria results indicated that there might be a modest stabilisation of Liz at high $f(O_2)$. The thermodynamic modelling performed in this chapter support that this also occurs for Atg but it also shows that it results from a decrease in the ferrous Fe content as more Fe partitions into Hem, rather than an effect of ferric Fe.

The thermodynamic calculations performed in the previous chapter assumed a fixed total Fe content in Atg. In this chapter, however, the development of a model that can be used in a global minimisation indicates that the Fe content of Atg changes in a closed system as a function of PT-$f(O_2)$. The $f(O_2)$, in particular, has a major impact on the Fe speciation. At both high and low $f(O_2)$ Fe partitions strongly into either Hem or Fe-metal, respectively, leaving pure Mg-silicates behind. Si-rich phases, such as Tlc and Opx become stable together with Atg due to a higher Si/(Fe+Mg) ratio in the silicate fraction. In the more geologically relevant mid range of $f(O_2)$ there are fields of Mgt-bearing and Mgt-free Atg. The boundary between these fields can be determined for the first time using the results from this study because it depends on the maximum limit of Fe^{3+} that can be substituted into Atg at a given temperature before Mgt becomes stable. As will be discussed in the next chapter, this limit increases very slightly with temperature and can cause Mgt to be absorbed into Atg, as observed in natural and experimental assemblages. However, the amount of Mgt that can be absorbed in this way is too small ($\ll$1 wt%) to explain these previous observations. A more likely explanation is that the disappearance of Mgt from some assemblages results from buffering of the $f(O_2)$ by additional equilibrium and thus changing the bulk $Fe^{3+}/\Sigma Fe$ ratio in experiments rather than keeping it constant.

A further pseudosection calculation where the fluid phase is a two-component H_2O-H_2 mixture shows that at low $f(O_2)$ Atg becomes unstable due to reduction of H_2O to an H_2-rich fluid. These findings are strongly supported by the experimental data reported in chapter 3 on Liz coexisting with Fe-metal. This redox dehydration process might be particularly important for the stability of hydrous minerals in the lower mantle where Fe-metal might be present (Frost and McCammon, 2008).

7 The redox state of serpentinites in subduction zones

The thermodynamic model for ferri-alumina-Tschermak antigorite derived in the previous chapters is used here to examine how the redox state of serpentinites in subduction zones will evolve with pressure and temperature. In addition to the H_2O content, serpentinisation also raises the ferric Fe content of the lithosphere (Evans, 2008). The subduction of the resulting oxidised material has been proposed to be one explanation for the generally more oxidised nature of arc magmas and the mantle wedge (Debret et al., 2014, 2015). However, it remains unclear through which processes serpentinites end up influencing the redox state of the mantle wedge. In the forearc region of the mantle wedge serpentinites will form upon infiltration of H_2O released from pores and clays in the sediment layer (fig. 1.1) and its redox state might be strongly affected by this hydration process. If this region is then dragged to deeper levels through coupling with the slab, its oxidation state might influence the processes of metasomatism and arc melting.

In addition to ferric Fe subducted serpentinites also carry volatiles such as C and S into subduction zones (Frost, 1985; Kodolanyi et al., 2012). The redox state of the slab may influence the speciation of volatile components leaving the slab once serpentine starts to dehydrate. The presence of serpentine in subduction zones thus has the potential to create important redox fronts in the mantle, which have only been poorly explored in the past.

In the first part of this chapter, the relationship between the $Fe^{3+}/\Sigma Fe$ ratio in antigorite and the magnetite stability is examined. As seen in the previous chapter, ferric Fe is hosted in both phases. The $f(O_2)$ of a serpentinite assemblage, however, will be influenced by whether magnetite is present and how Fe is distributed between the coexisting phases. Although the general phase relations including magnetite can be computed with Perple_X through a free energy minimisation (see chapter 6), an understanding of the equilibria which actually control the stability of magnetite and the $f(O_2)$ is important not only to ensure that such minimisations are correct but also to examine other factors that may influence the redox conditions.

In the second part of this chapter mass balance calculations are used to evaluate changes in ferric Fe partitioning in subduction zones. Serpentinites formed at the ocean floor generally contain magnetite as a result of a disequilibrium process (Evans, 2008), which is, nonetheless, one of the main oxidation processes affecting the lithosphere: The serpentinisation process transforms olivine and pyroxene to the serpentine minerals chrysotile and lizardite at near surface temperatures. These hydrous minerals, however, contain less Fe^{2+} than the anhydrous phases. At the low temperatures at which they form the diffusion of the excess Fe^{2+} back into untransformed anhydrous silicates is too slow to account for all the excess Fe and a separate Fe-oxide is formed. Although the Fe is initially Fe^{2+}, wüstite (FeO) is not stable at these conditions and instead Fe^{2+} reacts with H_2O to produce magnetite and H_2. As a consequence of Fe oxidation the $f(O_2)$ is very low and beside 2 - 3 wt% magnetite most serpentinites additionally contain Fe-metal and -sulfides (Frost, 1985; Kodolanyi et al., 2012). One intriguing aspect is that there are a number of studies that report the disappearance of magnetite from serpentinite assemblages at high pressures and temperatures for both experimental and natural samples. Although Merkulova et al. (2016) used a serpentinite starting material prepared with an additional 5 wt% synthetic magnetite, for example, they did not find magnetite in any of the run products at $T \geq 550\,°C$, which could result from serpentine incorporating more Fe^{3+}. Using X-ray absorption near edge structure (XANES) spectroscopy measurements Debret et al. (2015) and Merkulova et al. (2017) reported a significant decrease in the bulk $Fe^{3+}/\Sigma Fe$ ratio, in natural and experimental serpentine assemblages, respectively, with increasing temperature. This could also in part be attributed to the loss of magnetite. Debret et al. (2015), however, also propose that prograde metamorphic reactions result in a decrease in the $Fe^{3+}/\Sigma Fe$ ratio of serpentinites, potentially due to the loss of an oxygen-rich sulphur- and/or carbon-bearing fluid phase that may ultimately oxidise the mantle wedge. It is, therefore, crucial to be able to estimate the $f(O_2)$ of serpentinites during subduction in order to determine the speciation and redox state of volatile components leaving the slab. The PT-variation of the $f(O_2)$ of a serpentinite assemblage is determined here for different bulk $Fe^{3+}/\Sigma Fe$ ratios. These relations allow the redox state of volatiles leaving the slab to be determined for various serpentinite bulk compositions. The data also allow to determine how ferric and ferrous Fe are distributed between the other coexisting phases. It is thus possible to directly evaluate the processes that result in the loss of magnetite. The same type of calculation is then performed for a hydrated peridotite bulk composition. This allows to examine phase relations and mineral compositions in the mantle wedge. Serpentinites formed in the mantle wedge above a subducting slab would be likely magnetite-free and to calculate the $f(O_2)$ of such an assemblage requires thermodynamic data for a ferric Fe component in serpentine.

7.1 The stability of oxides in subduction zone serpentinites

In order to understand how $f(O_2)$ affects the stability of magnetite and the Fe^{3+} content of antigorite it is useful to explore the effects of the equilibria used to calibrate the free energy of the ferri-alumina-Tschermak antigorite endmember ($Mg_{1.824}Fe^{3+}|AlSi|O_5(OH)_{3.647}$). Three mineral equilibria (equilibria 5.4 - 5.6) including the phases clinochlore (Clin), fayalite (Fa), forsterite (Fo), enstatite (En), brucite (Br), magnetite (Mgt), hematite (Hem) and ferri-alumina-Tschermak antigorite (f3Atgts) were used, which are written as

$$\text{A:} \qquad \mathrm{Mgt + Clin = \tfrac{1}{2}\ Fo + \tfrac{1}{2}\ Fa + 2\ f3Atgts + \tfrac{6}{17}\ Br}$$

$$\text{B:} \qquad \mathrm{\tfrac{2}{3}\ Mgt + \tfrac{1}{6}\ O_2 + Clin = \tfrac{1}{2}\ En + 2\ f3Atgts + \tfrac{6}{17}\ Br}$$

$$\text{C:} \qquad \mathrm{Fa + Fo + Clin + \tfrac{1}{2}\ O_2 = \tfrac{3}{2}\ En + 2\ f3Atgts + \tfrac{6}{17}\ Br.}$$

For $f(O_2)$ conditions above the hematite-magnetite (HM) equilibrium reactions A and B are rewritten according to equilibria 5.9 and 5.10 as

$$\text{A:} \qquad \mathrm{\tfrac{3}{2}\ Hem + Clin = \tfrac{1}{4}\ O_2 + \tfrac{1}{2}\ Fo + \tfrac{1}{2}\ Fa + 2\ f3Atgts + \tfrac{6}{17}\ Br}$$

$$\text{B:} \qquad \mathrm{Hem + Clin = \tfrac{1}{2}\ En + 2\ f3Atgts + \tfrac{6}{17}\ Br.}$$

It should be noted that for convenience of calculation these equilibria are written in terms of Br rather than free H_2O, which avoids the use of an equation of state to calculate the H_2O fugacity, but makes no difference to the position of the equilibria. Following from figure 5.6, the $Fe^{3+}/\Sigma Fe$ ratio of Atg is now also calculated for the equilibria A and B at 500 °C and 600 °C at 3 GPa (fig. 7.1). At these conditions the HM equilibrium is at ΔFMQ+1.5 and ΔFMQ+2, respectively. The reactions that are $f(O_2)$-independent are shown as dashed lines. The total Al content of Atg, being solely a function of temperature is 0.085 and 0.169 Al pfu (eq. 5.37), whereas the total Fe content of Atg is fixed to an assigned value. The composition of all coexisting silicates is correlated to the Mg# of Atg via equations 4.3, 4.4 and 4.5.

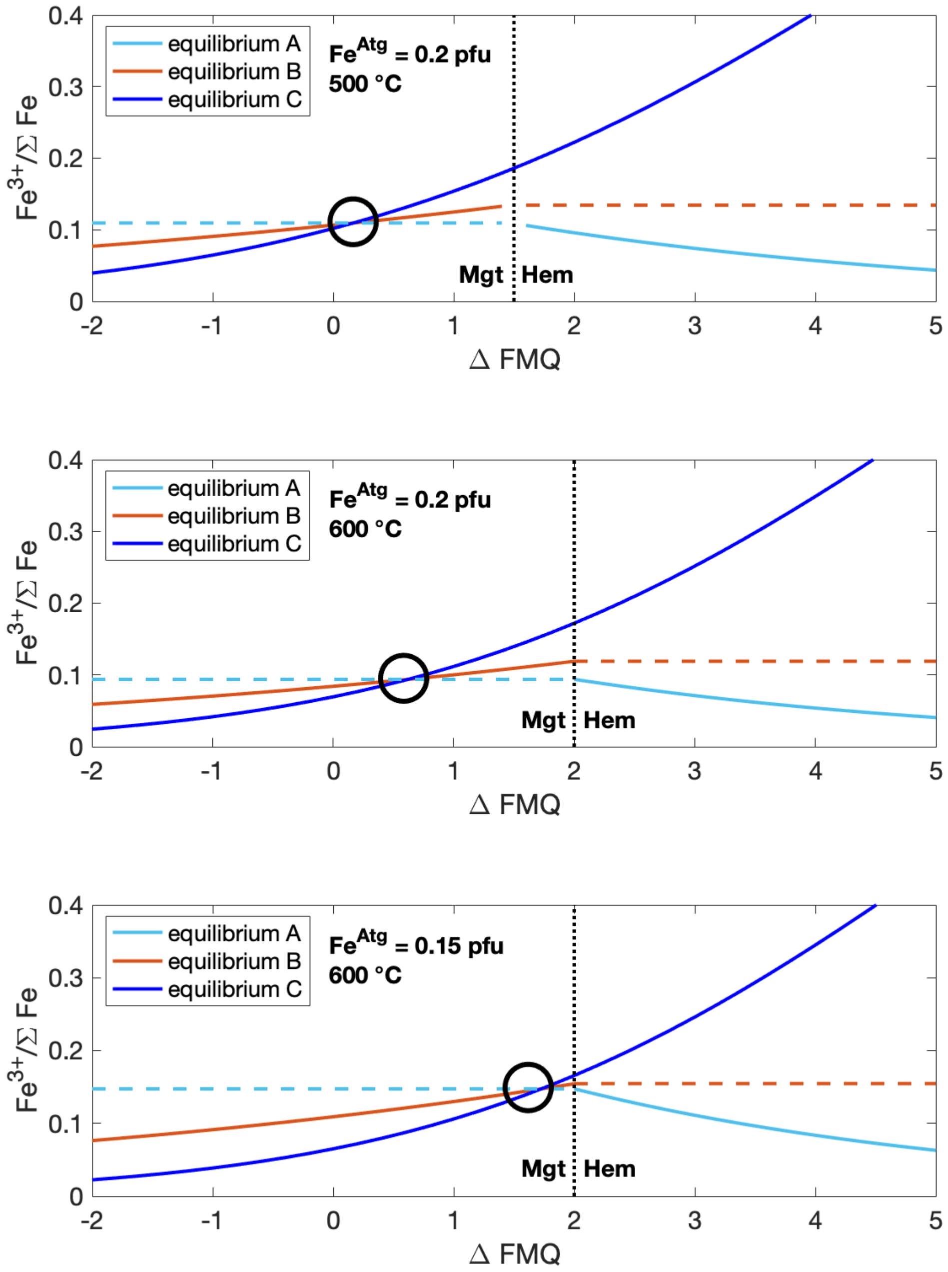

(a)

(b)

(c)

Figure 7.1: The $Fe^{3+}/\Sigma Fe$ ratio calculated for Atg as a function of $f(O_2)$ for the three equilibria A, B and C at 3 GPa. a: 500 °C and 0.2 Fe pfu in Atg. b: 600 °C and 0.2 Fe pfu in Atg. c: 600 °C and 0.15 Fe pfu in Atg. The HM equilibrium is indicated by a vertical dotted line. The $f(O_2)$-independent branch of equilibria A (ΔFMQ <HM) and B (ΔFMQ >HM) is indicated by a dashed line. Black circles mark conditions at which all reactions results in the same $Fe^{3+}/\Sigma Fe$ ratio.

Reaction A defines the ferric Fe content in Atg in the presence of Ol and Mgt for a given total Fe content in Atg. The redox reaction is given by

$$[\mathrm{Fe}^{2+}\mathrm{Fe}^{3+}{}_2]^{Mgt} = \tfrac{1}{2}\,[\mathrm{Fe}^{2+}{}_2]^{Ol} + 2\,[\mathrm{Fe}^{3+}]^{f3Atgts}. \tag{7.1}$$

This equilibrium is independent of $f(O_2)$ but is dependent on the total Fe content and the temperature as shown in figure 7.1. It is important to note that for a fixed total Fe content in Atg, such as 0.2 Fe pfu shown in figure 7.1a and 7.1b, the Atg equilibrium $Fe^{3+}/\Sigma Fe$ ratio, indicated by the black circle, decreases from 0.11 to 0.09 as the temperature increases from 500 °C to 600 °C. This decrease in ferric Fe content in Atg seems to imply that it is not possible to decrease the proportion of Mgt with temperature as it was proposed for natural assemblages by Debret et al. (2015). This is in contrast with the findings in the previous chapter where it was shown that the maximum ferric Fe content in Atg increases with temperature and thereby might cause Mgt to disappear. However, in natural samples the bulk composition remains constant rather than a component in a single phase as it is assumed here. Consequently, the Fe contents of all phases change with P, T and $f(O_2)$ due to PT-dependent Fe^{2+}-Mg exchange and changes in the Mgt mode. Thus, if more Mgt is formed at higher $f(O_2)$ in a particular bulk composition, the Fe contents in the other phases will decrease due to mass balance constraints. This is illustrated in figure 7.1b and 7.1c, where equilibrium A predicts an increase in the Atg $Fe^{3+}/\Sigma Fe$ ratio with decreasing total Fe content. It is thus possible for the relative $Fe^{3+}/\Sigma Fe$ ratio of Atg to increase further with $f(O_2)$ in equilibrium with Mgt by simply changing the proportions of the oxide. To assess this, however, mass balance constraints are required.

As soon as Mgt reacts to Hem with increasing $f(O_2)$ the equation becomes dependent on $f(O_2)$ and the redox reaction is written as

$$\tfrac{3}{2}\,[\mathrm{Fe}^{3+}{}_2]^{Hem} + \tfrac{1}{2}\,\mathrm{O}^{2-} = \tfrac{1}{4}\,\mathrm{O}_2 + \tfrac{1}{2}\,[\mathrm{Fe}^{2+}{}_2]^{Ol} + 2\,[\mathrm{Fe}^{3+}]^{f3Atgts}. \tag{7.2}$$

An increase in the $f(O_2)$ thus forms Hem by the consumption of Fe^{3+}-bearing Atg and Ol. This results in a decrease the $Fe^{3+}/\Sigma Fe$ in Atg at fixed PT and total Fe in Atg. However, this equilibrium is again dependent on the total Fe content in Atg. In a mass balanced system, as more Hem is formed, the total Fe content in Atg decreases, which would lead to an increase in its $Fe^{3+}/\Sigma Fe$ ratio.

Reaction B is described with the half reactions in the Mgt- and Hem-bearing regimes as

$$\tfrac{2}{3}\ [\mathrm{Fe}^{2+}\mathrm{Fe}^{3+}{}_2]^{Mgt} + \tfrac{1}{6}\ \mathrm{O}_2 = 2\ [\mathrm{Fe}^{3+}]^{f3Atgts} + \tfrac{1}{3}\ \mathrm{O}^{2\text{-}} \tag{7.3}$$

$$[\mathrm{Fe}^{3+}{}_2]^{Hem} = 2\ [\mathrm{Fe}^{3+}]^{f3Atgts}. \tag{7.4}$$

In contrast to reaction A, the Mgt-bearing reaction B is dependent on $f(O_2)$. An increase in $f(O_2)$ shifts the equilibrium to higher absolute Fe^{3+} content in Atg by the consumption of Mgt. As the temperature increases from 500 °C to 600 °C, the equilibrium Atg Fe^{3+} content decreases. Above the HM-transition, however, the equilibrium becomes independent of $f(O_2)$, resulting in a constant $Fe^{3+}/\Sigma Fe$ ratio.
The third reaction, C, does not involve Mgt or Hem and can be written in the form

$$[\mathrm{Fe}^{2+}{}_2]^{Ol} + \tfrac{1}{2}\ \mathrm{O}_2 = 2\ \mathrm{Fe}^{3+f3Atgts} + \mathrm{O}^{2\text{-}} \tag{7.5}$$

An increase in $f(O_2)$ decreases the Fa-component in Ol while the Atg Fe^{3+} content increases. A change in the total Fe content in Atg does not affect equilibrium C (compare also fig. 5.7a), where as an increase in temperature decreases the Atg $Fe^{3+}/\Sigma Fe$ ratio as seen also for equilibria A and B. The basis of this T-dependence is the Atg Al content, which increases with temperature as it is buffered by coexisting Chl. If Al compositions were low enough to not have Chl present then $Fe^{3+}/\Sigma Fe$ ratios in Atg would presumably be higher. This can, however, not be calculated with the equilibria proposed here.

Since the three equilibria shown here are used to describe the same system, they have to result in the same $Fe^{3+}/\Sigma Fe$ ratio at fixed conditions. This is only observed at one single point in each graph in figure 7.1, marked by a black circle. With decreasing total Fe content in Atg, this circle moves towards higher $f(O_2)$. It thus follows that although an increase in $f(O_2)$ leads to a higher $Fe^{3+}/\Sigma Fe$ ratio, in a system with a fixed composition the total Fe content in Atg and all coexisting silicates would in fact decrease. Such a relation is indeed observed in the experiments: At very high $f(O_2)$, e.g. Ru-RuO_2 buffer, high $Fe^{3+}/\Sigma Fe$ contents are measured in Liz, whereas the Fe# is extremely low in comparison with experiments conducted at lower $f(O_2)$ (fig. 5.8b).
In conclusion, the absolute $Fe^{3+}/\Sigma Fe$ ratio in Atg is influenced by the total Fe content in the silicates and also by the temperature. With increasing temperature the equilibria

examined cause a decrease in the Atg $Fe^{3+}/\Sigma Fe$ ratio, outside of the Hem field. In a system with a fixed bulk composition the total Fe content of Atg will be affected by the formation of Mgt or Hem. To further evaluate how the proportion of oxides affects the compositions of other phases in a particular system, mass balance equations are needed in order to keep the bulk composition constant.

7.2 The $f(O_2)$ of a serpentinite assemblage determined through a mass balance calculation

During subduction serpentinites are subject to changing PT conditions. Although the element partitioning between coexisting phases will change upon prograde subduction, the sum of each element will remain constant unless material is either added or removed by a fluid. If additionally no redox reactions take place involving other components, such as C or S, the bulk $Fe^{3+}/\Sigma Fe$ ratio will also remain constant. Ferric Fe is partitioned between Mgt and Atg, whereas the Chl and Px ferric Fe contents will be smaller (Dyar et al., 1992; Canil and O'Neill, 1996).

In the following calculation a mass balance is performed on a fixed serpentinite bulk composition (Zer_1701) in order to constrain the mineral compositions and proportions at given PT conditions and bulk $Fe^{3+}/\Sigma Fe$ ratios. The $f(O_2)$ of the assemblage arising from the Fe distribution is then determined from the compositions of coexisting minerals.

The Zer_1701 bulk composition contains 97 wt% antigorite and 3 wt% magnetite (recalculated for major elements considered here: SiO_2 = 39.91 wt%, FeO = 6.96 wt%, Al_2O_3 = 2.42 wt%, MgO = 36.83 wt%, H_2O = 13.89 wt%). The ferric Fe content was calculated from the FeO content by changing bulk $Fe^{3+}/\Sigma Fe$ ratio between 0.01 and 0.4. Imposing fluid saturated conditions in the calculation with 0.1 wt% H_2O ensures that the assemblage also contains minor amounts of Ol, Px and Chl but remains Atg-rich. At temperatures >600 °C the water content was gradually increased to 14 wt% at 700 °C. In this way a continuous dehydration of Atg and the final Atg-out at 690 °C is achieved, in agreement with the phase relations shown in figure 6.6. The mineral compositions are constrained following the description in chapter 5: Br and Mgt are pure endmembers. The Mg# of Chl, Px and Ol are correlated to the Mg# of Atg via equations 4.3, 4.4 and 4.5. The Mg# in Atg is calculated using only the ferrous Fe content. The octahedral site in Atg is filled by Mg, Fe^{2+}, Fe^{3+} and Al^{VI} and summed to 2.824. The octahedral trivalent cations are charge balanced by Al^{IV}. Si is thus given by $2 - Al^{IV}$. The total Al content in Atg is a function of temperature according to equation 5.37. In Chl the Al content is fixed to 1.6 Al pfu for a total of 10 cations pfu, in agreement with the experimental data (table B.2). At significantly low bulk $Fe^{3+}/\Sigma Fe$ ratios the proportion of Mgt is zero and the $f(O_2)$ is calculated based on equilibrium C (eq. 5.6). By increasing the bulk $Fe^{3+}/\Sigma Fe$ ratio Mgt becomes stable. The $f(O_2)$ in subducted serpentinised peridotite that contains Fe^{2+}-bearing Ol, Px and Mgt can be simply calculated from the *fayalite − ferrosilite − magnetite*-equilibrium (FFM),

$$\begin{array}{lcccccccc} \text{FFM:} & 2\ Fe_2SiO_4 & + & \frac{1}{3}\ O_2 & = & Fe_2Si_2O_6 & + & \frac{2}{3}\ Fe_3O_4. \\ & \text{Fa} & & O_2 & & \text{Fs} & & \text{Mgt} \end{array} \tag{7.6}$$

In the presence of Mgt both equilibrium C and FFM are constrained to give the same $f(O_2)$. Similarly, at high $Fe^{3+}/\Sigma Fe$ ratio the $f(O_2)$ reaches the HM buffer. If so, equilibrium C is constrained to give the respective $f(O_2)$ and Hem is added as an additional phase. An example is shown in figure 7.2, which is calculated at 3.24 GPa and 600 °C. As the $Fe^{3+}/\Sigma Fe$ ratio increases the $f(O_2)$ follows the black arrows, which indicate the Mgt-free (labeled 1), the Mgt-bearing (labeled 2) and the Mgt+Hem (labeled 3) regimes. Equilibrium C, shown by the red curve, crosses the FFM equilibrium (blue curve) at a bulk $Fe^{3+}/\Sigma Fe$ ratio of 0.09, which marks the value where Mgt becomes stable. In the Mgt-bearing regime the amount of Mgt increases with the bulk $Fe^{3+}/\Sigma Fe$ ratio. The $Fe^{3+}/\Sigma Fe$ ratio of Atg increases more gradually than in Mgt-free regimes due to the buffering capacity of Mgt. The Hem regimes is reached at a bulk $Fe^{3+}/\Sigma Fe$ ratio of 0.35, which corresponds to an $f(O_2)$ of ΔFMQ+1.8. The Mgt content of the Zer_1701 serpentinite as Hem starts to form is approximately 3 wt%. Between a bulk $Fe^{3+}/\Sigma Fe$ ratio of 0.35 and 0.5 the proportion of Mgt decreases as Hem increases but the $f(O_2)$ remains buffered by the coexistence of Mgt and Hem. The $f(O_2)$ will only increase to above the HM equilibrium when all Mgt is consumed.

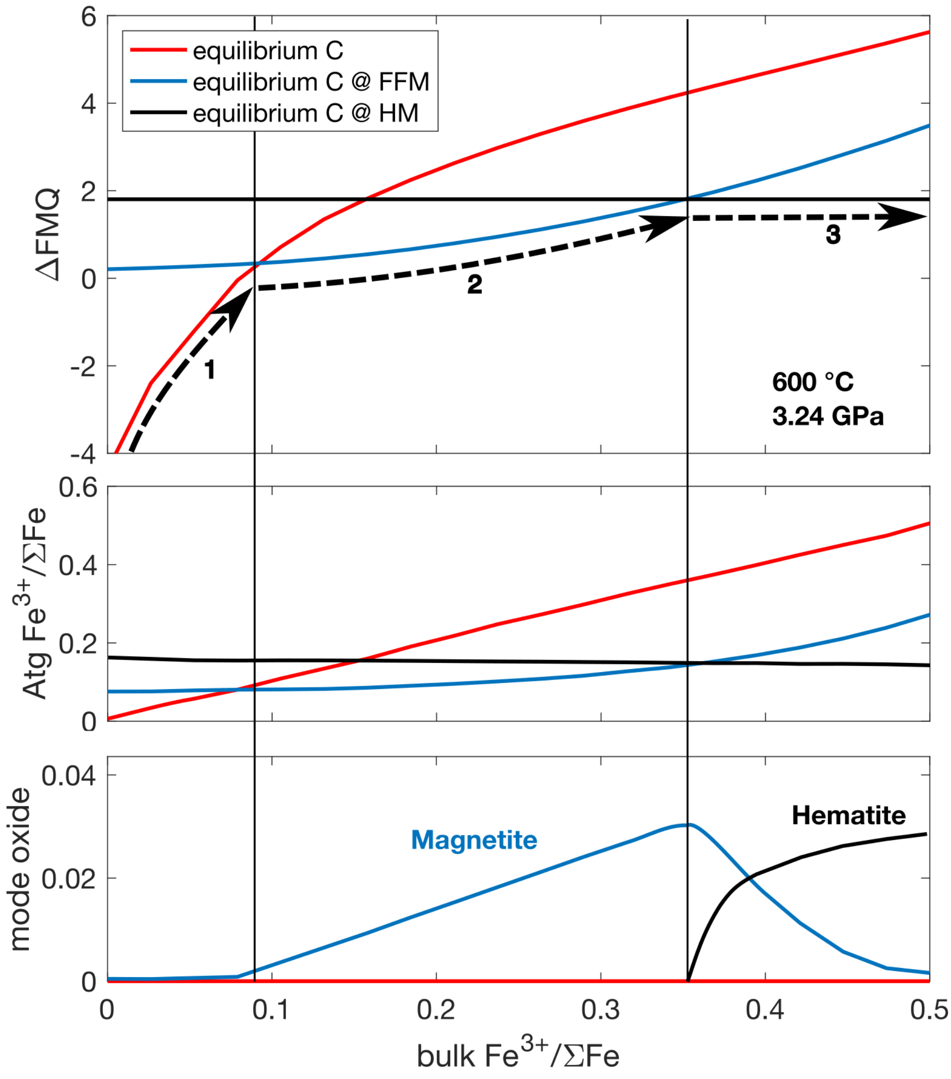

Figure 7.2: The results of mass balance calculations for a serpentinite composition with varying bulk $Fe^{3+}/\Sigma Fe$ ratio. For Atg the fully disordered model was used with the endmember Gibbs free energy derived in chapter 5. An increase in the relative ferric Fe content at fixed PT conditions leads to an increase in the $f(O_2)$ shown by the black arrow. Label 1, 2 and 3 mark the Mgt-free, Mgt-bearing and Mgt+Hem regime. The $f(O_2)$ is buffered at the respective mineral equilibrium.

In figure 7.3 the same calculation as described above is used to calculate the $f(O_2)$ within a serpentinite composition along a subduction zone PT-gradient. The gradient of the northern Honshu subduction zone (Syracuse et al., 2010) is employed. The calculation is performed for different bulk $Fe^{3+}/\Sigma Fe$ ratios. At temperatures below 500 °C Br can be stable in Px-free serpentinite assemblages. The $f(O_2)$ in such assemblages can be determined from

$$\begin{array}{lcccc} \text{D:} & Fe_2SiO_4 & + \; Mg_5Al_2Si_3O_{10}(OH)_8 & + \; \frac{1}{2}\, O_2 & + \; \frac{45}{17}\, Mg(OH)_2 = \\ & \text{Fa} & \text{Clin} & O_2 & \text{Br} \end{array}$$

$$\begin{array}{ccc} 2\; Mg_2SiO_4 & + \; 2\; Mg_{1.824}Fe^{3+}AlSiO_5(OH)_{3.647} & + \; 3\; H_2O, \\ \text{Fo} & \text{f3Atgts} & H_2O \end{array} \tag{7.7}$$

where the fugacity of H_2O is calculated based on the equation of state by Pitzer and Sterner (1995). The $f(O_2)$ values in the Br-bearing regime (dashed lines) are lower by about 2 log units compared to equilibrium C, which is used after Br has dehydrated. The dehydration of Br thus causes a significant jump in the $f(O_2)$. The $f(O_2)$ continues to increase quite strongly with temperature in the Mgt-free regime (equilibrium C). At a bulk $Fe^{3+}/\Sigma Fe$ ratio below 0.1 the Mgt-stability field is not reached before the onset of Atg dehydration. At a bulk $Fe^{3+}/\Sigma Fe$ ratio above 0.1 the $f(O_2)$ of the serpentinite assemblage remains essentially in the Mgt-stability field throughout subduction. However, for a bulk $Fe^{3+}/\Sigma Fe$ ratio above 0.3 Hem will start to form and the $Fe^{3+}/\Sigma Fe$ ratio is fixed at the HM buffer. As mentioned previously Mgt and Hem will continue to coexist. The Hem only regime is reached as soon as all Mgt is oxidised. However, for the calculated conditions even at a bulk $Fe^{3+}/\Sigma Fe$ ratio of 0.7 this point is not reached. As the majority of Atg-serpentinites have a bulk $Fe^{3+}/\Sigma Fe$ ratio between 0.2 and 0.6 (Iacovino et al., 2020; Debret et al., 2014, 2015; Mayhew and Ellison, 2020), the $f(O_2)$ will be quite narrowly constrained after the breakdown of Br between ΔFMQ−0.5 and ΔFMQ+2.

In the Mgt-stability field the $Fe^{3+}/\Sigma Fe$ ratio of Atg decreases with temperature and the proportion of Mgt increases. In the experiments of Merkulova et al. (2017) 5 wt% Mgt were added to the serpentine starting material but completely disappeared at temperatures above 550 °C. As shown in figure 7.3 the Mgt-free regime corresponds to a bulk composition with a $Fe^{3+}/\Sigma Fe$ ratio of less than 0.1 at an $f(O_2)$ below FMQ. Merkulova et al. (2017) propose that the $f(O_2)$ of their piston cylinder experiments was probably controlled by the graphite furnace linked by hydrogen diffusion through the walls of their metal capsules. They argue that this implies an $f(O_2)$ between FMQ and ΔFMQ−2. This is in good agreement with the Mgt-free regime as indicated in figure 7.3. Reduction by

H_2, therefore, provides the best explanation for the disappearance of Mgt from the assemblages produced in this previous study. On the basis of XANES measurements Merkulova et al. (2017) propose that the bulk serpentinite $Fe^{3+}/\Sigma Fe$ ratio sharply decreases to 0.2 at temperatures <700 °C, where all ferric Fe is in Atg due to the disappearance of Mgt. Such high bulk $Fe^{3+}/\Sigma Fe$ ratios are inconsistent with absence of Mgt as shown in the present study and most likely imply that the XANES measurements overestimate the bulk rock $Fe^{3+}/\Sigma Fe$ ratio.

In figure 7.3 two previous attempts at determining the $f(O_2)$ of a serpentinite assemblage are shown. The thermodynamic calculations of Piccoli et al. (2019) do not take explicit account of changes in Fe partitioning between phases and do not consider ferric Fe in Atg. Their model predicts the expected strong increase in $f(O_2)$ between conditions where Br is stable and those where Px forms. It nevertheless does not consider the fact that the $f(O_2)$ is dependent on the bulk $Fe^{3+}/\Sigma Fe$ ratio and thereby underestimates the $f(O_2)$ followed by the Mgt-bearing serpentinites. Maurice et al. (2020) calculated the $f(O_2)$ from experimentally produced serpentinite assemblages with an initial bulk $Fe^{3+}/\Sigma Fe$ ratio of 0.52. In agreement with the current model they found that Hem was formed in addition to Mgt. The $f(O_2)$ was, therefore, buffered at the HM equilibrium. The calculated $f(O_2)$, plotting above the HM buffer, is too high based on equilibria using only Hem and not considering the coexistence of both oxides. In order to oxidise all Mgt an additional significant amount of oxygen would be required. An $f(O_2)$ of approximately ΔFMQ+2 is, therefore, likely to be the highest value attained by natural serpentinite assemblages in subduction zones, as opposed to values of ΔFMQ+3 to ΔFMQ+4 proposed by Maurice et al. (2020).

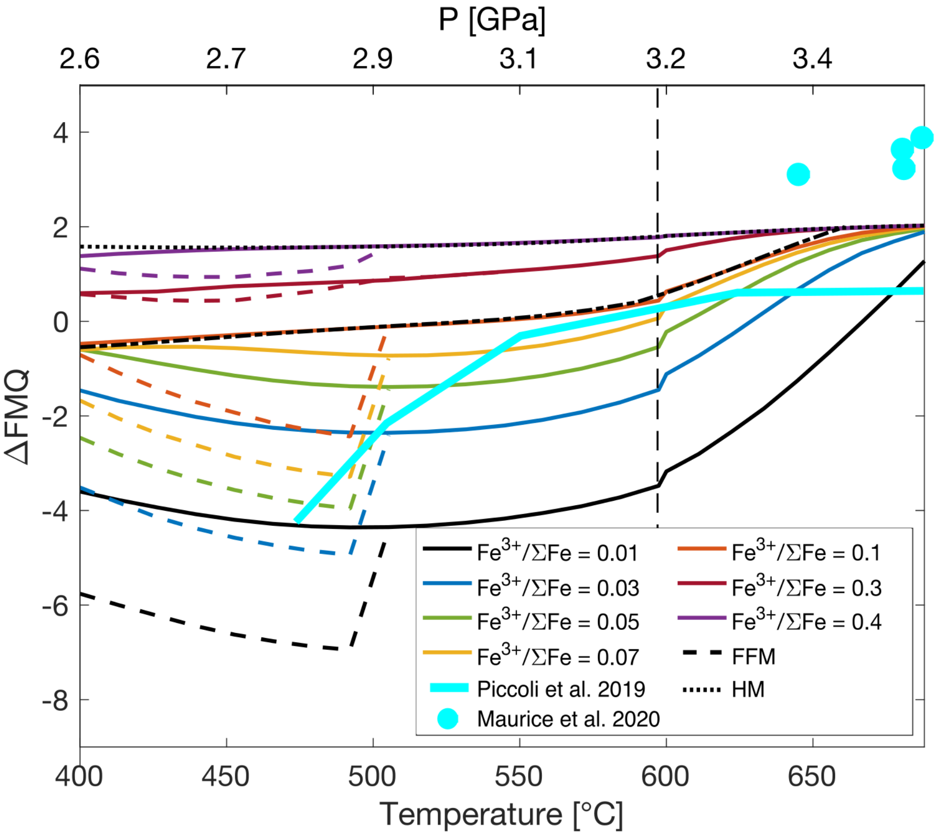

Figure 7.3: The $f(O_2)$ of a serpentinite calculated for different bulk rock $Fe^{3+}/\Sigma Fe$ ratios along a PT-gradient consistent with a subducting slab. At low temperatures it is possible for Br to be stable. Depending on the bulk composition the $f(O_2)$ becomes approximately 2 log units lower in Br-bearing assemblages with respect to Br-free assemblages. The Mgt stability field is reached for bulk $Fe^{3+}/\Sigma Fe$ ratios ≥ 0.1. The vertical dashed line marks the onset of Atg dehydration. The $f(O_2)$ for typical serpentinite $Fe^{3+}/\Sigma Fe$ ratios converge towards the HM buffer.

7.3 Implications for the mantle wedge

Serpentine is also formed in the mantle wedge above subducting slabs as a result of the dehydration of clay minerals in subducting sediments and expulsion of pore water (Rüpke et al., 2004). Serpentinised peridotite formed as a consequence of H_2O infiltration will not contain Mgt due to the elevated temperature with respect to ocean floor settings. Natural serpentinite samples associated with the mantle wedge indeed reveal no Mgt to be stable (Smith, 2010) at a bulk $Fe^{3+}/\Sigma Fe$ ratio of less than 0.03 as expected for typical upper mantle (Frost and McCammon, 2008). An experimental electrical conductivity study proposed that high conductivities in the mantle wedge may be caused by the formation of a Mgt-network that was found to form after the breakdown of Chl (Manthilake et al., 2016). However, the $f(O_2)$ was not well constrained in these experiments and Mgt was only formed once the hydrous mineral had broken down.

To examine the effect of mantle wedge serpentinisation on the $f(O_2)$ similar mass balance calculations, as described above, were performed for a peridotite composition at 1.5 GPa. A primitive upper mantle composition was used (Grove et al., 2006) and recalculated for the compositional space used in this study, i.e. SiO_2 = 43.6 wt%, total FeO = 7.2 wt%, Al_2O_3 = 3.85 wt%, MgO = 35.86 wt%, H_2O = 9.45 wt%. The water content was determined iteratively by adding water until the mass balance resulted in a free fluid phase.

The results of this calculation are shown in figure 7.4. At 600 °C and a bulk $Fe^{3+}/\Sigma Fe$ ratio of 0.03 the assemblage is comprised of approximately 68 wt% Atg, 10 wt% Chl, 19 wt% Px and 3 % Ol. In the calculation it is assumed that Chl and Px have $Fe^{3+}/\Sigma Fe$ ratios of 0.05 and 0.02, in accordance with previous studies (Dyar et al., 1992; Canil and O'Neill, 1996), although these values make very little difference to the calculation. Recalling that typical mantle is considered to have a $Fe^{3+}/\Sigma Fe$ ratio of less than 0.03 the $f(O_2)$ in the coldest parts of the mantle wedge are predicted to be at relatively reducing conditions of ΔFMQ-1 to ΔFMQ-2, which represents some of the most reduced regions in the top 100 km of the mantle. It is to note that the $f(O_2)$ depends also on the pressure. Serpentinisation near the top of the slab, which occurs at pressures $\geq$2 GPa, results in a drop of $f(O_2)$ of almost one log unit so that values $< \Delta$FMQ-2.5 are reached. However, with increasing temperature the $f(O_2)$ rises steeply after Atg starts to break down at approximately 600 °C and Mgt is formed in most compositions. This is in agreement with relatively high electrical conductivity measured in the mantle wedge region, which might be based on a free fluid but also on the presence of a Mgt network (Manthilake et al., 2016).

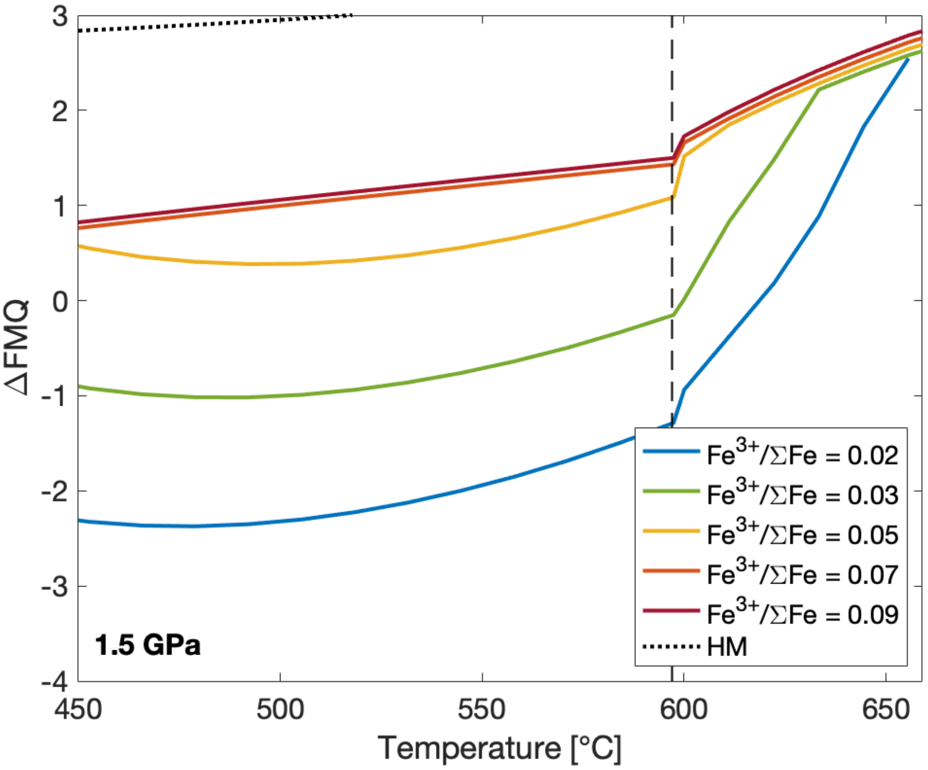

Figure 7.4: The $f(O_2)$ of a hydrated mantle wedge peridotite as a function of $Fe^{3+}/\Sigma Fe$ ratio at P=1.5 GPa. For typical mantle $Fe^{3+}/\Sigma Fe$ ratios of less than 0.03 reducing conditions are encountered in the coolest parts of the forearc region. With increasing pressure the $f(O_2)$ will drop to even lower values at a given temperature. Atg starts to break down at 600 °C causing a sharper increase in the $f(O_2)$ with respect to temperature.

8 Carbon and carbonates in subduction zones

The two most abundant volatile components in subduction zones are water and carbon. To understand how these volatiles are transported and cycled in the mantle it is important to determine their stable forms at different conditions. While water is mainly fixed in hydrous silicates during subduction and released through a series of dehydration reactions as an H_2O-rich fluid, carbon may have various forms depending on its environment. Carbon is transported as carbonate minerals, but organic material, that undergoes graphitisation upon subduction, is also present (Plank and Manning, 2019). While in the subducting sediment layer organic and inorganic remains of organisms are the major carbon source, carbonates precipitating from circulating ocean water is the main carbon source in the serpentinite layer, forming so called ophicarbonates (Driesner, 1993; Schwarzenbach et al., 2013; Clerc et al., 2014). Graphite can form through the reduction of carbonates if the $f(O_2)$ is sufficiently low (Kelemen et al., 2011; Galvez et al., 2013). The solubility of graphite in H_2O at subduction zone PT conditions is low and graphite thus effectively fixes carbon in the slab where it can be transported into the deeper mantle (Plank and Manning, 2019). The release of carbon from subducting serpentinites and from the overlying sediments occurs mostly by dissolution of carbonates in H_2O-rich fluids. Although the solubility of carbonate in H_2O is relatively low at subduction zone PT conditions (Manning et al., 2013), continuous fluid flow can result in a considerable net carbon flow from the slab towards the mantle wedge by direct dissolution of carbonates (Frezzotti et al., 2011; Ague and Nicolescu, 2014; Piccoli et al., 2016; Tian et al., 2019; Menzel et al., 2020). Therefore, the deep cycle of water and carbon are ultimately linked together.

In this chapter, the stability of carbonates within serpentinite assemblages is examined with respect to pressure, temperature and $f(O_2)$. This study provides the first detailed experimental investigation of the phase relations in an antigorite+carbonate assemblage, i.e. an ophicarbonate assemblage, at subduction zone conditions. The results are used to determine the composition of carbonates in equilibrium with dehydrating serpentinites and to examine the effects of carbonates on serpentinite stability.

Some experiments performed in this study contain a mixture of Ca-carbonate and graphite, from which the influence of $f(O_2)$ on the phase relations and mineral compositions can be constrained. In one experiment only graphite was added. When graphite is oxidised to CO_2 in a serpentine assemblage a pure CO_2-fluid forms rather than carbonates. The fugacity of CO_2 can therefore be determined at high PT conditions, which allows the results of extrapolated equations of state for CO_2 to be tested.

In the final section of this chapter estimates for the PT-$f(O_2)$ relationship in subducting serpentinites and in serpentinised portions of the mantle wedge are used to determine the redox stability of volatile-bearing phases containing carbon and sulphur.

8.1 Ophicarbonate phase relations

In a subset of multi-anvil experiments, antigorite (Atg) powder was mixed with 20 wt% pure $CaCO_3$ to form a typical ophicarbonate assemblage (table 3.1). The results indicate that the stability field of Atg decreases in the presence of $CaCO_3$ (fig. 3.15b). Using the phase relations in combination with mass balance calculations on the experimental charges and thermodynamic modelling it is possible to show that this effect results from the stabilisation of clinopyroxene (Cpx) with respect to orthopyroxene (Opx). This finding indicates that dissolved CO_2 or carbonate in the fluid phase is so minor that it has an undetectable effect on the topology of the phase diagram.

In the run products, pure Ca-carbonate is only observed to coexist with Atg at temperatures ≤550 °C in experiments V1079 and V1024. The Ca-carbonate is angular and does not indicate reaction with the surrounding Atg (fig. 3.1b). At temperatures above 550 °C dolomite (Dol) forms and appears to be the stable carbonate. At low temperature Dol is found in equilibrium with Chl and indicates that it formed upon Atg dehydration. The dehydration of Atg in the pure MSH system is given in equilibrium 1.10. This reaction, however, forms Opx, which is not stable in a Ca-bearing system with respect to Cpx. The Ca-Mg exchange between pyroxenes and carbonates is given as

$$\underset{\text{Cal}}{2\,\mathrm{CaCO_3}} + \underset{\text{Opx}}{\mathrm{Mg_2Si_2O_6}} = \underset{\text{Dol}}{\mathrm{CaMg(CO_3)_2}} + \underset{\text{Cpx}}{\mathrm{CaMgSi_2O_6}}. \tag{8.1}$$

Therefore, the Atg dehydration in the presence of $CaCO_3$ alters to

$$\begin{aligned}\underset{\text{Atg}}{Mg_{48}Si_{34}O_{85}(OH)_{62}} \quad + \quad \underset{\text{Cal}}{20\ CaCO_3} \quad = \\ \underset{\text{Ol}}{14\ Mg_2SiO_4} \quad + \quad \underset{\text{Cpx}}{10\ MgCaSi_2O_6} \quad + \quad \underset{\text{Dol}}{10\ MgCa(CO_3)_2} \quad + \quad \underset{H_2O}{31\ H_2O}\end{aligned} \tag{8.2}$$

Dol in the experimental run products is generally close to ideal stoichiometry $CaMg(CO_3)_2$ with a Ca#, given as molar $CaO/(CaO+MgO)$, of 0.5 (fig. 3.8). Three samples (V1062, V1076 and V1050) deviate from the ideal stoichiometry and have raised Ca-contents. Judging from previous studies (Franzolin et al., 2011; Hermann et al., 2016), these most likely represent intergrowth of Dol and metastable $CaCO_3$.

To better understand the phase relations and fluid compositions in the experiments, global free energy minimisation calculations were performed using Perple_X. The version 6.8 was used with the HP'11 database and the CORK fluid equation of state (Holland and Powell, 2011). A summary of phases and solid solution models employed is given in table A.1. In the Cpx, Opx and Amph solid solutions the Al-Tschermak endmember was excluded. The absence of Al in both Cpx and Opx is in agreement with chemical analyses that show generally low Al contents in these silicates at the pressures of interest. The absence of Al in these phases prevents Chl from disappearing due to Al repartitioning, which is consistent with the experimental data.

A pseudosection calculated for the Al06-44 serpentinite from Padrón-Navarta et al. (2013) plus 20 wt% $CaCO_3$ is shown in figure 8.1. The experimental ophicarbonate data are shown with symbols that indicate the main carbonate phases present. The major dehydration reactions, Atg-out and Chl-out, of the carbonate-free system (fig. 1.4a) are shown as dashed lines for comparison and labelled with A, and B.

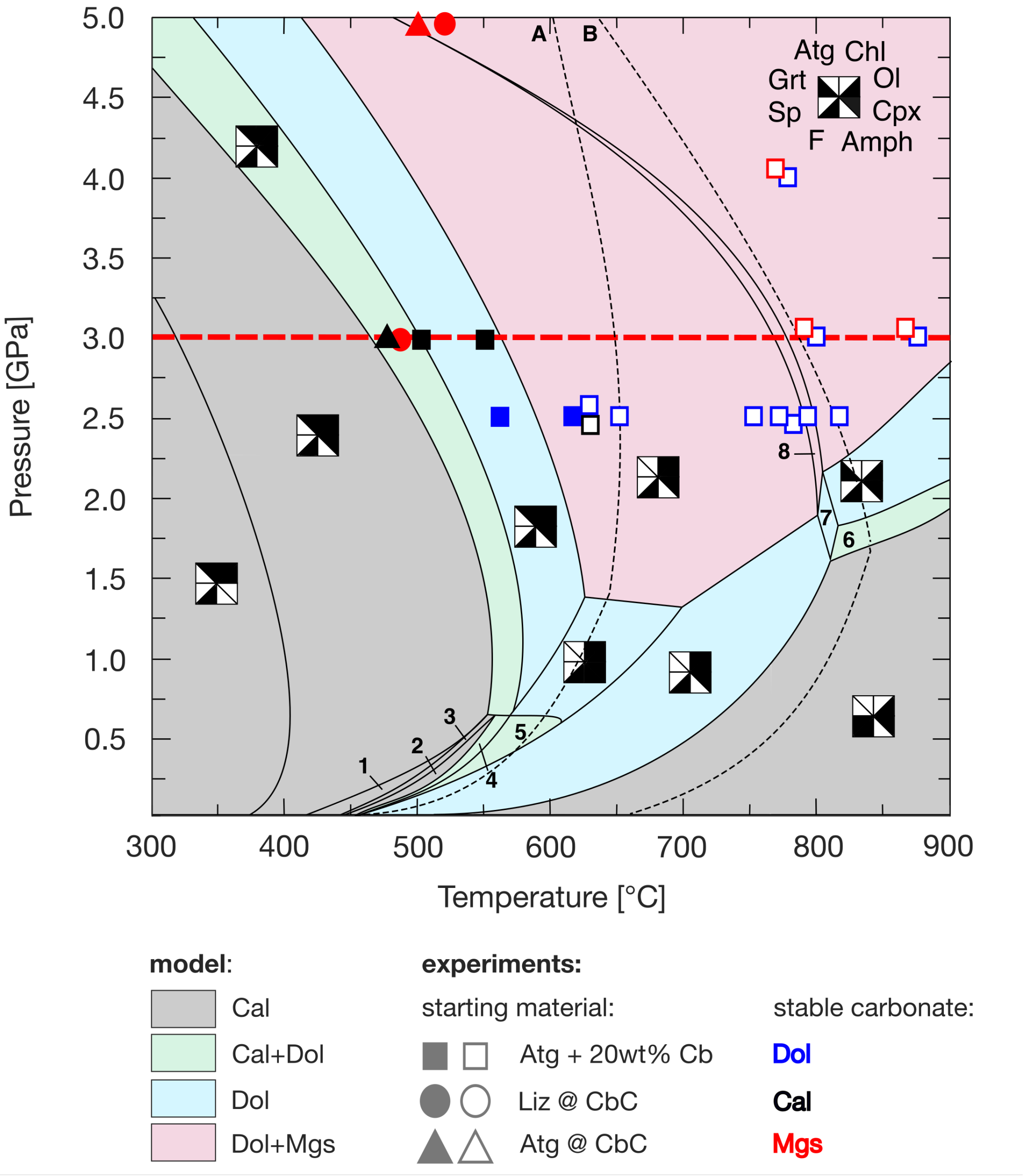

Figure 8.1: *PT*-pseudosection for a serpentinite with 20 wt% carbonate. Colour code indicates the type of carbonate in each stability field. Experiments are shown for comparison. Open symbols mark dehydration of Serp. Differences in the carbonate composition between the model and the experiments likely reflect slow reaction kinetics. The red line indicates the isobaric path along which data are extracted and shown in figure 8.2. Numbered fields contain the mineral assemblages 1: F Ol Atg Cpx Cal, 2: Chl F Amph Ol Atg Cal, 3: Chl F Atg Ol Dol Amph Cpx Cal, 4: Chl F Amph Ol Atg Cal Dol, 5: Chl F Amph Ol Cal Dol, 6: F Gt Ol Cpx Cal Dol, 7: F Chl Gt Ol Cpx Dol, 8: F Chl Gt Ol Cpx Dol Mgs. Dashed lines mark Atg-out (A) and Chl-out (B) in the carbonate-free system.

The phase abundances obtained from mass balance calculations are generally in good agreement with the model (fig. 8.2). The calculations indicate a shift of the Atg-out boundary to lower temperatures by almost 100 °C at 3 GPa. This is one of the largest shifts in Atg dehydration temperature observed for the addition of any component compared to the MSH system and results from the formation of Cpx upon dehydration of Atg as described above. Cpx has a constant Ca content over the whole T-range, as it is also observed in the experimental run products (table B.4). The calculation shows the same general trend of shifting carbonate composition towards higher Mg content with increasing temperature, as in the experiments. Since the mode of carbonates remains relatively constant, changes in carbonate compositions are achieved by changing the Cpx mode. However, the discrete change in carbonate composition appears in many experiments at temperatures far above the temperature where it would be expected from the calculation, indicating that reaction 8.2 is retarded due to slow reaction kinetics. Slow kinetics of cation exchange that prevent the Al content of Atg from reequilibrating in experiments have also been described in chapters 4 and 5. This likely explains inconsistencies between the model and the proportion of Atg in experiments, particularly for those experiments performed at temperatures ≤630 °C and at pressures below 3 GPa. However, this was found not to be the case for experiments on Liz, implying that it reacts faster and can equilibrate in experimental time scales.

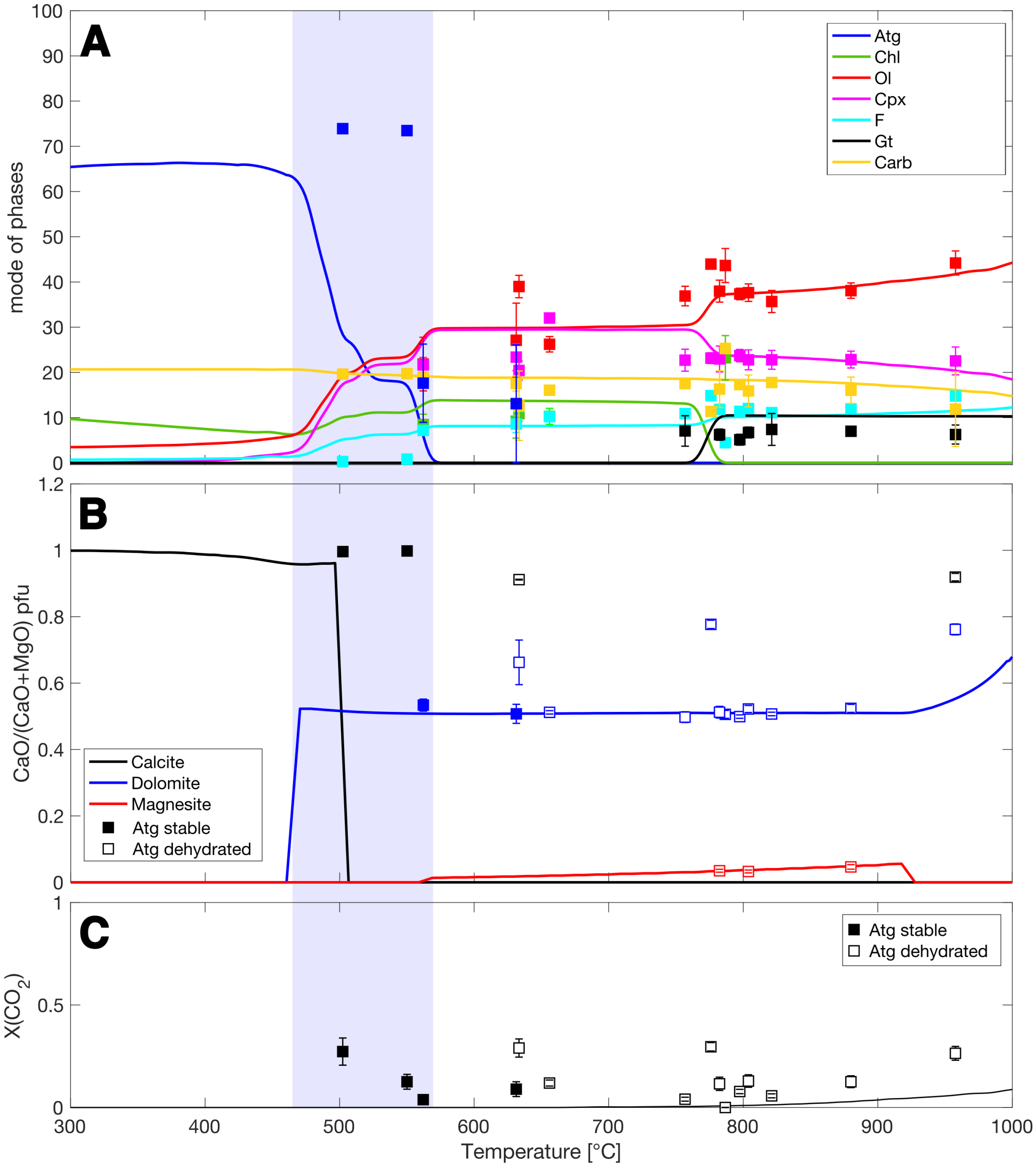

Figure 8.2: Results obtained from Atg+Cb experiments (symbols) and Perple_X energy minimisation (lines). a: Modes of all stable phases shown as a function of temperature. Experimental data are based on mass balance calculations (section 2.5.1). Atg observed at T>600 °C likely reflects slow reaction kinetics. Blue rectangle marks the divariant Atg-out in the Perple_X model and is in good agreement with experimental data. b: The composition of the carbonate as a function of temperature. c: The fluid composition given as X(CO_2). Experimental data are based on iterative fluid calculation during mass balance (section 2.5.1). The Perple_X calculations indicate even lower CO_2 content in the fluid as obtained from mass balance calculations. Open symbols in b and c mark Atg-dehydration.

In several experiments the $f(O_2)$ was buffered by adding a mixture of graphite+ Ca-carbonate to the serpentinite starting material (table 3.2). In the Liz-bearing experiments V1148b and V1153a Mgs was formed at T<550 °C in equilibrium with Liz, Cpx and graphite (G) as shown in figure 8.3a. The relatively high Ca# of Mgs indicates coexistence with metastable Ca-rich carbonate (fig. 8.3b). At the same conditions Atg and $CaCO_3$ remain unreacted in experiment V1148a (fig. 8.3c). Mgs, however, was observed in coexistence with Atg in experiment V1153b, which was performed at 5 GPa where the temperature overstep is larger with respect to 3 GPa. This further supports the hypothesis that Atg has slower reaction kinetics with respect to Liz but that the two sheet silicates behave similar if enough time and energy is provided. Thus, it can also be concluded that $CaCO_3$ remains metastable in Atg-bearing experiments but is not a stable phase at subduction zone conditions where Atg dehydrates.

In some studies it has been proposed that Atg can be stable along relatively cold subduction pathways to pressures where the dense hydrous magnesium silicate, phase A, is stable (Ohtani, 2020). Once this point is reached further hydrous minerals would enable water to be subducted into the deep mantle. Carbonation of serpentinites, however, leads to a significant decrease in the thermal stability of Atg that would prohibit Atg passing water to phase A even along the coldest subduction geotherms. This effect would depend on the proportion of $CaCO_3$ added to the serpentinite. It can nonetheless be expected that even small concentrations displace the onset of Atg dehydration to lower temperatures. This means that while carbonated serpentines may transport carbon into the deep mantle, they limit the amount of water that is transported, resulting in a mechanism for creating carbon-rich but water-poor mantle heterogeneities.

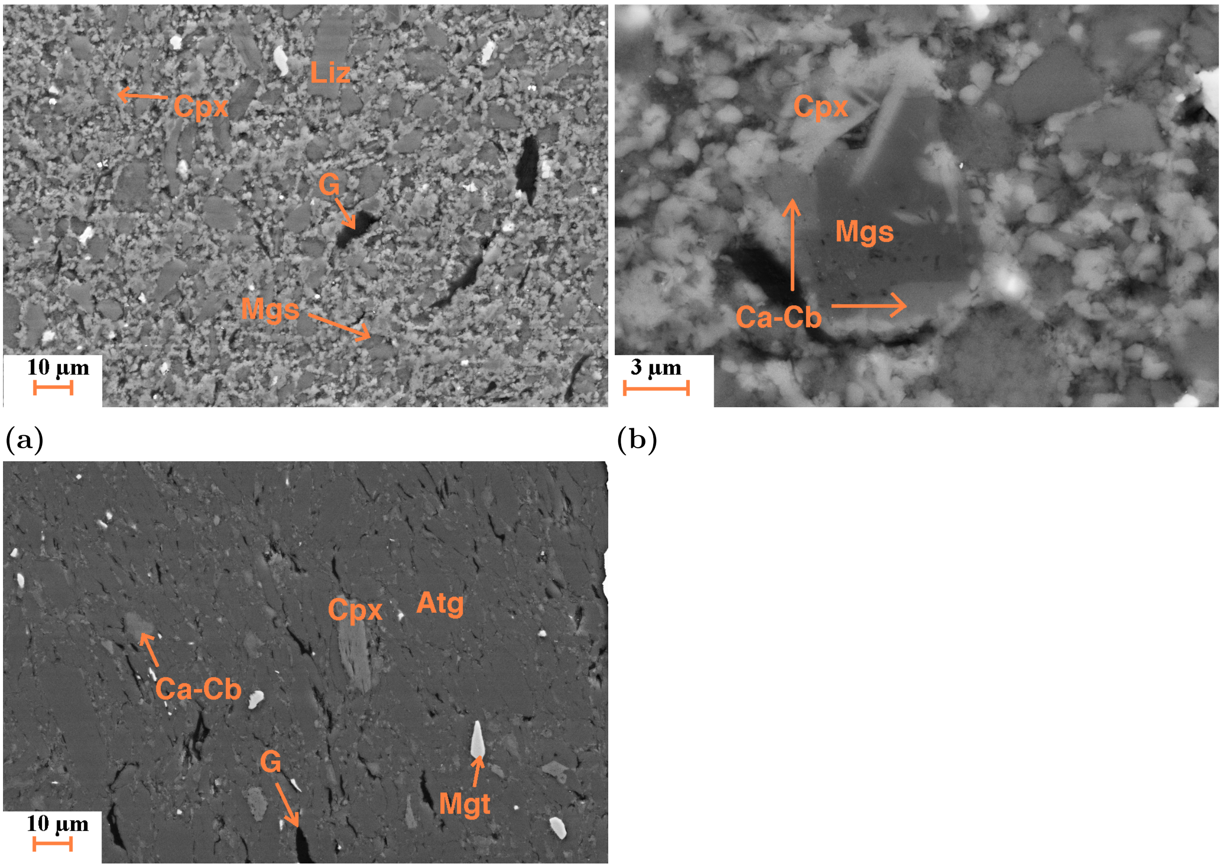

(a) (b)

(c)

Figure 8.3: a: In experiment V1148b (487 °C, 3 GPa) Liz reacted with G and Ca-carbonate to form Cpx and Mgs. b: Metastable Ca-carbonate intergrown with Mgs in experiment V1148b. Such intergrowth results in a shift in the Ca#. c: In experiment V1148a (487 °C, 3 GPa) individual Cpx grains are observed in the Atg matrix. The stable carbonate is Ca-carbonate.

At higher temperatures the experimental and thermodynamic calculations are also in good agreement and the phase relations and mineral compositions can be understood in terms of several reactions. The second dehydration reaction observed is the Chl-out. The products of the Chl-out reaction are P-dependent. At $P \leq 2$ GPa Dol reacts during dehydration to form a COH-fluid. The corresponding reaction (compare also figure 8.1) is given by

$$\underset{\text{Chl}}{Mg_5Al_2Si_3O_{10}(OH)_8} + 2\ \underset{\text{Dol}}{CaMg(CO_3)_2} = \underset{\text{Sp}}{MgAl_2O_4} + 3\ \underset{\text{Ol}}{Mg_2SiO_4} + 2\ \underset{\text{Cal}}{CaCO_3} + \underset{\text{F}}{\text{COH-fluid}} \qquad (8.3)$$

At pressures above the Sp stability field, Grt is formed upon Chl-out. At such high pressures the fluid $X(CO_2)$ is expected to be close to 0 from the thermodynamic model (fig. 8.4). Thus, carbonates appear to be largely unaffected by dehydration reactions. The high-pressure Chl-out reaction for the MASH system is given by Piccoli et al. (2019) and rewritten for the Ca-bearing system as

$$\underset{\text{Chl}}{Mg_5Al_2Si_3O_{10}(OH)_8} + \underset{\text{Cpx}}{MgCaSi_2O_6} = \underset{\text{Grt}}{Mg_2CaAl_2Si_3O_{12}} + 2\ \underset{\text{Ol}}{Mg_2SiO_4} + 4\ \underset{H_2O}{H_2O} \qquad (8.4)$$

This reaction effectively consumes clinopyroxene and repartitions Ca to Grt. Consequently, Grt-bearing experiments have again a lower Cpx mode of only 20 wt% (fig. 8.2). The Ca content in Grt is additionally subject to Ca-Mg exchange with carbonates via the reaction

$$\underset{\text{Py}}{Mg_3Al_2Si_3O_{12}} + 3\ \underset{\text{Ca-Cb}}{CaCO_3} = \underset{\text{Gr}}{Ca_3Al_2Si_3O_{12}} + 3\ \underset{\text{Mgs}}{MgCO_3} \qquad (8.5)$$

This reaction is mainly P-dependent and observed experimentally as an increase in the Ca content in Grt from 0.8±0.3 Ca pfu at 2.5 GPa (experiment V1077) to 1.8±0.1 Ca pfu at 4 GPa and 800 °C (experiment V1089). This compares very well with the thermodynamic calculations which give values of 0.78 Ca pfu at 2.5 GPa and 1.68 Ca pfu at 4 GPa. As a consequence of the increase in garnet Ca content Mgs becomes stable at high PT conditions.

8.2 Equilibrium fluid composition

The experimentally observed shift in carbonate composition from Atg-bearing to Grt-bearing assemblages can be fully explained by Ca-Mg exchange reactions between the coexisting silicate and carbonate fraction. The decrease in the stability field of Atg can also be explained by the formation of Cpx rather than Opx in the Ca-bearing assemblage. These reactions do not involve the release of CO_2, which appears to remain locked in carbonate minerals. Thermodynamic calculations indicate that significant CO_2 contents in the fluid are only present at pressures <2.5 GPa as shown in figure 8.4. At 3 GPa a maximum CO_2 content of up to 10 wt% at 1000 °C is obtained in the Grt stability field, whereas the fluid is essentially a pure H_2O fluid at lower temperatures. The model considers the fluid as a simple H_2O-CO_2 binary and does not involve the solubility of $CaCO_3$. However, as determined in previous studies (Manning et al., 2013), the $CaCO_3$ solubility should be below 1 wt% at conditions where Atg breaks down. This value is expected to be too low to influence the reaction boundary. This finding gets support also from Raman spectra conducted on synthetic fluid inclusions (chapter 3). In these spectra very minor amounts of both oxidised and reduced carbon species were observed, as shown in figure 3.17, which requires an H_2O-rich fluid (Huizenga, 2011; Cesare, 1995), with a composition at the so called water maximum.

The mass balance calculations (section 2.5.1) were used to estimate CO_2 concentrations in the fluids but as shown in the last panel of figure 8.2 the large variation in estimated concentrations, at least below 800 °C, indicates that this method is not sensitive enough under these conditions and returns spurious results. Above 800 °C, however, a quiet consistent increase in the fluid CO_2 content is observed in the experiments, which mirrors the predicted increase by the calculations, although at lower concentration. It is possible that the higher concentrations in the experimental mass balance results follow from the fact that $CaCO_3$ is dissolving in the fluid rather than just CO_2 as predicted in the calculations. Further experiments would be required to test this however.

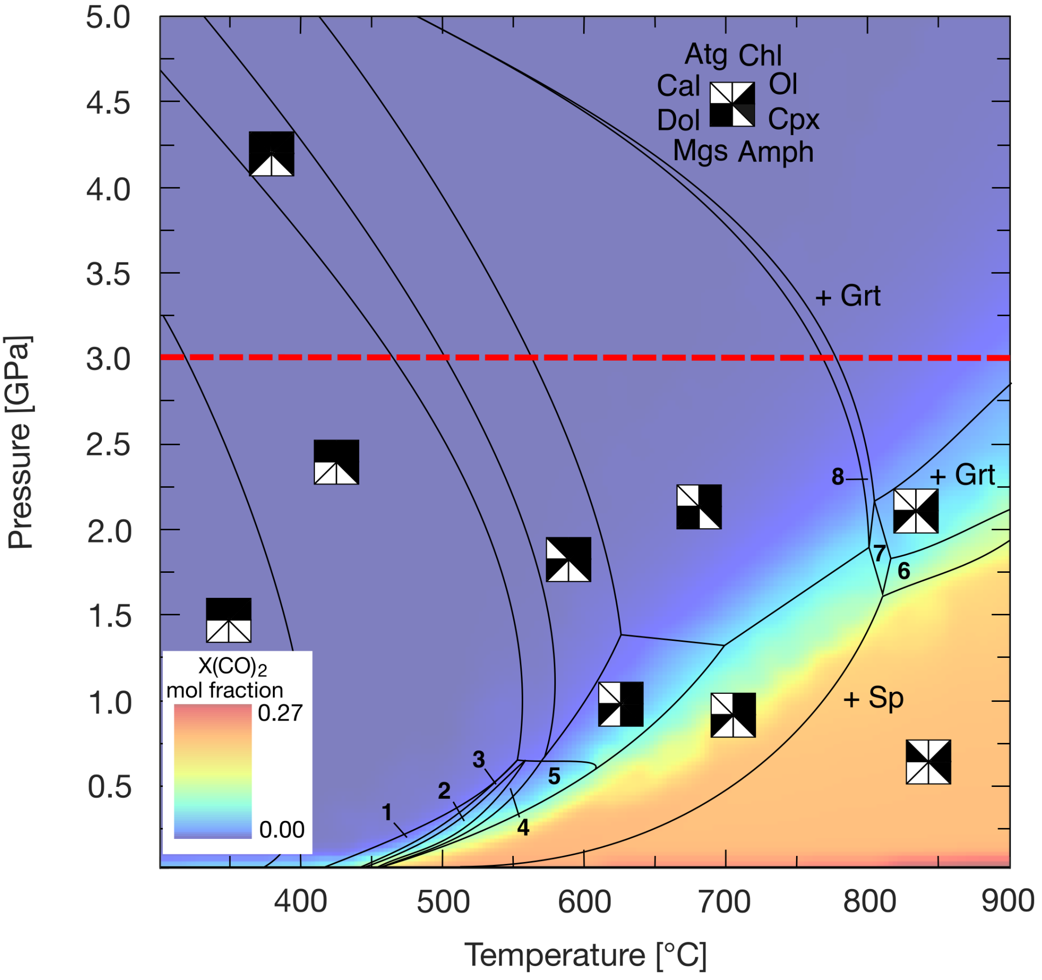

Figure 8.4: *PT*-pseudosection from figure 8.1 coloured for fluid $X(CO_2)$. The CO_2 content in the fluid at elevated *PT* conditions is very low. This implies that the large shift of the Atg dehydration reaction is based on the Ca-Mg exchange between carbonates and silicates rather than on the activity of H_2O. Numbered fields contain the mineral assemblages 1: F Ol Atg Cpx Cal, 2: Chl F Amph Ol Atg Cal, 3: Chl F Atg Ol Dol Amph Cpx Cal, 4: Chl F Amph Ol Atg Cal Dol, 5: Chl F Amph Ol Cal Dol, 6: F Gt Ol Cpx Cal Dol, 7: F Chl Gt Ol Cpx Dol, 8: F Chl Gt Ol Cpx Dol Mgs.

8.3 CO_2 fugacity ($f(CO_2)$)

Experiment V1143b from 494 °C and 3 GPa contains graphite but no carbonate. Mgt is present although it has a porous texture, making it difficult to analyse using EPMA. Liz has a lower $Fe^{3+}/\Sigma Fe$ ratio compared to the starting material as indicated in figure

3.13, which indicates reduction. The sample also contains Ol, which had to form upon H_2O release. By determining the $f(O_2)$ of the experiment constraints can be placed on the nature of the fluid that was in equilibrium with the graphite at the experimental PT conditions.

In the experiment the $f(O_2)$ can be calculated from the Fe content of the Ir metal alloy, fayalite (Fa) and ferrosilite (Fs) using two equilibria,

$$\begin{array}{ccccc} 3\ \mathrm{Fe} & + & 2\ \mathrm{O_2} & = & \mathrm{Fe_3O_4} \\ \text{alloy} & & \mathrm{O_2} & & \text{Mgt} \end{array} \tag{8.6}$$

$$\begin{array}{ccccccc} 2\ \mathrm{Fe} & + & \mathrm{O_2} & + & \mathrm{Fe_2Si_2O_6} & = & 2\ \mathrm{Fe_2SiO_4}. \\ \text{alloy} & & \mathrm{O_2} & & \text{Fs} & & \text{Fa} \end{array} \tag{8.7}$$

The $f(O_2)$ based on these two reactions is given by

$$\log(f(\mathrm{O_2}))_{\mathrm{eq.}\ 8.6} = \frac{1}{2}\left[\frac{G^{\mathrm{Mgt}} - 2G^{\mathrm{O_2}} - 3G^{\mathrm{Fe}}}{R\ T\ln(10)} - 3\log a^{Fe}\right] \tag{8.8}$$

$$\log(f(\mathrm{O_2}))_{\mathrm{eq.}\ 8.7} = \frac{2G^{\mathrm{Fa}} - G^{\mathrm{Fs}} - 2G^{\mathrm{Fe}} - G^{\mathrm{O_2}}}{R\ T\ln(10)} + 2\log(a^{Fa}) - \log(a^{Fs}) - 2\log(a^{Fe}), \tag{8.9}$$

where G^i is the Gibbs free energy of phase i at PT of interest and a^i is the respective activity of phase i. The standard state data from HP'11 database (Holland and Powell, 2011) and composition-activity relations for silicates and alloys as outlined in section 2.5.2 are used. It is assumed that Mgt is a pure Fe endmember and the composition of Fs in equation 8.7 is related to Ol via equation 4.4. The calculated $\log(f(O_2))$ at 3 GPa and 494 °C is -18.612 ± 0.204. This is 1.830 log units above the reference FMQ buffer and comparable to unbuffered Liz- and Atg-bearing experiments conducted at the same PT conditions (fig. 3.14). Since experiment V1143b contained pure graphite, the fugacity of CO_2 ($f(CO_2)$) can be directly calculated based on the equation

$$\mathrm{C} + \mathrm{O_2} = \mathrm{CO_2}. \tag{8.10}$$

Using the calculated $\log(f(O_2))$ the $\log(f(CO_2))$ is calculated as

$$\log(f(\mathrm{CO_2})) = -\frac{G^{\mathrm{CO_2}} - G^{\mathrm{O_2}} - G^{\mathrm{G}}}{R\,T\ln(10)} + \log(f(\mathrm{O_2})). \tag{8.11}$$

$\log(f(\mathrm{CO_2}))$ in this experiment is 9.363 ± 0.204. The fugacity of CO_2 can also be obtained from the PVT-equations of state (EoS) for CO_2 by Belonoshko and Saxena (1991). At experimental conditions of V1143b this EoS results in $\log(f(\mathrm{CO_2})) = 9.46$. This value is within the uncertainty of the experimental value and identifies the fluid as pure CO_2. Consequently, the H_2O formed upon the reduction of Liz must have reduced to hydrogen through reaction with graphite and diffused out of the capsule. For the same conditions the equation of state of Pitzer and Sterner (1994) results in a $\log(f(\mathrm{CO_2}))$ of 9.69, which is slightly less in agreement with the experimental value but still very close.

It is not clear why a carbonate phase did not form in this experiment. CO_2 would be expected to react with Ol and form $MgCO_3$. The most likely explanation is that this is kinetically inhibited. This kinetic issue, however, offers an opportunity to measure $f(\mathrm{CO_2})$, which for both tested EoS is in good agreement.

8.4 Carbon and sulfur in subduction zones

Natural serpentinites that were subducted before being trapped in the crust by orogenic processes can contain both oxidised and reduced carbon (Galvez et al., 2013; Frezzotti et al., 2011; Ague, 2014). While carbonates and organic material may be carried by serpentinites from the surface, it is also possible that they form upon interaction with ferrous and ferric Fe in serpentinites during subduction, i.e. graphite might form from carbonates or vice versa. Such interactions have implications for the transport of carbon in subduction zones, since carbon in the form of graphite cannot be significantly removed from the slab through dissolution (Plank and Manning, 2019).

As shown using mass balance calculations in section 7.2 mineral equilibria in ferric Fe-bearing serpentinites will tend to raise the $f(\mathrm{O_2})$ during prograde subduction. Here the $f(\mathrm{O_2})$ trend determined for serpentinite as a function of the bulk $\mathrm{Fe^{3+}}/\Sigma\,\mathrm{Fe}$ ratio is compared with the $f(\mathrm{O_2})$ at which carbonates reduce to graphite.

The calculations performed to calculate the $f(\mathrm{O_2})$ of a serpentinite with 97 wt% Atg and 3 wt% Mgt are outlined in detail in section 7.2. The experiments performed on the ophicarbonate composition described in this chapter showed that the stable carbonate at subduction zone conditions are Dol and Mgs, whereas Ca is fully partitioned into Dol, Cpx and eventually Grt. The reduction of carbonates to graphite in such an assemblage can, therefore, be described by a single equilibrium

$$\begin{array}{cccccccccccc} \frac{1}{2}\,\mathrm{CaMgSi_2O_6} & + & 2\,\mathrm{MgCO_3} & = & \frac{1}{2}\,\mathrm{CaMg(CO_3)_2} & + & \mathrm{Mg_2SiO_4} & + & \mathrm{C} & + & \mathrm{O_2} \\ \mathrm{Cpx} & & \mathrm{Mgs} & & \mathrm{Dol} & & \mathrm{Ol} & & \mathrm{G} & & \mathrm{O_2} \end{array} \tag{8.12}$$

Dol, Mgs, Cpx and Ol are all found to be close to endmember stoichiometry in the ophicarbonate experiments. For simplicity their activities are taken to be unity, resulting in a reference $f(O_2)$ for the CbC equilibrium, which is very close to the experimental $f(O_2)$ but does not depend on the bulk composition. The calculated $f(O_2)$ for this equilibrium is shown in figure 8.5 at conditions that follow a subduction zone geotherm. Graphite is stable at an $f(O_2)$ of $\leq \Delta\mathrm{FMQ}{-}1.74$ at 500 °C. The $f(O_2)$ of carbonate reduction decreases very slightly upon subduction. Below 500 °C the presence of graphite not only depends on the bulk $\mathrm{Fe^{3+}}/\Sigma$ Fe ratio but also on the presence of Br. The $f(O_2)$ in Br-bearing assemblages is significantly lower with respect to Br-free assemblages and might stabilise graphite with a bulk $\mathrm{Fe^{3+}}/\Sigma$ Fe ratio of $\leq$0.1. Above 500 °C only the most reduced serpentinites with a bulk $\mathrm{Fe^{3+}}/\Sigma$ Fe ratio $\leq$0.03 will contain graphite. Given that serpentinites frequently have bulk $\mathrm{Fe^{3+}}/\Sigma$ Fe ratios in the range 0.2 to 0.6 (Iacovino et al., 2020; Debret et al., 2014, 2015; Mayhew and Ellison, 2020) they are not expected to contain graphite as a result of reduction of carbonates during subduction. Furthermore, even the most reduced serpentinites would enter the carbonate stability field at conditions where Atg dehydration occurs, i.e. above 600 °C.

Also indicated in figure 8.5 is the sulfur-sulfate transition (SSO) as calculated from Piccoli et al. (2019). They calculated the transition at slightly lower pressures, i.e. 2.6 GPa at 600 °C, which, however, is unlikely to make a difference. A number of studies (Kelley and Cottrell, 2009; Iacovino et al., 2020) have proposed that sulfate dissolved in H_2O, originating from serpentinites, could be an oxidising agent for the overlying mantle wedge and thus explaining the more oxidised nature of arc magmas. However, the SSO transition is located above the HM transition. Since most serpentinites will have a $f(O_2)$ that converges towards HM with increasing temperature but will not reach higher values, it is unlikely that sulfate-bearing fluids are released from the slab upon dehydration of Atg. This is in agreement with experiments performed by Merkulova et al. (2017), who found the transition from pyrrhotite to pyrite but did not find indication for sulfide oxidation. Similarly, open system models from Evans and Powell (2015) do show the release of H_2S-bearing fluids upon dehydration but no indication on oxidation of the mantle wedge by sulfur-bearing fluids.

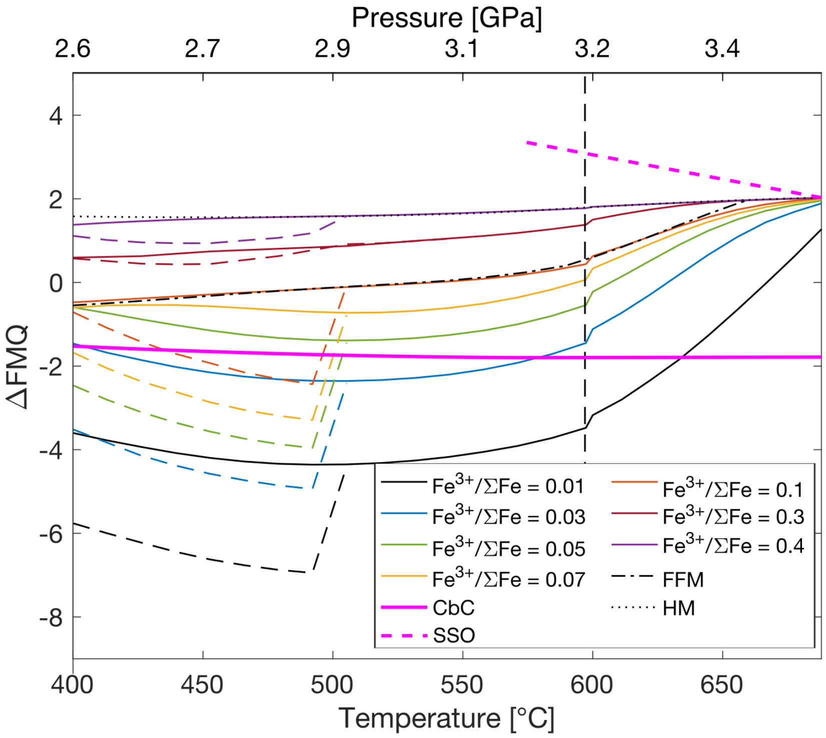

Figure 8.5: The evolution of $f(O_2)$ along a subduction PT-path for various bulk $Fe^{3+}/\Sigma Fe$ ratios. Shown is the CbC buffer, i.e. equilibrium 8.12. Br-bearing assemblages have the potential to stabilise graphite at low temperature. All serpentinite assemblages will end up in the carbonate-bearing regime at temperatures above the Atg-out.

It should be noted, however, that uncertainty remains as to the redox state of carbon as it enters the subduction zone. Especially the relationship between the serpentinite oxidation state and the presence of either graphite or carbonate is not well constrained. It is reasonable to assume that Ca-carbonates tend to form in more oxidised serpentinites, which result from high rock-water interaction or near surface incorporation of sedimentary carbonate. Graphite, on the other hand, could potentially form as a result of the initial incorporation of organic matter. There are thus two scenarios which need to be addressed specifically.

In the first scenario serpentinites containing Ca-carbonates are subducted. Such serpentinites are likely relatively oxidised and would remain in the carbonate stability field as described above. At low temperature prior to dehydration Ca-carbonate is the stable carbonate. At the onset of Atg dehydration, which is shifted significantly to lower temperature with respect to carbonate-free systems, Dol forms upon repartitioning of Ca into Cpx. Several studies have reported the apparent formation of graphite from carbonates in subduction related serpentinites (Galvez et al., 2013; Frezzotti et al., 2011; Ague, 2014). Galvez et al. (2013), for example, reported the formation of a graphite-bearing zone at the transition between serpentinite and an overlying metamorphosed sedimentary carbonate-rich rock from a locality in the northern Alpine Corsica. In this scenario a slightly reduced fluid released from the serpentinite is expected to reduce carbonates in the sediment layer and thereby form graphite, which is further preserved in the slab and transported into the deep mantle. Although no information is reported concerning the oxidation state of the serpentinites it is clear that reduction could only occur in the most reduced serpentinites, which seem to be more the exception in world wide serpentinite compositions (Evans, 2008). However, even if it is considered that the serpentinites contained 10 wt% FeO but had a bulk Fe^{3+}/Σ Fe ratio of zero, i.e. no Mgt, the oxidation of all FeO to Fe_2O_3 would need a total of 1.1 wt% O_2 and could therefore only account for 0.42 wt% graphite. The graphite-bearing sedimentary layer is reported to contain up to 4 wt% graphite. The serpentinites themselves can thus not be considered to be the cause of this reduction. The reduction more likely occurs from interaction with a reducing fluid component possibly originating from subducted organic material, as in the second scenario.

In the second scenario serpentinites contain organic material incorporated at the surface, which can transform to graphite during prograde metamorphism. This transformation changes the C/H ratio of the solid fraction (Nakamura et al., 2020). Hydrogen components released from such graphitisation could potentially account for the reduction of carbonates as described above. The $f(O_2)$ is expected to be low in such settings and any carbonates present might be reduced.

8.5 Implications for carbon speciation in subduction zones

As described in section 7.3, serpentinisation also occurs in the mantle wedge above the slab in the forearc region, where fluids released from the slab interact with the overlying mantle peridotite. Mass balance calculations were performed on a peridotite composition and it was shown that for a typical mantle $Fe^{3+}/\Sigma Fe$ ratio of $\leq$0.03 the $f(O_2)$ in the serpentinised mantle wedge can reach values as low as ΔFMQ−2 at temperatures below ≤500 °C. The question remains as to whether it is possible to oxidise the mantle wedge through an influx of volatiles.

In figure 8.6 the $f(O_2)$ of CbC, i.e. where magnesite in the wedge would reduce to graphite (eq. 8.12), is indicated and it can be seen that for a typical mantle $Fe^{3+}/\Sigma Fe$ ratio the mantle would be in the graphite stability field. Any CO_2 entering the mantle would be reduced to graphite and the mantle would oxidise up to the CbC curve. This would not raise the $Fe^{3+}/\Sigma Fe$ ratio of the mantle significantly. As the temperature increases, possibly due to the wedge being dragged down into the deeper mantle, the mantle would become more oxidised and rise out of the graphite stability field. At this point the graphite would oxidise to form carbonate and the $Fe^{3+}/\Sigma Fe$ ratio of the mantle would return to the level from before the influx of CO_2. Oxidation of the mantle by pure CO_2 is therefore not effective in the mantle wedge.

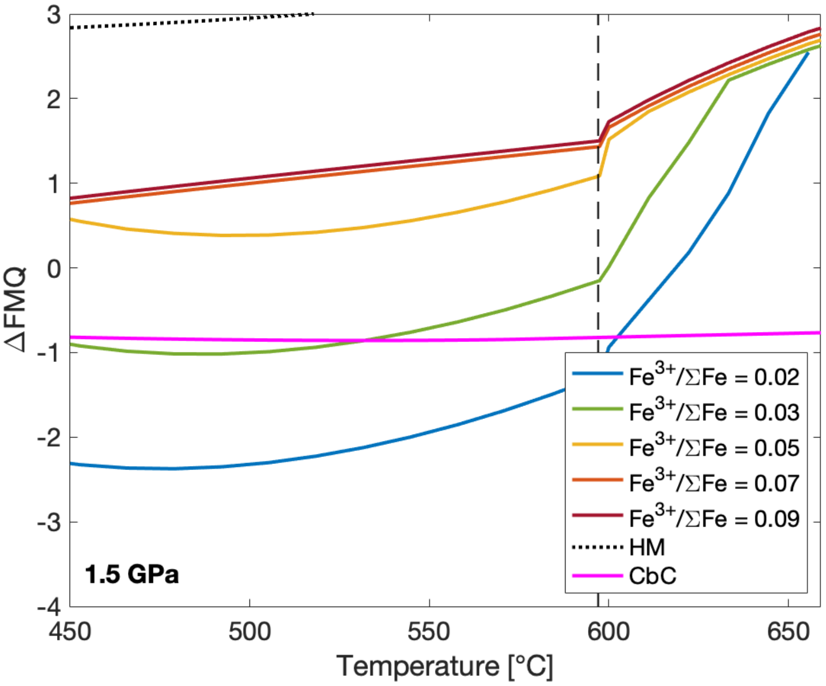

Figure 8.6: The evolution of $f(O_2)$ in a serpentinised peridotite within the mantle wedge at 1.5 GPa for various bulk $Fe^{3+}/\Sigma Fe$ ratios. The carbon-graphite transition is reached only at low $Fe^{3+}/\Sigma Fe$ ratios of $\leq$0.03. CbC refers to equilibrium 8.12.

Fluids coming from the slab are likely H_2O-dominated with carbon making up a much smaller component. Figure 8.7 shows calculations for CH_4 content of H_2O-dominated fluids as a function of oxygen fugacity. The calculation is performed using the equations of state of Belonoshko and Saxena (1991) and assumes that a COH-fluid can be comprised of the neutral species H_2O, CO_2, CO, CH_4 and H_2 (Holloway, 1987). As can be seen in figure 8.7 for typical mantle $Fe^{3+}/\Sigma Fe$ ratios the equilibrium fluid CH_4 content can be up to 10 mol% at temperatures below 550 °C. The remaining fluid would be H_2O-dominated. If H_2O-dominated CO_2-bearing fluids entered the mantle wedge from oxidised sediments at these conditions then the mantle would be oxidised as the CO_2 is reduced to CH_4. Mantle wedge oxidation by dilute CO_2-bearing fluids could increase the bulk $Fe^{3+}/\Sigma Fe$ ratio of the mantle until the proportion of CH_4 in the resulting fluid was equal to the proportion of CO_2. At 500 °C this occurs at an $f(O_2)$ of $\Delta FMQ-0.5$ where the bulk $Fe^{3+}/\Sigma Fe$ ratio of the mantle would be raised to 0.04. This may seem like a minor increase. However, for the most reduced regions of the mantle wedge this process still doubles the ferric Fe content. If these regions were then further subducted then its $f(O_2)$ would rise as Atg breaks down. This would at least produce a more oxidised region of mantle above the slab that may help to explain the raised oxidation state of the arc mantle source.

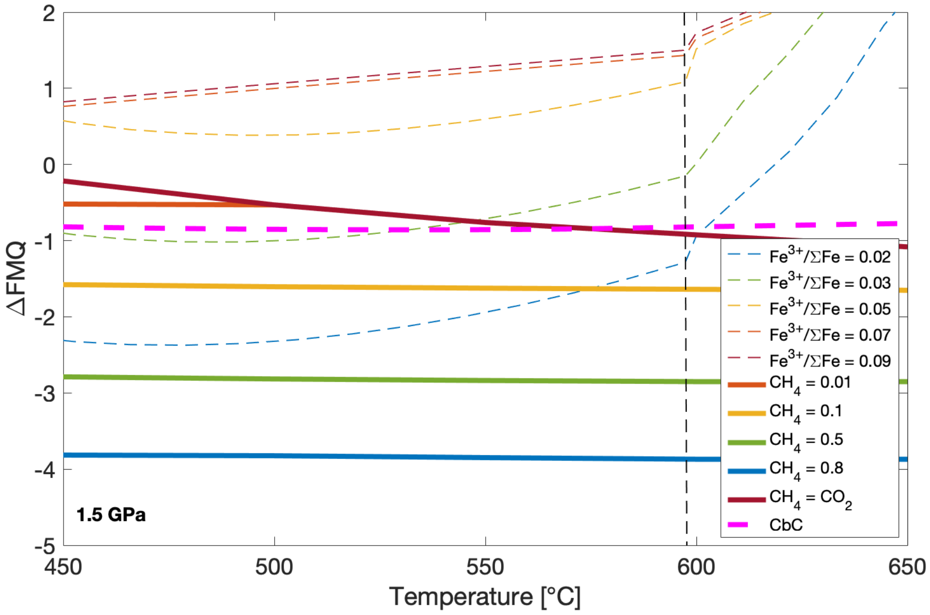

Figure 8.7: The composition of a COH-fluid according to the equation of state from Belonoshko and Saxena (1991). Methane is stable in the reduced regions of the mantle wedge.

So far the fluid was always considered to contain neutral species. However, an H_2O-rich fluid with neutral carbon species does not accurately enough reproduce nature as shown by spectroscopic fluid inclusion analyses as well as fluid-rock interaction (e.g. Frezzotti et al., 2011; Galvez et al., 2013; Manning et al., 2013; Ague, 2014; Ague and Nicolescu, 2014). Both thermodynamic and experimental studies confirmed the presence of charged carbon species, such as HCO_3^- and $CaHCO_3^+$, in the fluid, which can increase the total carbon content (e.g. Tumiati et al., 2017; Menzel et al., 2020). Since charged species are redox-dependent, the $f(O_2)$ is important in terms of how much and what kind of carbon species are dissolved in the fluid. In previous chapters it was found that the composition of serpentinite, i.e. the bulk $Fe^{3+}/\Sigma Fe$ ratio, has direct implication on the fluid $f(O_2)$. Depending on the $f(O_2)$ the fluid composition changes as shown by the proportions of reduced neutral species methane (fig. 8.7) and H_2 (fig. 6.6). Sulfur in this scenario will be present only as reduced species, while sulfate components are unlikely. This is based on the fact the the maximum $f(O_2)$ encountered by a subducted serpentinite is buffered at the HM equilibrium, which is below the SSO buffer. However, for future work it would be interesting to combine redox reactions in dehydrating serpentinites with aqueous fluid chemistry calculations.

9 High pressure determination of serpentinite permeability using a new method

9.1 Introduction

Permeability is a material property of porous solid media and quantifies the capability to allow a fluid to pass through. It is thus an important measure in geosciences whenever liquids or gases percolate through a rock, for example for fluid and magma flow in metamorphic and igneous petrology (Ague, 2007; Al Reda et al., 2020; Hatakeyama et al., 2017; Keller and Holzer, 2018; Wheaton, 2016).

The nature of fluid flow in subduction zones is a critical aspect in the global volatile cycle. Flux estimations suggests that large amounts of fluid must be efficiently transported from the slab towards the mantle wedge and further back to the Earth surface in order to balance the global water budget. Estimates for total water influx in subduction zones are in the range of $0.1 \cdot 10^{12}$ - $3 \cdot 10^{12}\,\mathrm{kg\,yr^{-1}}$ (Cai et al., 2018; Korenaga, 2017; Magni et al., 2014; Rüpke et al., 2004; van Keken et al., 2011). van Keken et al. (2011) estimated that only one third is transported below 230 km depth, where it contributes to a total increase in mantle water content of 370 ppm (approximately 1 ocean mass) over the age of the Earth. The majority of the water is released via dehydration reactions and supposed to drain towards the mantle wedge. If the fluids migrate too slowly they would risk to remain in the slab and being subducted into the deeper mantle. The fact that the Earth's oceans have not drained significantly into the mantle over time indicates that there must be an effective fluid transport mechanism. It has been argued that this requires fluids to organise into channelised network rather than migrating through unfocused pervasive fluid flow (Plümper et al., 2016).

Serpentine minerals are 1:1 trioctahedral sheet silicates. Because of their platy habit, they have a strong crystal preferred orientation. Experiments performed at low pressures and room temperature indicate a strong permeability anisotropy as a result of the serpentinite fabric (Kawano et al., 2011). Flow parallel to the foliation has been determined to be approximately one order of magnitude higher than in the normal direction. This might allow fluids to move more rapidly parallel to the slab mantle interface. Anisotropy might even be enhanced by shear-deformation along unconformities (Okazaki et al., 2013). For example, within the region known as the outer rise, where the rigid oceanic lithosphere bends to subduct (fig. 1.1), major normal faulting occurs, which has been proposed to allow hydration of the lithosphere down to 20 - 30 km (Faccenda et al., 2009; Korenaga, 2017). During subduction, these normal faults might play an important role in terms of forming zones of distinctively higher permeability, which can enable channelised fluid flow to occur.

Fluids released by dehydration reactions within subduction zones are also often linked to deep Earthquakes, hydration of the mantle wedge and island arc volcanism (Iwamori, 2007; Peacock, 1990). In addition they are important in terms of element recycling. Dissolution of carbonate minerals in H_2O-rich fluids, for example, has the potential to transport almost all carbon from the slab towards the mantle wedge (e.g. Kelemen and Manning, 2015; Menzel et al., 2019, 2020; Tian et al., 2019). However, the nature of fluid flow will have implications for the dissolution of volatile components. The extent of dissolution is likely to vary strongly depending on whether pervasive or channelised flow occurs. Factors that might influence fluid permeability and the occurrence and direction of channelised flow are, therefore, important in terms of placing constraints on both the rate and efficiency of volatile removal from the slab (Tian et al., 2019).

High temperature and pressure conditions, as they are encountered in subduction zones, might significantly influence the permeability and thus the way fluids migrate within subducting slabs. At high temperatures the dehydration of water-bearing lithologies changes the porosity and consequently the permeability as shown in experiments conducted by Tenthorey and Cox (2003). On the other hand, studies on continental drilling sites indicated that the permeability decreases with increasing depth and becomes constant at sufficiently high pressures in a depth of 12 km (Manning and Ingebritsen, 1999). Due to experimental limitations, however, previous studies on serpentinite permeability have not been performed at simultaneous high pressures and temperatures conditions compatible with those in subduction zones (Kawano et al., 2011; Okazaki et al., 2013; Tenthorey and Cox, 2003). Low pressure fluid permeability experiments generally require measurements of fluid pressure on a test sample. This is very difficult to achieve at pressures above 1 GPa where solid media high pressure devices are generally used.

In this study a relatively simple technique is developed to estimate fluid flux within a sample of antigorite in a multi-anvil apparatus (MA) at the conditions where it would dehydrate in a subduction zone. The antigorite (Atg) dehydration reaction is divariant and occurs over a pressure and temperature interval throughout which Atg itself controls the permeability. A solid drill core of a natural Atg-serpentinite sample is embedded in an MgO sleeve (fig. 9.2). Upon increasing temperature, the Atg starts to dehydrate and a fluid pressure gradient is produced between the fluid-bearing serpentine cylinder and the dry MgO sleeve. The setup allows the fluid to migrate from the serpentine towards the MgO, where brucite (Br) is formed via the reaction

$$\mathrm{MgO} + \mathrm{H_2O} = \mathrm{Mg(OH)_2}. \tag{9.1}$$

The stability field of Br is relatively large and the dehydration of Br only takes place at temperatures >1000 °C at 3 GPa (Johnson and Walker, 1993). This is far above the dehydration temperature of Atg, which is completed at temperatures <700 °C and makes Br useful for fluid flux estimations. The extent of Br formation on each side of the Atg sample directly reflects the fluid flux in the particular direction and might even be used to quantify anisotropy in fluid flux. This methodology could in principle be expanded to study permeability anisotropy in any mineral assemblage.

9.2 Theoretical basis

A key parameter in a fluid dynamic calculation is the fluid flux q, which expresses how much fluid passes in a certain time through a certain area. The volume flux q_V is thus given as

$$q_V = V_{fluid} \cdot t^{-1} \cdot A^{-1}, \tag{9.2}$$

with V_{fluid} being the volume of the discharged fluid, t the time and A the cross sectional area. Historically, the fluid volume flux was measured through a column sample of known length, either by applying a constant flux or a known pressure gradient. The first empirical relation between the fluid volume flux and the pressure gradient was derived by Henry Darcy and is known as Darcy's law (Darcy, 1856):

$$q_V = -\frac{k}{\eta}\,\Delta P, \tag{9.3}$$

where k is the permeability, η the dynamic fluid viscosity and ΔP denotes the pressure difference between the two endpoints of the column. The minus sign indicates the direction of flow, which is always towards lower pressure as indicated in figure 9.1.

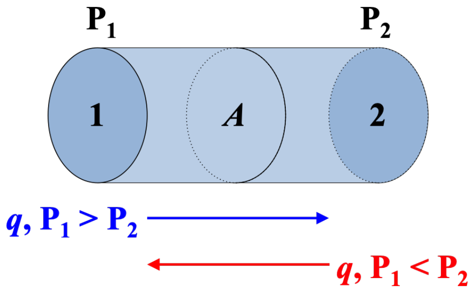

Figure 9.1: The flux denotes how much fluid migrates through an area A per time t. The direction of the flux is given by difference in pressure P between the two endpoints and always goes towards lower pressure as indicated by the blue and red arrow.

Using the fluid density ρ_{fluid}, the volume flux can be written as mass flux:

$$q_m = \rho_{fluid} \cdot V_{fluid} \cdot t^{-1} \cdot A^{-1} = \rho \cdot q_V. \tag{9.4}$$

Since the unit of the volume flux is $\mathrm{m\,s^{-1}}$, q_V also denotes the relative velocity $\vec{v}$ of the fluid with respect to the porous medium and becomes directional. Thus, the mass flux can be written as

$$\vec{q_m} = \rho\ \vec{q_V} = \rho\vec{v}. \tag{9.5}$$

The redistribution of mass m has to follow mass conservation, i.e. the influx and outflux of material in the system has to balance the time-dependent change in the composition of the system. With respect to figure 9.1 the inflow and outflow of the fluid, assuming the fluid flows from end 1 to end 2, is given by

$$\vec{m}_{in} = \rho\vec{v} \cdot A_1 = \vec{q}_{m,in} \cdot A_1 \tag{9.6}$$

$$\vec{m}_{out} = \rho\vec{v} \cdot A_2 = \vec{q}_{m,out} \cdot A_2, \tag{9.7}$$

where $A_{1,2}$ is the cross sectional area on end 1 and 2 in figure 9.1. The total fluid mass

m_{fluid} in the system is obtained from the fluid fraction by

$$m_{fluid} = A\ dx\ \phi\ \rho, \tag{9.8}$$

where dx is the thickness over which the fluid flux is analysed. ϕ is the porosity, i.e. the volume fraction filled with fluid. The mass conservation equation is given as

$$\frac{\partial}{\partial t}(A\ dx\ \phi\ \rho) = (\rho \vec{v}_{in} \cdot A_1) - (\rho \vec{v}_{out} \cdot A_2) \tag{9.9}$$

and for an infinitesimally small dx and a constant cross sectional area as

$$\frac{\partial \rho \phi}{\partial t} + \frac{\partial}{\partial x}(\rho \vec{v_x}) = 0, \tag{9.10}$$

where $\vec{v_x}$ is the velocity in direction x along the fluid flux. In three dimensions equation 9.10 is written as

$$\frac{\partial \rho \phi}{\partial t} + \nabla(\rho \vec{v}) = 0, \tag{9.11}$$

Substituting Darcy's law into the mass conservation equation results in the expression

$$\frac{\partial \rho \phi}{\partial t} + \nabla\left(-\rho \frac{k}{\eta} \nabla P\right) = 0. \tag{9.12}$$

The constitutional equations relate the compressibility of fluids c_f and solids c_r with pressure P at a constant temperature T:

$$c_r = \frac{1}{\rho}\left(\frac{\partial \rho}{\mathrm{d}P}\right)_T \tag{9.13}$$

$$c_f = \frac{1}{\phi}\left(\frac{\partial \phi}{\mathrm{d}P}\right)_T. \tag{9.14}$$

Equation 9.12 can then be rewritten in terms of pressure as

$$\frac{\partial P}{\partial t} + \nabla\left(-\frac{1}{(c_f + c_r)\phi}\ \frac{k}{\eta} \nabla P\right) = 0. \tag{9.15}$$

The fluid flux thus depends on the compressibility of the fluid and solid, the fluid viscosity, the solid permeability and solid porosity. The fluid flux is driven by the pressure gradient across the system. The permeability is thereby a critical parameter depending on the porosity and the relative fluid volume. However, there is evidence that the permeability also depends on the 3-dimensional shape of the pores. This relationship can be difficult to constrain for geological samples (Garcia et al., 2009).

The new experimental design presented in this study, however, allows to determine the amount of fluid released from the Atg by mass balance. The fluid discharge from the dehydrated Atg to the MgO sleeve is directly assessed from the extend of Br formation. Without knowing the exact pore space geometry, the present method allows the fluid flux and the permeability of a dehydrating assemblage to be determined.

9.3 Experimental methods

9.3.1 High-pressure experiments

Pressures between 2 and 5 GPa at temperatures across the Atg dehydration (470 - 830 °C) were achieved in MA-experiments at BGI and TU (section 2.3). The experimental run time was varied from 0.5 h up to 216 h in order to also investigate the effects of possible time-dependent processes on the permeability.

For the purpose of this study drill cores of 1.5 mm height and 1.5 mm diameter were prepared from a natural Atg-serpentinite sample, which exhibited a strong foliation. The drill cores were oriented so that the preferred orientation of the Atg was either perpendicular or parallel to the cylinder axis. Due to the rather fragile nature of strongly foliated serpentinites this was challenging and only possible for sample Zer_1801. A detailed description of the sample can be found in section 2.1.1.

Each drill core was placed inside an MgO sleeve and covered with MgO discs on top and bottom, which served as a sink for H_2O expelled from the serpentine cylinder at the experimental conditions (figure 9.2a). The full package of serpentine+MgO was welded shut inside a gold capsule and placed in a standard BGI 25/17 assembly.

Most experiments were conducted with the preferred orientation perpendicular to the cylinder axis. Two experiments (V1171, V1175) were conducted with the preferred orientation in the axial direction. These experiments were performed in order to distinguish anisotropic fluid flow caused by a pressure gradient applied by the assembly, from anisotropic fluid flow resulting from preferred orientation of the sample.

For two experiments, V1155 and V1157, the serpentine cylinder was cored and filled with reagent grade $Al(OH)_3$ powder and covered with a thin serpentine disc. Gibbsite, the most commercial $Al(OH)_3$ polymorph, dehydrates around 300 °C at ambient pressure (MacKenzie, 1973; Demichelis et al., 2008). The goal was to examine the fluid flow through the serpentine prior to the actual Atg dehydration reaction by having a further fluid source inside the serpentine. A further experiment (V1170) with the same goal was run in a standard BGI 18/11 assembly without the surrounding MgO sleeve (fig. 9.2b). The serpentine cylinder in this experiments was fit in an AuPd capsule. Below the cylinder $Al(OH)_3$ powder was employed as an H_2O source, whereas a disc of sintered MgO powder was put on top of the sample forming an H_2O sink.

After quenching the samples were embedded in epoxy and polished for further analyses. Accurate phase compositions were measured with EPMA. SEM was used for semi-quantitative phase identification as well as examination of the Br-layer formation. Measuring conditions were as outlined in section 2.4.1.

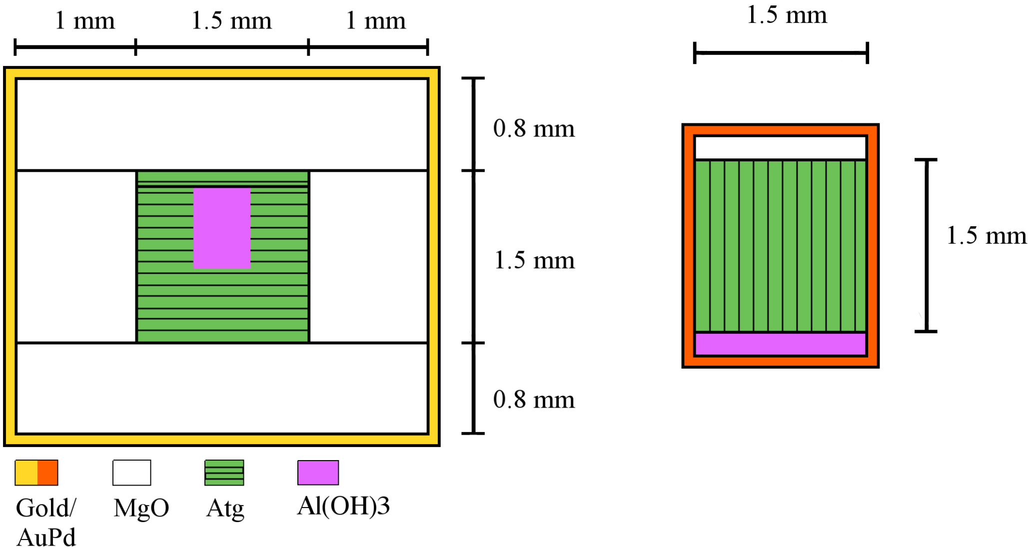

(a) **(b)**

Figure 9.2: Sketch showing the geometry of the permeability experiments. The serpentine drill core is placed inside an MgO sleeve and covered with MgO discs on the top and bottom. The foliation direction of Atg is indicated by parallel lines. a: Standard setup. The position of the $Al(OH)_3$ filled drill hole in experiments V1155 and V1157 is indicated. The drill hole is covered with an Atg disc. b: Experiment V1170 was run in an 18/11 assembly without the MgO sleeve. $Al(OH)_3$ and MgO are added as an H_2O source and sink respectively.

9.4 Analytical methods

9.4.1 Image analyses of Br in permeability experiments

SEM back-scattered electron (BSE) images were taken for all samples, from which Br-layers could be readily distinguished from MgO and silicates by their dark shading. Phase confirmation was performed with energy dispersive X-ray spectroscopy. Figure 9.3 shows the geometry and the resulting SEM image of a typical run product, in which a Br-layer formed from MgO all around the serpentine cylinder.

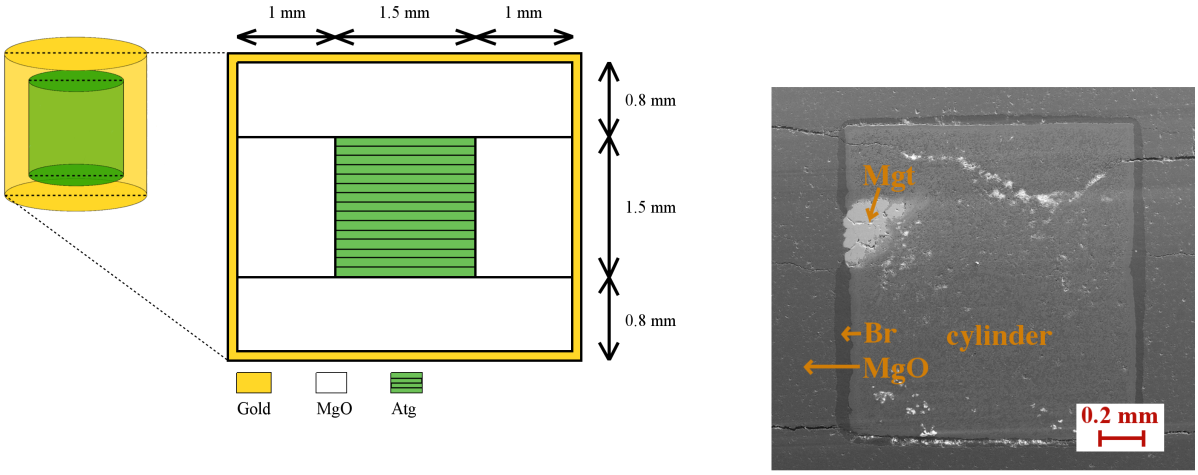

(a) **(b)**

Figure 9.3: a: Geometry of the permeability experiments. The serpentine cylinder is fully surrounded by an MgO-sleeve. The Atg has a square cross section. b: A typical BSE image showing a Br-layer around the Atg cylinder. Experiment V1172, 216 h at 645 °C, 2 GPa.

The Br-layers observed are generally quite irregular. In order to get statistically significant widths for the Br-layers in each sample, several BSE images on each side were taken with different magnification. The BSE images were analysed using GIMP 2.8.14, an open source raster graphics editor. In each image the Br-layer was coloured and the proportion of coloured pixels was extracted with the histogram tool of GIMP. Using the length of a reference line parallel to the Br-layer as well as the length of the scale bar in pixels, simple geometric relations of a parallelogram can be used to calculate the mean thickness d of the Br-layer in µm, i.e.

$$d = \left(\frac{Px^{tot}}{l_{ref}}\right) s_{px}^{-1}\; s_{\mu m} \tag{9.16}$$

where Px^{tot} is the total amount of pixels, l_{ref} and s_{px} are the length of the reference line and the scale bar in px and $s_{\mu m}$ is the length of the scale bar in µm. If extreme irregularities, such as MgO-filled cavities, are observed, these parts of the picture were excluded since they would significantly influence the mean values.

9.4.2 Analyses of error sources

Among the possible sources of errors are those that arise from resolution of the BSE images, from possible incorrect phase identification and from imprecise colouring. These errors are generally small and simply contribute to the standard deviation of the thickness from all analysed BSE images. A more important source of absolute error arises from the sample preparation. After the experiment the samples were embedded in epoxy and carefully ground/polished from one side. The cross section of the serpentine cylinder on the polished surface is a rectangle, whose size varies with the polishing depth. In figure 9.4 a schematic section through a serpentinite cylinder with a Br-layer is shown. The thickness of the Br-layer x at a certain polishing depth h is calculated based on the chord length of the outer (s_a) and inner (s_i) circular segment, i.e. the serpentine cylinder with and without Br-layer:

$$x = \left(\frac{s_a - s_i}{2}\right) \tag{9.17}$$

$$s_a = 2\sqrt{(r_0 + d)^2 - (r_0 - h)^2} \tag{9.18}$$

$$s_i = 2\sqrt{r_0^2 - (r_0 - h)^2}, \tag{9.19}$$

where r_0 is the radius of the Atg cylinder and $r_i = 0.5(s_i)$ is the apparent radius at polishing depth h.

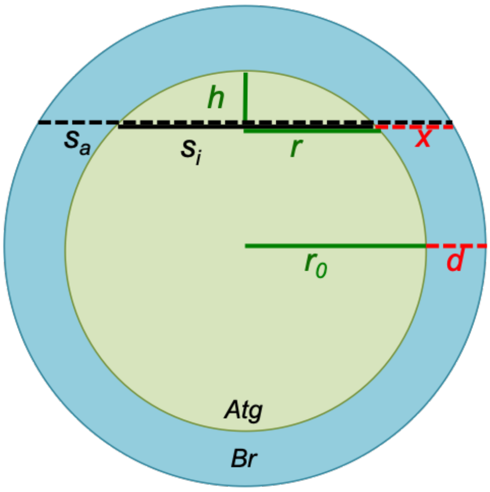

Figure 9.4: Schematic planar section through a serpentinite cylinder with Br-layer. r_0 is the real radius of the Atg cylinder and d the real Br-layer thickness. r is the apparent radius at polishing depth h, which corresponds to an apparent Br-layer thickness x.

Figure 9.5 shows that the apparent Br-layer thickness x increases with decreasing polishing depth h. For example, a real Br-layer thickness d of 10 µm at a polishing depth of 400 µm leads to an apparent thickness of 11.3 µm, i.e. an overestimation of 13%. If the polishing depth is only 200 µm the thickness is overestimated by 46%. Assuming negligible compression of the cylinder the polishing depth in each sample can be derived from the same geometrical relations. In most samples the polishing depth ranges from 350 to 500 µm. Consequently, an error of 20% has been assigned to the Br-layer thickness in each samples. Only samples ES363 and ES367 have a polishing depth of $\leq$100 µm. Unfortunately, these samples were cut for micro-CT analyses and repolishing is thus not possible. These samples where therefore excluded from further calculations.

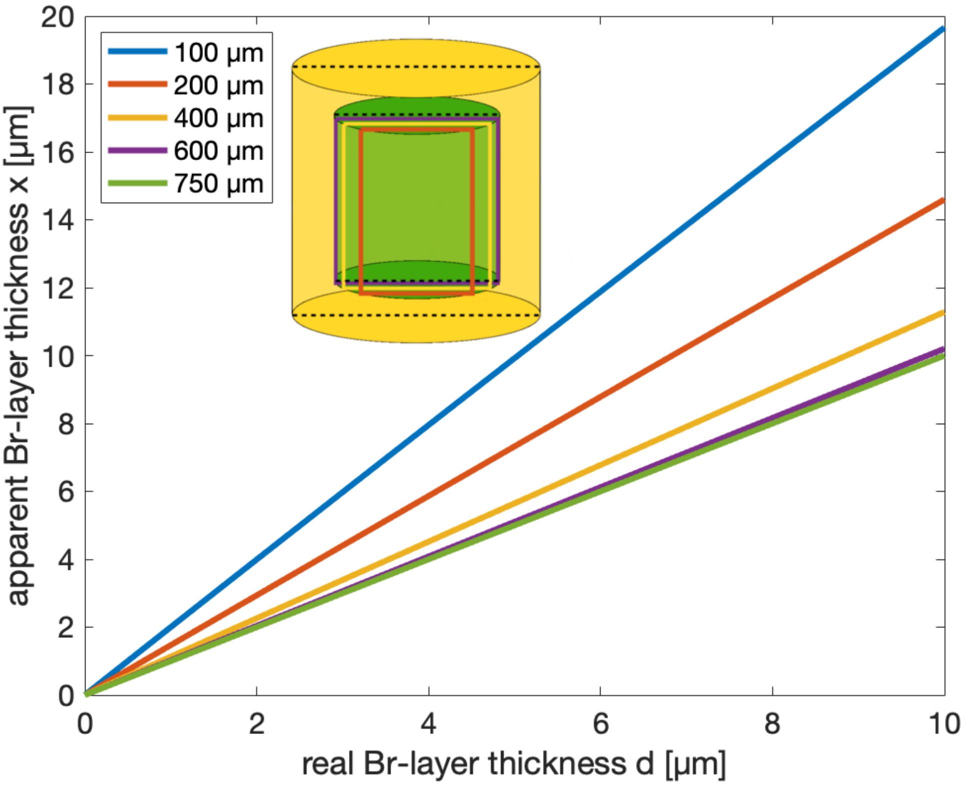

Figure 9.5: The aspect ratio of the Atg cross section changes with h. The apparent Br-layer thickness x decreases with increasing polishing depth h. Only at the middle of the serpentinite layer ($h = r = 750\,\mu m$) the apparent thickness x is the same as the real thickness d.

9.5 Results

9.5.1 General phase relations

With increasing temperature Atg dehydrates and releases its crystallographically bound water. In a simple MSH system the Atg-out reaction is univariant (fig. 1.4a). In the more realistic FMASH system, however, the dehydration of Atg is divariant and takes place over the temperature range 620 - 640 °C (fig. 1.4b). The Atg cylinder thus changes its mineralogy and texture continously with increasing temperature. The run product mineralogy of each experiment is summarised in table 9.1. While experiments V1149, V1157 and V1170, performed below 540 °C have the same mineralogy as the starting material, the onset of dehydration above 600 °C is marked by the formation of minor amounts of Fe-rich silicates along the Atg grain boundaries (fig. 9.6a). Upon further dehydration, more olivine (Ol) and pyroxene (Px) form and arrange in patches (fig. 9.6b). The hydrous silicate in these samples is chlorite (Chl). The final anhydrous mineral assemblage consists of an Ol+Px mesh with a large potential porosity of >20 wt%. Garnet (Grt) is present at P above 2.5 GPa (fig. 9.6c), where as at lower P Al is partitioned into the Opx. Similar textural and mineralogical changes as a function of temperature were obtained in experiments on powder samples in section 3.1.

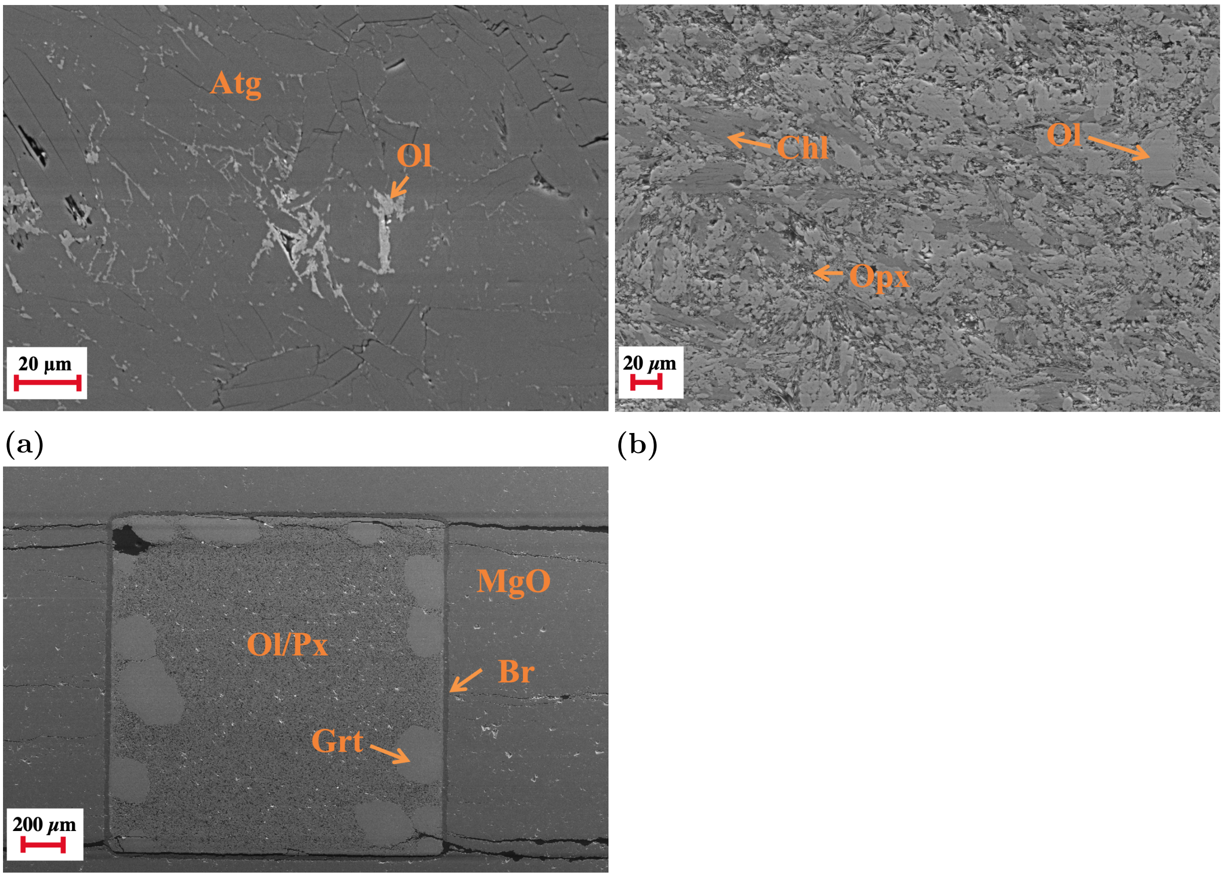

(a) **(b)** **(c)**

Figure 9.6: Representative samples at various temperatures. a: At 600 °C $< T <$ 700 °C Ol starts to form along Atg grain boundaries (V1165: 616 °C, 2 GPa, 96 h). b: At $T >$ 700 °C the stable hydrous phase is Chl, surrounded with Ol+Px (V1166: 700 °C, 2 GPa, 96 h). c: The final assemblage after complete dehydration is Ol+Px+Grt (V1156: 830 °C, 5 GPa, 6 h).

Mass balance calculations, as described in section 2.5.1, are used to calculate the modes of each phase. Figure 9.7 shows the mode of hydrous phases Atg and Chl as a function of temperature. Modes of Atg and Chl obtained for sample Zer_1701 from figure 3.15a are shown for comparison. Since the serpentinite sample used for the drill cores (Zer_1801) is structurally and mineralogically similar to the sample Zer_1701, it is expected that the dehydration temperature of Atg is similar in both samples. However, as the experimental run time of fluid flux experiments in this chapter is much shorter compared to those performed on sample Zer_1701, Atg is found to persist metastable to higher temperatures in a number of cases (e.g. ES369 and ES372). The metastability of Atg does not play a role in determining the permeability. However, phase relations are clearly shifted and need to be interpreted accordingly.

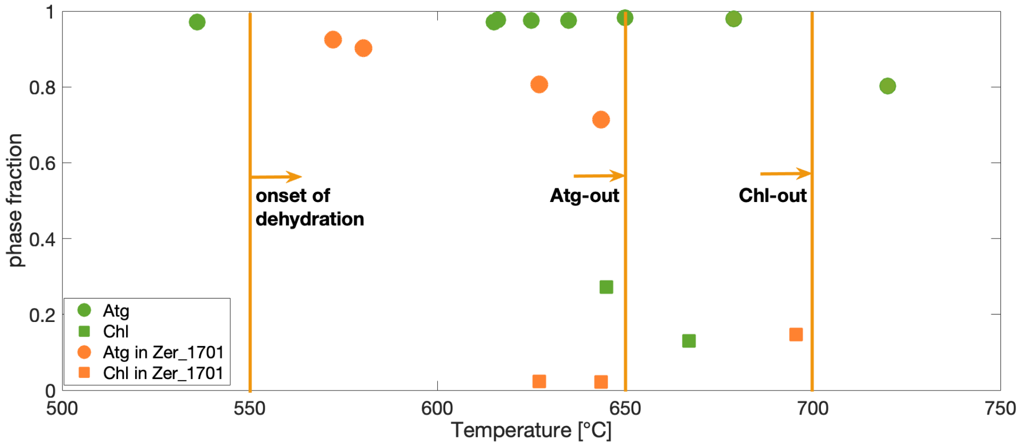

Figure 9.7: Modes of Atg and Chl as derived from mass balance calculations for the permeability experiments on sample Zer_1801. Shown in orange are Atg and Chl modes from Atg-bearing experiments on sample Zer_1701 described in chapter 3. The dehydration reactions in Zer_1701-bearing experiments as observed from SEM analyses are indicated by vertical lines. With respect to those dehydration reactions fluid flux experiments in this chapter dehydrate at higher temperature. This results from slow reaction kinetics and shorter experimental run time.

Table 9.1: Experimental conditions and run products in permeability experiments. Mass fractions of Atg and Chl obtained by mass balance (section 2.5.1) are given. * mark Chl obtained from interaction between $Al(OH)_3$ and Atg rather than dehydration. ** are experiments performed at TU. Minerals in brackets were quantitatively confirmed but too small to be accurately measured with EPMA.

experimental conditions				mineral composition in run products						notes
name	T [°C]	P [GPa]	t [h]	Atg	Chl	Grt	Ol	En	Mgt	
V1170	470	2	96	0.97(1)	x^*				x	no MgO sleeve
V1157	507	5	6	0.97(1)					x	$Al(OH)_3$ filling
V1149	536	2	24	0.97(1)					x	
V1171	615	2	96	0.97(1)			(x)		x	vertical orientation
V1165	616	2	96	0.98(1)			(x)		x	
V1163	625	2	216	0.97(1)			(x)		x	
V1152	635	2	24	0.98(1)			(x)		x	
V1155	650	2	6	0.98(1)			(x)			$Al(OH)_3$ filling
ES363**	640	2.5	6	x			x		x	no EPMA data available (CT sample)
V1172	645	2	216		0.27(4)		x	(x)	x	
V1175	643	2	96		x		x	x		vertical orientation, no EPMA data
ES369**	679	2.5	1	0.97(1)			(x)		x	
V1166	700	2	96		0.12(2)		x	x	x	
ES372**	720	2.5	0.5	0.80(13)			x	(x)		
ES367**	755	2.5	0.5		x		x	x	x	no EPMA data available (CT sample)
V1167	755	2	24		x		x	x		serpentine in AuPd without $Al(OH)_3$ and MgO
V1156	830	5	6			x	x	(x)		

9.5.2 Br formation

The majority of experiments show the development of a Br-layer at the interface between the Atg cylinder and the MgO sleeve. The thickness of the Br-layer varies with time, temperature and pressure. In experiments performed between 500 °C and 550 °C, (i.e. V1149 and V1157) no Br-layer is detected (table 9.1, fig. 9.8a), which is likely due to the low temperature. At slightly higher temperature a Br-layer can be observed although Atg is still stable within the bulk of the sample and does not show further signs of dehydration. Adjacent to the Br-layer, these experiments show a second inner monomineralic Ol-layer covering the Atg cylinder as shown in figure 9.8b. The thickness of the Br-layer in these experiments is slightly smaller than the thickness of the Ol-layer. At temperatures above Atg-out the mineral assemblage consists of Chl+Ol+Px and shows a significant porosity. The Br-layer and the adjacent Ol-layer are still observed. However, the relative thickness of the two layers changes so that the thickness of the Br-layer significantly exceeds that of the Ol-layer (fig. 9.8c). Measured Br-layer and Ol-layer thicknesses are given in table 9.2.

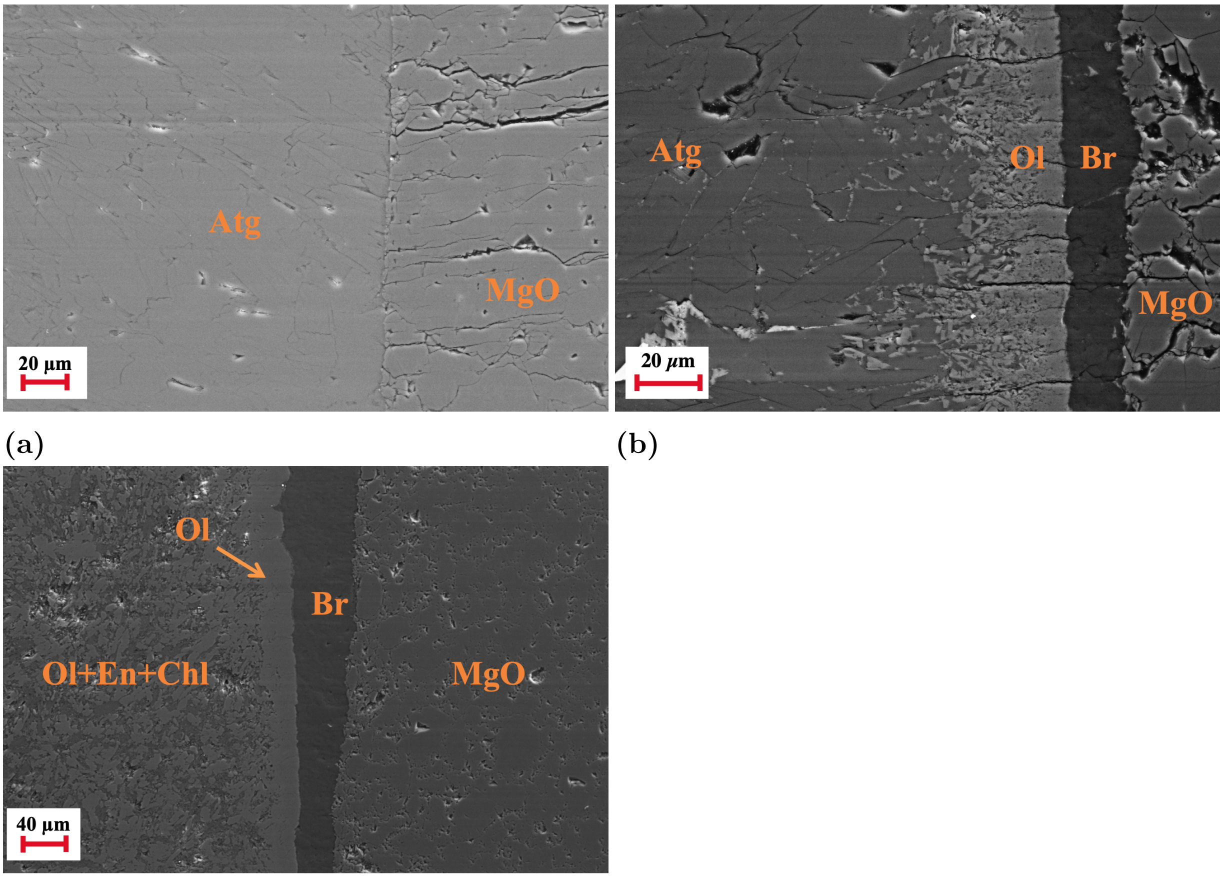

(a)

(b)

(c)

Figure 9.8: SEM pictures of the interface Atg-MgO. a: At $T < 600\,°C$ no Br-layer formed (V1157: 507 °C, 5 GPa, 6 h). b: Between Atg and MgO a double layer of monomineralic Ol and Br forms (V1163: 625 °C, 2 GPa, 216 h). c: At temperatures above Atg-out the stable assemblage is Ol+En+Chl. The Br-layer thickness is strongly increased with respect to the Ol-layer formed at the rim of the cylinder (V1172: 645 °C, 2 GPa, 216 h).

Table 9.2: Mean thickness of Br- and Ol-layers in each experiment in axial and radial directions and the total layer volume. All values are in µm and µm^3. The error on the thickness is estimated to be about 20%. The thickness of the Br-layer around the cylinder wall in samples ES363 and ES367 is very thick in comparison with the top. This is due to polishing, which was not performed deep enough in these samples.

experimental conditions				Br-layer			Ol-layer			ratio
name	T °C	P GPa	time h	d_{lid} µm	d_{wall} µm	V_{tot} µm^3	d_{lid} µm	d_{wall} µm	V_{tot} µm^3	V_{Br}/V_{Ol}
solid state Br formation										
V1149	536	2.0	24	-	-	-	-	-	-	-
V1152	635	2.0	24	5.245	6.632	65.622	6.713	8.612	83.709	0.784
ES367	755	2.5	0.5	4.753	13.510	-	-	-	-	-
ES369	679	2.5	1	1.473	2.687	24.234	2.836	4.660	42.732	0.567
V1155	650	2.0	6	5.573	5.109	55.932	5.833	6.060	62.947	0.889
V1157	507	5.0	6	-	-	-	-	-	-	-
V1163	625	2.0	216	8.981	14.769	137.169	18.673	26.167	243.209	0.564
V1165	616	2.0	96	8.605	12.144	116.952	18.777	24.664	233.545	0.501
V1167	755	2.0	24	-	-	-	-	-	-	-
V1170	470	2.0	96	-	-	-	-	-	-	-
V1171	615	2.0	96	5.262	7.296	70.424	7.305	9.576	92.418	0.762
fluid flux Br formation										
ES363	640	2.5	6	2.886	11.945	-	-	-	-	-
ES372	720	2.5	0.5	5.806	8.860	83.520	5.362	7.097	68.520	1.219
V1156	830	5.0	6	14.886	19.706	193.738	12.305	11.369	121.933	1.589
V1166	667	2.0	96	33.443	38.139	394.645	12.908	17.282	164.296	2.402
V1172	645	2.0	216	33.192	46.497	456.168	22.762	27.870	267.920	1.703
V1175	643	2.0	96	32.044	46.087	449.031	16.463	21.389	203.946	2.202

It was expected that the formation of Br directly reflects the fluid flux out of the entire sample. However, there are several experiments that contain a Br-layer without any indication that dehydration throughout the Atg sample has occurred. Therefore, prior to the actual dehydration of Atg, there is a reaction between Atg and MgO that results in the formation of a Br-layer and an adjacent Ol-layer. The reaction, in the MSH system, can be written as

$$\underset{\text{Atg}}{Mg_{2.824}Si_2O_5(OH)_{3.647}} + \underset{\text{MgO}}{3\ MgO} = \underset{\text{Ol}}{2\ Mg_2SiO_4} + \underset{\text{Br}}{\tfrac{31}{17}\ Mg(OH)_2}. \tag{9.20}$$

Ol formed along the interface in this way will differ from the Ol formed upon dehydration due to the contribution from MgO. Indeed, EPMA data (appendix B) show a Mg#$\geq$ 0.95 ± 0.01 for Ol at the interface, which is higher than Mg# of Ol formed in the middle of the serpentine cylinder (0.92 ± 0.01). Furthermore, this reaction shows that the amount Ol formed is directly related to the amount of Br formed. Knowing the thickness of the Ol-layer allows the amount of Br formed through this reaction to be determined. The Ol-thickness is determined similarly to the Br-layer thickness as outlined in section 9.4.1. A unit volume of pure forsterite (Mg_2SiO_4) with the dimensions $1\times1\times1\,\mathrm{cm}^3$ has the mass of 3.22 g, based on its density of $3.22\,\mathrm{g\,cm^{-3}}$. This accounts for 0.023 mol of Ol. Due to the above reaction 0.025 mol of Br are formed, which is equal to 1.45 g or $0.61\,\mathrm{cm}^3$. For a contact area of $1\times1\,\mathrm{cm}^2$, the thickness of the formed Br-layer is 0.61 cm or simply $0.61\ d_{\mathrm{Ol}}$, with d_{Ol} being the thickness of the Ol-layer. This simple calculation is valid for the top and bottom layer. At the side of the cylinder the thickness of the Br-layer formed from the solid state reaction 9.20 will be $< 0.61\ d_{\mathrm{Ol}}$, since the volume depends on the radius. However, this effect will be within the 20 % error.

Figure 9.9 shows the volume of Ol- and Br-layers. The reference line marks the $V_{Br} = 0.61\ V_{\mathrm{Ol}}$ hypothetical relationship. Experiments conducted at temperatures below Atg dehydration are shown in blue and follow this trend very well, indicating that Br is only formed through reaction 9.20. Experiments conducted above the Atg dehydration do show a thicker Br-layer. In these experiments a part of the fluid in the Br-layer indeed comes from the dehydration reaction and reflects a fluid flux throughout the sample.

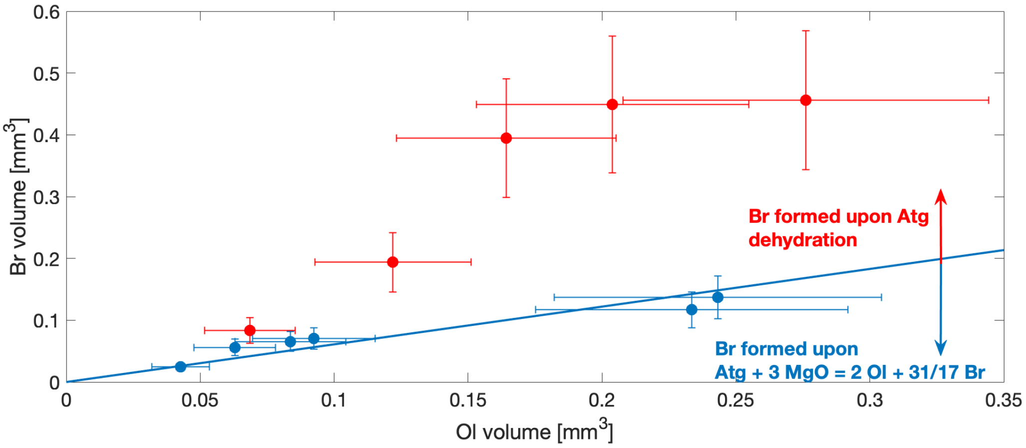

Figure 9.9: Volume of Br-layer vs. Ol-layer: in a simple MSH system the volume ratio is about 0.61 if formed through the solid state reaction Atg+3 MgO = 2 Ol+$\frac{31}{17}$ Br. Experiments showing more Br indicate the presence of a fluid formed upon Atg dehydration.

9.5.3 Experiments to test the permeability of Atg before dehydration

In a first attempt to determine the flux of water throughout Atg prior to dehydration, samples V1155 and V1157 were cored and filled with $Al(OH)_3$ as a fluid source. $Al(OH)_3$ dehydrates around 300 °C and provides H_2O at conditions were Atg is stable. In experiment V1157 an Al-hydroxide is still observed. However, the EPMA results indicate a total Al_2O_3 content of 83.43(25) wt% and an H_2O content of 13.36(12) wt%. The total H_2O content is therefore below that of gibbsite and indicates a stoichiometric formula of AlO(OH). Thus, this experiment indicates the formation of diaspore from gibbsite at elevated temperature, in agreement with the phase diagram shown by Grevel et al. (2000). The porosity, resulting from the release of water during the transition from $Al(OH)_3$ to AlO(OH), is restricted to the drill hole and indicates that the fluid did not move through the serpentine. Experiment V1155 was run at 650 °C, where the final dehydration of the Al-hydroxide is expected according to Grevel et al. (2000). EPMA results show complete dehydration of the Al-hydroxide, whereas Atg in this sample is still stable. Also in this sample pronounced porosity within the drill hole indicates that the majority of the fluid stayed in place. A Br-layer formed all around the sample based on the reaction between Atg and MgO, but, it can be seen that the Br-layer on top of the sample is thicker than on any other side (fig. 9.10). It would appear, therefore, that a part of the fluid migrated upward along the drill core. Since the Atg lid placed atop the drill hole shows pronounced deformation, fluids might have migrated through fractures. The results of these experiments are a first indication that the permeability of Atg is low at temperatures below its dehydration.

A second approach to determine the fluid flux through Atg before dehydration was attempted in experiment V1170, in which a fluid source ($Al(OH)_3$) was placed below the Atg cylinder and a fluid sink (MgO) was placed atop (fig. 9.11a). Although the Al-hydroxide fully dehydrated, high porosity is observed between the Al-oxide grains (fig. 9.11b) indicating that the fluid was trapped in the lower part of the capsule rather than passing through the serpentine. At the interface between Atg and Al-oxide a Chl-rich layer formed as a result of the high Al_2O_3 environment. On the other side of the Atg cylinder, a thin Br-layer formed at the contact to the MgO-disc due to the reaction between Atg and MgO. A more extensive Br-area formed, however, right at the capsule wall (fig. 9.11c). It formed as some fluid released from the $Al(OH)_3$ moved upwards along the interface between the Atg and the capsule wall, rather than migrating through the cylinder, giving a further indication that the permeability through the Atg is very high prior to dehydration.

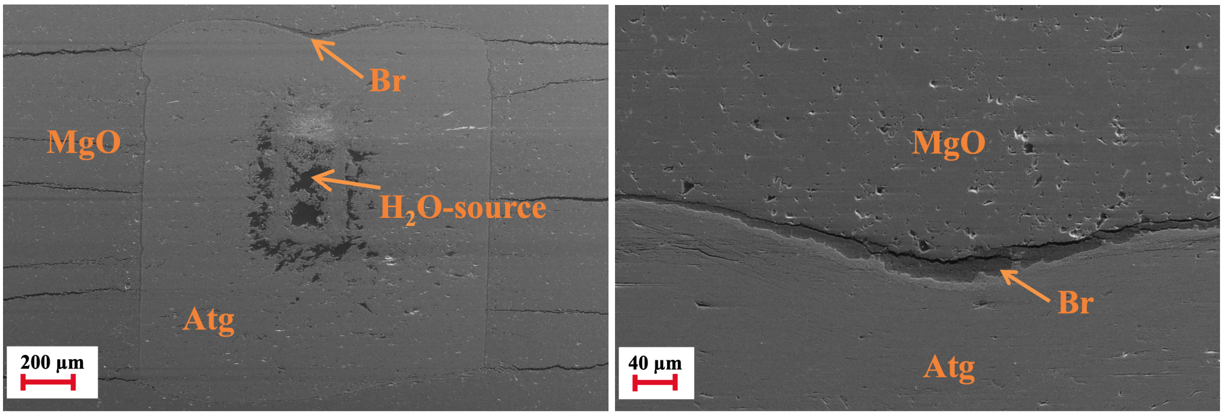

(a) **(b)**

Figure 9.10: Sample V1155 (650 °C, 2 GPa, 6 h) a: The $Al(OH)_3$-fluid source placed in the middle of the sample completely dehydrated. b: Upon fluid migration upward a rather thick Br-layer formed directly atop the drill hole. The Atg lid shows pronounced deformation.

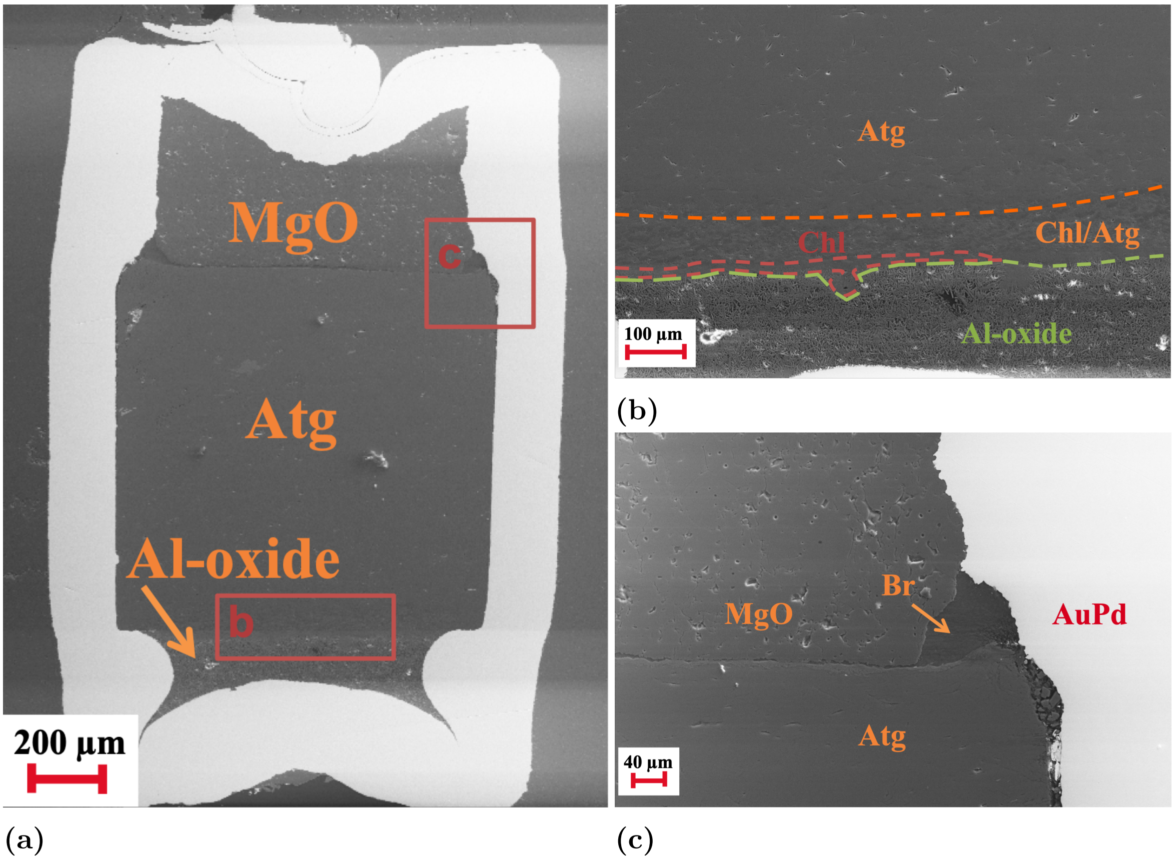

(a) (b) (c)

Figure 9.11: Sample V1170 (470 °C, 2 GPa, 96 h) a: The experiment was run in a smaller capsule with an H_2O source below and an H_2O sink above the serpentine cylinder. Rectangles indicate positions of the subfigures b and c. b: The Al-hydroxide completely dehydrated to Al-oxide. The released fluid was trapped in the bottom layer of the samples, indicated by high porosity. At the interface between the Atg and the Al-oxide a Chl-layer evolved. c: Br preferentially formed at the capsule wall, where fluid was able to pass along the interface Atg-AuPd.

9.5.4 Time-dependency

A time-dependency of the Br-layer growth can be obtained from experiments performed at the same temperature for different durations as shown in figure 9.12. Experiments indicating Br formation upon dehydration (table 9.2) show a 6 times thicker Br-layer after 216 h compared to the thickness obtained after 0.5 h. The trends show major growth of the Br-layer in the first 10 h. The growth rate decreases with increasing time due to the loss of the initial pressure gradient created by the fluid upon dehydration. Between 96 h and 216 h no significant change is observed.

Experiments which did not dehydrate show Br-formation upon solid state reaction. These experiments also show an increase of the Br-layer thickness with increasing run time. As shown in figure 9.9 the thickness of this Br-layer is always proportional to an adjacent Ol-layer, i.e. $d_{Br} = 0.61\ d_{Ol}$.

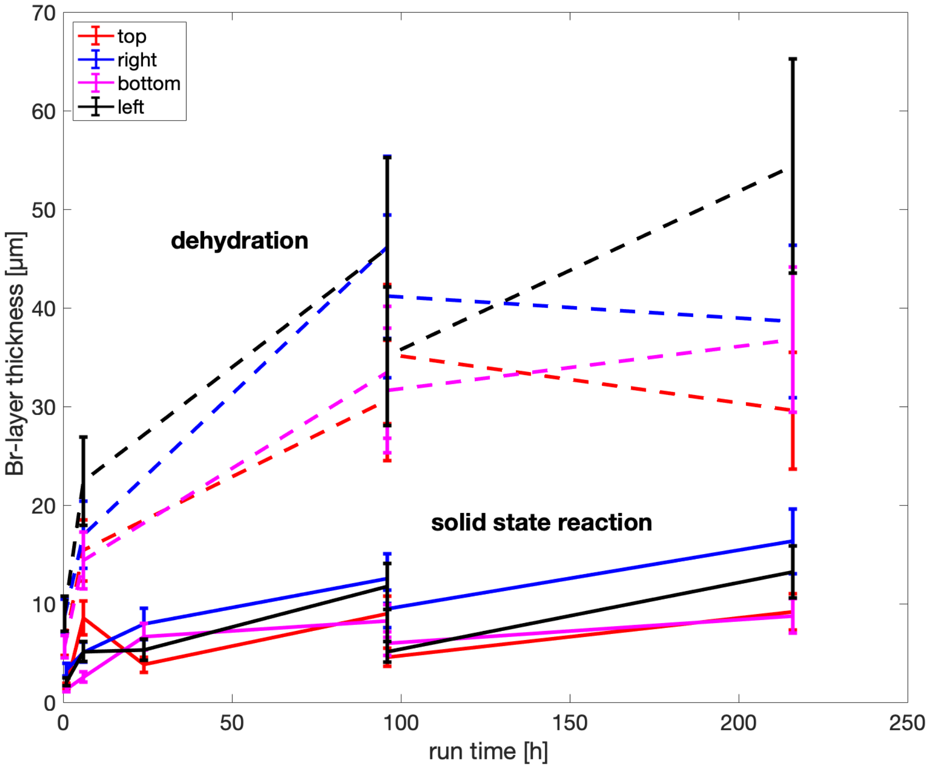

Figure 9.12: The Br-layer thickness as measured from SEM images increases with run time. In experiments conducted at temperatures below Atg dehydration the Br-layer formed only upon solid state reaction. The time-dependent growth of the Br-layer is significantly smaller with respect to experiments where Br formed upon dehydration.

9.5.5 Evaluation of anisotropy

Atg has a strong lattice preferred orientation (LPO), which has been proposed to influence the fluid flux (Kawano et al., 2011). The Atg c-axis is perpendicular to the foliation of the crystals. The drill cores in most experiments are oriented with the cylinder axis perpendicular to the foliation, i.e. parallel to the Atg c-axis, whereas only a few experiments had the preferred orientation parallel to the cylinder axis.

The orientation and strength of an LPO can be quantified by EBSD measurements. The quality of the sample surface in an EBSD measurement is critical for the indexation efficiency because only the very top 50 nm are analysed (van de Moortèle et al., 2010).

Figure 9.13 shows the pole figures of two representative samples, ES372 with the foliation perpendicular to the cylinder axis and V1171 with the foliation parallel to the cylinder axis. For the measurements the cylinder axis was oriented north-south. In the pole figure of sample ES372 the crystallographic c axis {001} shows a concentration of measured orientations close to the south pole. The a and b axes, {001} and {010}, are also distributed on a rather narrow range, indicating extreme orientation of the individual crystals. The overall orientation of the Atg crystals in this sample is such that the crystallographic c axis is almost parallel to the cylinder axis and the b axis is aligned in the horizontal direction of the cylinder. This confirms the macroscopic preferred orientation being perpendicular to the cylinder axis. In sample V1171 however, the b axis shows a clear preferred orientation in horizontal direction whereas the c axis shows a distribution from north to south. The drill core was cut parallel to the preferred orientation and thus the c axis is expected to be aligned along the x-axis of the pole figure. The cylindrical geometry of assembly itself, e.g. the heater, MgO and sample as well as the location of the thermocouple, result in an increased pressure along the cylinder axis. The north-south distribution of the Atg c-axis indicates deformation and rearrangement of the Atg due to the anisotropic pressure distribution in the assembly.

Although the preferred orientation of Atg in sample V1171 and V1175 is perpendicular to all other samples, the ratio between Br-layer thickness on top and on the side does not differ from the general trend (table 9.2). The observed difference in Br-layer thickness between radial and axial direction in each experiment thus simply arises from anisotropic stress distribution in the assembly. Thus, although Atg has a strong LPO, dehydration induced fluid flow does not show any shape-related anisotropy.

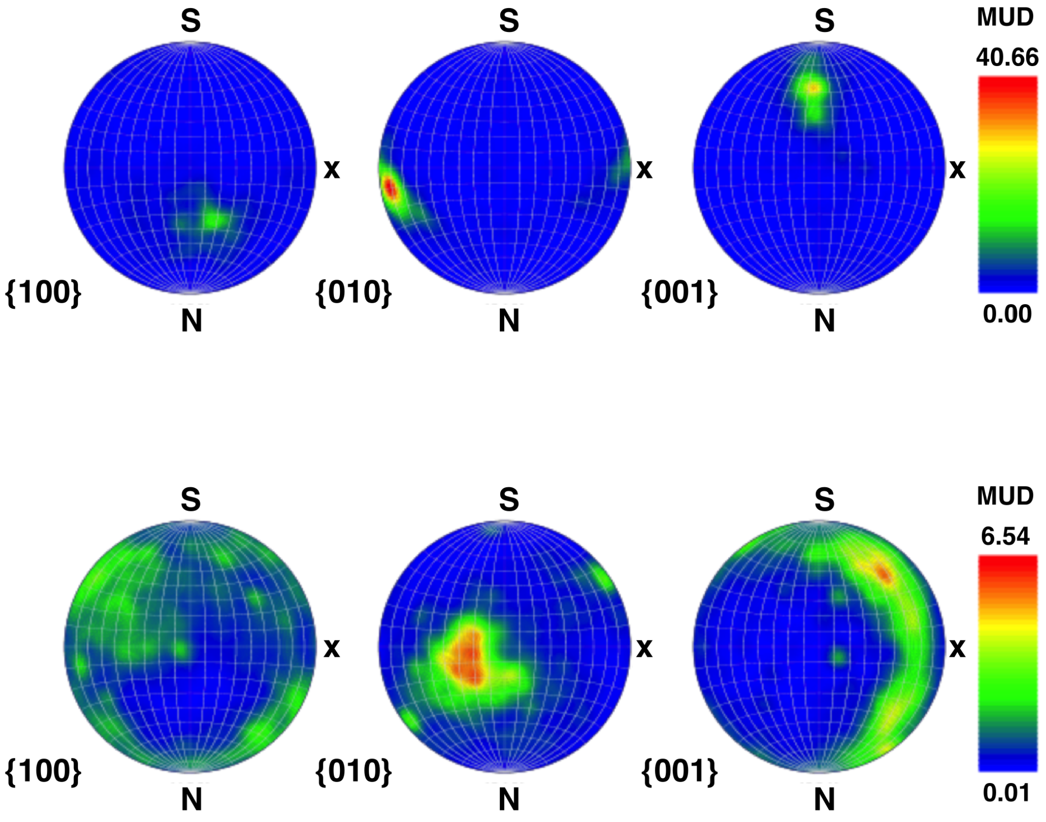

(b)

Figure 9.13: Pole figures of EBSD analyses of two selected samples. Both samples were analysed on a section containing the cylinder axis vertical and the radial direction horizontal in the image plane (fig. 9.3). a: sample ES372 (720 °C, 2.5 GPa, 0.5 h) shows the c-axis {001} almost parallel the cylinder axis. b: sample V1171 (615 °C, 2 GPa, 96 h) has a different orientation of the drill core and indicates the orientation of the c-axis {001} parallel to the normal of the image plane. MUD refers to multiples of uniform distribution and indicates a much lower indexing rate for sample V1171.

9.6 Fluid flux determination

To calculate the serpentinite permeability it is necessary to assess the total fluid discharge from the serpentine cylinder to the MgO sleeve. From figure 9.9 the experiments where the Br-layer formed only due to the solid state reaction between Atg and MgO can be filtered out. The total discharge of water in the remaining experiments is calculated based on the volume of Br produced in both radial and axial direction, i.e. at the wall and the lids of the serpentine cylinder. Equations used are

$$V_{Br,wall} = [(r_{serp} + d_{Br}^{wall})^2 \; - \; r_{serp}^2]\pi h \tag{9.21}$$

$$V_{Br,lid} = r_{serp}^2 \pi d_{Br}^{lid}, \tag{9.22}$$

where $r_{serp} = 0.75 \cdot 10^{-3}$ m and $h = 1.5 \cdot 10^{-3}$ m are the radius and height of the serpentine cylinder. d_{Br} is the mean thickness of the Br-layer at the lid ($d_{Br}^{lid} = 0.5 \; (top + bottom)$) and the wall ($d_{Br}^{wall} = 0.5 \; (left + right)$). With the density of Br of 2390 kg m^{-3} and a water content of 30.9 wt% (Deer et al., 1992), the mass of Br and the equivalent fluid mass is

$$m_{Br} = 2390 \; V_{Br} \tag{9.23}$$

$$m_{H_2O} = 0.309 \; m_{Br}, \tag{9.24}$$

Since the Br formed represents the time-integrated water discharge, the time-averaged fluid flux q is calculated by dividing the fluid mass by the surface area A of the serpentine cylinder and the run time t:

$$q = 0.309 \; \rho_{Br} \; \frac{V_{Br}}{A \cdot t}, \tag{9.25}$$

The ratio V_{Br}/A is the thickness of the Br-layer. Thus, the fluid flux can be expressed as

$$q = 0.309 \rho_{Br} \frac{d_{Br}}{t}, \tag{9.26}$$

which allows the fluid flux to be determined directly from the BSE images and the run time. The calculated fluid flux for each experiment is given in table 9.3.
Figure 9.14a shows the calculated fluid fluxes in the range $4 \cdot 10^{-8}$ - $3 \cdot 10^{-6}$ kg m^{-2} s^{-1}. A part of this fluid volume actually results from Br formed by the solid state reaction between Atg and MgO. The contribution can be subtracted from the Br volume using the thickness of the adjacent Ol-layer as shown in figure 9.14b. The Atg-MgO interaction does not contribute significantly to the result. The mass flux increases with temperature with only experiment V1156, performed at 830 °C, deviating from this general trend. This experiment, however, was performed at 5 GPa. Due to the negative Clapeyron-slope of Atg dehydration at this pressure the pore overpressure is expected to be negative as will

be described later, resulting in this significant deviation.
An important observation in figure 9.14a is the difference in fluid flux between experiments V1172 and V1175, which were both run at 2 GPa and 643 - 645 °C. The latter experiment, however, was run for 96 h compared to 216 h for experiment V1172. Figure 9.12 suggests that the fluid migration ceases within the first 100 h. If the experimental run time in experiment V1172 is decreased to about 96 h with the assumption that the migration ceased after the same amount of time as in experiment V1175, the calculated fluid flux indeed increases to $9.2 \cdot 10^{-8}\,\mathrm{kg\,m^{-2}\,s^{-1}}$, similar to experiment V1175. This example demonstrates that it is important to know the time period over which fluid flux is active. If the experimental run time is significantly longer than the time of fluid migration, equation 9.26 results in an underestimation of the actual fluid flux. For example, if double the time is taken, the mass flux is underestimated by 50%. For a given pressure gradient thus also the permeability is underestimated by 50% as given by equation 9.31.
Although all fluid fluxes are larger in the direction of the wall compared to the direction of the lid, the difference is relatively small. Also experiment V1175, where the Atg foliation direction was aligned in the vertical direction, has a greater fluid flux towards the wall. As mentioned previously this most likely results from differences in the multi-anvil stress regime between the vertical and horizontal directions and not from permeability anisotropy, which is apparently undetectable during dehydration.

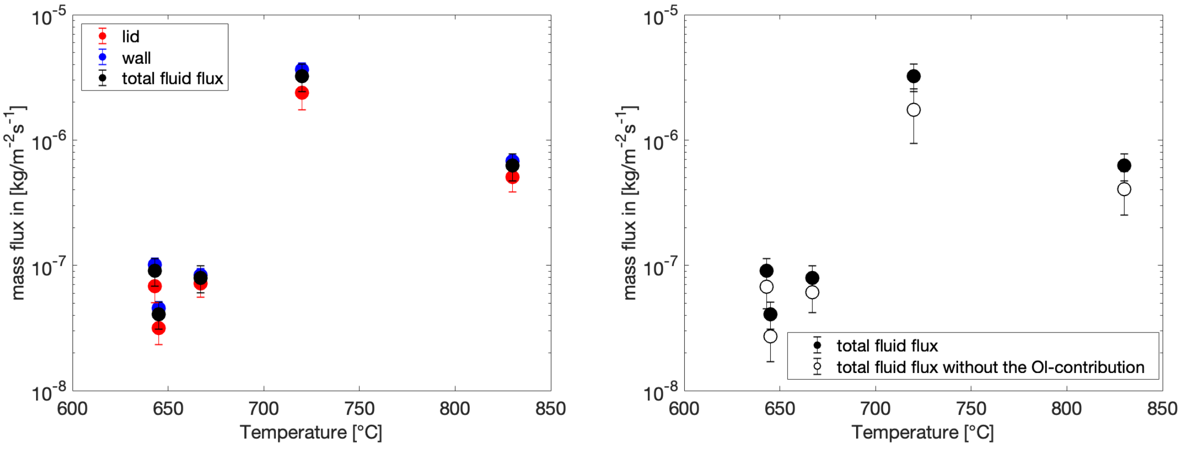

(a) **(b)**

Figure 9.14: a: The mass flux of fluid through the cylinder wall and lid per unit time increases with temperature. In all experiments the flux through the cylinder wall is larger than through the lids. b: Subtracting the Br volume formed upon the Atg-MgO interaction results in a slightly lower fluid flux but does not significantly change the results.

9.7 Permeability determination

According to Darcy's law the fluid flux is driven by a fluid overpressure (Miller et al., 2004), i.e. a pore pressure exceeding the confining pressure, which can be equated to the lithostatic pressure. This overpressure can also be negative, i.e. if under pressure occurs, resulting in a reversal of the fluid flux as shown in figure 9.1. The phase diagrams in figure 1.4 show a change in the slope of the Atg dehydration curve from positive below $P<3$ GPa to negative above $P>3$ GPa. An overpressure can thus be expected upon dehydration at low P conditions according to the Clausius-Clapeyron relations, given as

$$\frac{dP}{dT} = \frac{\Delta S}{\Delta V}, \tag{9.27}$$

with $\frac{dP}{dT}$ being the slope of the dehydration reaction, ΔS and ΔV being the entropy and the volume change of the reaction. ΔS for Atg dehydration is always positive. At low P the volume change thus has to be positive which creates an overpressure on dehydration. At pressures above 3 GPa, however, an underpressure is expected based on the negative volume change resulting from the negative Clausius-Clapeyron slope. In order to estimate the absolute pressure gradient in the experiments, the dehydration reaction in a simple MSH system, given as

$$\begin{array}{cccc} \mathrm{Mg_{48}Si_{34}O_{85}(OH)_{62}} & = 14\ \mathrm{Mg_2SiO_4} & +10\ \mathrm{Mg_2Si_2O_6} & +31\ \mathrm{H_2O}, \\ \mathrm{Atg} & \mathrm{Ol} & \mathrm{Opx} & \mathrm{H_2O} \end{array}$$

is considered. The volume of the solid fraction at equilibrium can be calculated from the molar volumes of each contributing mineral phase using the explicit formulation given by equation 2.25 (section 2.5.2). Assuming that the volume of the cylinder remains instantaneously constant upon dehydration, which is reasonable given that time is required for the entire assembly and gaskets to flow in order for the sample volume to change, then the molar volume occupied by the fluid, i.e. the pore volume, is given as

$$V_{H_2O} = \frac{V_{Atg} - 14V_{Ol} - 10V_{Opx}}{31}. \tag{9.28}$$

The equation of state of Pitzer and Sterner (1995) can be used to calculate the pressure of water as a function of molar volume:

$$P = RT\Big(c_1\rho^2 - \rho\left(\frac{c_3 + 2c_4\rho + 3c_5\rho^2 + 4c_6\rho^3}{(c_2 + c_3\rho + c_4\rho^2 + c_5\rho^3 + c_6\rho^4)^2}\right) + c_7\rho^2\exp(-c_8\rho) + c_9\rho^2\exp(-c_{10}\rho)\Big), \tag{9.29}$$

were c_i are constants depending on T and ρ is the molar density,

$$\rho_{H_2O} = \frac{1}{V_{H_2O}}. \tag{9.30}$$

The excess pressure can be calculated from the difference between the fluid pressure determined for the pore volume calculated using equation 9.28, and the applied confining pressure. In figure 9.15 the excess pressure calculated as a function of temperature for different applied pressures is shown. Experiments conducted at P=2.5 GPa thus have an overpressure, whereas experiments conducted at P=5 GPa are expected to have a large under pressure and thus limited fluid flux and Br growth. The calculated excess pressures for experiments showing Atg dehydration are given in table 9.3.

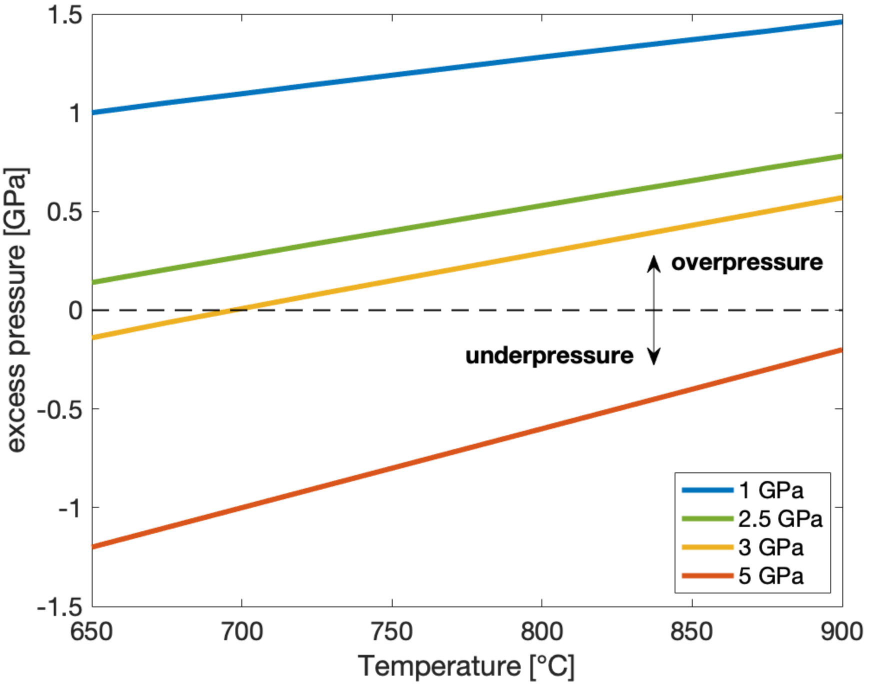

Figure 9.15: The excess pressure, i.e. the pressure difference between pore and lithostatic pressure as a function of temperature corresponding to the range of Atg dehydration. The dashed line marks the transition from an over to an under pressure, which corresponds to the change in slope of the dehydration curve in PT-pseudosections.

Based on Darcy's law the time-averaged permeability can be determined from,

$$k_x = -\frac{\eta q_x}{\partial P / \partial x}. \tag{9.31}$$

where q_x is the mass fluid flux in direction x and $\partial P / \partial x$ denotes the gradient in pressure along x. The pressure gradient arises from the excess pore pressure in the cylinder and becomes zero in the MgO sleeve as the fluid is consumed. However, the term $\partial P / \partial x$ depends on the length scale employed. In figure 9.16 the evolution of the pressure gradient with time is illustrated schematically. Upon instantaneous dehydration, a certain pore pressure P_0 develops in the partially dehydrated serpentine cylinder, whereas no pore pressure is expected in the MgO sleeve. The pressure gradient is a discrete step and the term $\partial P / \partial x$ becomes infinite. With time however, fluid is migrating outwards and a Br-layer grows. Water passing through this layer thus results in a pore pressure outside of the partially dehydrated serpentine cylinder. The boundary conditions in this time step are zero pressure in the MgO and a reduced pressure in the cylinder due to fluid migration. The latter boundary conditions is *a priori* unknown from the experiment. For the calculations the pressure gradient is thus assumed to vary from the total pore pressure at the centre of the cylinder to zero at the outside edge of the Br-layer, i.e. $dx = r_{Atg} + d_{Br}$, as shown by the dashed red line in figure 9.16.

For simplicity the ambient fluid viscosity of 0.001 Pa s is assumed to be constant. The permeability calculated from equation 9.31 is given in table 9.3. Mirroring differences in the Br-layer thickness in axial and radial directions, the permeability is always higher in the radial direction.

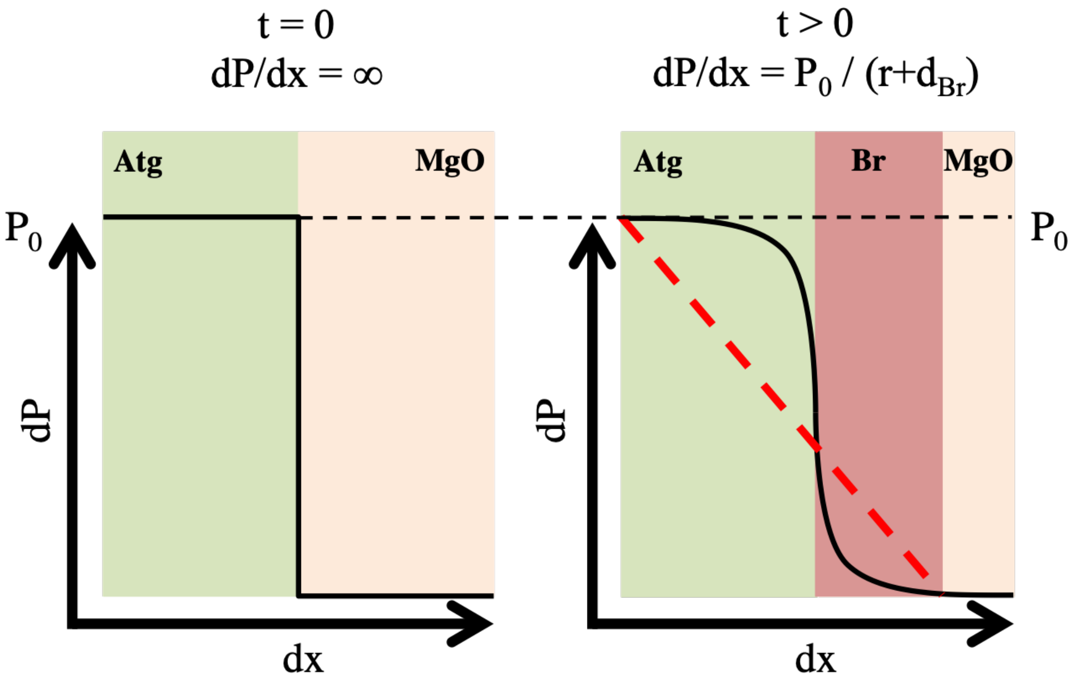

Figure 9.16: Sketch of the evolution of the pressure gradient as a function of time. In the left figure ($t = 0$) the pressure gradient is a discrete step at the interface. The pressure P_0 inside the partially dehydrated serpentine cylinder is simply the excess pressure. In the right figure it is shown that with progressing time, the pressure gradient decreases due to fluid migration. The pressure in the partially dehydrated serpentine cylinder at any time $t > 0$ is unknown. The only known boundary condition is $P = 0$ in the MgO sleeve, which is now separated from the serpentine cylinder by a Br-layer.

Table 9.3: Fluid flux and excess pressure calculated for each experiment as well as the corresponding permeability.

conditions							
name	P GPa	T °C	time h	excess pressure $\mathrm{J\,bar^{-1}}$	fluid flux $\mathrm{kg\,m^{-2}\,s^{-1}}$	permeability $\mathrm{m^2}$ *lid*	 *wall*
V1175	2	643	96	0.41	$9.050 \cdot 10^{-8}$	$0.961 \cdot 10^{-20}$	$1.469 \cdot 10^{-20}$
V1172	2	645	216	0.41	$4.086 \cdot 10^{-8}$	$0.392 \cdot 10^{-20}$	$0.598 \cdot 10^{-20}$
V1166	2	667	96	0.46	$7.954 \cdot 10^{-8}$	$0.970 \cdot 10^{-20}$	$1.080 \cdot 10^{-20}$
ES372	2.5	720	0.5	0.39	$3.232 \cdot 10^{-6}$	$2.876 \cdot 10^{-19}$	$4.981 \cdot 10^{-19}$
V1156	5	830	6	-0.44	$6.247 \cdot 10^{-7}$	$-4.495 \cdot 10^{-20}$	$-7.471 \cdot 10^{-20}$

9.8 Numerical modelling

In order to test for the sensitivity of various parameters on the permeability, an explicit 3-dimensional axis-symmetric finite difference code (kindly written by Marcel Thielmann for this project) has been developed. This numerical approach allows effects such as the permeability contrast between Atg and MgO, the porosity and anisotropy on fluid flux to be explored. This information is especially important in order to improve the experimental setup for future experiments.

The governing equation used is the hydraulic diffusion equation obtained by substituting Darcy's law into the mass conservation equation (eq. 9.15). In cylinder coordinates, due to axis symmetric rotation, the cylindrical sample is fully determined by the spatial coordinates r and z, representing the radial and axial direction. The governing equation is thus written as

$$\frac{\partial P}{\partial t} = \frac{1}{\eta\phi(c_f + c_r)} \left[k_r \, \frac{1}{r}\frac{\partial}{\partial r}\left(r\frac{\partial P}{\partial r} \right) + \, k_z \, \frac{\partial}{\partial z}\left(\frac{\partial P}{\partial z} \right) \right], \tag{9.32}$$

where k_i is the permeability and $\partial P/\partial i$ is the pressure gradient in direction i. For simplicity, η and ϕ are assumed to be constant, as their variations over the experimental PT-range would be small. The constants in equation 9.32 on the right hand side can be combined to the diffusivity constant D, so that

$$\mathrm{D}_i = \frac{k_i}{\phi\eta(c_f + c_r)}. \tag{9.33}$$

The simplifications involved will be evaluated later. The cylinder cross section can be divided into 4 quadrants with dimensions 1.75 × 1.55 mm in total and Atg dimensions of 0.75 × 0.75 mm as shown in figure 9.17. A mesh grid with a resolution of 0.01 × 0.01 mm was used. To each node in the grid the material properties of either Atg or MgO were assigned. These parameters include the permeability in axial and radial directions, the porosity and the initial water content. It is only necessary to solve equation 9.32 for one quadrant. The full sample is ultimately obtained by integrating over the azimuth $\varphi = 2\pi$ and mirroring along r.

While the initial water content in MgO is set to zero, the initial water content in Atg is set to 10.4 wt%. This corresponds to a partially dehydrated model serpentinite at 2.5 GPa and 700 °C as calculated for sample Al06-44 (Padrón-Navarta et al., 2013) (fig. 6.3b). At these conditions, a fluid overpressure of 0.27 GPa is estimated (fig. 9.15). The difficulty arises from the fact that equation 9.32 takes a fluid pressure gradient rather than a fluid content. A conversion between the two measures is thus needed. Assuming a simple linear relation between the overpressure P_{fluid} and the fluid content c_{fluid} results in a conversion factor Γ_f of

$$\Gamma_f = \frac{\mathrm{P}_{fluid}}{\mathrm{c}_{fluid}} = \frac{2700\,\mathrm{bar}}{10.4\,\mathrm{wt\%}}. \tag{9.34}$$

The permeability as estimated from the experiments is of the order of $1 \cdot 10^{-20}\,\mathrm{m}^2$. Thermodynamic calculations on a serpentinite bulk composition result in a volume fluid fraction, i.e. porosity, of 0.2 - 0.3 after complete Atg dehydration. Combined with a dynamic fluid viscosity of 0.001 Pa s, being the ambient condition value, and compressibilities set to unity, D is in the order of $1 \cdot 10^{-16}\,\mathrm{m}^2\,\mathrm{Pa}^{-1}\,\mathrm{s}^{-1}$.

The main difference to the experiments conducted in this study is that the fluid simply flows outward in the numerical model whereas it is absorbed by the MgO in the experiments. In order to also model the absorption, reactive fluid flow would be needed, which is out of the scope in this study. However, it is still possible to obtain first order estimates on the effects of time, absolute D value and D contrasts on the fluid flux by simply varying D, which is done in the following.

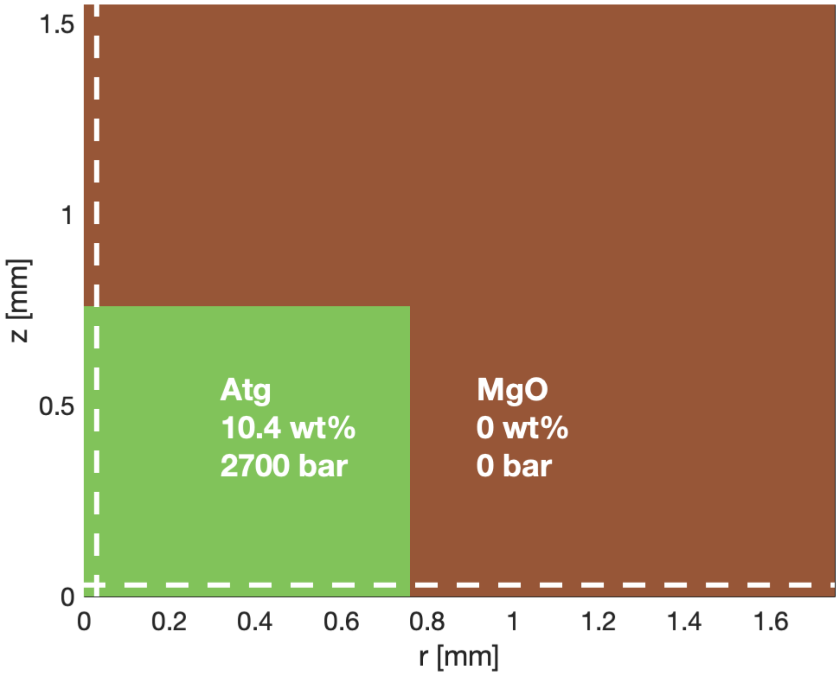

Figure 9.17: Geometry of the numerical model. One quarter of the two dimensional section of the Atg cylinder is calculated. An initial water content of 10.4 wt% is assigned to each node in the serpentine cylinder, giving rise to an overpressure of 2700 bar. The surrounding MgO is initially water free. The two white dashed lines mark the profiles in the axial and radial directions used to analyse the fluid content.

9.8.1 Time

The water content is calculated at different time steps in the simulation along profiles in axial and radial direction (fig. 9.17). For Atg and MgO the same porosity and permeability was used, so that $D_{Atg} = D_{MgO} = 1 \cdot 10^{-16}\,m^2\,Pa^{-1}\,s^{-1}$, as outlined in the previous section. In this first isotropic simulation, the permeability in axial and radial direction is equal. This results in symmetric diffusion profiles that change only as a function of time shown in figure 9.18. With ongoing fluid flow, the total amount of water in Atg decreases whereas MgO becomes water-rich. In the experiments the fluid reacts with MgO forming a Br-layer. The fluid is thus restricted to a small area around the Atg cylinder. In this numerical simulation, however, the fluid is allowed to spread over the whole MgO. It can be seen that already after 50 h of simulation the fluid reaches the rim of the sample. For longer simulations boundary effects play a role in that the bulk water content in the system decreases. Differences in radial and axial directions result from the radial symmetry, i.e. the factor $1/r$ and r in equation 9.32.

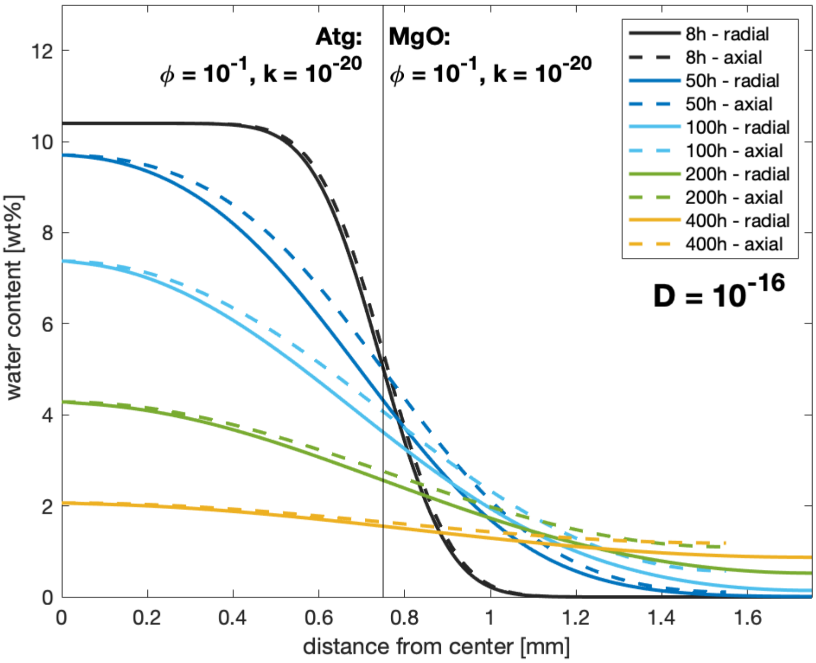

Figure 9.18: Water content in radial and axial directions at different time steps. The equal ϕ and k in Atg and MgO results in symmetric diffusion profiles. The vertical line shows the boundary between Atg and MgO. With increasing time the difference in water content between the two phases diminishes.

9.8.2 Diffusivity

In the simulation shown in figure 9.19 the diffusivity D is changed, which is achieved by changing the permeability of both Atg and MgO by the same amount while the porosity is kept constant. However, the same results would also be achieved by changing any other variable contributing to D in equation 9.33. The fluid flux decreases with decreasing D, which is indicated by less fluid discharge. Since D is the same in both materials, although the absolute amount of fluid at a given time changes, the symmetric character of the diffusion profile remains.

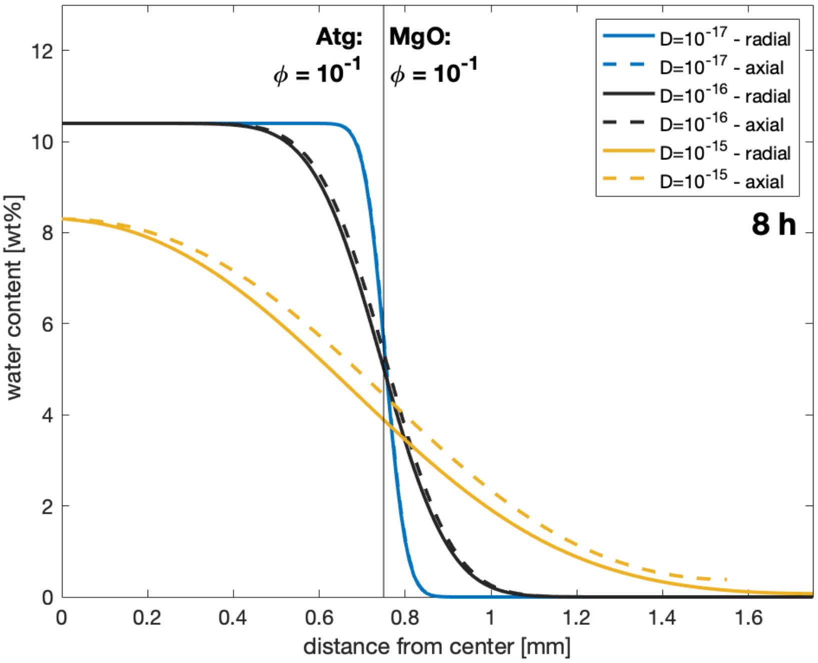

Figure 9.19: Water content in radial and axial directions for different absolute D values. D was changed by changing k while ϕ was kept constant. Simulations were run for 8 h.

9.8.3 Diffusivity contrast

It is likely that Atg and MgO have different porosity and permeability. However, both the porosity and permeability of MgO are unknown. Therefore, it is only possible to calculate relative changes in D between Atg and MgO via D contrasts. The effect of a contrast in D is illustrated in figure 9.20a ($D_{MgO} > D_{Atg}$) and figure 9.20b ($D_{MgO} < D_{Atg}$).
The most obvious result is an asymmetric diffusion profile. D mostly affects the diffusion length scale. For example, by changing D_{MgO}, the area of Atg affected by diffusion does not change, whereas in the MgO the fluid is spread over a larger area with increasing D. Similarly, by changing D_{Atg}, the hydrated area in MgO remains constant, whereas more Atg is affected by diffusion. It can be concluded that a small D_{MgO} with respect to the dehydrating Atg cylinder will retain fluids in the cylinder rather than showing strong diffusion outwards.

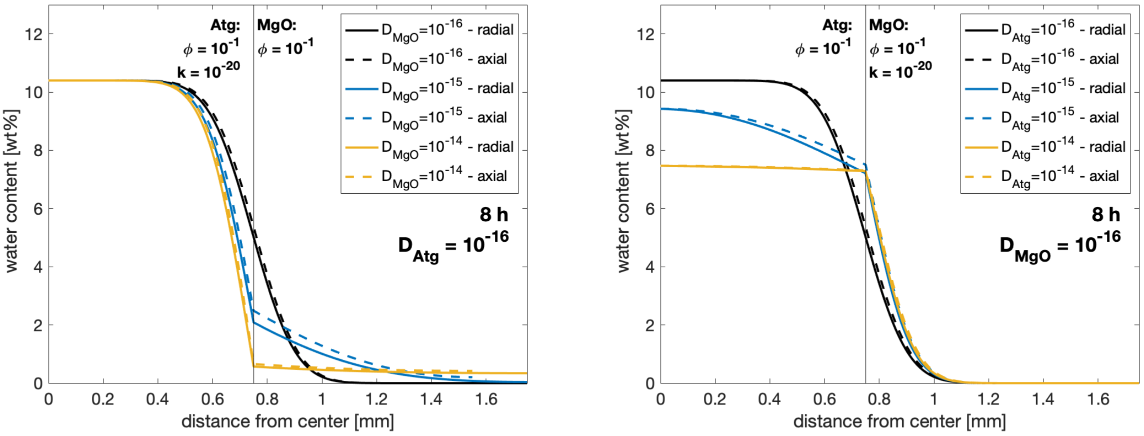

(a) **(b)**

Figure 9.20: Asymmetric diffusion models. a: Variable D_{MgO} at a fixed D_{Atg}. b: Variable D_{Atg} at a fixed D_{MgO}. Changes in D are obtained from changing k of the respective phase. The respective smaller D limits the overall water discharge.

9.8.4 Anisotropy

The initial intention of the experiments was to quantify an anisotropy in the fluid flux. However, the experimental results show that the fluid flow is in fact isotropic despite the preferred orientation of antigorite. The numerical simulations can be used to illustrate what would be expected in case of anisotropic fluid flow. Figure 9.21a shows the change in water content in the system after 50 h for the isotropic case, with $k_r = k_z = 1 \cdot 10^{-20}\,\mathrm{m}^2$. The parameters for MgO are chosen to be identical to Atg, i.e. as in figure 9.18. Figure 9.21b shows the case for a decreased axial and increased radial permeability in Atg. Changing the permeability of Atg relative to MgO, introduces a diffusivity contrast between Atg and MgO and results in an asymmetric diffusion profile.

In the diffusion profiles shown in figure 9.22a there is a sharp decrease in water content in the axial direction for the anisotropic simulation. In the radial direction, however, the water content remains high, up to the contact with MgO. Thus, in case of anisotropy in the experiments, it is indeed expected that a Br-layer forming upon reaction would be thicker in radial direction.

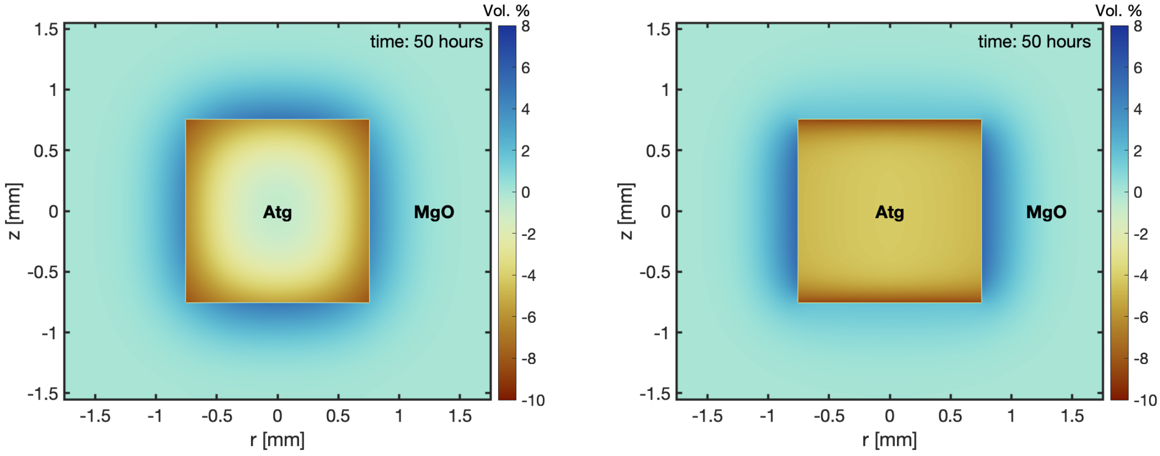

(a) **(b)**

Figure 9.21: Model results for isotropic and anisotropic case illustrating the change in water content after 50 h. a: isotropic. the permeability of Atg in axial and radial direction and in MgO with $k = 1 \cdot 10^{-20}\,\mathrm{m}^2$. b: anisotropic. k_r of Atg is increased to $1 \cdot 10^{-19}\,\mathrm{m}^2$, k_z of Atg is decreased to $1 \cdot 10^{-21}\,\mathrm{m}^2$. A D contrast between Atg and MgO thus occurs in radial and axial direction.

A major limitation of the code is that it does not use reactive fluid flow. Therefore, differences in Br-layer thickness observed in experiments, can not directly be compared to the simulation. However, it is possible to compare the total water in Br in the experiments to the total water content in the MgO obtained from the simulations. To do so the water in MgO needs to be integrated over the cylinder volume. Figure 9.22b shows the total water in MgO for the two simulations in figure 9.21. The water content in radial direction is significantly larger than in axial direction for the isotropic model. This results from difference in the surface area in axial and radial direction. In the anisotropic case the difference in the total water between the axial and radial direction increases. Also shown are the experimental results, where the water is calculated as the mass fraction of the total Br formed. The experimental data are in agreement with the isotropic model.

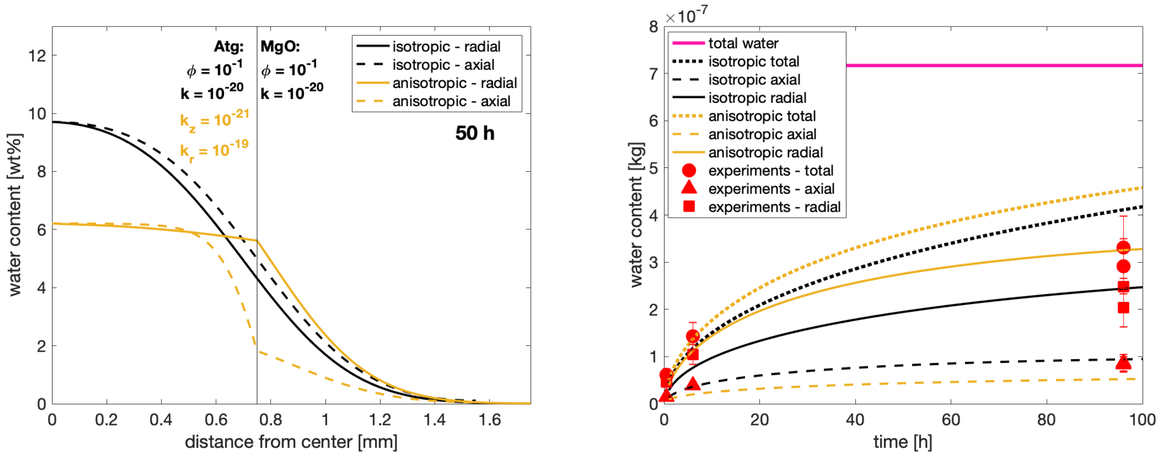

(a) **(b)**

Figure 9.22: a: Water content in axial and radial direction for the anisotropic model as shown in figure 9.21a and 9.21b after 50 h. b: The total water in MgO obtained by integrating over the cylinder volume for the anisotropic and isotropic model. The experimentally determined water content is in agreement with the isotropic model.

9.9 Comparison with existing data

Several previous studies have examined the permeability of Atg at near room pressure conditions (≤150 MPa confining pressure) and either at room temperature (Kawano et al., 2011; Okazaki et al., 2013) or under conditions of Atg dehydration (Tenthorey and Cox, 2003). These results indicate low Atg permeability at temperatures below Atg dehydration. Using a Paterson deformation apparatus, that controls both the confining pressure and pore pressure, Tenthorey and Cox (2003) reported a value of $1 \cdot 10^{-22}\,\mathrm{m}^2$ at room temperature and a confining pressure of 100 MPa (fig. 9.23a). In the experiments performed here very low permeabilities were also encountered below dehydration. In experiment V1170, for example, performed with an $Al(OH)_3$ fluid source, fluid did not pass through the serpentine layer but rather migrated along the interface between the serpentinite and the capsule wall. The movement of fluid along the interface might mirror the behaviour in natural serpentinites in subducting slabs, where the high permeability forces fluid along pathways created by heterogeneities (Plümper et al., 2016).

Tenthorey and Cox (2003) further performed permeability experiments on Atg at elevated temperatures. Their results show an increase of the permeability by two orders of magnitude across the Atg-out transformation. This increase results from the formation of a free fluid upon dehydration and an associated porosity increase of up to 30 %. The data are in excellent agreement with experimental data obtained in this study (fig. 9.23a). Slightly lower absolute values obtained in the current study would be consistent with what would be expected for the higher pressure conditions.

Kawano et al. (2011) reported a strong decrease in Atg permeability at room temperature between room pressure and 50 MPa and an increase in permeability anisotropy. Measurements on crustal rocks also show a decrease in permeability with increasing depth (Manning and Ingebritsen, 1999). This results from compaction, which decreases the porosity and suppresses fracturing. Manning and Ingebritsen (1999) showed that for crustal rocks the permeability drops from $1 \cdot 10^{-14}\,\mathrm{m}^2$ at the Earth surface to an almost limiting value of $10 \cdot 10^{-19}\,\mathrm{m}^2$ by 30 km depth. This latter value might be important for metamorphism because it allows a suitable fluid and solute flow while still limiting the amount cooling due to advective flow. The values for average crustal rocks are illustrated in figure 9.23b as a dashed line, they are higher than the values reported by Kawano et al. (2011), which likely results from different rock textures but might also be due to temperature differences.

Kawano et al. (2011) also reported permeability anisotropy resulting from strong Atg fabric at room pressure with the anistropy increasing from near zero at room pressure to over an order of magnitude by 50 MPa. Okazaki et al. (2013) also reported the development of permeability anisotropy in Atg samples deformed at room temperature in experiments to simulate the behaviour of fault gouge. This was attributed to the development of shape preferred orientation of serpentinite grains. The current study also aimed to test whether this anisotropy persists to high pressures. However, small differences in permeabilities observed between vertical and radial directions in the experiments could be fully attributed to anisotropy in the stress field of the experiment. As shown in the simulations reported in the last section, much larger differences in Br-layer thicknesses would have resulted if permeability anisotropy was of an order of magnitude, as in the experiments of Kawano et al. (2011). This indicates that any anisotropy in permeability disappears as soon as Atg starts to dehydrate.

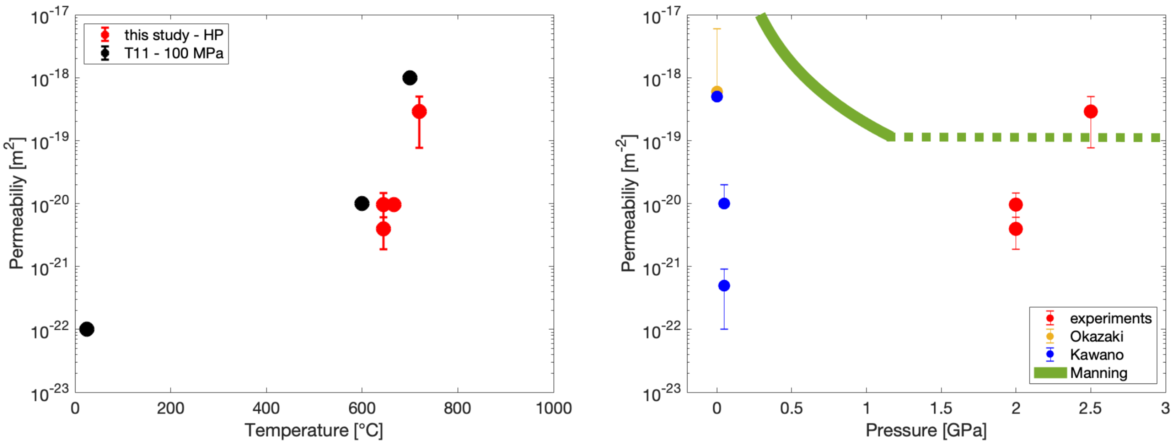

(a) **(b)**

Figure 9.23: a: The permeability as a function of temperature. The permeability increases across the Atg dehydration due to an increase in the porosity. Data from Tenthorey and Cox (2003) performed near room pressure are in agreement with high pressure data from this study. b: Permeability data as a function of pressure. M99 are data along a crustal geotherm. The dashed line indicates constant permeability due to various limiting factors. References: K11 = Kawano et al. (2011), M99 = Manning and Ingebritsen (1999), O13 = Okazaki et al. (2013), T11 = Tenthorey and Cox (2003).

9.10 Discussion and conclusions

In this chapter the results of an entirely new method for the determination of permeability are reported that can be employed in solid media devices at pressures in excess of 1 GPa. Conventional permeability measurements have much greater control and precision over fluid flux and pore pressure measurements but are limited to pressures below approximately 300 MPa. Although such measurements are more accurate, differences in confining pressure and fluid solubilities could affect the permeability and thus influence extrapolation to higher pressures. The experimental approach outlined in this study provides a relatively straight forward possibility for determining permeabilities at simultaneously high pressure and temperature conditions and could be used at significantly higher pressures than those studied here. The permeabilities derived from the experiments in this study are the first data to be reported at such high pressure and temperature conditions and are compatible with the conditions of dehydration reactions in subduction zones.

In this method water is forced out of a dehydrating Atg sample into the surrounding MgO sleeve, through the development of a fluid overpressure, and forms Br on contact. The amount of Br produced gives an approximation of the volume fluid flux. The overpressure can be calculated from the volume change of the solid phases. With an estimate for the fluid viscosity the permeability is then determined using Darcy's law (eq. 9.3).

An important observation is that Br is also formed through solid state reaction between MgO and Atg, even below the Atg dehydration temperature. This solid state reaction produces a layer of Br and an adjacent inner layer of olivine. From the thickness of the olivine layer the amount of Br formed by the solid state reaction can be determined from stoichiometric relations. The Br volume resulting from dehydration induced fluid flow is obtained by difference.

This study illustrates that numerical simulations provide a powerful tool to examine the influence of individual parameters that cannot be constrained in the experiments, some of which change during the course of the experiment. The numerical results indicate that the diffusivity contrast between the serpentine and the surrounding material influences the length over which diffusion takes place, for example. Fluid could be potentially retained in the serpentine cylinder as a result of slow diffusion into this medium, which would lower the apparent permeability. In the experiments the formation of Br is relatively rapid, even in the solid state. The simulations show that the Br permeability is a critical parameter which should be investigated more rigorously. The most important test provided by the simulations concerns the determination of the fluid overpressure. In the simple experimental permeability estimate the overpressure is assumed to be constant, however, in the simulation the initial state relaxes as the fluid flows into the surrounding medium. In figure 9.22b the comparison between the amount of water expelled in the simulation and that in the experiments, however, is found to be in very good agreement when the same approximate permeability is employed. This implies that the assumption of a constant overpressure is a reasonable approximation.

Experiment V1156 performed at 830 °C and 5 GPa provides the first experimental evidence for the effect of the negative Atg dehydration Clapeyron slope on fluid pressure. In this experiment an anomalously small fluid flux occurs even though complete Atg dehydration has taken place. This is consistent with the calculated under pressure of the fluid at these conditions, which results in most of the fluid being retained inside the sample. Whether overpressures result in intermediate depth earthquakes is still a major discussion and alternative explanations are proposed (Ferrand et al., 2017; Gasc et al., 2011). A pore underpressure might, however, explain the relatively sharp decrease in deep focus earthquakes at depths equivalent to pressures of approximately 4 GPa in the subduction zone beneath Southern Chile (Merkulova et al., 2016). Although the fluid flux under such conditions will not be driven by a pore pressure, advective fluid flux might still occur if the buoyancy is larger than the retarding force resulting from the underpressure.

By using $Al(OH)_3$ as the fluid source below a layer of Atg and a layer of MgO on top, it was possible to show that the permeability of Atg before dehydration is very low and is effectively impermeable under an applied overpressure of approximately 1.5 GPa. Natural serpentinites often contain Br (Evans, 2008) and it is possible that the dehydration of Br raises permeabilities at approximately 500 °C. However, Br dehydration produces approximately 2 wt% H_2O and due to the low intrinsic permeability of the remaining serpentinites these fluids might be trapped and build up large overpressures, possibly leading to microfracturing. Such textural features could provide important heterogeneities that also influence the migration of fluids formed at higher PT conditions, e.g. at the beginning of the Atg dehydration (Plümper et al., 2016). This would need to be examined in further experiments.

An important finding is that dehydration causes a major increase in permeability in experiments performed at conditions where Atg actually dehydrates in subduction zones. At 2 GPa the permeability was found to change from $4 \cdot 10^{-21}\,\mathrm{m}^2$ at 645 °C to $3 \cdot 10^{-19}\,\mathrm{m}^2$ at 720 °C. Although these data show a time-averaged permeability, which might be biased by the actual run time, they also show a relative increase of 2 orders of magnitude per 100 °C. As described in the previous section this is in very good agreement with the results obtained at near ambient pressures by Tenthorey and Cox (2003) and implies that pressure does not influence the increase in permeability upon dehydration. Low pressure and temperature permeabilty studies indicate that sample compaction causes permeability to decrease with pressure (Kawano et al., 2011; Manning and Ingebritsen, 1999). For serpentinite in a subduction zone there are, therefore, two competing processes being compaction and dehydration. While compaction appears to increase anisotropy (Kawano et al., 2011) in samples with a strong fabric, the experiments conducted in this study show that anisotropy is lost during dehydration. The fluid flux in radial and axial directions was found to not depend on the orientation of the fabric in the dehydrating serpentine. The small apparent anisotropy in fluid flux most likely resulted from deviatoric stresses in the multi-anvil assembly.

Subducting serpentinite with a strong fabric due to shear deformation may have strong permeability anisotropy but the permeability is low and likely increases with increasing pressure due to compaction. Although the dehydration of Br in serpentinites may raise the permeability, Atg-layers may be quite impermeable up to conditions where dehydration starts. As soon as the Atg dehydration temperature is reached the permeability will increase by several orders of magnitude. This increase in permeability is expected to be anisotropic and fluid migration will be pervasive rather than being focused into higher permeability directions parallel to the dip of the subduction zone. This will have important implications for the mobilisation of other volatile components such as carbon. It has been proposed that carbonate dissolution by H_2O rich fluids is the main mechanism through which carbon is removed from the slab Menzel et al. (2020). Pervasive rather than focused fluid flow would favour large scale dissolution of carbonates from the slab.

9.11 Future work

In order to not underestimate the fluid flux and thus the permeability, it is of major importance to accurately determine the duration of fluid flux. This can be achieved by a series of experiments at similar PT conditions but varying time. Such a time series was started within this study. However, the results indicate the already after 96 h the Br-layer thickness is constant. It would thus be important to especially explore the time range between 12 and 96 h.

So far only one experiment was performed at conditions were an underpressure is expected. A Br-layer however also formed in this experiment. It would be important to explore in a few more experiments how this Br-layer formed if no outwards pointing fluid flux is expected. This likely originates from compaction of the multi-anvil assembly and could be studied more rigorously through a time series of experiments.

No anisotropic fluid flux was observed in the experiments. The absence of an anisotropic permeability would indicate that the very high porosity in dehydrated serpentinites results in diminishing textural effects. However, the fluid flux affects the total amount of fluid in the Atg cylinder and might also affect the overall porosity. There are two endmember scenarios potentially important to the experiments. 1) It might be that the porosity stays constant. In this case a fluid flux leads to a decrease in the pore pressure. Fluid migration is observed until the pore pressure reaches zero. 2) The pores are only open due to the overpressure and shrink with migrating fluids. In this case fluid migration takes place as long as the porosity is non-zero. In order to measure the full 3 dimensional pore space including the pore shape, distribution and connectivity, CT-scans could be performed. Analysing both experiments of the type V1176, which keeps all the fluid inside the dehydrated assemblage and actual fluid flux experiments would show how the fluid flux changes the pore space with time. Numerical simulations including reactive fluid flow might help to better understand the relation between fluid flux and Br formation and how this relation influences the porosity.

Since serpentinites might contain Br, it is important to also study Br-bearing serpentinites. The dehydration of Br at temperatures below the Atg-out reaction might influence the permeability of serpentinites. It is also possible that fracturing occurs due to a fluid overpressure, which might influence the permeability and even might be anisotropic at these conditions.

10 Major conclusions

10.1 Redox state of serpentinites

In the course of the deep Earth volatile cycle, volatiles fixed in the oceanic lithosphere are subducted and returned to the interior. A portion of these volatiles are released from the slab via a series of devolatilisation reactions and recycled back to the surface through arc volcanism, while some portion is retained in the slab and transported into the deeper mantle. Serpentinisation is one of the main mechanisms through which H_2O is fixed in the oceanic lithosphere. However, this process also oxidises ferrous to ferric Fe such that the oxidation state of the oceanic lithosphere is increased. Although the subduction of serpentinites is one of the most important redox mechanisms operating as it removes O_2 from the surface and cycles it into the mantle, very little petrological data exists on the consequences of this process. The principal aim of this thesis is to provide the first experimental data through which the relationship between the oxidation state of Fe in serpentinites and the $f(O_2)$ can be determined. Using this relationship the implications for the phase relations within subducting slabs and the speciation of volatile components can be calculated.

Multi-anvil experiments were conducted at subduction zone conditions on both natural antigorite and lizardite. The $f(O_2)$ was buffered using different metal-oxide pairs or monitored using sliding redox sensors. Detailed analyses of the resulting phase relations allow the high *PT* stability of antigorite and lizardite to be directly compared for the first time. The phase relations for both phases are found to be near identical. Between 2.5 and 5 GPa, a gradual decrease in the serpentine fraction is observed above 550 °C as the proportions of chlorite, pyroxene and olivine increase. Dehydration is complete for both phases at approximately 650 °C. Although antigorite is considered to be the high *PT* polymorph of the serpentine group, lizardite appears to be as stable as antigorite, at least on experimental time scales.

Oxygen fugacities were varied in the experiments between IW and the Ru-RuO_2 buffer. A small increase in the stability of lizardite could be determined at the highest $f(O_2)$. This effect does not result from stabilisation due to ferric Fe but is due to low total Fe contents in lizardite at high $f(O_2)$ when hematite is formed as revealed by thermodynamic modelling.

The first measurements of $Fe^{3+}/\Sigma Fe$ ratios of serpentine minerals recovered from buffered high pressure experiments are reported. The $Fe^{3+}/\Sigma Fe$ ratio of lizardite samples varied in line with the different $f(O_2)$ buffers employed. The Fe^{2+}-Mg exchange between lizardite and coexisting silicates follows expected trends with only few exceptions where equilibrium was not achieved. The Al content of lizardite also varies as a function of temperature as a result of being in equilibrium with chlorite. These are the first experimental data that report the T-dependence of the Al content of a serpentine mineral. The results indicate that this is a useful thermometer.

Although the antigorite $Fe^{3+}/\Sigma Fe$ ratio decreased in some experiments it could not be manipulated using redox buffering assemblages, although the $f(O_2)$ could be determined in antigorite experiments using IrFe-alloy as a sliding redox sensor. The Al content of antigorite did not change with temperature. This can also be confirmed by looking at the Al contents reported for antigorite from previous high pressure experiments. In all cases the Al content remains identical to the starting material. However, Fe^{2+}-Mg exchange between antigorite and coexisting silicates does reach equilibrium at experimental conditions, which can be confirmed by a comparison of the partition coefficients with natural assemblages. It is concluded that the antigorite tetrahedral site does not reequilibrate in experimental timescales, whereas the octahedral site does. It is thus the modulation in the antigorite crystallographic structure, i.e. the reversal of the tetrahedral layer every half unit cell length a, that decreases the rate of cation diffusion in the tetrahedral layer in experimental time scales. This explains why the Al content in antigorite does not change upon changing PT-$f(O_2)$ conditions and why the $Fe^{3+}/\Sigma Fe$ ratio cannot be manipulated. This is clearly not the case in natural samples where the Al content can be seen to increase with temperature(Schwartz et al., 2013). Comparison of the T-dependent Al content in lizardite with natural antigorite data shows that the two sheet silicates behave similarly given sufficient time for equilibration.

The Mössbauer measurements indicate that ferric Fe is dominantly partitioned onto the octahedral site in both antigorite and lizardite. The stoichiometric relations indicate that ferric Fe is charge balanced by Al in both serpentinites, which implies a Tschermak-substitution mechanism, rather than trivalent cations being charge-balanced by cation vacancies or alkali metals. With this information new ferri-alumina-Tschermak endmembers are defined as $Mg_2Fe^{3+}|AlSi|O_5(OH)_4$ and $Mg_{1.824}Fe^{3+}|AlSi|O_5(OH)_{3.647}$ for lizardite and antigorite, respectively.

Using a series of equilibria involving phases with known thermodynamic properties expressions were derived from which the Gibbs free energy of the new ferri-alumina-Tschermak endmembers could be determined as a function of pressure and temperature. Mixing of the ferri-alumina-Tschermak component was considered to be ideal as its proportion does not change enough to cause significant changes in the Gibbs free energy. Different site mixing models were examined but a model that assumes complete disordered mixing on both the octahedral and tetrahedral sites was found to provide the best fit with the lizardite experimental data, which vary over large ranges of $f(O_2)$. An important aspect is that it was only possible to derive this model because lizardite equilibrates on experimental time scales. The broad range of $f(O_2)$ imposed made it possible to explore the nature of ferric Fe mixing in the serpentinite structure. The resulting model could then be applied to the more limited experimental dependence obtained for antigorite. Given the similarities in the crystallographic sites it seems reasonable to assume that the thermodynamics of mixing are similar between the two structures, even if kinetic properties are different. The same model was thus assumed for antigorite.

A simple comparison with the free energies of other serpentine endmembers indicates that Al increases the stability of serpentine, whereas ferric Fe, similar to ferrous Fe, decreases the stability. Using the thermodynamic properties for the new endmembers the $Fe^{3+}/\Sigma Fe$ ratio of lizardite and antigorite can be calculated as a function of $f(O_2)$. The resulting values are in generally good agreement with the experimental data. The model shows that the $Fe^{3+}/\Sigma Fe$ ratio increases with $f(O_2)$ but decreases with temperature. This results from the temperature-dependence of the free energy and from the increase in the serpentine Al content with increasing temperature. Generally, lizardite displays higher $Fe^{3+}/\Sigma Fe$ ratio than antigorite under similar conditions. For example, at an $f(O_2)$ of approximately 2 log units above FMQ and at approximately 500 °C the $Fe^{3+}/\Sigma Fe$ ratio of lizardite is just over twice the value found for antigorite. This observation seems to be broadly in line with natural samples (Evans et al., 2012). The transition between lizardite and antigorite may, therefore, result in the formation of magnetite.

In order to perform more complex analysis of serpentinite phase relations, particularly during dehydration, the new endmembers were included into Perple_X, a global free energy minimisation software package. Additionally, a new alumina-Tschermak endmember was calibrated consistent with the formulation of the ferri-alumina-Tschermak endmember. This new model reproduces observed trends from experimental and natural samples, and shows an increase in the Al content of serpentinite from 0.1 at 530 °C to 0.3 Al pfu at 700 °C. The new model is in much better agreement with the available data compared to a previous model attempt (Padrón-Navarta et al., 2013). In the new model the Al content in serpentine is found to be pressure-independent, in agreement with lizardite experimental data from this study conducted at 3 and 5 GPa and natural antigorite samples, equilibrated at 1.2 GPa in the range of 350 - 500 °C (Schwartz et al., 2013).

A T-$f(O_2)$-phase diagram was calculated for an antigorite-bearing serpentinite bulk composition using Perple_X. The diagram can be separated into regions of Fe-metal, no additional Fe-phases, magnetite and hematite stability in the order of increasing $f(O_2)$. The highest Fe content in antigorite is consequently observed in the regions without additional Fe-phases, which is also the region where the lowest dehydration temperatures of antigorite are obtained. In the Fe-metal and Hem fields the Fe content in antigorite becomes low and the thermal stability increased. The shift in dehydration temperature due to Fe, whether ferric or ferrous, however, is small and of the order of 20 - 30 °C. Similarly, when the new alumina-Tschermak model is used to calculate the effect of Al on antigorite stability, antigorite is shown to be stabilised by the presence of Al but only by 20 °C. The stability field of antigorite has been shown to vary by approximately 100 °C at 3 GPa between different experimental studies (Ulmer and Trommsdorff, 1995; Wunder and Schreyer, 1997; Bromiley and Pawley, 2003; Merkulova et al., 2016). When previous studies are considered in detail there seems to be no consistent variation in dehydration temperature with composition.

An important conclusion from this study is that the Al content of antigorite does not change during the course of an experiment. With increasing temperature the Al content of antigorite should increase and thus expand the antigorite stability field to higher temperatures. As the Al content does not change, the antigorite stability field is likely to be underestimated in phase equilibria experiments. The thermodynamic calculations reported here, however, are based on the experimental behaviour of lizardite, which does reequilibrate in composition, and are therefore likely to provide a more reliable representation of the phase relations.

In experiments performed in the presence of Fe-metal the lizardite stability field is quite strongly reduced in temperature. These results are consistent with thermodynamic calculations that model the fluid as a mixture of H_2O and H_2. The dominance of H_2 in the fluid coexisting with Fe-metal leads to a strong decrease in the antigorite stability field that can be referred to as redox dehydration. This could be an important process in the mantle of Mars, for example, where the $f(O_2)$ is known to be lower than in the Earth (Herd et al., 2002; Herd, 2003; Papike et al., 2004).

Mass balance calculations that consider the partitioning of ferric and ferrous Fe within a serpentinite assemblage were used to calculate how the $f(O_2)$ of such an assemblage varies during subduction for different bulk $Fe^{3+}/\Sigma Fe$ ratios. At 500 °C the boundary between a

Mgt-free and Mgt-bearing assemblage occurs at a bulk $Fe^{3+}/\Sigma Fe$ ratio of approximately 0.1, where the bulk of this ferric Fe resides in antigorite. Below this level the $f(O_2)$ rises strongly with bulk $Fe^{3+}/\Sigma Fe$ ratio but when Mgt becomes stable, which occurs at an $f(O_2)$ around FMQ, the $f(O_2)$ rises less steeply as the proportion of Mgt increases. At a bulk $Fe^{3+}/\Sigma Fe$ ratio of 0.35 Hem starts to form and the $f(O_2)$ is perfectly buffered by Mgt-Hem at an $f(O_2)$ of ΔFMQ+2. Most serpentinites have compositions that would render oxygen fugacities in the range ΔFMQ−0.5 to ΔFMQ+2 at 500 °C. With increasing temperature, however, the Al content of antigorite rises and as antigorite starts to dehydrate the $f(O_2)$ increases as more Mgt forms. In the main phase of antigorite dehydration above 600 °C the $f(O_2)$, regardless, of the initial bulk $Fe^{3+}/\Sigma Fe$ ratio, becomes buffered by the presence of Mgt and Hem. This conclusion is in contrast to recent studies that have proposed $f(O_2)$ at antigorite dehydration which are both higher (Iacovino et al., 2020) and lower (Piccoli et al., 2019) than this but have not considered the ferric Fe content of antigorite.

Previous experimental and natural observations of Mgt loss from serpentinite assemblages at or near dehydration must result from the action of external reducing agents. In experiments this likely results from hydrogen diffusion into the capsule.

Antigorite dehydration is, therefore, one of the few processes in the mantle that will take place under a buffered $f(O_2)$ conditions. Even though this $f(O_2)$ is relatively high, in contrary to previous arguments (Kelley and Cottrell, 2009; Iacovino et al., 2020), there is no obvious mechanism by which fluids can transfer these oxidising conditions to the overlying mantle. The previously proposed transfer of sulphate-rich fluids from serpentinites is contradicted by the current model, because at the $f(O_2)$ of the Mgt-Hem buffer fluids do not contain significant levels of dissolved sulphate (Merkulova et al., 2017; Evans and Powell, 2015). The generally raised oxidation state of arc magmas is most likely not inherited from the oxidised nature of serpentinites.

Antigorite will also form in the peridotite rocks of the mantle wedge as water expelled from subducting sediments rises into the overlying mantle. By applying the same model on a peridotite composition at typical mantle wedge conditions, it can be shown that the mantle wedge will not contain magnetite, which is in agreement with natural observations of mantle wedge related serpentinites (Smith, 2010). As a consequence of the low bulk $Fe^{3+}/\Sigma Fe$ ratio of the typical mantle, the $f(O_2)$ in the antigorite stability field in the wedge will be in the range ΔFMQ−1 to ΔFMQ−2.

Calculations show that if H_2O-rich CO_2-bearing fluids entered the wedge from underlying sediments then they would be reduced to a CH_4-bearing fluid and the mantle would be oxidised. The formation of CH_4 in this way would oxidise the mantle up to oxygen fugacities where the amount of CH_4 in the fluid becomes equal to the amount of CO_2. If the resulting oxidised mantle wedge were further dragged down by coupling with the subducting lithosphere, this might help to explain the apparently raised oxidation state of island arc mantle.

10.2 The stability of carbonates in serpentinites and their effect on antigorite stability

Calcium carbonate is the main carrier of carbon in serpentinites, forming so called ophicarbonates. The experiments performed in this study on ophicarbonate assemblages show that they cause antigorite to breakdown at lower temperatures. This is because clinopyroxene forms as a result of Ca-Mg exchange between carbonate and silicate fraction. The replacement of orthopyroxene by clinopyroxene in the antigorite breakdown products decreases the antigorite dehydration temperature by almost 100 °C at 3 GPa. This is much larger than the effect of any component on antigorite stability. This reaction, however, does not release CO_2, which remains locked in the carbonates. A continuous and large H_2O fluid flow would be required in order to remove a significant amount of carbonate from the serpentinites because the carbonate solubility is very low (Manning and Ingebritsen, 1999). The reduction in the dehydration temperature of antigorite likely prevents the antigorite stability field from reaching conditions where dense hydrous magnesium silicates form, that might transport water into the deeper mantle. Thus, the presence of ophicarbonates may favour the subduction of carbonate-rich but water-poor assemblages into the deep mantle.

For typical serpentinite $Fe^{3+}/\Sigma Fe$ ratios the $f(O_2)$ during subduction will remain in the carbonate rather than the graphite stability field. Only unusually low serpentinite bulk $Fe^{3+}/\Sigma Fe$ ratios of <0.05 would result in $f(O_2)$ entering the graphite stability field. The reduction of graphite from carbonates observed in rocks associated with serpentinites (Galvez et al., 2013) therefore more likely results from hydrogen released from the graphitisation of organic material in serpentinites.

By adding graphite to lizardite experiments a new method was found for determining the fugacity of CO_2. In the presence of graphite ferric Fe in lizardite is reduced and the O_2 released forms CO_2. Due to kinetic limitations at 3 GPa and 500 °C carbonates are not formed upon interaction with olivine. This allows the fugacity of CO_2 to be obtained using the $f(O_2)$, which is determined using an IrFe-alloy sliding redox sensor. The $f(CO_2)$ value obtained is in very good agreement with certain equations of state, which serves as a good test as the equations of state are all extrapolated at pressure above approximately 1 GPa.

10.3 Antigorite permeability during dehydration

In the final part of this thesis a new experimental approach to estimate permeabilities is presented, from which important implications on the extent of fluid-rock interaction can be obtained. The simple setup consists of a serpentinite drill core embedded in an MgO sleeve. A strongly foliated serpentinite sample was chosen. The fluid formed upon serpentine dehydration reacts with MgO to produce brucite. From the amount of brucite formed it is possible to calculate the fluid flux. Combined with an estimate on the pore overpressure the permeability of the dehydrating assemblage can be calculated using Darcy's law. The amount of brucite formed in the sleeve relative to the serpentinite foliation indicates whether the fluid flow and permeability were isotropic.

The results indicate a large increase in permeability of about 2 log units upon dehydration at 3 GPa from below $1 \cdot 10^{-20}\,\mathrm{m}^2$ to near $1 \cdot 10^{-18}\,\mathrm{m}^2$. Experiments using an $Al(OH)_3$ water source indicate that serpentinites are essentially impermeable below the dehydration temperature.

Experiments performed in a previous study at near room pressure and temperature indicated that foliated serpentinites exhibit strong permeability anisotropy (Kawano et al., 2011). If this were the case it would favour the organisation of fluids into bands and veins rather than pervasive flow. The results of this study performed at subduction zone conditions, however, show that all permeability anisotropy is lost once dehydration commences. Based on a 3-dimensional finite difference code the influence of the diffusivity constant and especially the diffusivity contrast could be investigated. The technique could be applied to measure permeabilities in a range of materials at high pressure and temperature by using different fluid sources and sinks.

An anomalously low fluid flux measured at 5 GPa provides the first experimental confirmation for pore fluid underpressure upon antigorite dehydration at pressures above 3 GPa. This would mean that fluids would have to leave the slab through buoyancy forces alone.

In conclusion, carbonates are the stable carbon-bearing phase rather than graphite at conditions where serpentinites dehydrate in subduction zones. The large increase in permeability and the fate of anisotropy upon the dehydration of antigorite will result in a pervasive fluid flow, which increases the fluid-rock interaction. Pervasive rather than channelised flow favours the removal of carbonates from the slab by dissolution in H_2O-rich fluids.

References

Adams, B. L., Wright, S. I., and Kunze, K. (1993). Orientation imaging: The emergence of a new microscopy. *Metallurgical Transactions A*, 24:819–831.

Ague, J. J. (2007). Models of permeability contrasts in subduction zone mélange: Implications for gradients in fluid fluxes, Syros and Tinos Islands, Greece. *Chemical Geology*, 239:217–227.

Ague, J. J. (2014). Deep carbon: Subduction goes organic. *Nature Geoscience*, 7:860–861.

Ague, J. J. and Nicolescu, S. (2014). Carbon dioxide released from subduction zones by fluid-mediated reactions. *Nature Geoscience*, 7:355–360.

Al Reda, S. M., Yu, C., Berthe, G., and Matray, J.-M. (2020). Study of the permeability in the Opalinus clay series (Mont Terri - Switzerland) using the steady state method in Hassler cell. *Journal of Petroleum Science and Engineering*, 184:106457.

Alt, J. C. and Teagle, D. A. H. (1999). The uptake of carbon during alteration of ocean crust. *Geochimica et Cosmochimica Acta*, 63:1527–1535.

Angiboust, S., Agard, P., Jolivet, L., and Beyssac, O. (2009). The Zermatt-Saas ophiolite: The largest (60-km wide) and deepest (c. 70-80km) continuous slice of oceanic lithosphere detached from a subduction zone? *Terra Nova*, 21:171–180.

Annersten, H., Olesch, M., and Seifert, F. A. (1978). Ferric iron in orthopyroxene: a Moessbauer spectroscopic study. *Lithos*, 11:301–310.

Armstrong, K. (2018). Redox Evolution of the Earth's Mantle. *Doctoral thesis, Bayreuther Graduiertenschule für Mathematik und Naturwissenschaften - BayNAT. University of Bayreuth.*

Auzende, A. L., Daniel, I., Reynard, B., Lemaire, C., and Guyot, F. (2004). High-pressure behaviour of serpentine minerals: A Raman spectroscopic study. *Physics and Chemistry of Minerals*, 31:269–277.

Bailey, S. (1969). Polytiypism of trioctahedral 1:1 layer silicates. *Clays and Clay Minerals*, 17:355–371.

Bailey, S., editor (1988). *Hydrous Phyllosilicates (exclusive micas). Reviews in Mineralogy*, volume 19. American Mineralogical Society.

Belonoshko, A. and Saxena, S. K. (1991). A molecular dynamics study of the pressure-volume-temperature properties of supercritical fluids: II. CO2, CH4, CO, O2, and H2. *Geochimica et Cosmochimica Acta*, 55:3191–3208.

Bose, K. and Ganguly, J. (1995). Quartz-coesite transition revisited: reversed experimental determination at 500-1200°C and retrieved thermochemical properties. *American Mineralogist*, 80:231–238.

Bretscher, A., Hermann, J., and Pettke, T. (2018). The influence of oceanic oxidation on serpentinite dehydration during subduction. *Earth and Planetary Science Letters*, 499:173–184.

Bromiley, G. D. and Pawley, A. R. (2003). The stability of antigorite in the system MgO-SiO2-H2O (MSH) and MgO-Al2O3-SiO2-H2O (MASH): The effects of Al3+ substitution on high-pressure stability. *American Mineralogist*, 88:99–108.

Burns, R. G. and Solberg, T. C. (1990). 57Fe-bearing Oxide, Silicate, and Aluminosilicate minerals. Crystal Structure Trends in Mossbauer Spectra. *ACS Symposium Series*, 415:262–283.

Cai, C., Wiens, D. A., Shen, W., and Eimer, M. (2018). Water input into the Mariana subduction zone estimated from ocean-bottom seismic data. *Nature*, 563:389–392.

Campbell, J., Danielson, L., Righter, K., Wang, Y., and Davidson, G. (2006). Oxygen Fugacity at high Pressure: Equations of state of Metal-Oxide pairs. *Lunar and Planetary Science XXXVII.*

Canil, D. and O'Neill, H. S. C. (1996). Distribution of ferric iron in some upper-mantle assemblages. *Journal of Petrology*, 37:609–635.

Capitani, G. and Mellini, M. (2004). The modulated crystal structure of antigorite: The m = 17 polysome. *American Mineralogist*, 89:147–158.

Caruso, L. J. and Chernosky, J. V. (1979). The stability of lizardite. *Canadian Mineralogist*, 17:757–769.

Cesare, B. (1995). Graphite precipitation in C-O-H fluid inclusions: closed system compositional and density changes, and thermobarometric implications. *Contributions to Mineralogy and Petrology*, 122:25–33.

Clerc, C., Boulvais, P., Lagabrielle, Y., and de Saint Blanquat, M. (2014). Ophicalcites from the northern Pyrenean belt: A field, petrographic and stable isotope study. *International Journal of Earth Sciences*, 103:141–163.

Connolly, J. A. D. (2005). Computation of phase equilibria by linear programming: A tool for geodynamic modeling and its application to subduction zone decarbonation. *Earth and Planetary Science Letters*, 236:524–541.

Connolly, J. A. D. and Trommsdorff, V. (1991). Petrogenetic grids for metacarbonate rocks: pressure-temperature phase-diagram projection for mixed-volatile systems. *Contributions to Mineralogy and Petrology*, 108:93–105.

Cook-Kollars, J., Bebout, G. E., Collins, N. C., Angiboust, S., and Agard, P. (2014). Subduction zone metamorphic pathway for deep carbon cycling: I. Evidence from HP/UHP metasedimentary rocks, Italian Alps. *Chemical Geology*, 386:31–48.

Darcy, H. (1856). Les fontaines publiques de la Ville de Dijon. *Paris*.

Dasgupta, R. (2013). Ingassing, Storage, and Outgassing of Terrestrial Carbon through Geologic Time. *Reviews in Mineralogy and Geochemistry*, 75:183–229.

Dasgupta, R. and Hirschmann, M. M. (2010). The deep carbon cycle and melting in Earth's interior. *Earth and Planetary Science Letters*, 298:1–13.

Debret, B., Andreani, M., Muñoz, M., Bolfan-Casanova, N., Carlut, J., Nicollet, C., Schwartz, S., and Trcera, N. (2014). Evolution of Fe redox state in serpentine during subduction. *Earth and Planetary Science Letters*, 400:206–218.

Debret, B., Bolfan-Casanova, N., Padrón-Navarta, J. A., Martin-Hernandez, F., Andreani, M., Garrido, C. J., Lopez Sanchez-Vizcaino, V., Gomez-Pugnaire, M. T., Muñoz, M., and Trcera, N. (2015). Redox state of iron during high-pressure serpentinite dehydration. *Contributions to Mineralogy and Petrology*, 169:1–18.

Deer, W., Howie, R., and Zussmann, J. (1992). *An Introduction to the Rock-Forming Minerals*. Pearson education limited, 2nd edition.

Demichelis, R., Civalleri, B., Noel, Y., Meyer, A., and Dovesi, R. (2008). Structure and stability of aluminium trihydroxides bayerite and gibbsite: A quantum mechanical ab initio study with the Crystal06 code. *Chemical Physics Letters*, 465:220–225.

Driesner, T. (1993). Aspects of petrographical, structural and stable isotope geochemical evolution of ophicarbonate breccias from ocean floor to subduction and uplift: an example from Chatillon, Middle Aosta Valley, Italian Alps. *Schweizerische Mineralogische Und Petrographische Mitteilungen*, 73:69–84.

Dyar, M., Guidotti, C., Harper, G., McKibben, M., and Saccocia, P. (1992). Controls on ferric iron in chlorite. *Geological Society of America Abstracts with Progams, annual meeting of the Geological Society of America (GSA), Cincinnati, OH (United States)*, 24.

Dyar, M. D., Agresti, D. G., Schaefer, M. W., Grant, C. A., and Sklute, E. C. (2006). Mössbauer Spectroscopy of Earth and Planetary Materials. *Annual Review of Earth and Planetary Sciences*, 34:83–125.

Evans, B. W. (2004). The Serpentinite Multisystem Revisited: Chrysotile Is Metastable. *International Geology Review*, 46:479–506.

Evans, B. W. (2008). Control of the Products of Serpentinization by the Fe2+ Mg-1 Exchange Potential of Olivine and Orthopyroxene. *Journal of Petrology*, 49:1873–1887.

Evans, B. W. (2010). Lizardite versus antigorite serpentinite: Magnetite, hydrogen, and life(?). *Geology*, 38:879–882.

Evans, B. W., Dyar, D. M., and Kuehner, S. M. (2012). Implications of ferrous and ferric iron in antigorite. *American Mineralogist*, 97:184–196.

Evans, B. W., Kuehner, S. M., and Chopelas, A. (2009). Magnetite-free, yellow lizardite serpentinization of olivine websterite, Canyon Mountain complex, N.E. Oregon. *American Mineralogist*, 94:1731–1734.

Evans, K. A. and Powell, R. (2015). The effect of subduction on the sulphur, carbon and redox budget of lithospheric mantle. *Journal of Metamorphic Geology*, 33:649–670.

Fabrichnaya, O., Saxena, S., Richet, P., and Westrum, E. (2004). *Thermodynamic Data, Models and Phase Diagrams in Multicomponent Oxide Systems: An Assessment for Materials and Planetary Scientists Based on Calorimetric, Volumetric and Phase Equilibrium Data*. Springer-Verlag Berlin Heidelberg, 1st edition.

Faccenda, M., Gerya, T. V., and Burlini, L. (2009). Deep slab hydration induced by bending-related variations in tectonic pressure. *Nature Geoscience*, 2:790–793.

Ferrand, T. P., Hilairet, N., Incel, S., Deldicque, D., Labrousse, L., Gasc, J., Renner, J., Wang, Y., Green, H. W., and Schubnel, A. (2017). Dehydration-driven stress transfer triggers intermediate-depth earthquakes. *Nature Communications*, 8:15247.

Franzolin, E., Schmidt, M. W., and Poli, S. (2011). Ternary Ca-Fe-Mg carbonates: Subsolidus phase relations at 3.5 GPa and a thermodynamic solid solution model including order/disorder. *Contributions to Mineralogy and Petrology*, 161:213–227.

Frezzotti, M. L., Selverstone, J., Sharp, Z. D., and Compagnoni, R. (2011). Carbonate dissolution during subduction revealed by diamond-bearing rocks from the Alps. *Nature Geoscience*, 4:703–706.

Frost, D. J. and McCammon, C. A. (2008). The Redox State of Earth's Mantle. *Annual Review of Earth and Planetary Sciences*, 36:389–420.

Frost, D. J., Poe, B. T., Trønnes, R. G., Liebske, C., Duba, A., and Rubie, D. C. (2004). A new large-volume multianvil system. *Physics of the Earth and Planetary Interiors*, 143:507–514.

Frost, D. J. and Wood, B. J. (1997). Experimental measurements of the fugacity of C02 and graphite/diamond stability from 35 to 77kbar at 925 to 1650°C. *Geochimica et Cosmochimica Acta*, 61:1565–1574.

Frost, R. B. (1985). On the Stability of Sulfides, Oxides, and Native Metals in Serpentinite. *Journal of Petrology*, 26:31–63.

Früh-Green, G. L., Kelley, D. S., Bernasconi, S. M., Karson, J. A., Ludwig, K. A., Butterfield, D. A., Boschi, C., and Proskurowski, G. (2003). 30,000 Years of Hydrothermal Activity at the Lost City Vent Field. *Science*, 301:495–498.

Galvez, M. E., Beyssac, O., Martinez, I., Benzerara, K., Chaduteau, C., Malvoisin, B., and Malavieille, J. (2013). Graphite formation by carbonate reduction during subduction. *Nature Geoscience*, 6:473–477.

Ganguly, J. and Ghose, S. (1979). Aluminous orthopyroxene: Order-disorder, thermodynamic properties, and petrologic implications. *Contributions to Mineralogy and Petrology*, 69:375–385.

Garcia, X., Akanji, L. T., Blunt, M. J., Matthai, S. K., and Latham, J. P. (2009). Numerical study of the effects of particle shape and polydispersity on permeability. *Physical Review E*, 80:021304.

Gasc, J., Schubnel, A., Brunet, F., Guillon, S., Mueller, H. J., and Lathe, C. (2011). Simultaneous acoustic emissions monitoring and synchrotron X-ray diffraction at high pressure and temperature: Calibration and application to serpentinite dehydration. *Physics of the Earth and Planetary Interiors*, 189:121–133.

Gerya, T. V., Stockhert, B., and Perchuk, A. L. (2002). Exhumation of high-pressure metamorphic rocks in a subduction channel: A numerical simulation. *Tectonics*, 21:1056.

Gorman, P. J., Kerrick, D. M., and Connolly, J. A. D. (2006). Modeling open system metamorphic decarbonation of subducting slabs. *Geochemistry, Geophysics, Geosystems*, 7:Q04007.

Grevel, K.-D., Burchard, M., and Faßhauer, D. W. (2000). Pressure-volume-temperature behavious of diaspore and corundum: An in situ X-ray diffraction study comparing different pressure media. *Journal of Geophysical Research*, 105:27877–27887.

Grove, T. L., Chatterjee, N., Parman, S. W., and Médard, E. (2006). The influence of H2O on mantle wedge melting. *Earth and Planetary Science Letters*, 249:74–89.

Gudmundsson, G. and Wood, B. J. (1995). Experimental tests of garnet peridotite oxygen barometry. *Contributions to Mineralogy and Petrology*, 119:56–67.

Guillot, S., Hattori, K. H., and De Sigoyer, J. (2000). Mantle wedge serpentinization and exhumation of eclogites: Insights from eastern Ladakh, northwest Himalaya. *Geology*, 28:199–202.

Hatakeyama, K., Katayama, I., Hirauchi, K. I., and Michibayashi, K. (2017). Mantle hydration along outer-rise faults inferred from serpentinite permeability. *Scientific Reports*, 7:13870.

Herd, C. D. K. (2003). The oxygen fugacity of olivine-phyric martian basalts and the components within the mantle and crust of Mars. *Meteoritics and Planetary Science*, 38:1793–1805.

Herd, C. D. K., Borg, L. E., Jones, J. H., and Papike, J. J. (2002). Oxygen fugacity and geochemical variations in the martian basalts: Implications for martian basalt petrogenesis and the oxidation state of the upper mantle of Mars. *Geochimica et Cosmochimica Acta*, 66:2025–2036.

Hermann, J., Troitzsch, U., and Scott, D. (2016). Experimental subsolidus phase relations in the system CaCO3-CaMg(CO3)2 up to 6.5 GPa and implications for subducted marbles. *Contributions to Mineralogy and Petrology*, 171:84.

Hernlund, J., Leinenweber, K., Locke, D., and Tyburczy, J. A. (2006). A numerical model for steady-state temperature distributions in solid-medium high-pressure cell assemblies. *American Mineralogist*, 91:295–305.

Hilairet, N., Daniel, I., and Reynard, B. (2006). P-V equations of state and the relative stabilities of serpentine varieties. *Physics and Chemistry of Minerals*, 33:629–637.

Hinsken, T., Bröcker, M., Strauss, H., and Bulle, F. (2017). Geochemical, isotopic and geochronological characterization of listvenite from the Upper Unit on Tinos, Cyclades, Greece. *Lithos*, 282-283:281–297.

Holland, T., Baker, J., and Powell, R. (1998). Mixing properties and activity-composition relationships of chlorites in the system MgO-FeO-Al2O3-SiO2-H2O. *European Journal of Mineralogy*, 10:395–406.

Holland, T. and Powell, R. (1991). A Compensated-Redlich-Kwong (CORK) equation for volumes and fugacities of CO2 and H2O in the range 1 bar to 50 kbar and 100-1600Â°C. *Contributions to Mineralogy and Petrology*, 109:265–273.

Holland, T. and Powell, R. (1996). Thermodynamics of order-disorder in minerals: II . Symmetric formalism applied to solid solutions. *American Mineralogist*, 81:1425–1437.

Holland, T. J. and Powell, R. (1998). An internally consistent thermodynamic data set for phases of petrological interest. *Journal of Metamorphic Geology*, 16:309–343.

Holland, T. J. and Powell, R. (2011). An improved and extended internally consistent thermodynamic dataset for phases of petrological interest, involving a new equation of state for solids. *Journal of Metamorphic Geology*, 29:333–383.

Holloway, J. R. (1987). Igneous fluids. In Carmichael, S. and Eugster, H., editors, *Thermodynamic Modeling of Geological Materials: Minerals, Fluids and Melts. Reviews in Mineralogy*, volume 17, pages 211–233. American Mineralogical Society.

Horn, C., Bouilhol, P., and Skemer, P. (2020). Serpentinization, Deformation, and Seismic Anisotropy in the Subduction Mantle Wedge. *Geochemistry, Geophysics, Geosystems*, 21.

Huang, Y., Nakatani, T., Nakamura, M., and McCammon, C. (2019). Saline aqueous fluid circulation in mantle wedge inferred from olivine wetting properties. *Nature Communications*, 10:5557.

Huizenga, J. M. (2011). Thermodynamic modelling of a cooling C-O-H fluid-graphite system: Implications for hydrothermal graphite precipitation. *Mineralium Deposita*, 46:23–33.

Iacovino, K., Guild, M. R., and Till, C. B. (2020). Aqueous fluids are effective oxidizing agents of the mantle in subduction zones. *Contributions to Mineralogy and Petrology*, 175:36.

Iwamori, H. (2007). Transportation of H2O beneath the Japan arcs and its implications for global water circulation. *Chemical Geology*, 239:182–198.

Jakobsson, S. (2012). Oxygen fugacity control in piston-cylinder experiments. *Contributions to Mineralogy and Petrology*, 164:397–406.

Jennings, E. S. and Holland, T. J. (2015). A simple thermodynamic model for melting of peridotite in the system NCFMASOCr. *Journal of Petrology*, 56:869–892.

Johnson, M. C. and Walker, D. (1993). Brucite [Mg(OH)2] dehydration and the molar volume of H2O to 15 GPa. *American Mineralogist*, 78:271–284.

Kawamoto, T. (2006). Hydrous phases and water transport in the subducting slab. *Reviews in Mineralogy & Geochemistry*, 62:273–290.

Kawano, S., Katayama, I., and Okazaki, K. (2011). Permeability anisotropy of serpentinite and fluid pathways in a subduction zone. *Geology*, 39:939–942.

Kelemen, P. B. and Manning, C. E. (2015). Reevaluating carbon fluxes in subduction zones, what goes down, mostly comes up. *Proceedings of the National Academy of Sciences*, 112:E3997–E4006.

Kelemen, P. B., Matter, J., Streit, E. E., Rudge, J. F., Curry, W. B., and Blusztajn, J. (2011). Rates and Mechanisms of Mineral Carbonation in Peridotite: Natural Processes and Recipes for Enhanced, in situ CO2 Capture and Storage. *Annual Review of Earth and Planetary Sciences*, 39:545–576.

Keller, L. M. and Holzer, L. (2018). Image-Based Upscaling of Permeability in Opalinus Clay. *Journal of Geophysical Research: Solid Earth*, 123:285–295.

Kelley, D. S., Karson, J. A., Früh-Green, G. L., Yoerger, D. R., Shank, T. M., Butterfield,

D. A., Haxes, J. M., Schrenk, M. O., Olson, E. J., Prokurowski, G., Jakuba, M., Bradley, A., Larson, B., Ludwig, K., Glickson, D., Buckman, K., Bradley, A. S., Brazelton, W. J., Roe, K., Elend, M. J., Delacour, A., Bernasconi, S. M., Lilley, M. D., Baross, J. A., Summons, R. E., and Sylva, S. P. (2005). A Serpentinite-Hosted Ecosystem: The Lost City Hydrothermal Field. *Science*, 307:1428–1434.

Kelley, K. A. and Cottrell, E. (2009). Water and the oxidation state of subduction zone magmas. *Science*, 325:605–607.

Kerrick, D. M. and Connolly, J. A. D. (2001). Metamorphic devolatilization of subducted oceanic metabasalts: Implications for seismicity, arc magmatism and volatile recycling. *Earth and Planetary Science Letters*, 189:19–29.

Klein, F. and Garrido, C. J. (2011). Thermodynamic constraints on mineral carbonation of serpentinized peridotite. *Lithos*, 126:147–160.

Kodolanyi, J., Pettke, T., Spandler, C., Kamber, B. S., and Gmeling, K. (2012). Geochemistry of Ocean Floor and Fore-arc Serpentinites: Constraints on the Ultramafic Input to Subduction Zones. *Journal of Petrology*, 53:235–270.

Komabayashi, T. and Fei, Y. (2010). Internally consistent thermodynamic database for iron to the Earth's core conditions. *Journal of Geophysical Research*, 115:B03202.

Korenaga, J. (2017). On the extent of mantle hydration caused by plate bending. *Earth and Planetary Science Letters*, 457:1–9.

Li, K., Li, L., Pearson, D. G., and Stachel, T. (2019). Diamond isotope compositions indicate altered igneous oceanic crust dominates deep carbon recycling. *Earth and Planetary Science Letters*, 516:190–201.

Loewenstein, M. (1953). The ditribution of aluminum in the tetrahedra of silicates and aluminates. *American Mineralogist*, 38:92–96.

MacKenzie, K. J. D. (1973). Thermal reactions of inorganic hydroxy-compounds under applied electric fields, II. *Journal of Thermal Analysis*, 5:19–32.

Magni, V., Bouilhol, P., and van Hunen, J. (2014). Deep water recycling through time. *Geochemistry, Geophysics, Geosystems*, 15:4203–4216.

Manning, C. E. and Ingebritsen, S. E. (1999). Permeability of the continental crust:

Implications of geothermal data and metamorphic systems. *Reviews of Geophysics*, 37:127–150.

Manning, C. E., Shock, E. L., and Sverjensky, D. A. (2013). The Chemistry of Carbon in Aqueous Fluids at Crustal and Upper-Mantle Conditions: Experimental and Theoretical Constraints. *Reviews in Mineralogy and Geochemistry*, 75(1):109–148.

Manthilake, G., Bolfan-casanova, N., Novella, D., Mookherjee, M., and Andrault, D. (2016). Dehydration of chlorite explains anomalously high electrical conductivity in the mantle wedges. *Science Advances*, 2:e1501631.

Mantovani, R. (1889). Les fractures de l'ecorce terrestre et la theorie de Laplace. *Bull. Soc. Sc. Et Arts Reunion*, pages 41–53.

Maurice, J., Bolfan-Casanova, N., Demouchy, S., Chauvigne, P., Schiavi, F., and Debret, B. (2020). The intrinsic nature of antigorite breakdown at 3 GPa: Experimental constraints on redox conditions of serpentinite dehydration in subduction zones. *Contributions to Mineralogy and Petrology*, 175:94.

Mayhew, L. E. and Ellison, E. T. (2020). A synthesis and meta-analysis of the Fe chemistry of serpentinites and serpentine minerals. *Philosophical Transactions of the Royal Society A: Mathematical, Physical and Engineering Sciences*, 378:20180420.

Mellini, M. (1982). The crystal structure of lizardite 1T: hydrogen bonds and polytypism. *American Mineralogist*, 67:587–598.

Mellini, M., Trommsdorff, V., and Compagnoni, R. (1987). Antigorite polysomatism: behaviour during progressive metamorphism. *Contributions to Mineralogy and Petrology*, 97:147–155.

Menzel, M. D., Garrido, C. J., and López Sánchez-Vizcaíno, V. (2020). Fluid-mediated carbon release from serpentinite-hosted carbonates during dehydration of antigorite-serpentinite in subduction zones. *Earth and Planetary Science Letters*, 531:115964.

Menzel, M. D., Marchesi, C., and Garrido, C. J. (2019). Subduction metamorphism of serpentinite-hosted carbonates beyond antigorite-serpentinite dehydration (Nevado-Filabride Complex, Spain). *Journal of Metamorphic Geology*, 37:1–35.

Merkulova, M., Muñoz, M., Vidal, O., and Brunet, F. (2016). Role of iron content on serpentinite dehydration depth in subduction zones: Experiments and thermodynamic modeling. *Lithos*, 264:441–452.

Merkulova, M. V., Muñoz, M., Brunet, F., Vidal, O., Hattori, K., Vantelon, D., Trcera, N., and Huthwelker, T. (2017). Experimental insight into redox transfer by iron- and sulfur-bearing serpentinite dehydration in subduction zones. *Earth and Planetary Science Letters*, 479:133–143.

Miller, S. A., Collettini, C., Chiaraluce, L., Cocco, M., Barchi, M., and Kaus, B. J. (2004). Aftershocks driven by a high-pressure CO2 source at depth. *Nature*, 427:724–727.

Nakamura, Y., Yoshino, T., and Satish-Kumar, M. (2020). Pressure dependence of graphitization: implications for rapid recrystallization of carbonaceous material in a subduction zone. *Contributions to Mineralogy and Petrology*, 175:32.

Ohtani, E. (2020). Role of water in the Earth's mantle. *National Science Review*, 7:224–232.

Okazaki, K., Katayama, I., and Noda, H. (2013). Shear-induced permeability anisotropy of simulated serpentinite gouge produced by triaxial deformation experiments. *Geophysical Research Letters*, 40:1290–1294.

O'Neill, H. S. C. (1987). Quartz-fayalite-iron and quartz-fayalite-magnetite equilibria and the free energy of formation of fayalite (Fe2SiO4) and magnetite (Fe3O4). *American Mineralogist*, 72:67–75.

O'Neill, H. S. C. and Nell, J. (1997). Gibbs free energies of formation of RuO2, IrO2, and OsO2: A high-temperature electrochemical and calorimetric study. *Geochimica et Cosmochimica Acta*, 61:5279–5293.

O'Neill, H. S. C. and Wood, B. J. (1979). An Experimental Study of Fe - Mg Partitioning Between Garnet and Olivine and Its Calibration as a Geothermometer. *Contributions to Mineralogy and Petrology*, 70:59–70.

Padrón-Navarta, J. A., Hermann, J., Garrido, C. J., López Sánchez-Vizcaíno, V., and Gómez-Pugnaire, M. T. (2010). An experimental investigation of antigorite dehydration in natural silica-enriched serpentinite. *Contributions to Mineralogy and Petrology*, 159:25–42.

Padrón-Navarta, J. A., Lopez Sanchez-Vizcaino, V., Garrido, C. J., and Gomez-Pugnaire, M. T. (2011). Metamorphic Record of High-pressure Dehydration of Antigorite Serpentinite to Chlorite Harzburgite in a Subduction Setting (Cerro del Almirez, Nevado-Filabride Complex, Southern Spain). *Journal of Petrology*, 52:2047–2078.

Padrón-Navarta, J. A., Sánchez-Vizcaíno, V. L., Hermann, J., Connolly, J. A. D., Garrido, C. J., Gómez-Pugnaire, M. T., and Marchesi, C. (2013). Tschermak's substitution in antigorite and consequences for phase relations and water liberation in high-grade serpentinites. *Lithos*, 178:186–196.

Papike, J., Karner, J., and Shearer, C. (2004). Comparative planetary mineralogy : V/(Cr + Al) systematics in chromite as an indicator of relative oxygen fugacity. *American Mineralogist*, 89:1557–1560.

Peacock, S. M. (1987). Serpentinization and infiltration metasomatism in the Trinity peridotite, Klamath province, northern California: implications for subduction zones. *Contribution to Mineralogy and Petrology*, 95:55–70.

Peacock, S. M. (1990). Fluid Processes in Subduction Zones. *Science*, 248:329–337.

Piccoli, F., Hermann, J., Pettke, T., Connolly, J. A., Kempf, E. D., and Vieira Duarte, J. F. (2019). Subducting serpentinites release reduced, not oxidized, aqueous fluids. *Scientific Reports*, 9:19573.

Piccoli, F., Vitale Brovarone, A., Beyssac, O., Martinez, I., Ague, J. J., and Chaduteau, C. (2016). Carbonation by fluid-rock interactions at high-pressure conditions: Implications for carbon cycling in subduction zones. *Earth and Planetary Science Letters*, 445:146–159.

Pirard, C. and Hermann, J. (2015). Focused fluid transfer through the mantle above subduction zones. *Geology*, 43(10):915–918.

Pitzer, K. S. and Sterner, S. M. (1994). Equations of state valid continuously from zero to extreme pressures for H2O and CO2. *Journal of Chemical Physics*, 101:3111–3116.

Pitzer, K. S. and Sterner, S. M. (1995). Equations of State Valid Continuously from Zero to Extreme Pressures with H20 and CO2 as Examples. *International Journal of Thermophysics*, 16:511–518.

Plank, T. and Manning, C. E. (2019). Subducting carbon. *Nature*, 574:343–352.

Plümper, O., John, T., Podladchikov, Y. Y., Vrijmoed, J. C., and Scambelluri, M. (2016). Fluid escape from subduction zones controlled by channel-forming reactive porosity. *Nature Geoscience*, 10:150–156.

Pownceby, M. I. and O'Neill, H. S. C. (1994). Thermodynamic data from redox reactions at high temperatures. IV. Calibration of the Re-ReO_2 oxygen buffer from EMF and NiO+Ni-Pd redox sensor measurements. *Contributions to Mineralogy and Petrology*, 118:130–137.

Prescher, C., McCammon, C., and Dubrovinsky, L. (2012). MossA: A program for analyzing energy-domain Mössbauer spectra from conventional and synchrotron sources. *Journal of Applied Crystallography*, 45:329–331.

Rinaudo, C., Gastaldi, D., and Belluso, E. (2003). Characterization of chrysotile, antigorite and lizardite by FT-Raman spectroscopy. *Canadian Mineralogist*, 41:883–890.

Rüpke, L. H., Morgan, J. P., Hort, M., and Connolly, J. A. (2004). Serpentine and the subduction zone water cycle. *Earth and Planetary Science Letters*, 223:17–34.

Santis, R. D., Breedveld, G. J. F., and Prausnitz, J. M. (1974). Thermodynamic Properties of Aqueous Gas Mixtures at Advanced Pressures. *Industrial & Engineering Chemistry Process Design and Development*, 13:374–377.

Schmidt, M. W. and Poli, S. (1998). Experimentally based water budgets for dehydrating slabs and consequences for arc magma generation. *Earth and Planetary Science Letters*, 163:361–379.

Schmidt, M. W. and Poli, S. (2014). 4.19 - Devolatilization during subduction. In Holland, H. D. and Turekian, K. K., editors, *Treatise on Geochemistry*, pages 669–701. Elsevier Ltd., 2nd edition.

Schwartz, S., Guillot, S., Reynard, B., Lafay, R., Debret, B., Nicollet, C., Lanari, P., and Auzende, A. L. (2013). Pressure-temperature estimates of the lizardite/antigorite transition in high pressure serpentinites. *Lithos*, 178:197–210.

Schwarzenbach, E. M., Caddick, M. J., Beard, J. S., and Bodnar, R. J. (2016). Serpentinization, element transfer, and the progressive development of zoning in veins: evidence from a partially serpentinized harzburgite. *Contributions to Mineralogy and Petrology*, 171:5.

Schwarzenbach, E. M., Früh-Green, G. L., Bernasconi, S. M., Alt, J. C., and Plas, A. (2013). Serpentinization and carbon sequestration: A study of two ancient peridotite-hosted hydrothermal systems. *Chemical Geology*, 351:115–133.

Schwerdtfeger, K. and Zwell, L. (1968). Activities in Solid Iridium-Iron and Rhodium-Iron Alloys at 1200°C. *Transactions of the Metallurgical Society of AIME*, 242:631–633.

Sengor, A. M. C. (2014). Eduard Suess and Global Tectonics: an Illustrated ‘Short Guide’. *Austrian Journal of Earth Sciences*, 107:6–82.

Shen, T., Zhang, C., Chen, J., Hermann, J., Zhang, L., Padrón-Navarta, J. A., Chen, L., Xu, J., and Yang, J. (2020). Changes in the cell parameters of antigorite close to its dehydration reaction at subduction zone conditions. *American Mineralogist*, 105:569–582.

Shilobreeva, S., Martinez, I., Busigny, V., Agrinier, P., and Laverne, C. (2011). Insights into C and H storage in the altered oceanic crust: Results from ODP/IODP Hole 1256D. *Geochimica et Cosmochimica Acta*, 75:2237–2255.

Shirey, S. B., Cartigny, P., Frost, D. J., Keshav, S., Nestola, F., Nimis, P., Pearson, D. G., Sobolev, N. V., and Walter, M. J. (2013). Diamonds and the Geology of Mantle Carbon. *Reviews in Mineralogy and Geochemistry*, 75:355–421.

Sieber, M. J., Yaxley, G. M., and Hermann, J. (2020). Investigation of Fluid-driven Carbonation of Hydrated, Forearc Mantle Wedge using Serpentinite Cores in High-pressure Experiments. *Journal of Petrology*, 61:egaa035.

Smit, M. A. and Mezger, K. (2017). Earth’s early O2 cycle suppressed by primitive continents. *Nature Geoscience*, 10:788–793.

Smith, D. (2010). Antigorite peridotite, metaserpentinite, and other inclusions within diatremes on the Colorado plateau, SW USA: Implications for the mantle wedge during low-angle subduction. *Journal of Petrology*, 51:1355–1379.

Stagno, V. (2011). The carbon speciation in the Earth’s interior as function of pressure, temperature and oxygen fugacity. *Doctoral thesis, Bayreuther Graduiertenschule für Mathematik und Naturwissenschaften - BayNAT. University of Bayreuth*, 115.

Stagno, V., Ojwang, D. O., McCammon, C. A., and Frost, D. J. (2013). The oxidation state of the mantle and the extraction of carbon from Earth’s interior. *Nature*, 493:84–88.

Stanley, S. (2005). *Earth System History.* W.H. Freeman and Company, 2nd edition.

Stern, R. J. (2018). The evolution of plate tectonics. *Philosophical Transactions of the Royal Society A*, 376:20170406.

Swartzendruber, L. J. (1984). The Fe-lr (Iron-Iridium) System Fe-ir. *Bulletin of Alloy Phase Diagrams*, 5:48–52.

Syracuse, E. M., van Keken, P. E., and Abers, G. A. (2010). The global range of subduction zone thermal models. *Physics of the Earth and Planetary Interiors*, 183:73–90.

Tenthorey, E. and Cox, S. F. (2003). Reaction-enhanced permeability during serpentinite dehydration. *Geology*, 31:921–924.

Thomson, A. R., Walter, M. J., Kohn, S. C., and Brooker, R. A. (2016). Slab melting as a barrier to deep carbon subduction. *Nature*, 529:76–79.

Tian, M., Katz, R. F., Rees Jones, D. W., and May, D. A. (2019). Devolatilization of Subducting Slabs, Part II: Volatile Fluxes and Storage. *Geochemistry, Geophysics, Geosystems*, 20:6199–6222.

Trommsdorff, V. and Evans, B. W. (1977). Antigorite-Ophicarbonates: Phase Relations in a Portion of the System CaO-MgO-SiO2-H2O-CO2. *Contributions to Mineralogy and Petrology*, 60:39–56.

Tumiati, S., Tiraboschi, C., Sverjensky, D. A., Pettke, T., Recchia, S., Ulmer, P., Miozzi, F., and Poli, S. (2017). Silicate dissolution boosts the CO2 concentrations in subduction fluids. *Nature Communications*, 8:616.

Ulmer, P. and Trommsdorff, V. (1995). Serpentine Stability to Mantle Depths and Subduction-Related Magmatism. *Science*, 268:858–861.

van de Moortèle, B., Bezacier, L., Trullenque, G., and Reynard, B. (2010). Electron backscattering diffraction (EBSD) measurements of antigorite lattice-preferred orientations (LPO). *Journal of Microscopy*, 239:245–248.

van Keken, P. E., Hacker, B. R., Syracuse, E. M., and Abers, G. A. (2011). Subduction factory: 4. Depth dependent flux of H2O from subducting slabs worldwide. *Journal of Geophysical Research*, 116:B01401.

von Seckendorff, V. and O'Neill, H. S. C. (1993). An experimental study on Fe-Mg partitioning between olivine and orthopyroxene at 1173, 1273 and 1473 K and 1.6 GPa. *Contributions to Mineralogy and Petrology*, 113:196–207.

Wegener, A. (1912). Die Entstehung der Kontinente. *Geologische Rundschau*, 3:276–292.

Wei, C. and Powell, R. (2003). Phase relations in high-pressure metapelites in the system KFMASH (K2O-FeO-MgO-Al2O3-SiO2-H2O) with application to natural rocks. *Contributions to Mineralogy and Petrology*, 145:301–315.

Wheaton, R. (2016). *Fundamentals of Applied Reservoir Engineering*. Gulf Professional Publishing, 1st edition.

White, R. W., Powell, R., and Phillips, G. N. (2003). A mineral equilibria study of the hydrothermal alteration in mafic greenschist facies rocks at Kalgoorlie, Western Australia. *Journal of Metamorphic Geology*, 21:455–468.

Whitney, D. L. and Evans, B. W. (2010). Abbreviations for names of rock-forming minerals. *American Mineralogist*, 95:185–187.

Woodland, A. and O'Neill, H. S. C. (1997). Thermodynamic data for Fe-bearing phases obtained using noble metal alloys as redox sensors. *Geochimica et Cosmochimica Acta*, 61:4359–4366.

Wunder, B., Baronnet, A., and Schreyer, W. (1997). Ab-initio synthesis and TEM confirmation of antigorite in the system MgO-SiO2-H2O. *American Mineralogist*, 82:760–764.

Wunder, B. and Schreyer, W. (1997). Antigorite: High-pressure stability in the system MgO-SiO2-H2O (MSH). *Lithos*, 41:213–227.

Wunder, B., Wirth, R., and Gottschalk, M. (2001). Antigorite: Pressure and temperature dependence of polysomatism and water content. *European Journal of Mineralogy*, 13:485–495.

Appendix

A Solid solution models

Table A.1: Phases and solid solution models used to derive *PT*-pseudosections. The name of solid solution models refers to the name in the Perple_X input file.

Phase	solid solution model	comments	reference
Carbonate-bearing systems			
Olivine	O(HP)		Holland and Powell (1998)
Orthopyroxene	Opx(HP)	without Al-endmembers	Holland and Powell (1996)
Clinopyroxene	Cpx(HP)	without Al-endmembers	Holland and Powell (1996)
Amphibole	GlTrTsPg	without Al-endmembers	Wei and Powell (2003); White et al. (2003)
Antigorite	Atg(PN)		Padrón-Navarta et al. (2013)
Chlorite	Chl(HP)		Holland et al. (1998)
Garnet	Gt(HP)		Holland and Powell (1998)
Spinel	Sp(JH)		Jennings and Holland (2015)
Carbonate	oCcM(EF)		Franzolin et al. (2011)
Fluid	F		Connolly and Trommsdorff (1991)
Brucite	B		ideal
Talc	T		ideal
Carbonate-free systems			
Olivine	O(HP)		Holland and Powell (1998)
Orthopyroxene	Opx(HP)	without Al-endmembers	Holland and Powell (1996)
Orthoamphibole	Anth		ideal
Antigorite	Atg(PN)	for reference model	Padrón-Navarta et al. (2013)
Antigorite	Atg(LE)	with new endmembers	this study
Chlorite	Chl(HP)		Holland et al. (1998)
Garnet	Gt(HP)		Holland and Powell (1998)
Spinel	Sp(JH)		Jennings and Holland (2015)
Fluid	F		Connolly and Trommsdorff (1991)
Brucite	B		ideal
Talc	T		ideal

Solution model used for ferri-alumina-Tschermak antigorite

```
                --------------------------------------------------------
begin_model
                Antigorite with Tschermak's substitution (PadrÛn-Navarta et al., 2013, Lithos)
                Adding ferric iron endmember. LE, 2020.

                This model requires make definition:
                    atgts_LE = 17 clin -37 br - 51/2 en + 17 fo       | high DFQ needed to stabilise Chl
                    DQF = 1.57e6 -455.3*T_K -12*P_bar

                    fatgts = 17 clin -37 br - 51/2 en + 17 fo + 496/48 fta - 496/48 ta
                    DQF = 1.57e6 -455.3*T_K -12*P_bar

                    f3atg = 17 clin - 1 atg - 6 br - 17/2 cor + 17/2 hem
                    DQF = 1.78e6 -455.3*T_K -12*P_bar

                    ff3atg = 17 clin - 1 atg - 6 br - 17/2 cor + 17/2 hem - 496/48 ta + 496/48 fta
                    DQF = 1.78e6 -455.3*T_K -12*P_bar


                                    M                   T
                                    ____________________________
                  Mutliplicity      48                  34
                                    ____________________________
                  1 atg             Mg                  Si
        Species:  2 fatg            Fe                  Si
                  3 atgts_LE        Mg31 Al17           AlSi
                  4 fatgts          Fe31 Al17           AlSi
                  5 f3atg           Mg31 Fe3+17         AlSi
                  6 ff3atg          Fe31 Fe3+17         AlSi
                                    ____________________________

Atg(LE)
abbreviation Atg
full_name    serpentine

7                         | model type: reciprocal, macroscopic
2                         | 2 site reciprocal solution, T is defined by m3+ on site M
2  3                    | 4 species on site M
atg      fatg           | endmember names
atgts_LE  fatgts
f3atg    ff3atg

0                      | 0 dependent endmember

0 0 0 0 0 0            | endmember flags, indicate if the endmember is part of the solution.

                       | subdivision model for the octahedral site
0.0 1. 0.2  0          | range and resolution for X(Mg) on site 1, imod = 0 -> Cartesian subdivision
0.0 1. 0.2  0          | range and resolution for X(Al) on site 1, imod = 0 -> cartesian subdivision
0.0 1. 0.2  0          | range and resolution for X(Fe3+) on site 1, imod = 0 -> cartesian subdivision

ideal

2                      | 2 site (M, T) configurational entropy model

2 34.                  | 2 species on T, 34 sites per formula unit.
z(al,t) = 1/2 atgts_LE + 1/2 fatgts + 1/2 f3atg + 1/2 ff3atg

4 48.                  | 4 species on M, 48 site per formula unit.
z(mg,m) = 1 atg + 31/48 atgts_LE + 31/48 f3atg
z(fe,m) = 1 fatg + 31/48 fatgts + 31/48 ff3atg
z(al,m) = 17/48 atgts_LE + 17/48 fatgts

end_of_model
```

B EPMA data

Table B.1: Major oxide composition of serpentine in run products: Mean values and 1σ standard deviation of EPMA measurements. H_2O is calculated by difference for each point measurement. Only major oxides are reported. Stoichiometry is reported as mean values of all point measurements and normalised to 5 cations per formula in Liz and 4.824 cations per formula unit in Atg. Mg# refers to molar MgO/(MgO+FeO), not corrected for ferric Fe.

sample		SiO_2 wt%	Cr_2O_3 wt%	FeO wt%	Al_2O_3 wt%	MgO wt%	H_2O wt%	total wt%	Si pfu	Fe pfu	Al pfu	Mg pfu	Mg#
V1087	mean	41.88	0.21	3.76	2.51	37.20	13.96	99.51	1.95	0.15	0.14	2.58	0.95
	σ	1.03	0.08	0.57	0.15	0.37	1.75		0.02	0.02	0.01	0.04	
V1090	mean	40.42	0.24	4.82	2.54	36.80	14.68	99.51	1.90	0.19	0.14	2.57	0.93
	σ	0.64	0.07	0.44	0.17	0.69	0.95		0.02	0.02	0.01	0.03	
V1104	mean	42.05	0.19	4.65	2.54	37.64	12.47	99.52	1.92	0.18	0.14	2.57	0.94
	σ	0.48	0.07	0.33	0.20	0.35	0.47		0.02	0.01	0.01	0.02	
V1105	mean	41.93	0.16	4.35	2.44	37.91	12.75	99.55	1.92	0.17	0.13	2.59	0.94
	σ	0.54	0.06	0.09	0.20	0.25	0.48		0.02	0.01	0.01	0.02	
V1111	mean	41.70	0.17	4.33	2.55	37.52	13.29	99.56	1.92	0.17	0.14	2.58	0.94
	σ	0.48	0.08	0.11	0.23	0.20	0.44		0.02	0.01	0.01	0.01	
V1159b	mean	41.09	0.22	4.70	2.46	37.44	13.57	99.48	1.90	0.18	0.13	2.58	0.93
	σ	0.54	0.09	0.32	0.21	0.38	0.71		0.02	0.01	0.01	0.02	
V1057	mean	41.90	0.19	3.88	2.45	37.01	14.06	99.49	1.95	0.15	0.13	2.57	0.94
	σ	0.34	0.09	0.51	0.19	0.94	1.09		0.04	0.02	0.01	0.03	
V1079	mean	40.34	0.20	4.32	2.43	37.84	14.30	99.44	1.88	0.17	0.13	2.62	0.94
	σ	0.32	0.12	0.12	0.22	0.28	0.31		0.01	0.01	0.01	0.02	
V1082	mean	40.74	0.14	4.60	2.47	38.08	13.45	99.48	1.88	0.18	0.13	2.62	0.94
	σ	0.31	0.05	0.15	0.24	0.20	0.26		0.01	0.01	0.01	0.01	
V1124	mean	41.33	0.22	4.72	2.49	37.35	13.27	99.39	1.91	0.18	0.14	2.57	0.93
	σ	0.36	0.15	0.29	0.23	0.34	0.45		0.01	0.01	0.01	0.02	
V1143a	mean	41.96	0.15	3.41	2.44	37.91	13.79	99.67	1.94	0.13	0.13	2.61	0.95
	σ	0.28	0.05	0.21	0.23	0.39	0.35		0.01	0.01	0.01	0.02	
V1148a	mean	40.86	0.19	4.14	2.67	36.19	15.57	99.63	1.94	0.16	0.15	2.55	0.94
	σ	0.41	0.09	0.12	0.14	0.23	0.46		0.01	0.01	0.01	0.01	
V1153b	mean	41.15	0.22	4.14	2.72	35.65	15.72	99.6	1.96	0.17	0.15	2.53	0.94
	σ	0.41	0.18	0.13	0.33	0.34	0.42		0.02	0.01	0.02	0.02	
V1160b	mean	40.81	0.19	4.49	2.51	37.60	14.12	99.72	1.89	0.17	0.14	2.60	0.94
	σ	0.29	0.09	0.18	0.19	0.33	0.41		0.01	0.01	0.01	0.02	

Table B.1 continued

sample		SiO_2 wt%	Cr_2O_3 wt%	FeO wt%	Al_2O_3 wt%	MgO wt%	H_2O wt%	total wt%	Si pfu	Fe pfu	Al pfu	Mg pfu	Mg#
V1149	mean	41.33	0.18	4.52	2.47	37.09	14.05	99.64	1.92	0.18	0.14	2.57	0.94
	σ	0.27	0.06	0.17	0.22	0.25	0.36		0.01	0.01	0.01	0.01	
V1152	mean	41.17	0.27	4.45	2.56	36.71	14.51	99.66	1.93	0.17	0.14	2.56	0.94
	σ	0.18	0.07	0.10	0.19	0.74	0.67		0.03	0.01	0.01	0.03	
ES369	mean	40.14	0.21	4.56	2.61	37.44	14.73	99.69	1.88	0.18	0.14	2.61	0.94
	σ	0.62	0.07	0.11	0.16	0.34	0.92		0.01	0.01	0.01	0.01	
ES372	mean	40.81	0.09	4.40	2.46	37.18	14.82	99.75	1.91	0.17	0.14	2.59	0.94
	σ	0.34	0.06	0.10	0.15	0.31	0.48		0.01	0.01	0.01	0.01	
V1155	mean	40.19	0.22	5.05	2.75	36.97	14.49	99.66	1.88	0.20	0.15	2.58	0.93
	σ	1.18	0.09	0.54	0.31	0.43	1.07		0.04	0.02	0.02	0.03	
V1157	mean	40.67	0.23	4.49	2.63	37.51	14.19	99.71	1.89	0.17	0.14	2.60	0.94
	σ	0.46	0.12	0.13	0.21	0.25	0.61		0.02	0.01	0.01	0.01	
V1163	mean	40.58	0.13	4.50	2.56	37.53	14.31	99.61	1.89	0.18	0.14	2.60	0.94
	σ	0.35	0.06	0.12	0.20	0.27	0.39		0.01	0.01	0.01	0.01	
V1165	mean	40.45	0.25	4.50	2.65	37.15	14.70	99.7	1.89	0.18	0.15	2.59	0.94
	σ	0.48	0.06	0.16	0.18	1.16	1.19		0.04	0.01	0.01	0.04	
V1170	mean	41.26	0.23	4.50	2.74	37.22	13.77	99.72	1.91	0.18	0.15	2.57	0.94
	σ	0.33	0.06	0.10	0.12	0.32	0.38		0.02	0.01	0.01	0.02	
V1171	mean	41.13	0.22	4.44	2.75	37.34	13.79	99.68	1.91	0.17	0.15	2.58	0.94
	σ	0.23	0.07	0.10	0.23	0.44	0.42		0.01	0.01	0.01	0.02	
V1114	mean	39.56	0.42	5.44	1.90	37.05	15.29	99.65	1.94	0.22	0.11	2.70	0.92
	σ	1.67	0.46	1.17	1.44	0.95	0.91		0.07	0.05	0.08	0.05	
V1116	mean	37.17	0.94	5.13	4.77	36.36	15.23	99.6	1.82	0.21	0.28	2.65	0.93
	σ	0.66	0.34	0.34	0.95	0.71	0.76		0.03	0.01	0.06	0.04	
V1117	mean	38.17	0.71	4.80	3.52	37.03	15.45	99.68	1.87	0.20	0.20	2.70	0.93
	σ	1.70	0.54	0.79	1.91	1.22	0.93		0.07	0.03	0.11	0.07	
V1125	mean	39.18	0.26	5.99	1.54	38.13	14.48	99.57	1.90	0.24	0.09	2.75	0.92
	σ	1.93	0.34	2.58	1.22	1.47	0.54		0.07	0.11	0.07	0.07	
V1159a	mean	37.74	0.98	4.19	4.67	36.94	15.10	99.63	1.84	0.17	0.27	2.68	0.94
	σ	1.46	0.73	0.55	1.41	0.95	0.71		0.06	0.02	0.08	0.05	
V1127	mean	36.34	0.93	3.72	5.10	37.06	16.69	99.83	1.79	0.15	0.30	2.72	0.95
	σ	0.87	0.28	1.18	1.08	0.66	0.57		0.04	0.05	0.06	0.04	
V1128	mean	36.47	0.91	4.73	5.12	35.88	16.75	99.86	1.81	0.20	0.30	2.65	0.93
	σ	0.47	0.23	0.51	0.85	0.63	0.80		0.03	0.02	0.05	0.04	

Table B.1 continued

sample		SiO_2 wt%	Cr_2O_3 wt%	FeO wt%	Al_2O_3 wt%	MgO wt%	H_2O wt%	total wt%	Si pfu	Fe pfu	Al pfu	Mg pfu	Mg#
V1132a	mean	40.07	0.29	3.77	1.64	39.16	14.87	99.8	1.93	0.15	0.09	2.81	0.95
	σ	1.86	0.34	1.28	1.30	1.01	0.55		0.07	0.05	0.08	0.05	
V1132b	mean	38.86	0.38	5.44	1.93	38.05	15.15	99.81	1.89	0.22	0.11	2.76	0.93
	σ	1.61	0.38	1.52	1.59	1.00	0.53		0.07	0.06	0.09	0.06	
V1139	mean	38.90	0.65	3.94	2.67	37.73	15.97	99.85	1.90	0.16	0.15	2.75	0.94
	σ	1.66	0.55	0.62	1.65	1.08	0.56		0.07	0.03	0.10	0.06	
V1143b	mean	39.56	0.56	3.78	2.66	38.42	14.65	99.63	1.91	0.15	0.15	2.76	0.95
	σ	2.12	0.47	0.78	1.87	1.34	0.72		0.08	0.03	0.11	0.07	
V1146a	mean	39.46	0.47	2.19	2.21	38.57	16.79	99.69	1.93	0.09	0.13	2.82	0.97
	σ	2.18	0.51	0.94	2.05	1.16	0.68		0.09	0.04	0.12	0.07	
V1146b	mean	39.69	0.28	3.16	1.40	37.82	17.33	99.67	1.97	0.13	0.08	2.80	0.96
	σ	1.23	0.35	0.74	1.29	0.62	0.67		0.06	0.03	0.08	0.04	
V1148b	mean	38.51	0.65	3.49	2.89	37.31	16.79	99.64	1.90	0.14	0.17	2.75	0.95
	σ	1.92	0.54	0.85	1.83	1.45	0.79		0.08	0.04	0.11	0.08	
V1150a	mean	38.63	0.74	2.36	3.81	37.88	16.30	99.72	1.89	0.10	0.22	2.76	0.97
	σ	1.60	0.50	0.71	1.86	1.05	0.43		0.07	0.03	0.11	0.06	
V1150b	mean	37.88	0.98	3.19	4.12	36.61	16.97	99.74	1.88	0.13	0.24	2.70	0.95
	σ	0.83	0.50	0.46	1.30	0.68	0.49		0.04	0.02	0.08	0.04	
V1153a	mean	39.17	0.62	2.28	3.20	37.27	17.12	99.65	1.94	0.09	0.19	2.75	0.97
	σ	1.14	0.37	0.36	1.29	0.78	0.69		0.05	0.02	0.08	0.04	

Table B.2: Major oxide composition of chlorite in run products: Mean values and 1σ standard deviation of EPMA measurements. H_2O is calculated by difference for each point measurement. Only major oxides are reported. Stoichiometry is calculated for each point measurement and normalised to 5 cations per formula unit. Mg# refers to molar MgO/(MgO+FeO), not corrected for ferric Fe.

sample		SiO_2 wt%	Cr_2O_3 wt%	FeO wt%	Al_2O_3 wt%	MgO wt%	H_2O wt%	total wt%	Si pfu	Cr pfu	Fe pfu	Al pfu	Mg pfu	Mg#
V1113	mean	32.56	2.00	3.29	14.60	33.06	14.00	99.5	1.57	0.08	0.13	0.83	2.38	0.95
	σ	1.52	0.41	0.72	1.91	0.50	0.64		0.07	0.02	0.03	0.11	0.03	

Table B.2 continued

sample		SiO_2 wt%	Cr_2O_3 wt%	FeO wt%	Al_2O_3 wt%	MgO wt%	H_2O wt%	total wt%	Si pfu	Cr pfu	Fe pfu	Al pfu	Mg pfu	Mg#
V1114	mean	33.30	1.59	3.07	13.22	33.05	15.20	99.43	1.63	0.06	0.13	0.76	2.41	0.95
	σ	0.67	0.03	0.06	0.26	0.66	0.30		0.02	0.01	0.01	0.01	0.02	
V1115	mean	32.79	1.68	3.52	13.14	32.93	15.49	99.54	1.61	0.07	0.14	0.76	2.41	0.94
	σ	1.44	0.30	0.33	2.51	1.01	0.73		0.07	0.01	0.01	0.14	0.07	
V1116	mean	33.04	1.39	3.08	12.28	33.12	16.84	99.76	1.64	0.06	0.13	0.72	2.45	0.95
	σ	0.66	0.03	0.06	0.25	0.66	0.34		0.02	0.01	0.01	0.01	0.02	
V1117	mean	32.11	1.59	2.94	15.28	33.54	14.18	99.63	1.54	0.06	0.12	0.87	2.40	0.95
	σ	0.23	0.06	0.16	0.32	0.13	0.32		0.01	0.01	0.01	0.01	0.02	
V1092	mean	34.38	0.76	3.73	12.58	33.95	14.06	99.46	1.66	0.03	0.15	0.71	2.44	0.94
	σ	0.83	0.09	0.09	1.02	0.15	0.80		0.04	0.01	0.01	0.05	0.02	
V1105	mean	34.60	0.74	3.97	11.78	34.53	13.85	99.46	1.66	0.03	0.16	0.67	2.47	0.94
	σ	0.62	0.08	0.13	0.83	0.57	0.63		0.04	0.01	0.01	0.04	0.03	
V1111	mean	35.14	0.65	3.29	12.64	34.21	13.58	99.51	1.68	0.03	0.13	0.71	2.44	0.95
	σ	0.13	0.10	0.58	0.36	0.59	0.71		0.02	0.01	0.02	0.02	0.02	
V1057	mean	33.33	0.83	4.02	12.88	33.99	14.24	99.29	1.61	0.03	0.16	0.73	2.44	0.94
	σ	0.83	0.31	0.26	0.40	0.52	1.08		0.04	0.01	0.01	0.02	0.02	
V1060	mean	32.09	0.51	4.22	15.75	33.79	13.04	99.4	1.52	0.02	0.17	0.88	2.39	0.93
	σ	0.69	0.04	0.17	1.44	1.33	0.62		0.03	0.01	0.01	0.09	0.07	
V1071	mean	32.70	0.66	3.92	13.95	34.31	13.89	99.43	1.57	0.03	0.16	0.79	2.45	0.94
	σ	0.28	0.25	0.19	0.66	0.58	0.44		0.01	0.01	0.01	0.04	0.04	
V1076	mean	32.05	0.72	3.54	15.13	33.33	14.67	99.45	1.55	0.03	0.14	0.86	2.40	0.94
	σ	0.77	0.13	0.15	0.80	0.67	0.79		0.03	0.01	0.01	0.05	0.03	
V1082	mean	33.51	0.69	4.06	12.44	34.00	14.12	98.81	1.62	0.03	0.16	0.71	2.45	0.94
	σ	0.67	0.01	0.08	0.25	0.68	0.28		0.02	0.01	0.01	0.01	0.02	
V1127	mean	34.26	1.00	2.03	10.79	35.74	15.94	99.76	1.66	0.04	0.08	0.62	2.59	0.97
	σ	1.62	0.54	0.34	1.76	1.40	0.96		0.06	0.02	0.01	0.11	0.08	
V1128	mean	31.77	1.92	2.70	14.38	33.19	15.80	99.75	1.55	0.07	0.11	0.83	2.42	0.96
	σ	0.26	0.37	0.09	0.83	0.32	0.92		0.01	0.02	0.01	0.04	0.01	
V1132b	mean	33.56	1.64	2.83	12.32	34.96	14.54	99.85	1.61	0.06	0.11	0.70	2.51	0.96
	σ	0.67	0.03	0.06	0.25	0.70	0.29		0.02	0.01	0.01	0.01	0.03	
V1135a	mean	33.28	0.93	1.55	13.52	36.79	13.59	99.66	1.56	0.04	0.06	0.75	2.58	0.98
	σ	0.37	0.15	0.14	0.41	0.72	0.35		0.02	0.01	0.01	0.03	0.04	
V1135b	mean	32.67	1.82	3.48	14.20	34.02	13.50	99.71	1.56	0.07	0.14	0.80	2.42	0.95
	σ	0.52	0.47	0.34	0.79	0.87	0.93		0.04	0.02	0.01	0.04	0.03	

Table B.2 continued

sample		SiO_2 wt%	Cr_2O_3 wt%	FeO wt%	Al_2O_3 wt%	MgO wt%	H_2O wt%	total wt%	Si pfu	Cr pfu	Fe pfu	Al pfu	Mg pfu	Mg#
V1140	mean	32.06	1.36	3.67	14.07	33.37	15.26	99.79	1.56	0.05	0.15	0.81	2.42	0.94
	σ	0.48	0.23	0.64	1.20	0.64	0.32		0.02	0.01	0.03	0.07	0.04	
V1146a	mean	31.61	1.27	1.87	15.31	33.28	16.05	99.39	1.55	0.05	0.08	0.88	2.43	0.97
	σ	0.63	0.03	0.04	0.31	0.67	0.32		0.02	0.01	0.01	0.01	0.02	
V1166	mean	33.22	0.65	3.18	14.02	34.31	14.30	99.67	1.59	0.02	0.13	0.79	2.45	0.95
	σ	0.85	0.23	0.22	0.61	0.24	0.61		0.04	0.01	0.01	0.04	0.02	
V1167	mean	32.80	0.76	3.40	14.83	34.02	13.83	99.63	1.57	0.03	0.14	0.83	2.42	0.95
	σ	0.83	0.12	0.33	0.56	0.42	0.42		0.04	0.01	0.01	0.03	0.03	
V1170	mean	30.33	0.12	3.44	21.19	30.43	14.11	99.6	1.46	0.01	0.14	1.20	2.18	0.94
	σ	1.01	0.08	0.54	1.56	0.41	0.47		0.05	0.01	0.02	0.09	0.03	
V1172	mean	34.38	0.78	2.90	13.67	34.17	13.76	99.66	1.64	0.03	0.12	0.77	2.43	0.95
	σ	1.33	0.25	0.38	0.95	0.29	0.91		0.05	0.01	0.02	0.06	0.02	

Table B.3: Major oxide composition of garnets in run products: Mean values and 1σ standard deviation of EPMA measurements. Only major oxides are reported. Stoichiometry is calculated for each point measurement and normalised to 8 cations per formula unit. Not corrected for ferric Fe.

sample		SiO_2 wt%	Cr_2O_3 wt%	FeO wt%	Al_2O_3 wt%	MgO wt%	CaO wt%	total wt%	Si pfu	Cr pfu	Fe pfu	Al pfu	Mg pfu	Ca pfu	Mg#
V1102	mean	44.05	1.25	9.81	19.92	24.75	0.43	100.2	3.09	0.07	0.58	1.65	2.58	0.03	0.82
	σ	0.89	0.28	0.66	2.10	2.33	0.20		0.06	0.02	0.04	0.18	0.22	0.02	
V1050	mean	42.08	1.21	7.50	20.39	18.68	9.77	99.63	3.01	0.07	0.45	1.72	1.99	0.75	0.82
	σ	1.22	0.38	0.71	2.59	2.19	1.94		0.11	0.02	0.04	0.21	0.21	0.16	
V1064	mean	42.29	1.24	8.57	22.29	15.97	10.26	100.62	3.03	0.07	0.51	1.88	1.71	0.79	0.77
	σ	0.19	0.24	0.29	0.42	0.90	1.28		0.01	0.01	0.02	0.03	0.09	0.10	
V1065	mean	43.28	0.85	7.86	17.54	21.86	9.40	100.78	3.04	0.05	0.46	1.46	2.27	0.71	0.83
	σ	1.20	0.41	0.61	5.97	7.78	2.88		0.12	0.02	0.04	0.51	0.75	0.23	
V1077	mean	42.71	0.73	7.53	16.00	21.49	10.59	99.04	3.06	0.04	0.45	1.37	2.26	0.82	0.83
	σ	2.43	0.48	1.16	6.96	10.14	4.18		0.22	0.03	0.07	0.61	0.95	0.34	
V1089	mean	37.47	1.88	7.55	20.61	8.02	21.66	97.19	2.86	0.11	0.48	1.85	0.91	1.77	0.65
	σ	1.70	1.53	1.36	1.01	0.56	1.12		0.12	0.09	0.09	0.09	0.06	0.09	

Table B.3 continued

sample		SiO_2 wt%	Cr_2O_3 wt%	FeO wt%	Al_2O_3 wt%	MgO wt%	CaO wt%	total wt%	Si pfu	Cr pfu	Fe pfu	Al pfu	Mg pfu	Ca pfu	Mg#
V1099	mean	40.65	1.82	8.13	21.33	16.53	9.86	98.32	2.98	0.11	0.50	1.84	1.80	0.77	0.78
	σ	0.84	0.65	0.41	0.61	0.94	1.12		0.03	0.04	0.03	0.04	0.09	0.10	
V1103	mean	40.75	1.24	8.84	20.17	12.05	16.75	99.8	2.99	0.07	0.54	1.75	1.32	1.32	0.71
	σ	0.69	0.58	0.44	0.76	0.19	0.66		0.02	0.03	0.03	0.05	0.03	0.05	
V1156	mean	43.51	0.41	5.93	9.26	38.48	1.78	99.37	2.92	0.02	0.33	0.74	3.84	0.13	0.92
	σ	1.57	0.18	0.17	5.09	7.43	1.39		0.16	0.01	0.01	0.42	0.65	0.10	

Table B.4: Major oxide composition of clinopyroxene in run products: Mean values and 1σ standard deviation of EPMA measurements. Stoichiometry is normalised to 4 cations per formula unit. Reported are only major oxides. Mg# refers to molar MgO/(MgO+FeO).

sample		SiO_2 wt%	FeO wt%	Al_2O_3 wt%	MgO wt%	CaO wt%	total pfu	Si pfu	Fe pfu	Al pfu	Mg	Ca	Mg#
V1050	mean	48.99	3.27	2.43	19.56	20.06	94.3	1.85	0.10	0.11	1.10	0.81	0.91
	σ	0.93	1.13	1.33	4.04	4.75		0.06	0.03	0.06	0.21	0.19	
V1057	mean	51.46	2.50	0.94	17.69	24.01	96.59	1.92	0.08	0.04	0.98	0.96	0.93
	σ	1.23	1.42	1.32	0.72	0.86		0.04	0.04	0.06	0.04	0.03	
V1062	mean	53.11	2.54	2.33	17.74	23.24	98.96	1.94	0.08	0.10	0.97	0.91	0.93
	σ	0.73	0.18	0.39	0.59	0.85		0.02	0.01	0.02	0.03	0.03	
V1064	mean	52.97	2.77	2.16	18.55	22.61	99.06	1.93	0.08	0.09	1.00	0.88	0.92
	σ	0.84	0.40	0.42	1.57	1.15		0.04	0.01	0.02	0.07	0.06	
V1065	mean	53.57	2.57	1.68	19.19	22.06	99.07	1.94	0.08	0.07	1.04	0.86	0.93
	σ	1.27	0.21	0.17	1.37	1.07		0.04	0.01	0.01	0.08	0.04	
V1071	mean	50.35	3.30	0.99	23.79	19.38	97.81	1.82	0.10	0.04	1.28	0.75	0.93
	σ	0.46	0.43	0.47	0.48	0.54		0.02	0.01	0.02	0.02	0.03	
V1076	mean	52.97	2.65	0.66	19.56	22.43	98.26	1.94	0.08	0.03	1.07	0.88	0.93
	σ	0.91	0.50	0.27	1.31	1.91		0.03	0.02	0.01	0.07	0.08	
V1077	mean	53.01	2.34	2.45	18.03	23.07	98.89	1.93	0.07	0.11	0.98	0.90	0.93
	σ	0.85	0.04	0.50	0.40	0.44		0.03	0.01	0.02	0.02	0.02	

Table B.4 continued

sample		SiO_2 wt%	FeO wt%	Al_2O_3 wt%	MgO wt%	CaO wt%	total pfu	Si pfu	Fe pfu	Al pfu	Mg	Ca	Mg#
V1082	mean	53.29	2.83	1.01	19.12	23.00	99.24	1.93	0.09	0.04	1.03	0.89	0.92
	σ	0.18	0.74	0.41	0.95	0.01		0.02	0.01	0.01	0.01	0.01	
V1089	mean	53.63	2.11	2.09	18.61	23.00	99.44	1.94	0.06	0.09	1.00	0.89	0.94
	σ	1.42	0.06	0.43	0.74	0.01		0.02	0.01	0.01	0.01	0.01	
V1099	mean	52.57	2.05	1.11	17.78	23.93	97.43	1.95	0.06	0.05	0.98	0.95	0.94
	σ	0.98	0.19	0.44	0.29	0.32		0.03	0.01	0.02	0.02	0.01	
V1103	mean	51.90	2.22	1.53	17.74	23.20	96.6	1.94	0.07	0.07	0.99	0.93	0.93
	σ	1.36	0.09	0.47	0.67	0.96		0.02	0.01	0.02	0.01	0.01	
V1148a	mean	53.66	2.90	0.36	17.57	23.21	97.7	1.99	0.09	0.02	0.97	0.92	0.92
	σ	0.64	1.27	0.08	1.30	0.46		0.02	0.04	0.01	0.07	0.02	
V1153b	mean	53.29	2.74	0.57	18.48	21.75	96.82	1.99	0.09	0.03	1.03	0.87	0.92
	σ	0.86	1.10	0.24	1.51	0.82		0.04	0.04	0.01	0.08	0.03	

Table B.5: Major oxide composition of orthopyroxene in run products: Mean values and 1σ standard deviation of EPMA measurements. Stoichiometry is normalised to 4 cations per formula unit. Mg# refers to molar MgO/(MgO+FeO).

sample		SiO$_2$ wt%	FeO wt%	Al$_2$O$_3$ wt%	MgO wt%	total wt%	Si pfu	Fe pfu	Al pfu	Mg pfu	Mg#
V1113	mean	53.39	4.66	3.08	35.92	97.05	1.86	0.14	0.13	1.87	0.93
	σ	0.83	0.70	0.99	1.43		0.01	0.02	0.04	0.05	
V1115	mean	54.94	5.78	0.55	36.65	97.92	1.95	0.17	0.03	1.84	0.92
	σ	1.64	0.12	0.21	1.67		0.02	0.01	0.01	0.02	
V1048	mean	53.95	5.75	5.00	34.48	99.18	1.85	0.17	0.20	1.76	0.91
	σ	0.66	0.31	0.40	0.36		0.02	0.01	0.02	0.02	
V1056	mean	54.36	5.65	5.33	34.05	99.39	1.86	0.16	0.22	1.74	0.91
	σ	1.25	0.37	1.22	0.64		0.03	0.01	0.05	0.03	
V1092	mean	57.88	5.04	1.10	35.96	99.99	1.97	0.14	0.04	1.83	0.93
	σ	0.31	0.37	0.49	0.40		0.02	0.01	0.01	0.02	
V1102	mean	55.86	5.38	3.25	34.45	98.93	1.92	0.16	0.13	1.77	0.92
	σ	0.20	0.48	0.10	0.43		0.02	0.01	0.01	0.02	
V1127	mean	58.01	0.78	0.61	39.33	98.73	1.96	0.02	0.02	1.98	0.99
	σ	0.56	0.20	0.13	0.32		0.01	0.01	0.01	0.01	
V1128	mean	55.90	6.04	0.63	35.71	98.28	1.94	0.18	0.03	1.85	0.91
	σ	1.30	0.58	0.19	1.19		0.05	0.02	0.01	0.05	
V1135a	mean	56.27	1.66	2.67	38.93	99.53	1.89	0.05	0.11	1.95	0.98
	σ	0.80	0.13	0.45	0.97		0.03	0.01	0.02	0.04	
V1135b	mean	55.15	5.41	2.72	35.00	98.28	1.91	0.16	0.11	1.81	0.92
	σ	0.54	1.02	0.41	0.44		0.02	0.03	0.02	0.03	
V1138a	mean	55.39	1.59	3.23	37.51	97.72	1.90	0.05	0.13	1.92	0.98
	σ	1.15	0.29	0.56	0.62		0.03	0.01	0.02	0.04	
V1138b	mean	55.66	3.91	3.39	34.28	97.23	1.94	0.11	0.14	1.79	0.94
	σ	0.90	0.44	0.65	0.70		0.02	0.01	0.03	0.03	
V1166	mean	56.23	4.58	1.22	35.96	97.99	1.95	0.13	0.05	1.86	0.93
	σ	0.26	0.10	0.45	0.42		0.01	0.01	0.02	0.02	
V1167	mean	55.95	4.51	1.63	36.34	98.42	1.92	0.13	0.07	1.86	0.93
	σ	0.01	0.05	0.08	0.55		0.02	0.01	0.01	0.01	

Table B.6: Major oxide composition of olivine in run products: Mean values and 1σ standard deviation of EPMA measurements. Stoichiometry is calculated for each point measurement and normalised to 3 cations per formula unit. Mg# refers to molar MgO/(MgO+FeO).

sample		SiO$_2$ wt%	FeO wt%	MgO wt%	total wt%	Si pfu	Fe pfu	Mg pfu	Mg#
V1113	mean	41.56	7.66	46.04	95.26	1.06	0.16	1.75	0.91
	σ	0.56	0.86	0.90		0.02	0.02	0.02	
V1115	mean	41.47	7.53	49.31	98.31	1.02	0.16	1.81	0.92
	σ	0.70	0.55	0.79		0.02	0.01	0.02	
V1116	mean	40.69	9.47	48.25	98.41	1.01	0.20	1.78	0.9
	σ	0.22	0.77	0.68		0.01	0.02	0.02	

Table B.6 continued

sample		SiO_2 wt%	FeO wt%	MgO wt%	total wt%	Si pfu	Fe pfu	Mg pfu	Mg#
V1117	mean	39.22	8.62	49.50	97.34	0.97	0.18	1.83	0.91
	σ	0.80	1.19	1.46		0.02	0.03	0.03	
V1159a	mean	38.73	11.75	47.76	98.23	0.97	0.25	1.78	0.88
	σ	0.76	2.99	2.26		0.02	0.07	0.06	
V1048	mean	40.98	8.51	50.96	100.45	0.99	0.17	1.83	0.91
	σ	0.50	0.22	0.54		0.01	0.01	0.02	
V1056	mean	40.83	8.56	51.35	100.74	0.98	0.17	1.84	0.91
	σ	0.18	0.15	0.18		0.01	0.01	0.01	
V1092	mean	40.80	8.01	50.24	99.05	1.00	0.16	1.83	0.92
	σ	0.21	0.24	0.27		0.01	0.01	0.02	
V1102	mean	41.66	8.51	49.22	99.39	1.02	0.17	1.79	0.91
	σ	0.37	0.49	1.43		0.02	0.01	0.03	
V1105	mean	42.16	8.60	48.47	99.23	1.03	0.18	1.77	0.91
	σ	0.83	0.55	1.61		0.03	0.01	0.04	
V1111	mean	40.72	9.62	48.45	98.79	1.00	0.20	1.78	0.9
	σ	0.64	1.14	1.40		0.02	0.02	0.04	
V1050	mean	40.38	9.06	50.80	100.25	0.98	0.18	1.83	0.91
	σ	0.62	0.16	0.35		0.01	0.01	0.01	
V1057	mean	40.67	9.84	49.09	99.6	0.99	0.20	1.79	0.9
	σ	0.77	0.08	0.53		0.02	0.01	0.02	
V1060	mean	40.93	8.20	49.80	98.93	1.00	0.17	1.81	0.92
	σ	0.40	0.83	1.04		0.01	0.02	0.03	
V1062	mean	40.55	8.85	50.34	99.73	0.98	0.18	1.82	0.91
	σ	0.46	0.30	0.55		0.01	0.01	0.01	
V1064	mean	41.20	9.18	50.23	100.62	0.99	0.19	1.81	0.91
	σ	0.28	0.34	0.66		0.01	0.01	0.02	
V1065	mean	41.24	9.35	50.15	100.73	0.99	0.19	1.80	0.91
	σ	0.39	0.42	0.57		0.01	0.01	0.01	
V1071	mean	40.26	8.72	50.84	99.82	0.97	0.18	1.83	0.91
	σ	0.47	0.95	0.89		0.01	0.02	0.03	
V1076	mean	40.42	10.27	48.80	99.49	0.99	0.21	1.78	0.89
	σ	0.59	0.58	0.96		0.02	0.01	0.02	
V1077	mean	40.86	8.62	50.07	99.55	0.99	0.18	1.81	0.91
	σ	0.55	0.20	0.63		0.01	0.01	0.02	
V1082	mean	39.16	12.40	46.91	98.47	0.97	0.26	1.74	0.87
	σ	0.41	1.26	1.12		0.02	0.02	0.03	
V1089	mean	40.72	8.97	50.08	99.77	0.99	0.18	1.81	0.91
	σ	0.81	0.36	0.38		0.01	0.01	0.01	
V1099	mean	40.14	8.62	49.88	98.64	0.99	0.18	1.82	0.91
	σ	0.31	0.19	0.35		0.01	0.01	0.01	
V1103	mean	41.32	8.57	50.95	100.85	0.99	0.17	1.82	0.91
	σ	0.13	0.14	0.15		0.01	0.01	0.01	
V1127	mean	42.46	0.65	56.21	99.32	1.00	0.01	1.98	0.99
	σ	1.06	0.08	0.75		0.03	0.01	0.03	
V1128	mean	40.69	8.06	49.64	98.39	1.00	0.17	1.82	0.92
	σ	0.72	0.25	0.94		0.02	0.01	0.02	
V1135a	mean	42.20	1.32	56.73	100.25	0.99	0.03	1.98	0.99
	σ	0.73	0.69	0.81		0.01	0.01	0.02	

Table B.6 continued

sample		SiO_2 wt%	FeO wt%	MgO wt%	total wt%	Si pfu	Fe pfu	Mg pfu	Mg#
V1135b	mean	40.71	7.83	51.97	100.51	0.98	0.16	1.86	0.92
	σ	0.28	0.80	0.83		0.01	0.02	0.02	
V1138a	mean	41.86	1.83	54.69	98.38	1.00	0.04	1.95	0.98
	σ	0.75	0.74	1.04		0.02	0.02	0.03	
V1138b	mean	41.35	5.18	51.66	98.18	1.01	0.11	1.88	0.95
	σ	0.59	0.54	0.68		0.02	0.01	0.02	
V1139	mean	32.87	24.87	32.65	90.4	0.95	0.61	1.41	0.7
	σ	4.59	6.09	3.73		0.09	0.18	0.10	
V1140	mean	36.98	16.14	37.72	90.84	1.03	0.37	1.56	0.81
	σ	1.67	4.78	3.69		0.04	0.10	0.09	
V1140 Fa	mean	35.08	35.92	26.90	97.89	1.00	0.86	1.13	0.57
	σ	1.37	6.30	4.81		0.01	0.18	0.17	
V1143b	mean	37.49	17.25	43.14	97.88	0.96	0.37	1.65	0.82
	σ	1.68	4.32	1.95		0.04	0.10	0.07	
V1150a	mean	44.23	0.55	53.24	98.02	1.06	0.01	1.90	0.99
	σ	0.30	0.01	0.78		0.02	0.01	0.01	
V1150b	mean	41.29	5.85	52.09	99.22	1.00	0.12	1.87	0.94
	σ	0.25	0.93	0.81		0.01	0.01	0.02	
ES372	mean	43.51	6.48	48.30	98.28	1.07	0.13	1.77	0.93
	σ	2.59	0.47	2.84		0.08	0.01	0.08	
V1156	mean	42.24	5.74	50.10	98.08	1.03	0.12	1.82	0.94
	σ	1.44	0.38	2.03		0.05	0.01	0.06	
V1166	mean	41.76	6.60	50.38	98.74	1.02	0.14	1.83	0.93
	σ	1.47	0.79	1.84		0.04	0.02	0.05	
V1167	mean	41.68	7.00	49.97	98.65	1.02	0.14	1.82	0.93
	σ	2.09	0.91	2.13		0.06	0.02	0.06	
V1172	mean	41.72	7.56	49.54	98.81	1.02	0.16	1.81	0.92
	σ	0.85	0.29	0.64		0.02	0.01	0.02	

Table B.7: Major oxide composition of olivine at the interface Serp-MgO in permeability experiments: Mean values and 1σ standard deviation of EPMA measurements. Mg# refers to molar MgO/(MgO+FeO). Note the higher Mg content compared to Ol in table B.6. Note also that for some experiments showing an Ol-layer it was not possible to measure the grains due to intergrowth of several phases.

sample		SiO_2 wt%	FeO wt%	MgO wt%	total wt%	SiO_2 pfu	FeO pfu	MgO pfu	Mg#
ES372	mean	40.74	4.16	53.24	98.15	0.98	0.08	1.91	0.96
	σ	0.27	0.66	1.04		0.01	0.01	0.02	
V1156	mean	41.35	4.29	53.24	98.87	0.99	0.09	1.90	0.96
	σ	1.04	0.75	1.80		0.03	0.02	0.05	
V1163	mean	40.25	3.05	54.50	97.79	0.96	0.06	1.94	0.97
	σ	0.54	0.78	0.86		0.02	0.02	0.03	
V1165	mean	40.41	3.90	53.38	97.69	0.97	0.08	1.92	0.96
	σ	0.54	0.29	1.01		0.01	0.01	0.03	

Table B.7 continued

sample		SiO$_2$ wt%	FeO wt%	MgO wt%	total wt%	SiO$_2$ pfu	FeO pfu	MgO pfu	Mg#
V1166	mean	40.31	3.94	54.41	98.65	0.96	0.08	1.94	0.96
	σ	0.13	0.85	0.87		0.01	0.02	0.02	
V1172	mean	40.87	3.13	53.68	97.69	0.98	0.06	1.93	0.97
	σ	0.58	0.48	0.75		0.01	0.01	0.01	

Table B.8: Major oxide composition of calcite in run products: Mean values and 1σ standard deviation of EPMA measurements. CO$_2$ content is calculated by difference for each point measurement. Stoichiometry is calculated based on all oxides and normalised to 1 cation per formula unit. Ca# is defined as the molar ratio of Ca/(Ca+Mg+Fe). Note deviation from ideal stoichiometry in V1050, V1076 due to intergrowth of Cal and Dol.

sample		FeO wt%	MgO wt%	CaO wt%	CO$_2$ wt%	total wt%	Fe pfu	Mg pfu	Ca pfu	Ca#
V1050	mean	1.32	2.95	46.53	49.20	99.6	0.02	0.08	0.90	0.9
	σ	0.16	0.45	1.05	0.69		0.01	0.01	0.01	
V1076	mean	0.58	4.00	57.32	38.10	99.78	0.01	0.09	0.90	0.9
	σ	0.01	0.08	1.15	0.76		0.01	0.01	0.01	
V1079	mean	0.20	0.14	56.54	43.12	99.73	0.01	0.01	0.99	0.99
	σ	0.05	0.37	0.77	0.62		0.01	0.01	0.01	
V1124	mean	0.17	0.07	55.52	44.24	99.71	0.01	0.01	0.99	1
	σ	0.02	0.10	0.50	0.51		0.01	0.01	0.01	
V1148a	mean	0.15	0.20	55.90	43.75	99.71	0.01	0.01	0.99	0.99
	σ	0.03	0.17	0.89	0.84		0.01	0.01	0.01	

Table B.9: Major oxide composition of dolomite in run products: Mean values and 1σ standard deviation of EPMA measurements. CO$_2$ content is calculated by difference for each point measurement. Stoichiometry is calculated based on all oxides and normalised to 2 cations per formula unit. Ca# is defined as the molar ratio of Ca/(Ca+Mg+Fe). Note deviation from ideal stoichiometry in V1050, V1062, V1076 due to intergrowth of Cal and Dol.

sample		FeO wt%	MgO wt%	CaO wt%	CO$_2$ wt%	total wt%	Fe pfu	Mg pfu	Ca pfu	Ca#
V1050	mean	1.33	11.05	49.15	38.47	99.57	0.02	0.23	0.75	0.75
	σ	0.05	0.91	1.67	0.74		0.01	0.02	0.02	
V1057	mean	1.92	21.23	30.45	46.40	99.06	0.02	0.48	0.49	0.49
	σ	0.26	1.46	2.79	4.14		0.01	0.02	0.02	
V1060	mean	1.48	20.10	28.66	49.77	99.6	0.02	0.48	0.49	0.5
	σ	0.35	0.49	1.17	1.74		0.01	0.01	0.01	
V1062	mean	1.25	10.28	49.78	38.69	99.56	0.02	0.22	0.76	0.77
	σ	0.10	0.67	1.41	1.11		0.01	0.02	0.02	
V1064	mean	1.92	21.81	30.25	46.01	99.57	0.02	0.49	0.49	0.49
	σ	0.08	0.09	0.63	0.54		0.01	0.01	0.01	

Table B.9 continued

sample		FeO wt%	MgO wt%	CaO wt%	CO_2 wt%	total wt%	Fe pfu	Mg pfu	Ca pfu	Ca#
V1065	mean	2.16	21.23	30.38	46.23	99.61	0.03	0.48	0.49	0.49
	σ	0.14	0.28	0.50	0.59		0.01	0.01	0.01	
V1071	mean	1.64	20.58	30.04	47.74	99.28	0.02	0.47	0.50	0.5
	σ	0.15	0.33	0.39	0.45		0.01	0.01	0.01	
V1076	mean	1.49	14.28	38.98	45.26	99.39	0.02	0.33	0.64	0.65
	σ	0.30	3.58	6.37	2.93		0.01	0.09	0.09	
V1077	mean	2.49	20.92	28.81	47.79	99.8	0.03	0.49	0.48	0.48
	σ	0.15	1.00	1.24	0.49		0.01	0.02	0.02	
V1082	mean	2.52	20.05	31.96	45.47	99.62	0.03	0.45	0.52	0.52
	σ	0.23	1.17	1.43	2.25		0.01	0.01	0.01	
V1089	mean	1.97	21.40	31.31	45.32	99.33	0.02	0.47	0.50	0.5
	σ	0.11	1.45	0.61	1.52		0.01	0.02	0.02	
V1099	mean	2.05	20.82	31.92	45.21	99.76	0.03	0.46	0.51	0.51
	σ	0.14	0.73	1.04	0.54		0.01	0.02	0.02	
V1103	mean	1.86	20.95	31.83	45.36	99.62	0.02	0.47	0.51	0.51
	σ	0.07	0.43	1.16	1.38		0.01	0.01	0.01	

Table B.10: Major oxide composition of magnesite in run products: Mean values and 1σ standard deviation of EPMA measurements. CO_2 content is calculated by difference for each point measurement. Stoichiometry is calculated based on all oxides and normalised to 1 cation per formula unit. Ca# is defined as the molar ratio of Ca/(Ca+Mg+Fe). Note deviation from ideal stoichiometry in V1148b due to intergrowth of Mgs and Cal.

sample		FeO wt%	MgO wt%	CaO wt%	CO_2 wt%	total wt%	Fe pfu	Mg pfu	Ca pfu	Ca#
V1089	mean	4.32	43.48	2.19	50.01	99.38	0.05	0.91	0.03	0.03
	σ	0.07	0.48	0.27	0.30		0.00	0.01	0.00	
V1099	mean	4.27	43.06	2.90	49.77	99.84	0.05	0.91	0.04	0.04
	σ	0.22	0.54	0.45	0.29		0.00	0.01	0.01	
V1103	mean	4.40	44.13	2.07	49.41	99.41	0.05	0.91	0.03	0.03
	σ	0.14	0.52	0.29	0.32		0.00	0.01	0.00	
V1148b	mean	2.94	40.23	6.32	50.52	99.49	0.04	0.86	0.10	0.1
	σ	0.29	2.20	2.64	0.52		0.00	0.04	0.04	
V1153a	mean	2.98	43.48	1.38	52.16	99.51	0.04	0.94	0.02	0.02
	σ	0.13	0.91	0.51	0.88		0.00	0.01	0.01	
V1153b	mean	2.23	44.76	1.04	51.97	99.41	0.03	0.95	0.02	0.02
	σ	0.23	0.75	0.70	0.20		0.00	0.01	0.01	

Table B.11: Major oxide composition of spinel in run products: Mean values and 1σ standard deviation of EPMA measurements. Low totals are obtained in samples with porous texture and small grain size. Stoichiometry is calculated for each point measurement and normalised to 3 cations per formula unit. Not corrected for ferric Fe.

sample		Cr_2O_3 wt%	FeO wt%	Al_2O_3 wt%	MgO wt%	total wt%	Cr pfu	Fe pfu	Al pfu	Mg pfu	Mg#
V1056	mean	14.54	9.39	54.27	21.10	99.3	0.30	0.21	1.67	0.82	0.8
	σ	0.63	0.11	0.27	0.12		0.01	0.01	0.01	0.01	
V1062	mean	18.82	23.54	36.92	14.78	94.06	0.45	0.59	1.27	0.65	0.52
	σ	7.02	4.47	10.73	2.04		0.20	0.15	0.29	0.06	
V1064	mean	27.09	21.41	29.76	12.82	91.08	0.68	0.57	1.11	0.61	0.52
	σ	1.18	3.30	1.35	0.81		0.04	0.08	0.03	0.03	
V1065	mean	33.01	24.00	24.82	11.05	92.88	0.85	0.65	0.95	0.53	0.45
	σ	0.66	0.48	0.50	0.22		0.01	0.01	0.01	0.01	
V1076	mean	29.38	38.24	14.22	9.86	91.7	0.80	1.10	0.57	0.50	0.31
	σ	0.59	0.77	0.28	0.20		0.01	0.01	0.01	0.01	
V1103	mean	21.77	28.98	13.48	17.13	81.36	0.61	0.86	0.57	0.91	0.51
	σ	0.44	0.58	0.27	0.34		0.01	0.01	0.01	0.01	
V1138b	mean	23.15	43.85	10.63	10.85	88.47	0.65	1.30	0.44	0.57	0.31
	σ	2.34	3.83	2.39	0.76		0.08	0.11	0.09	0.03	
V1146b	mean	34.98	24.68	24.44	10.55	94.65	0.89	0.67	0.93	0.51	0.43
	σ	0.70	0.49	0.49	0.21		0.01	0.01	0.01	0.01	

Table B.12: Major oxide composition of Fe metal and Fe-beaing oxide in experiments buffered with Fe. Mean values and 1σ standard deviation of EPMA measurements.

sample		Cr_2O_3 wt%	FeO wt%	MgO wt%	total wt%
V1139 Fe-metal	mean	0.08	124.10	0.02	124.19
	σ	0.05	0.62	0.02	
V1140 Fe-metal	mean	0.07	124.44	0.02	124.52
	σ	0.04	0.55	0.03	
V1139 Fe-oxide	mean	0.03	73.70	0.29	74.02
	σ	0.04	3.45	0.23	

Table B.13: Major oxide composition of magnetite in run products: Mean values and 1σ standard deviation of EPMA measurements.

sample		Cr_2O_3 wt%	FeO wt%	MgO wt%	total wt%
V1113	mean	21.99	55.83	2.44	80.26
	σ	2.27	6.77	0.37	
V1115	mean	19.02	63.15	4.28	86.44
	σ	1.06	1.83	1.04	
V1116	mean	7.04	79.55	1.98	88.56
	σ	12.14	15.11	0.42	
V1117	mean	3.58	84.73	1.09	89.4
	σ	7.86	10.60	0.40	
V1125	mean	0.04	88.83	0.60	89.47
	σ	0.02	0.45	0.44	
V1087	mean	2.43	86.58	0.24	89.25
	σ	2.32	2.67	0.12	
V1090	mean	4.60	84.88	0.26	89.74
	σ	5.24	6.07	0.13	
V1092	mean	5.51	82.29	1.90	89.69
	σ	6.89	7.05	0.92	
V1104	mean	3.85	85.08	0.49	89.41
	σ	4.27	4.65	0.40	
V1105	mean	2.08	86.80	1.44	90.32
	σ	1.42	2.23	0.81	
V1159b	mean	2.47	86.31	0.31	89.09
	σ	1.92	2.12	0.15	
V1057	mean	3.77	83.30	2.36	89.42
	σ	3.56	4.26	0.93	
V1060	mean	20.18	60.99	5.28	86.45
	σ	0.40	1.22	0.11	
V1071	mean	3.56	83.98	1.36	88.89
	σ	3.48	3.64	0.87	
V1079	mean	3.86	85.59	0.26	89.72
	σ	6.03	6.84	0.20	
V1124	mean	4.07	85.57	0.31	89.96
	σ	3.61	4.39	0.24	
V1128	mean	11.93	70.33	1.76	84.01
	σ	11.00	12.87	0.84	
V1132b	mean	0.06	87.70	0.77	88.53
	σ	0.04	0.46	0.43	
V1135b	mean	23.30	57.93	4.93	86.16
	σ	1.98	2.89	0.84	
V1146b	mean	0.06	88.01	0.66	88.74
	σ	0.04	1.08	0.40	
V1148b	mean	0.08	88.00	0.79	88.86
	σ	0.03	1.31	0.50	
V1150b	mean	1.07	86.42	0.36	87.85
	σ	1.12	1.41	0.28	
V1143a	mean	2.52	82.75	0.24	85.52
	σ	2.28	3.18	0.14	
V1148a	mean	3.47	85.42	0.26	89.14
	σ	1.71	2.09	0.13	
V1153b	mean	8.25	79.78	0.22	88.25
	σ	0.17	1.60	0.00	
V1160b	mean	3.56	86.26	0.28	90.1
	σ	4.58	4.88	0.15	

Table B.14: Major oxide composition of hematite in run products: Mean values and 1σ standard deviation of EPMA measurements.

sample		Cr_2O_3 wt%	FeO wt%	MgO wt%	total wt%
V1127	mean	2.05	80.39	0.51	82.96
	σ	3.96	4.67	0.19	
V1132a	mean	0.06	86.17	0.77	86.99
	σ	0.03	0.58	0.40	
V1135a	mean	9.44	75.60	0.36	85.39
	σ	5.91	5.93	0.16	
V1138a	mean	10.71	69.16	0.30	80.16
	σ	5.27	5.28	0.09	
V1146a	mean	1.17	84.26	0.76	86.19
	σ	4.58	6.44	0.49	
V1150a	mean	3.42	81.77	0.58	85.77
	σ	8.19	12.90	0.49	

Table B.15: Major oxide composition of iridium alloy in run products. Mean values and 1σ standard deviation of EPMA measurements.

sample		FeO wt%	IrO$_2$ wt%	total wt%
V1113	mean	1.21	114.05	115.26
	σ	0.02	2.28	
V1114	mean	1.72	114.08	115.8
	σ	0.03	2.28	
V1115	mean	1.12	114.88	116
	σ	0.02	2.30	
V1116	mean	0.93	114.48	115.41
	σ	0.02	2.29	
V1117	mean	0.88	116.07	116.95
	σ	0.02	2.32	
V1125	mean	1.46	115.74	117.2
	σ	0.03	2.32	
V1159a	mean	0.99	114.23	115.22
	σ	0.02	2.29	
V1087	mean	0.82	114.91	115.73
	σ	0.02	2.30	
V1090	mean	1.68	114.74	116.42
	σ	0.03	2.30	
V1092	mean	0.82	114.64	115.46
	σ	0.02	2.29	
V1102	mean	5.04	110.88	115.92
	σ	0.10	2.22	
V1104	mean	1.13	113.94	115.07
	σ	0.02	2.28	
V1105	mean	1.12	115.18	116.3
	σ	0.02	2.30	
V1111	mean	6.59	110.08	116.67
	σ	0.13	2.20	
V1159b	mean	0.90	114.92	115.82
	σ	0.02	2.30	
V1062	mean	1.15	115.05	116.2
	σ	0.02	2.30	
V1064	mean	3.43	112.39	115.82
	σ	0.07	2.25	
V1065	mean	3.11	113.14	116.25
	σ	0.06	2.26	
V1071	mean	1.30	115.01	116.31
	σ	0.03	2.30	
V1076	mean	2.67	113.09	115.76
	σ	0.05	2.26	
V1077	mean	3.83	110.88	114.71
	σ	0.08	2.22	
V1079	mean	1.01	114.92	115.93
	σ	0.02	2.30	
V1082	mean	1.67	113.95	115.62
	σ	0.03	2.28	
V1089	mean	6.10	107.25	113.35
	σ	0.12	2.15	
V1099	mean	4.16	112.91	117.07
	σ	0.08	2.26	
V1103	mean	1.01	114.28	115.29
	σ	0.02	2.29	
V1124	mean	2.06	115.55	117.61
	σ	0.04	2.31	
V1143b	mean	1.11	113.62	114.73
	σ	0.02	2.27	

C Mössbauer data

Table C.1: Hyperfine parameters derived from Mössbauer spectroscopy of starting materials and run products. Phases in parentheses were observed but could not measured with EPMA due to small grain sizes. Mgt labelled with * fits better with Hem hyperfine parameters. It is assigned here as Mgt based on a XRD analyses from which Hem could be clearly excluded. Note that not all samples listed in table B.13 do show Mgt, this is mainly based on the Cr content in Mgt.

sample	$Fe^{3+}/\Sigma Fe$	CS	FWHM	Int	QS	BHF	x^2	phase
Zer_1701	0.28(1)	1.14(1)	0.35(1)	40.6(24)	2.68(1)	-(-)	1.96	Fe^{2+} Serp
		0.37(2)	0.51(4)	15.7(13)	0.70(2)	-(-)		Fe^{3+} Serp
		0.24(1)	0.24(4)	11.3(21)	0.00(-)	48.4(2)		Mgt
		0.67(2)	0.47(6)	32.5(34)	0.00(-)	45.3(2)		Mgt
Lig_1602	0.71(1)	1.12(1)	0.32(2)	18.6(23)	2.66(1)	-(-)	1.10	Fe^{2+} Serp
		0.40(2)	0.49(4)	29.5(42)	0.67(5)	-(-)		Fe^{3+} Serp (octahedral)
		0.18(9)	0.27(7)	12.7(43)	0.39(3)	-(-)		Fe^{3+} Serp (tetrahedral)
		0.25(2)	0.23(8)	8.93(31)	0.00(-)	48.7(3)		Mgt
		0.67(3)	0.51(12)	30.3(59)	0.00(-)	46.0(4)		Mgt
Zer_1701								
V1087 (12mm/s)	0.20(3)	1.15(1)	0.25(2)	53.9(34)	2.73(1)	-(-)	1.16	Fe^{2+} Serp
		0.40(4)	0.27(37)	13.6(20)	0.66(6)	-(-)		Fe^{3+} Serp
		0.25(3)	0.12(11)	10.7(27)	0.06(7)	49.3(3)		Mgt
		0.67(4)	0.40(13)	21.9(37	0.03(8)	45.6(3)		Mgt
V1087 (5mm/s)	0.19(2)	1.11(1)	0.25(2)	56.7(23)	2.66(1)	-(-)	1.34	Fe^{2+} Serp
		0.41(3)	0.23(29	12.9(13)	0.64(4)	-(-)		Fe^{3+} Serp
		0.25(-)	0.12(-)	6.3(18)	0.06(-)	49.34(-)		Mgt

Table C.1: continued

sample	$Fe^{3+}/\Sigma Fe$	CS	FWHM	Int	QS	BHF	x^2	phase
		0.67(-)	0.40(-)	24.1(24)	0.03(-)	45.6(-)		Mgt
V1090 (12mm/s)	0.16(2)	1.15(1)	0.25(2)	57.3(28)	2.75(1)	-(-)	1.65	Fe^{2+} Serp
		0.41(5)	0.33(30)	10.8(18)	0.64(7)	-(-)		Fe^{3+} Serp
		0.28(3)	0.13(9)	9.6(20)	-0.00(5)	49.2(2)		Mgt
		0.71(4)	0.51(12)	22.4(29)	0.02(7)	45.8(3)		Mgt
V1090 (5mm/s)	0.14(2)	1.12(1)	0.27(2)	58.1(27)	2.69(1)	-(-)	1.05	Fe^{2+} Serp
		0.40(4)	0.24(38)	9.6(14)	0.60(6)	-(-)		Fe^{3+} Serp
		0.28(-)	0.13(-)	5.8(18)	-0.00(-)	49.2(-)		Mgt
		0.71(-)	0.51(-)	26.4(28)	0.02(-)	45.8(-)		Mgt
V1159b (12mm/s)	0.13(2)	1.12(1)	0.31(2)	58.8(32)	2.71(1)	-(-)	0.70	Fe^{2+} Serp
		0.41(4)	0.23(40)	9.0(17)	0.60(7)	-(-)		Fe^{3+} Serp
		0.28(3)	0.19(11)	12.5(27)	0.06(6)	49.1(2)		Mgt
		0.68(4)	0.38(12)	19.6(32)	-0.02(7)	45.7(3)		Mgt
V1159b (5mm/s)	0.13(1)	1.14(1)	0.30(1)	60.4(15)	2.69(1)	-(-)	1.32	Fe^{2+} Serp
		0.44(3)	0.29(20)	9.0(10)	0.57(4)	-(-)		Fe^{3+} Serp
		0.27(-)	0.19(-)	9.1(11)	0.06(-)	49.1(-)		Mgt
		0.68(-)	0.38(-)	21.5(14)	-0.02(-)	45.7(-)		Mgt
V1104 (12mm/s)	0.18(2)	1.14(2)	0.24(2)	59.5(30)	2.72(1)	-(-)	1.40	Fe^{2+} Serp
		0.40(3)	0.21(37)	13.1(16)	0.62(5)	-(-)		Fe^{3+} Serp
		0.26(3)	0.10(10)	9.8(24)	0.04(6)	49.5(2)		Mgt
		0.67(3)	0.26(11)	17.6(30)	-0.03(6)	46.1(2)		Mgt
V1105 (12mm/s)	0.05(6)	1.15(1)	0.21(2)	66.3(52)	2.97(1)	-(-)	1.02	Fe^{2+} Serp/Chl/(Opx)

Table C.1: continued

sample	$Fe^{3+}/\Sigma Fe$	CS	FWHM	Int	QS	BHF	x^2	phase
		0.39(160)	0.18(180)	3.8(46)	0.63(300)	-(-)		Fe^{3+} Serp/Chl
		1.16(13)	0.20(6)	29.9(45)	2.17(25)	-(-)		Ol
V1105 (5mm/s)	0.06(4)	1.14(1)	0.26(2)	61.4(35)	2.94(1)	-(-)	0.90	Fe^{2+} Serp/Chl/(Opx)
		0.36(79)	0.23(107)	4.1(30)	0.58(145)	-(-)		Fe^{3+} Serp/Chl
		1.14(6)	0.18(9)	34.5(32)	2.16(12)	-(-)		Ol
V1111 (12mm/s)	-	1.16(1)	0.22(2)	68.3(23)	3.00(1)	-(-)	1.09	Fe^{2+} Serp/Chl/(Opx)
		1.16(1)	0.22(4)	31.7(23)	2.16(2)	-(-)		Ol
V1111 (5mm/s)	-	1.15(1)	0.24(1)	65.5(15)	2.98(1)	-(-)	0.87	Fe^{2+} Serp/Chl/(Opx)
		1.15(1)	0.14(9)	34.5(15)	2.13(1)	-(-)		Ol
V1092 (12mm/s)	0.04(5)	1.13(1)	0.22(3)	58.3(48)	2.94(1)	-(-)	0.96	Fe^{2+} Opx/Chl
		0.43(136)	0.20(146)	2.4(31)	0.71(158)	-(-)		Fe^{3+} Chl
		1.13(7)	0.16(10)	28.1(46)	2.12(14)	-(-)		Ol
		0.45(5)	0.24(16)	11.2(33)	-0.01(9)	49.7(3)		Hem^*
V1102 (12mm/s)	-	1.15(1)	0.20(1)	67.8(19)	3.01(1)	-(-)	1.02	Fe^{2+} Opx/Grt
		1.17(1)	0.25(4)	32.2(19)	2.17(2)	-(-)		Ol
V1102 (5mm/s)	-	1.15(1)	0.21(2)	70.5(16)	3.01(1)	-(-)	1.80	Fe^{2+} Opx/Grt
		1.16(1)	0.28(5)	29.5(16)	2.18(2)	-(-)		Ol
Zer_1701 with 20wt% $CaCO_3$								
V1079 (5mm/s)	0.20(4)	1.13(1)	0.37(3)	62.2(79)	2.70(1)	-(-)	0.82	Fe^{2+} Serp
		0.41(7)	0.47(19)	15.6(36)	0.67(9)	-(-)		Fe^{3+} Serp
		0.66(6)	0.30(25)	15.5(73)	0(-)	45.2(7)		Mgt
		0.28(6)	0.13(21)	6.7(50)	0(-)	47.9(8)		Mgt

Table C.1: continued

sample	$Fe^{3+}/\Sigma Fe$	CS	FWHM	Int	QS	BHF	x^2	phase
V1124 (5mm/s)	0.16(2)	1.14(1)	0.30(1)	55.4(15)	2.73(1)	-(-)	1.17	Fe^{2+} Serp
		0.44(5)	0.36(19)	10.7(17)	0.57(6)	-(-)		Fe^{3+} Serp
		0.24(3)	0.10(12)	7.8(33)	0(-)	48.2(4)		Mgt
		0.74(3)	0.26(12)	26.01(52)	0(-)	45.3(4)		Mgt
V1082 (5mm/s)	-	1.15(1)	0.16(2)	46.5(15)	3.07(3)	-(-)	0.70	Fe^{2+} Chl/Serp/Cpx
		1.11(1)	0.16(9)	53.5(15)	2.86(6)	-(-)		Ol
V1057 (5mm/s)	-	1.14(1)	0.24(2)	56.3(43)	2.93(1)	-(-)	1.17	Fe^{2+} Chl/Serp/Cpx
		1.22(2)	0.62(11)	43.7(43)	1.98(9)	-(-)		Ol
Lig_1602								
V1125 (12mm/s)	0.42(3)	1.15(1)	0.28(3)	43.3(36)	2.74(1)	-(-)	1.54	Fe^{2+} Serp
		0.42(4)	0.41(9)	30.9(35)	0.56(5)	-(-)		Fe^{3+} Serp
		0.27(5)	0.10(15)	8.0(30)	0.06(9)	49.1(4)		Mgt
		0.70(3)	0.19(11)	17.8(37)	0.04(6)	45.9(3)		Mgt
V1114 (5mm/s)	0.29(4)	1.13(1)	0.25(3)	57.9(76)	2.86(3)	-(-)	1.57	Fe^{2+} Serp/Chl/(Opx)
		0.35(3)	0.56(10)	23.3(41)	0.60(6)	-(-)		Fe^{3+} Serp/Chl
		1.15(2)	0.22(27)	18.8(88)	2.39(15)	-(-)		(Ol)
V1159a (5mm/s)	0.22(14)	1.13(2)	0.27(6)	58.7(249)	2.84(4)	-(-)	0.95	Fe^{2+} Serp
		0.41(14)	0.37(51)	16.6(111)	0.74(26)	-(-)		Fe^{3+} Serp
		1.06(9)	0.50(32)	24.7(278)	2.34(46)	-(-)		Ol
V1116 (5mm/s)	0.13(4)	1.14(1)	0.27(2)	69.7(68)	2.92(1)	-(-)	1.25	Fe^{2+} Serp/Chl/(Opx)
		0.36(6)	0.19(38)	10.2(32)	0.71(11)	-(-)		Fe^{3+} Serp/Chl
		1.27(5)	0.44(26)	20.1(71)	2.16(13)	-(-)		Ol

Table C.1: continued

sample	$Fe^{3+}/\Sigma Fe$	CS	FWHM	Int	QS	BHF	x^2	phase
V1117 (5mm/s)	0.29(6)	1.15(1)	0.30(3)	51.6(92)	2.89(2)	-(-)	1.39	Fe^{2+} Serp/Chl/(Opx)
		0.37(3)	0.35(20)	21.1(55)	0.60(12)	-(-)		Fe^{3+} Serp/Chl
		0.37(4)	0.10(13)	8.9(40)	0(-)	49.4(4)		Mgt
		0.57(12)	0.75(80)	13.0(120)	0(-)	44.5(21)		Mgt
		1.12(41)	0.58(86)	5.4(67)	2.05(128)	-(-)		Ol
V1113 (12mm/s)	-	1.14(1)	0.19(2)	68.0(32)	3.00(1)	-(-)	1.19	Fe^{2+} Chl/Opx
		1.16(1)	0.25(9)	32.0(33)	2.20(4)	-(-)		Ol
V1113 (5mm/s)	0.03(2)	1.14(5)	0.16(4)	25.0(20)	2.14(10)	-(-)	3.46	Ol
		1.13(1)	0.10(1)	73.0(21)	2.96(1)	-(-)		Fe^{2+} Chl/Opx
		0.43(42)	0.10(25)	2.0(13)	0.72(86)	-(-)		Fe^{3+} Chl
V1115 (5mm/s)	-	1.15(1)	0.13(3)	29.9(54)	3.08(4)	-(-)	1.22	Fe^{2+} Opx/Chl
		1.10(1)	0.18(4)	39.4(58)	2.90(4)	-(-)		Fe^{2+} Opx/Chl
		1.13(1)	0.19(4)	30.7(37)	2.13(1)	-(-)		Ol
Zer_1701 buffered								
V1143a (12mm/s)	0.19(3)	1.15(1)	0.24(3)	55.1(38)	2.69(1)	-(-)	1.34	Fe^{2+} Serp
		0.47(6)	0.33(32)	12.9(27)	0.57(8)	-(-)		Fe^{3+} Serp
		0.25(10)	0.10(10)	9.9(26)	-0.01(7)	49.1(3)		Mgt
		0.71(4)	0.37(13)	22.0(40	-0.04(8)	46.1(3)		Mgt
V1160b (12mm/s)	0.20(4)	1.13(1)	0.27(39)	45.7(32)	2.67(1)	-(-)	1.32	Fe^{2+} Serp
		0.43(7)	0.42(16)	11.4(26)	0.59(8)	-(-)		Fe^{3+} Serp
		0.25(6)	0.42(12)	20.3(34)	-0.15(7)	49.6(5)		Mgt
		0.77(7)	0.54(15)	22.5(36)	0.05(8)	46.2(5)		Mgt

Table C.1: continued

sample	$Fe^{3+}/\Sigma Fe$	CS	FWHM	Int	QS	BHF	x^2	phase
V1148a (5mm/s)	0.16(2)	1.13(1)	0.30(2)	66.9(38)	2.70(1)	-(-)	2.69	Fe^{2+} Serp
		0.43(9)	0.47(21)	12.8(20)	0.56(11)	-(-)		Fe^{3+} Serp
		0.23(5)	0.11(16)	6.2(25)	0(-)	48.3(6)		Mgt
		0.73(5)	0.30(18)	14.1(39)	0(-)	45.3(5)		Mgt
Lig_1602 buffered								
V1132a (12mm/s)	0.85(5)	1.20(4)	0.15(20)	7.2(29)	2.55(8)	-(-)	2.08	Fe^{2+} Serp
		0.34(3)	0.49(9)	40.5(29)	0.66(4)	-(-)		Fe^{3+} Serp
		0.38(1)	0.10(2)	52.3(30)	-0.19(1)	52.0(1)		Hem
V1146a 12(mm/s)	0.91(8)	1.28(7)	0.34(27)	4.5(42)	2.48(15)	-(-)	2.90	Fe^{2+} Serp/Chl
		0.52(8)	1.15(38)	42.6(43)	0.98(13)	-(-)		Fe^{3+} Serp/Chl
		0.30(1)	0.22(3)	52.9(43)	-0.40(2)	52.0(1)		Hem
V1150a (12mm/s)	0.88(10)	1.29(11)	0.40(35)	5.1(47)	2.46(24)	-(-)	2.70	Fe^{2+} Serp
		0.50(7)	0.83(21)	38.1(52)	0.96(11)	-(-)		Fe^{3+} Serp
		0.30(1)	0.21(3)	56.7(53)	-0.40(2)	52.0(1)		Hem
V1127 (12mm/s)	0.49(9)	1.18(8)	0.20(-)	5.2(14)	2.87(15)	-(-)	9.44	Fe^{2+} Serp/Chl
		0.42(10)	0.20(-)	5.0(12)	0.53(14)	-(-)		Fe^{3+} Serp/Chl
		0.37(1)	0.31(3)	89.8(18)	0.06(2)	51.8(1)		Hem
V1132b (12mm/s)	0.59(4)	1.17(1)	0.25(4)	27.7(33)	2.65(2)	-(-)	0.94	Fe^{2+} Serp/Chl
		0.40(3)	0.44(8)	39.5(37)	0.59(4)	-(-)		Fe^{3+} Serp/Chl
		0.26(3)	0.10(10)	12.5(31)	-0.01(6)	48.9(3)		Mgt
		0.73(3)	0.23(12)	20.4(39)	0.09(6)	46.3(3)		Mgt
V1146b (12mm/s)	0.42(5)	1.11(2)	0.37(7)	41.8(28)	2.75(3)	-(-)	0.96	Fe^{2+} Serp

Table C.1: continued

sample	$Fe^{3+}/\Sigma Fe$	CS	FWHM	Int	QS	BHF	x^2	phase
		0.42(3)	0.42(13)	30.3(53)	0.75(5)	-(-)		Fe^{3+} Serp
		0.31(5)	0.24(17)	14.1(57)	0(-)	49.3(4)		Mgt
		0.67(7)	0.30(22)	13.8(63)	0(-)	46.0(5)		Mgt
V1150b (5mm/s)	0.37(3)	1.13(1)	0.29(4)	41.5(36)	2.85(1)	-(-)	1.08	Fe^{2+} Serp
		0.41(2)	0.50(7)	24.1(26)	0.86(3)	-(-)		Fe^{2+} Serp
		0.44(2)	0.16(7)	26.7(36)	0(-)	50.8(3)		Mgt
		0.79(12)	0.36(49)	7.7(61)	0(-)	42.4(14)		Mgt
V1128 (12mm/s)	0.08(4)	1.13(1)	0.21(3)	66.1(62)	2.97(2)	-(-)	1.08	Fe^{2+} Serp/Chl/Opx
		0.41(6)	0.10(61)	5.6(32)	0.46(11)	-(-)		Fe^{3+} Serp/Chl
		1.11(2)	0.14(43)	28.3(61)	2.2(6)	-(-)		Ol
V1143b (5mm/s)	0.28(4)	1.14(1)	0.30(5)	71.79(45)	2.80(2)	-(-)	1.03	Fe^{2+} Serp
		0.42(7)	0.37(31)	28.21(54)	0.57(10)	-(-)		Fe^{3+} Serp
V1139 (12mm/s)	0.15(11)	1.15(1)	0.16(4)	37.4(26)	2.98(4)	-(-)	0.99	Fe^{2+} Serp
		0.44(6)	0.27(54)	6.4(36)	0.68(11)	-(-)		Fe^{3+} Serp
		1.12(1)	0.25(26)	44.4(255)	2.69(20)	-(-)		Ol
		-0.01(2)	0.15(6)	11.8(63)	0.01(5)	32.8(1)		Fe-phase

D Calculated oxygen fugacity

Table D.1: $f(O_2)$ and deviation from FMQ. The reactions used to calculate $f(O_2)$ are listed in table 2.3. $f(O_2)$ derived from buffer equilibria are marked as * Re + O_2 = ReO_2 (RRE), ** Ru + O_2 = RuO_2 (RRU), *** CCO from a parameterised form (Frost and Wood, 1997). **** refers to $f(O_2)$ calculated as outlined in chapter 8. Note that experiments V1139 and V1140 were buffered with Fe-metal. The $f(O_2)$ in these experiments is calculated from silicates and oxides and is higher than IW as equilibrium was probably not achieved through the whole sample.

sample	$f(O_2$	σ	ΔFMQ
V1113	-14.938	0.405	1.645
V1115	-13.819	0.165	1.616
V1116	-15.189	0.173	1.757
V1117	-14.596	0.315	1.928
V1125	-19.519	0.018	1.406
V1159a	-15.504	0.582	0.019
V1048	-6.912	0.137	3.262
V1056	-6.233	0.166	3.356
V1087	-19.602	0.016	1.905
V1090	-15.740	0.019	0.830
V1092	-12.074	0.186	1.678
V1102	-12.478	0.454	-0.130
V1104	-15.820	0.017	1.561
V1105	-14.148	0.140	1.850
V1111	-13.528	0.260	2.018
V1159b	-14.536	0.016	0.987
V1050	-6.134	0.037	3.522
V1057	-14.109	2.085	2.283
V1060	-9.447	0.231	3.212
V1062	-12.294	0.073	0.586
V1064	-12.842	0.128	-0.401
V1065	-12.275	0.098	-0.299
V1071	-14.045	0.345	1.667
V1076	-15.798	0.171	0.536
V1077	-13.885	0.049	-0.597

sample	$f(O_2$	σ	ΔFMQ
V1079	-18.417	0.017	1.712
V1082	-17.100	0.413	1.414
V1089	-13.220	0.087	-1.780
V1099	-11.266	0.083	-0.768
V1103	-11.403	0.038	0.476
V1124	-17.329	0.020	1.044
V1127**	-6.714	0.000	8.856
V1128*	-14.270	0.000	1.542
V1132a**	-10.049	0.000	10.823
V1132b*	-19.027	0.000	1.844
V1135a**	-5.982	0.000	8.432
V1135b*	-12.927	0.000	1.487
V1138a**	-4.614	0.000	7.653
V1138b*	-10.865	0.000	1.404
V1139	-20.722	0.368	-0.437
V1140	-16.400	0.604	0.607
V1143b****	-18.612	0.204	1.830
V1146a**	-7.547	0.000	9.282
V1146b*	-16.048	0.000	0.780
V1148b***	-19.390	0.000	1.235
V1150a**	-6.530	0.000	8.679
V1150b*	-14.482	0.000	0.728
V1153a***	-18.202	0.000	-1.306
V1148a***	-19.390	0.000	1.235
V1153b***	-18.202	0.000	-1.306

E Mass balance results

Table E.1: Mean value and 1σ standard deviation of phase modes from Monte Carlo simulation. Graphite was assumed to be pure C. Note that only phases which could be measured (table 3.1) were considered. Mg-hydroxide/-carbonate (labelled as MgO in table 3.1) was not considered since this phase was not further distinguished and generally only individual grains were observed in run products.

sample	phase wt%	mean wt%	1σ
V1113	Fluid	0.12	0.01
	Iridium	0.04	0.01
	Magnetite	0.03	0.03
	Olivine	0.6	0.11
	Orthopyroxene	0.15	0.11
	Chlorite	0.05	0.06
V1114	Fluid	$\leq$0.01	0.01
	Iridium	0.05	0.01
	Lizardite	0.86	0.09
	Chlorite	0.06	0.08
V1115	Fluid	0.12	0.02
	Magnetite	0.04	0.03
	Iridium	0.05	0.01
	Chlorite	0.09	0.09
	Olivine	0.49	0.1
	Orthopyroxene	0.2	0.1
V1116	Fluid	0.05	0.03
	Magnetite	0.03	0.02
	Iridium	0.05	0.01
	Lizardite	0.5	0.23
	Chlorite	0.02	0.05
	Olivine	0.35	0.17
V1117	Fluid	0.03	0.03
	Magnetite	0.03	0.03
	Iridium	0.05	0.01
	Lizardite	0.6	0.19
	Chlorite	0.03	0.05
	Olivine	0.24	0.15
V1125	Fluid	0.01	0.01
	Lizardite	0.89	0.03
	Iridium	0.05	0.01
	Magnetite	0.04	0.03
V1159a	Fluid	0.06	0.03
	Lizardite	0.47	0.22
	Iridium	0.05	0.01
	Olivine	0.4	0.19
V1048	Fluid	0.14	0.01
	Olivine	0.46	0.02
	Orthopyroxene	0.39	0.02
V1056	Fluid	0.14	0.01
	Olivine	0.45	0.02
	Orthopyroxene	0.39	0.03
V1087	Fluid	0.01	0.01
	Iridium	0.05	0.01
	Magnetite	0.03	0.01
	Antigorite	0.9	0.01
V1090	Fluid	$\leq$0.01	0.01
	Antigorite	0.92	0.01
	Iridium	0.05	0.01
	Magnetite	0.02	0.01
V1092	Fluid	0.11	0.01
	Chlorite	0.15	0.03
	Magnetite	0.02	0.01
	Iridium	0.05	0.01
	Olivine	0.38	0.02
	Orthopyroxene	0.29	0.02
V1102	Fluid	0.13	0.01
	Iridium	0.05	0.01
	Olivine	0.5	0.04
	Orthopyroxene	0.25	0.03
	Garnet	0.07	0.02
V1104	Fluid	0.02	0.01
	Antigorite	0.9	0.01
	Iridium	0.05	0.01
	Magnetite	0.03	0.01
V1105	Fluid	0.02	0.01
	Antigorite	0.81	0.07
	Magnetite	0.03	0.01
	Iridium	0.05	0.01
	Olivine	0.07	0.05
	Chlorite	0.02	0.02
V1111	Fluid	0.03	0.01
	Iridium	0.05	0.01
	Olivine	0.16	0.05
	Antigorite	0.71	0.07
	Chlorite	0.02	0.02
V1159b	Fluid	0.01	0.01
	Antigorite	0.74	0.01
	Iridium	0.04	0.01
	Magnetite	0.02	0.01
V1050	Fluid	0.15	0.01
	Garnet	0.06	0.02

Table E.1 continued

sample	phase	mean	1σ
	wt%	wt%	
	Olivine	0.44	0.03
	Calcite	0.03	0.04
	Dolomite	0.09	0.04
	Clinopyroxene	0.23	0.03
V1057	Fluid	0.09	0.02
	Magnetite	0.01	0.01
	Chlorite	0.09	0.04
	Antigorite	0.13	0.13
	Dolomite	0.18	0.02
	Clinopyroxene	0.23	0.03
	Olivine	0.27	0.08
V1060	Fluid	0.04	0.01
	Chlorite	0.23	0.05
	Dolomite	0.25	0.01
	Olivine	0.44	0.04
	Magnetite	≤0.01	0.01
V1062	Fluid	0.15	0.01
	Olivine	0.44	0.01
	Iridium	0.04	0.01
	Dolomite	0.11	0.01
	Clinopyroxene	0.23	0.01
	Spinel	0.02	0.01
V1064	Fluid	0.11	0.01
	Olivine	0.37	0.01
	Dolomite	0.17	0.01
	Clinopyroxene	0.24	0.01
	Garnet	0.05	0.01
	Iridium	0.04	0.01
	Spinel	≤0.01	0.01
V1065	Fluid	0.11	0.01
	Olivine	0.36	0.02
	Dolomite	0.18	0.01
	Clinopyroxene	0.23	0.02
	Iridium	0.04	0.01
	Garnet	0.07	0.04
	Spinel	0.01	0.01
V1071	Fluid	0.1	0.01
	Olivine	0.26	0.02
	Magnetite	0.01	0.01
	Iridium	0.04	0.01
	Chlorite	0.1	0.02
	Dolomite	0.16	0.01
	Clinopyroxene	0.32	0.01
V1076	Fluid	0.12	0.01
	Iridium	0.04	0.01
	Chlorite	0.11	0.02
	Calcite	0.08	0.04
	Dolomite	0.05	0.04
	Clinopyroxene	0.2	0.02

sample	phase	mean	1σ
	wt%	wt%	
	Olivine	0.39	0.02
	Spinel	≤0.01	0.01
V1077	Fluid	0.11	0.01
	Dolomite	0.18	0.01
	Diopside	0.23	0.02
	Olivine	0.37	0.02
	Iridium	0.04	0.01
	Garnet	0.07	0.03
V1079	Fluid	≤0.01	0.01
	Calcite	0.2	0.01
	Antigorite	0.74	0.01
	Iridium	0.04	0.01
	Magnetite	0.02	0.01
V1082	Fluid	0.07	0.01
	Iridium	0.04	0.01
	Dolomite	0.19	0.01
	Antigorite	0.18	0.09
	Chlorite	0.08	0.02
	Clinopyroxene	0.22	0.02
	Olivine	0.22	0.06
V1089	Fluid	0.12	0.01
	Dolomite	0.14	0.02
	Magnesite	0.02	0.02
	Iridium	0.04	0.01
	Olivine	0.38	0.02
	Garnet	0.06	0.01
	Clinopyroxene	0.23	0.03
V1099	Fluid	0.12	0.01
	Dolomite	0.15	0.01
	Magnesite	0.01	0.02
	Iridium	0.04	0.01
	Olivine	0.38	0.02
	Clinopyroxene	0.23	0.02
	Garnet	0.07	0.01
V1103	Fluid	0.12	0.01
	Dolomite	0.15	0.02
	Magnesite	0.01	0.02
	Iridium	0.04	0.01
	Olivine	0.38	0.02
	Garnet	0.07	0.01
	Clinopyroxene	0.23	0.02
	Spinel	0.01	0.01
V1124	Fluid	0.01	0.01
	Antigorite	0.73	0.01
	Calcite	0.2	0.01
	Iridium	0.04	0.01
	Magnetite	0.02	0.01
V1127	Fluid	0.1	0.03
	Hematite	0.09	0.03

Table E.1 continued

sample	phase wt%	mean wt%	1σ
	Chlorite	0.06	0.1
	Lizardite	0.16	0.21
	Olivine	0.33	0.12
	Orthopyroxene	0.25	0.11
V1128	Fluid	0.11	0.03
	Magnetite	0.04	0.03
	Lizardite	0.13	0.2
	Chlorite	0.05	0.08
	Olivine	0.45	0.15
	Orthopyroxene	0.2	0.11
V1132a	Fluid	0.01	0.01
	Lizardite	0.92	0.03
	Hematite	0.06	0.03
V1132b	Fluid	≤0.01	0.01
	Lizardite	0.88	0.09
	Chlorite	0.06	0.09
	Magnetite	0.04	0.03
V1135a	Fluid	0.13	0.01
	Chlorite	0.06	0.07
	Hematite	0.09	0.03
	Orthopyroxene	0.33	0.1
	Olivine	0.38	0.09
V1135b	Fluid	0.13	0.01
	Chlorite	0.07	0.08
	Magnetite	0.04	0.03
	Olivine	0.49	0.08
	Orthopyroxene	0.25	0.09
V1138a	Fluid	0.14	0.01
	Olivine	0.46	0.08
	Hematite	0.09	0.03
	Orthopyroxene	0.3	0.09
V1138b	Fluid	0.14	0.01
	Olivine	0.51	0.09
	Spinel	0.07	0.04
	Orthopyroxene	0.27	0.09
V1139	Fluid	0.05	0.04
	Fe	0.06	0.05
	Olivine	0.4	0.29
	Lizardite	0.47	0.28
	Fe-phase	0.01	0.03
V1140	Fluid	0.1	0.02
	Fe	0.02	0.03
	Fayalite	0.14	0.16
	Olivine	0.61	0.17
	Chlorite	0.11	0.09
V1143b	Fluid	0.06	0.04
	Graphite	0.09	0.01
	Lizardite	0.56	0.16
	Iridium	0.04	0.01
	Olivine	0.24	0.14

sample	phase wt%	mean wt%	1σ
V1146a	Fluid	≤0.01	0.01
	Hematite	0.07	0.03
	Chlorite	0.04	0.07
	Lizardite	0.88	0.07
V1146b	Fluid	≤0.01	0.01
	Magnetite	0.06	0.03
	Lizardite	0.92	0.03
	Spinel	0.01	0.02
V1148b	Fluid	≤0.01	0.01
	Graphite	0.02	0.01
	Magnetite	0.06	0.03
	Lizardite	0.83	0.05
	Magnesite	0.07	0.05
V1150a	Fluid	0.04	0.04
	Lizardite	0.59	0.23
	Hematite	0.08	0.03
	Olivine	0.28	0.18
V1150b	Fluid	0.03	0.03
	Lizardite	0.63	0.17
	Magnetite	0.05	0.03
	Olivine	0.28	0.14
V1153a	Fluid	≤0.01	0.01
	Graphite	0.02	0.01
	Lizardite	0.83	0.05
	Magnesite	0.08	0.05
V1143a	Fluid	0.01	0.01
	Antigorite	0.92	0.03
	Magnetite	0.05	0.03
V1148a	Fluid	≤0.01	0.01
	Graphite	0.02	0.01
	Magnetite	0.03	0.01
	Antigorite	0.88	0.01
	Calcite	0.06	0.01
	Diopside	0.01	0.01
V1153b	Fluid	0.01	0.01
	Graphite	0.01	0.01
	Magnetite	0.03	0.01
	Diopside	0.13	0.01
	Antigorite	0.71	0.02
	Magnesite	0.11	0.01
V1160b	Fluid	0.01	0.01
	Magnetite	0.04	0.03
	Antigorite	0.94	0.03

11 Acknowledgments

First I want to thank my supervisor Dan Frost. He gave me the opportunity to work on a very interesting topic with all the freedom needed to explore various aspects and to shape the project as a whole. It was a pleasure to learn a lot about experimental petrology and thermodynamics. Catherine McCammon is thanked for the help in Mössbauer spectroscopy and many fruitful discussions. Prof. Hans Keppler, Tiziana Boffa Ballaran and Florian Heidelbach is thanked for their help in the laboratory and in interpreting spectroscopy and diffraction data.

A big thank goes to the technical staff at BGI for their help in administrative and technical questions. A special thanks goes to Raphael Njul, Hubert Schulze and Alex Rother for the excellent sample preparation and for all the beautiful serpentine cylinders.

The IRTG brought me to Japan. I want to thank Prof. Akio Suzuki and the whole QUEST research group for all the help they provide in the lab and in daily life on the campus. Further I thank Shin-san and Shinobu-san for all the help in organising my stay in Japan. Prof. Michihiko Nakamura is further thanked for many discussions, field trips and the possibility to obtain synchrotron based CT-scans.

Prof. Gregor Golabek and Marcel Thielmann gave invaluable support in computation and organisation without that the Br project would not have been possible in this way.

A big thanks goes to all colleagues at BGI for the coffee breaks, dinners, excursions and discussions. Special thanks goes to Enrico, Nicco, Marija, Caterina, Serena, Egor and Nicki. It was a pleasure to experience the Japanese culture and explore the Japanese countryside with you.

Last but not least I want to thank my partner Stefan Wedler for all his support and patience during the last years. Not only he helped with numerous mathematical problems, he shared all the highs and lows that come along during graduate school. Thank you!

(Eidesstattliche) Versicherungen und Erklärungen

(§ 9 Satz 2 Nr. 3 PromO BayNAT)

Hiermit versichere ich eidesstattlich, dass ich die Arbeit selbstständig verfasst und keine anderen als die von mir angegebenen Quellen und Hilfsmittel benutzt habe (vgl. Art. 64 Abs. 1 Satz 6 BayHSchG).

(§ 9 Satz 2 Nr. 3 PromO BayNAT)

Hiermit erkläre ich, dass ich die Dissertation nicht bereits zur Erlangung eines akademischen Grades eingereicht habe und dass ich nicht bereits diese oder eine gleichartige Doktorprüfung endgültig nicht bestanden habe.

(§ 9 Satz 2 Nr. 4 PromO BayNAT)

Hiermit erkläre ich, dass ich Hilfe von gewerblichen Promotionsberatern bzw. -vermittlern oder ähnlichen Dienstleistern weder bisher in Anspruch genommen habe noch künftig in Anspruch nehmen werde.

(§ 9 Satz 2 Nr. 7 PromO BayNAT)

Hiermit erkläre ich mein Einverständnis, dass die elektronische Fassung meiner Dissertation unter Wahrung meiner Urheberrechte und des Datenschutzes einer gesonderten Überprüfung unterzogen werden kann.

(§ 9 Satz 2 Nr. 8 PromO BayNAT)

Hiermit erkläre ich mein Einverständnis, dass bei Verdacht wissenschaftlichen Fehlverhaltens Ermittlungen durch universitätsinterne Organe der wissenschaftlichen Selbstkontrolle stattfinden können.

………………………………………………………………………………………

Ort, Datum, Unterschrift